SLAC-131
UC-34
(TH) and (EXP)

LOW ENERGY PION-NUCLEON SCATTERING

BARBARA G. LEVI
STANFORD LINEAR ACCELERATOR CENTER
STANFORD UNIVERSITY
Stanford, California 94305

PREPARED FOR THE U. S. ATOMIC ENERGY
COMMISSION UNDER CONTRACT NO. AT(04-3)-515

July 1971

Printed in the United States of America. Available from National Technical Information Service, U. S. Department of Commerce, 5285 Port Royal Road, Springfield, Virginia 22151.
Price: Printed copy $3.00; Microfiche $0.95.

ABSTRACT

This report presents new data on the pion-nucleon scattering, both elastic and inelastic, in the energy region (1400-2000) MeV. Specifically, the following reactions have been studied:

$\pi^- p \rightarrow \pi^- p$	80,000 events	(1)
$\rightarrow \pi^- p \pi^0$	34,000 events	(2)
$\rightarrow \pi^- \pi^+ n$	52,000 events	(3)
$\rightarrow K^0 \Lambda$	1,000 events	(4)

The elastic scattering data (1), was critically compared with existing phase shift analysis solutions. A quasi-two-body phase shift analysis was applied to a subsample of reaction (3), $\pi^- p \rightarrow \pi^+ \Delta^-$, where Δ^- refers to the $N^*_{3/2^+}(1236)$ resonance, providing new understanding of the inelastic decay modes $N^*_{5/2^+}(1688)$, $N^*_{5/2^-}(1700)$.

A new phenomenological analysis combining the elastic and inelastic reactions has been developed. The method and some typical results are presented.

Finally, the data on strange particle final states, although sparse, fills in a hitherto uninvestigated energy region and allows a qualitative understanding of the πN interaction in this region.

TABLE OF CONTENTS

Page

LIST OF TABLES

LIST OF FIGURES

Page

Page

Page

Page

I. INTRODUCTION

The pion-nucleon interaction has been perhaps the most extensively studied interaction in particle physics. A wealth of data exists on the elastic scattering reactions, $\pi^{\pm}p \rightarrow \pi^{\pm}p$ and $\pi^{-}p \rightarrow \pi^{0}n$. These experimental data have encouraged development of rather sophisticated methods of analysis, so that we can now describe with a fair amount of confidence the behavior of many of the partial waves important in πN interactions. However, this progress has been made primarily in studies of the elastic channel below a center-of-mass energy of 2 GeV. To learn more about πN scattering at this stage requires not only extending present techniques to higher energies but also initiating studies of the other channels of πN scattering. Many features of the elastic channel are reflected more dramatically in these inelastic channels.

The first measurements of the πN interaction were measurements of the elastic and total cross sections. Plots of the elastic cross sections, shown in Fig. 1 for $\pi^{+}p$ and $\pi^{-}p$, indicate the presence of resonant behavior in the center-of-mass energy regions of 1236, 1520, 1680 and 1920 MeV. Because the $\pi^{+}p$ state is pure isospin 3/2, one can immediately identify the isospin of the "resonances". The first bump apparently has $I=3/2$ while the second and third, present only in the $\pi^{-}p$ cross section, have $I=1/2$. If each one of the bumps corresponded to a single resonant partial wave, we could furthermore identify its total angular momentum J; unitarity requirements give an upper limit on the cross section that depends on J. This upper bound was used to determine that the spin of the first resonance is $J=3/2$.

However, life is simple only at this first peak at 1236 MeV; the scattering amplitude grows increasingly complex at higher energies where more and more partial waves become important. The second and third bumps contain more

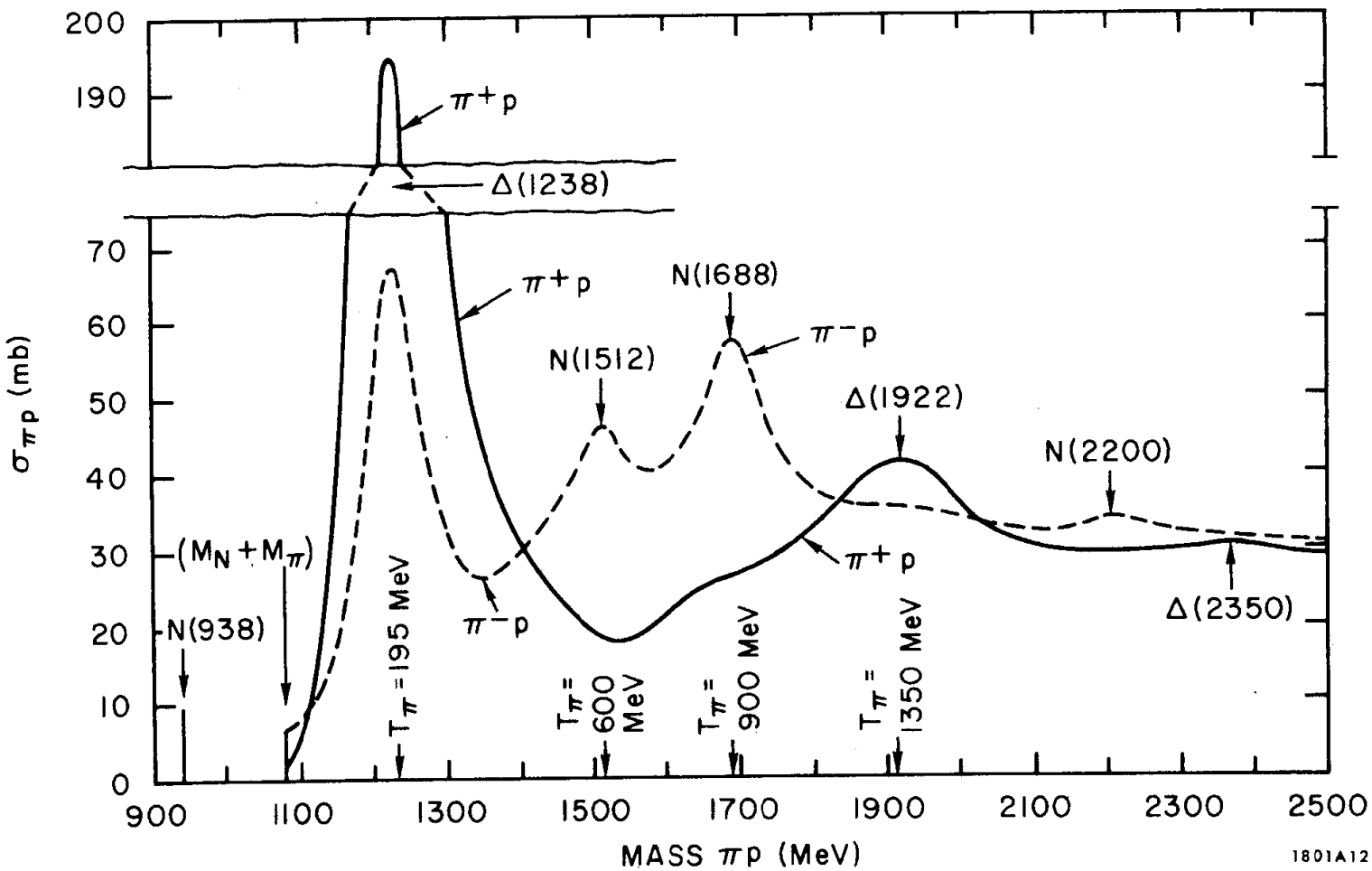

FIG. 1--Total cross sections for $\pi^- p$ and $\pi^+ p$ reactions.

than a single resonance each, and the absence of any sharp peaks beyond these may very well mean that the proliferation of partial wave resonances obscures the appearance of any one of them. Thus, at 1920 MeV, the broad, low bump probably indicates simultaneous activity of several partial waves. Measurement of the angular distributions and polarizations in elastic scattering were essential for the identification of the spin and parity of partial waves active in this area.

These angular distributions and polarizations can be fit with expansions in Legendre polynomials. From the energy dependence of the Legendre coefficients, one can then draw information regarding the behavior of the various partial waves. For example, the coefficients indicated an apparent interference of an s- and a p-wave near 1236 MeV. This observation led to the assignment of angular momentum $\ell = 1$ for the first resonance (commonly called P33, in the notation $\ell 2I2J$). Similar analyses identified the presence of a D13 wave near 1520 MeV and of both a D15 and F15 near 1690 MeV, with the F15 being stronger than the D15. Finally, there was evidence that an F37 partial wave was active near 1920 MeV.

Analysis of the Legendre coefficients was valuable in uncovering those partial waves primarily responsible for the gross features of elastic scattering especially at low energies. However, this type of study is limited to qualitative deductions. These deductions are based on assumptions about the behavior of other waves and can be deceptive when large numbers of partial waves are present. Finally, these arguments have not shed any light on highly inelastic partial waves that have small amplitudes for elastic scattering.

The method of phase-shift analysis has proved far more successful in extracting numerical parameters[1-11] that describe the behavior of the various

partial waves. We shall discuss the specific methods of parameterization at a later stage and focus attention here on the current results, as presented in Table I.[12] In this table, the resonances are described by their elasticities, masses and widths. Here one sees not only the P33, D13, D15, F15 and F37 that had been anticipated but also resonant behavior in many other partial waves. Table I is remarkable for the agreement among the various groups; yet there are still many resonances in dispute. Part of the discrepancies result because the groups use different methods and explore a very complex, multiparameter space. The discrepancies also arise from fluctuations among the data points themselves, which make it difficult to achieve a smooth energy dependence for the parameters. Thus one might hope that more accurate and systematic data could improve the phase shift solutions.

Even with improved data, there are inherent limitations in the phase-shift analysis, just as in all the methods previous to it. Because the complexities multiply as one goes to higher and higher energies, any future phase-shift analyses may have to incorporate some type of model. Phenomenological guidelines may help eliminate unreasonable parameters and direct the search for solutions. Some analyses that incorporate model dependency are already in progress; most attempt to relate what we know about high energy scattering to this transition region between low and high energy.

A supplement to the elastic scattering information is a measurement of the inelastic channels. A partial wave analysis of these could prove especially valuable because many of the partial waves disputed in Table I are highly inelastic.

It is against this necessary historical background that we must discuss the role of the present experiment. It is intended to provide systematic

TABLE I

S = 0 Baryon Resonances

I = 1/2 States

Phase Shift* Analysis	$P_{11}(1470)$			$D_{13}(1520)$			$S_{11}(1535)$			$D_{13}(1700)$			$D_{15}(1670)$			$F_{15}(1688)$		
	M	Γ	x	M	Γ	x	M	Γ	x	M	Γ	x	M	Γ	x	M	Γ	x
1	1470	255	0.68	1510	125	0.54	1535	155	-				1680	135	0.41	1690	110	0.64
2	1505	205	0.68	1515	110	0.54	1515	105	-	Possible			1655	105	0.41	1680	105	0.64
3	Definite			1526[a]	114[a]	0.57[a]	1548[a]	116[a]	0.326[a]	Possible			Definite			1692[a]	132[a]	0.68[a]
4	1466	211	0.658	1541	149	0.509	1591	(268)	0.696	-	-	-	1678	173	0.391	1687	177	0.56
5	1470	211	0.66	1520	114	0.57	1550	116	0.33	1730			1680	173	0.391	1690	132	0.68
6	1466	211	0.66	1526	115	0.57	1540	160	0.3	1680			1678	175	0.391	1692	130	0.68
7	1462	391	0.49	1512	106	0.45	1502	(36)	0.36	Not Present			1669	115	0.50	1685	104	0.54
8	1436	224	0.46	1512	125	0.49	1499	53	0.35	Not Present			1667	115	0.43	1684	123	0.54
Average	1468	244	0.61	1520	120	0.53	1535	118	0.39	1705			1672	142	0.42	1688	127	0.62
±	±19	±62	±.09	±10	±13	±.04	±28	±35	±.14	±25			±10	±29	±.04	±4	±22	±.06

	$S_{11}(1700)$			$P_{11}(1780)$			$P_{13}(1860)$			$F_{17}(1990)$			$D_{13}(2040)$			$G_{17}(2190)$		
	M	Γ	x	M	Γ	x	M	Γ	x	M	Γ	x	M	Γ	x	M	Γ	x
1	1710	260	-	Probable			Ambiguous[b]			b			b			b		
2	1665	110	-	Probable			Ambiguous[b]			b			b			b		
3	1709[a]	300[a]	0.786[a]	Probable			Ambiguous[b]			b			b			b		
4	-	-	-	1751	327	0.32	1863	296	0.207	1983	225	0.128	2057	293	0.26	2265	298	0.349
5	1710	300	0.79	1750	327	0.32	1860	296	0.21	-	-	-	2030	290	0.11	2190	300	0.35
6	1709	300	0.79	1860	270	0.32	1900	325	0.25	1995	250	0.09	2040	240	0.15	2265	300	0.35
7	1766	404	0.56	1770	445	0.43	1844	449	0.40	c			b			(1906)[c]	(319)[c]	(0.14)[c]
8	1671	121	0.51	(1867)	(525)	0.30	1854	307	0.26	c			b			c		
9							1860	-	-	2000	-	-	2030	-	-	2000		
Average	1706	256	0.69	1783	350	0.34	1864	335	0.27	1989	238	0.109	2039	274	0.17	2180	299	0.350
±	±31	±98	±.13	±45	±63	±.05	±17	±58	±.07	±6	±12	±.019	±11	±24	±.06	±35	±2	±.001

1801B27

Table I: S = 0 Baryon Resonances (cont'd.)

I = 3/2 States

Phase Shift* Analysis	$S_{31}(1650)$			$P_{33}(1690)$			$D_{33}(1670)$			$F_{35}(1890)$			$P_{31}(1910)$			$D_{35}(1960)$		
	M	Γ	x	M	Γ	x	M	Γ	x	M	Γ	x	M	Γ	x	M	Γ	x
1	1695	250	-	Ambiguous			Possible			Possible			Ambiguous[b]			Ambiguous[b]		
2	1650	130	-	Ambiguous			Possible			Possible			Ambiguous[b]			Ambiguous[b]		
3	Definite			Possible			Ambiguous			Probable			Probable[b]			b		
4	1635	177	0.284	1688	281	0.098	1691	269	0.14	1913	350	0.16	1934	339	0.30	1954	311	0.154
5	1640	177	0.28	1690	281	0.1	1690	269	0.14	1910	350	0.16	1930	339	0.3	-	-	-
6	1635	180	0.28	1690	240	0.08	1690	300	0.13	1910	380	0.15	1930	425	0.25	1970	400	0.12
7	1670	141	0.28	Not Present			1649	188	0.12	1841	136	0.2	1914	290	0.18		b	
8	1623	140	0.25	Not Present			1650	174	0.13	1852	150	0.19	1834	231	0.24		b	
9																1950	-	-
Average	1650	151	0.27	1689	267	0.93	1674	240	0.13	1885	273	0.17	1908	325	0.25	1958	356	0.14
±	±23	±89	±.12	±2	±19	±.09	±20	±50	±.01	±32	±107	±.02	±38	±64	±.04	±9	±44	±.02

	$F_{37}(1950)$			$P_{33}(2160)$		
	M	Γ	x	M	Γ	x
1	1975	180	0.57	b		
2	1980	140	-	b		
3	Definite			Possible[b]		
4	1946	221	0.386			
5	1950	221	0.39			
6	1946	220	0.39	2160	260	0.25
7	1935	221	0.51	b		
8	1935	212	0.39	b		
Average	1952	202	0.44	2160	260	0.25
±	±19	±29	±.07	-	-	-

*See Refs. 1 - 11 for various phase shift analyses.

() Values in parentheses have not been used in the averages.

a. Values quoted by Lovelace, rapporteur talk at Heidelberg Conference (1967), p. 109.

b. This state is very close to or beyond their highest energy.

c. Glasgow A has a G_{17} state at this mass; Glasgow B may have an F_{17} and a G_{17}, however, this energy is very close to their highest energy.

1801827

measurement of both the elastic channel and inelastic $\pi\pi N$ channels in $\pi^- p$ scattering from 1400 to 2000 MeV in center-of-mass energy. The elastic data should provide new input to the elastic phase-shift analysis. We anticipate such a use by comparing the predictions of the current phase shifts to our data.

We measured the inelastic reactions in order to study the branching ratios of the partial waves into these channels. Analysis of the three-body final state is more complex than that for the elastic reaction and we have taken basically two approaches to the problem. The first approach, along the lines of the isobar model, considers all possible quasi-two-body final states and the interactions among them. The second consists of a partial wave analysis of the $\Delta\pi$ final state. Both approaches are sensitive to the sign as well as the magnitude of the coupling of various waves and thus afford information not available in the elastic channel alone.

One extension of the quasi-two-body approach is to couple this $\Delta\pi$ channel to the elastic channel by the requirements of unitarity. The branching ratios into these two channels should simultaneously be consistent with unitarity. We outline such an approach and give preliminary results of this method applied to the elastic and inelastic data in our experiment. The coupled-channel analysis gives added sensitivity to the phase-shift type of analysis by including more information in the fits.

We also investigated the associated production reaction, $\pi^- p \rightarrow \Lambda^0 K^0$. This data falls in a region where very little data existed previously. Although the limited statistics preclude any quantitative analysis of partial waves, the behavior of the Legendre coefficients contains qualitative information regarding the partial waves. Finally, in light of the predictions of

exchange degeneracy, it is interesting to compare this data to the line-reversed reaction, $\bar{K}^0 p \rightarrow \Lambda^0 \pi^+$.

The second chapter deals with the details of the experiment and of the data analysis. Chapters III and IV present the results of the elastic and inelastic reactions, respectively. In Chapter V the technique of partial wave analysis in general is discussed and the predictions of elastic phase shifts are compared to our data. Chapter VI discusses the results of a partial wave analysis to our inelastic data. Chapter VII is devoted to a development of the coupled-channel approach and a presentation of preliminary results. Chapter VIII discusses the data analysis of the strange particle reaction, $\pi^- p \rightarrow \Lambda^0 K^0$, and contains the experimental results.

II. EXPERIMENTAL DETAILS AND DATA ANALYSIS

We studied elastic and inelastic $\pi^- p$ scattering, using the 30-inch hydrogen bubble chamber at the Argonne National Laboratory and the 72-inch Alvarez HBC at Berkeley. The Argonne exposure consists of approximately 500,000 pictures taken at 26 momenta between 550 and 865 MeV/c and between 1060 and 1600 MeV/c. The Berkeley exposure comprises about 200,000 pictures taken at 9 momenta between 925 and 1175 MeV/c. This latter film had been taken ten years previously, to study strange particle events above the Λ,Σ threshold,[13] but had not been used to investigate the two-prong events. Figure 2 illustrates the scope of the experiment. At each of the 35 momenta, the following reactions were measured:

$$\pi^- p \rightarrow \pi^- p \tag{2.1}$$

$$\rightarrow n\pi^+\pi^- \tag{2.2}$$

$$\rightarrow p\pi^-\pi^0 \tag{2.3}$$

$$\rightarrow \Lambda^0 K^0 \tag{2.4}$$

$$\rightarrow \Sigma^0_- K^0_+ \tag{2.5}$$

A. Beam

The Argonne film was taken during three separate exposures in 1967. The beam was the "7^0" separated beam[14] of the ZGS. The higher momentum exposures used the mode shown in Fig. 3a and b. Here the first stage provided at slit 1 both a momentum focus in the horizontal plane and an image of the target in the vertical plane. The second stage provided a momentum focus at the final slit together with an image of the target in both planes. A simplified version of the beam, Fig. 3c, was used for the low momentum

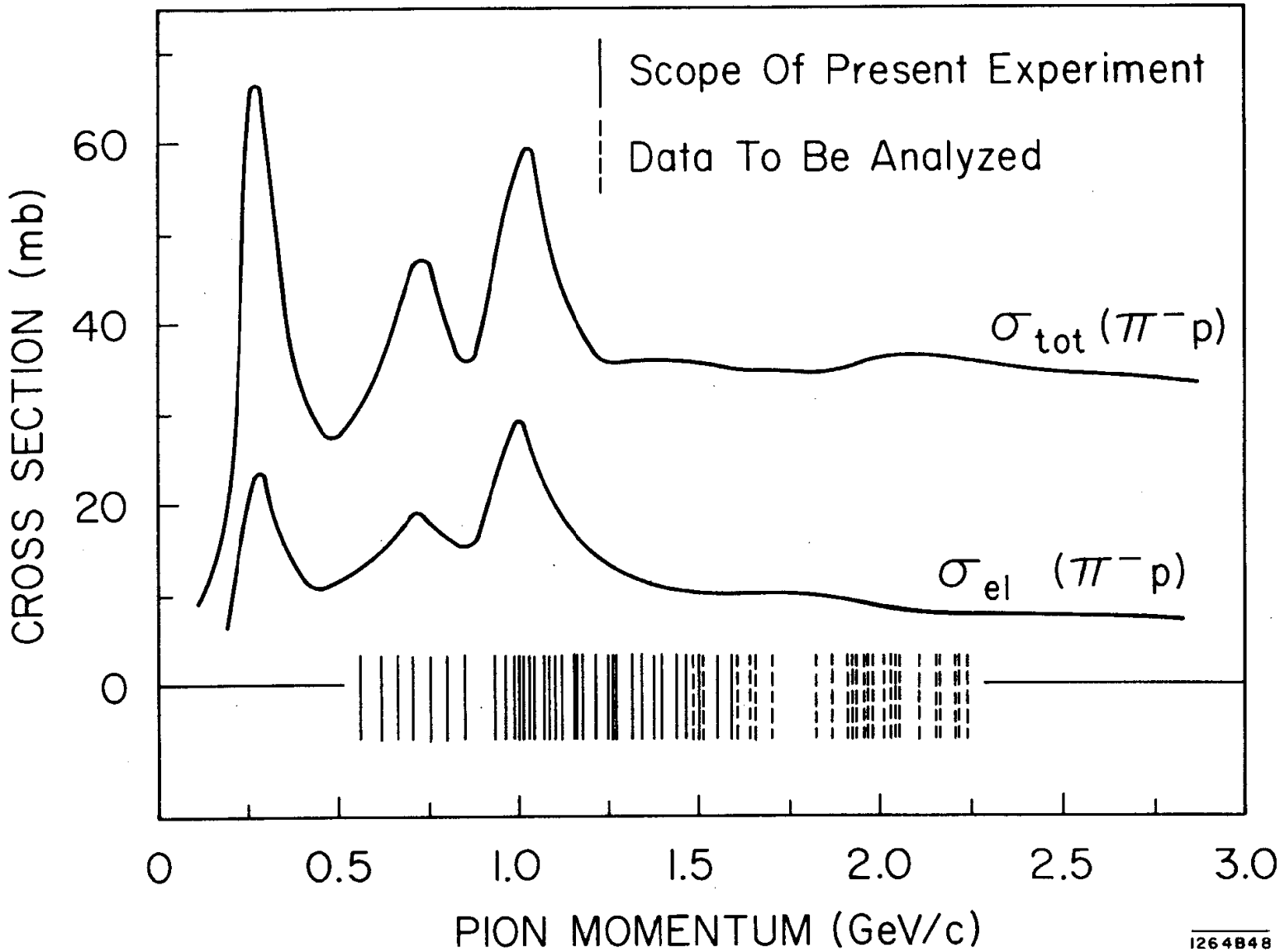

FIG 2--Scope of the present experiment. Solid lines mark the energies of the measurements that comprise this thesis.

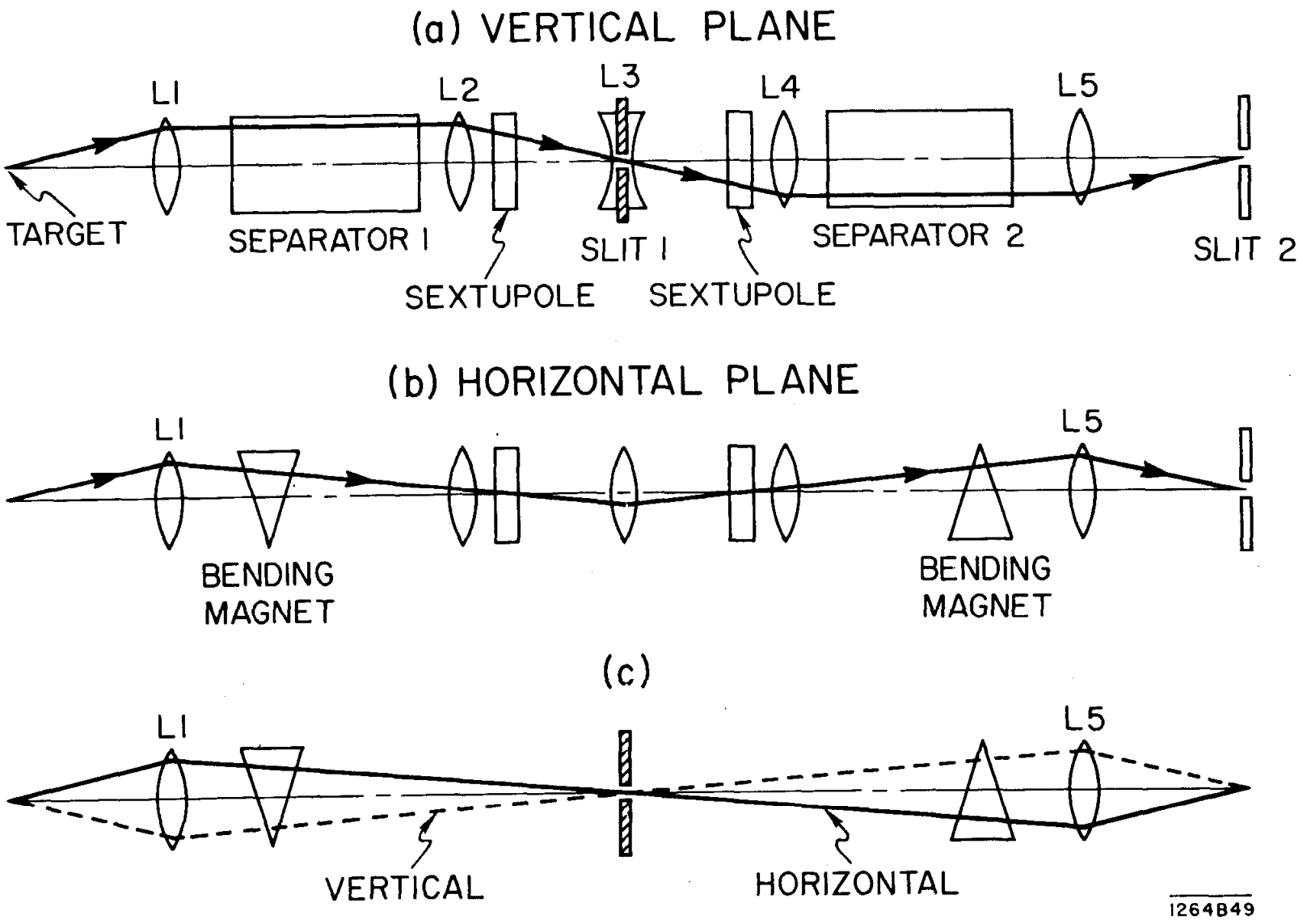

FIG. 3--Argonne beam optics. (a)-(b) Vertical and horizontal planes of the optics used for the second and third exposures. (c) Simplified mode used for the first exposure.

exposures (i.e., $p_\pi < 1$ GeV/c). The low energy pion flux was found to be much less than expected, and as a result it was not possible to obtain a useful beam below 580 MeV/c.

To produce an ideal shape (5" wide and 6" high) for the beam trajectory in the chamber further quadrupoles were used after the final slit. Since the image at the final slit had little vertical divergence, it was most effective to rotate the first quadrupole 45° to optically couple the vertical and horizontal planes. The second quadrupole then increased the vertical divergence and decreased the horizontal divergence.

The high field of the 30-inch HBC and the low momentum of the beam made it necessary to raise the center of the chamber 7" above the center beam line and then to pitch the beam downwards into the fringe field of the bubble chamber magnet to obtain a good trajectory of the beam through the chamber. Finally, for momenta below 870 MeV/c it was further necessary to lower the HBC magnet current from 20,000 amps to 12,000 amps, to maintain this trajectory.

The proton beam of the ZGS gave a pulse of pions once every 2.9 seconds. For part of the exposure, the bubble chamber was triple pulsed during each beam spill, allowing a rate of nearly 1 picture per second.

The π^- beam used for the Berkeley exposure is sketched in Fig. 4. It has been previously described[15] for a momentum setting of 1030 MeV/c. The characteristics remain the same at the momenta used in the present experiment. In particular the beam is characterized by good momentum resolution, the fractional momentum bite $\Delta p/p$ being on the order of $\pm .5\%$.

All beam interactions within the volume 34 cm wide, 122 cm long and 9 cm deep were accepted from the 72-inch chamber, while for the 30-inch

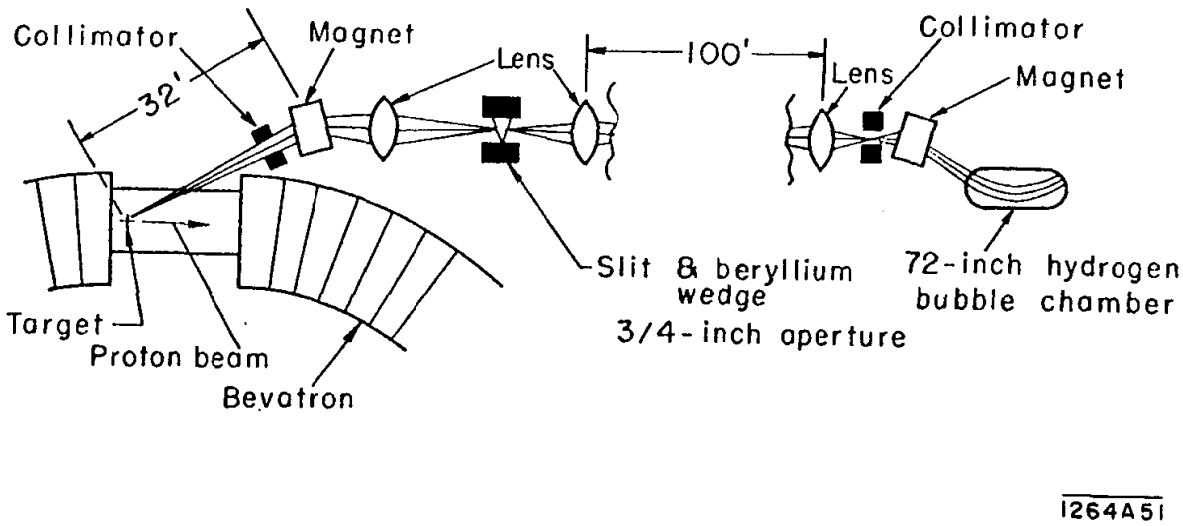

FIG. 4--Berkeley beam.

chamber, the fiducial volume was defined as 58 cm long, 58 cm wide and 16 cm deep.

The coordinate system for both chambers is defined with the camera axis as the z-axis and the beam coincident with the y-axis. In the Alvarez chamber, the camera axis is tilted $7\frac{1}{2}^{\circ}$ with respect to the vertical axis.

B. Magnetic Field

The magnetic fields of both chambers were determined by extrapolating from previously measured field maps. These existed for the 72-inch chamber at magnet current settings of 2400 A, 3500 A, and 4600 A. The measured values of the B_z at these currents were fitted with a 27-term polynomial expansion[16] and the horizontal components were calculated to satisfy Maxwell's equations to third power in xy. These coefficients were scaled where necessary to the settings of 3102 A, 3690 A, 2600 A, and 4600 A used in the present experiment. The value of B_z at the center of the chamber was determined by looking at K^o decays ($K^o \rightarrow \pi^+ + \pi^-$) and elastic scatters. We required that the distribution in the unfit invariant mass of the π^+ and π^- agree with the accepted K^o mass. We also required that the distributions in measured and fitted values of the momenta of each track in the four constraint (4C) elastic events agree. We found that both of these criteria were simultaneously satisfied in most regions of our film rather easily.

The same procedure was adopted to determine the field of the 30-inch chamber. It was necessary to scale from the field map measured at 20,000 A down to 12,000 A. Two precautions were taken here. The field measurement at 20,000 A agreed with the design calculations to within 1%. Furthermore the field shape was predicted to remain the same at lower current settings. As an additional check, the film taken at 853 MeV/c was

divided between the two values of the field. The elastic scatters from the two fields were compared and no discernible differences were detected. The unfit invariant mass of the π^+ and π^- from this film is plotted in Fig. 5, and agrees well with the accepted value of M = 497 MeV for the K^o mass.

Table II summarizes the currents and central values of the fields used.

C. Optical Constants

The optical constants required by the fitting programs were determined by making a 12 parameter least squares fit of measured fiducials to their known positions, using the program WEASEL. For the 72-inch HBC, 13 fiducials were measured, with many sets of measurements being obtained throughout the entire exposure. Several sets of measurements were averaged whenever appropriate with the program MONKEY. Each set of constants was checked by comparing measured quantities with corresponding fitted quantities of 4C elastic scattering events in all parts of the chamber. Although there was poor agreement at the edges of the chamber, satisfactory results were obtained within the fiducial volume. The pull distributions reflect the quality of spatial reconstruction. We plot the pulls on the beam track for the three final states, $\pi^- p$, $n\pi^+\pi^-$, $p\pi^-\pi^o$, in Figs. 6d, 7d, and 8d, respectively.

The same procedure was used to determine the optical constants for the 30-inch MURA HBC. However, the reconstruction was slightly less satisfactory, because there were not enough visible fiducials to enable determination of the high order distortion parameters. The pull distributions are given in Figs. 6a-c, 7a-c, and 8a-c.

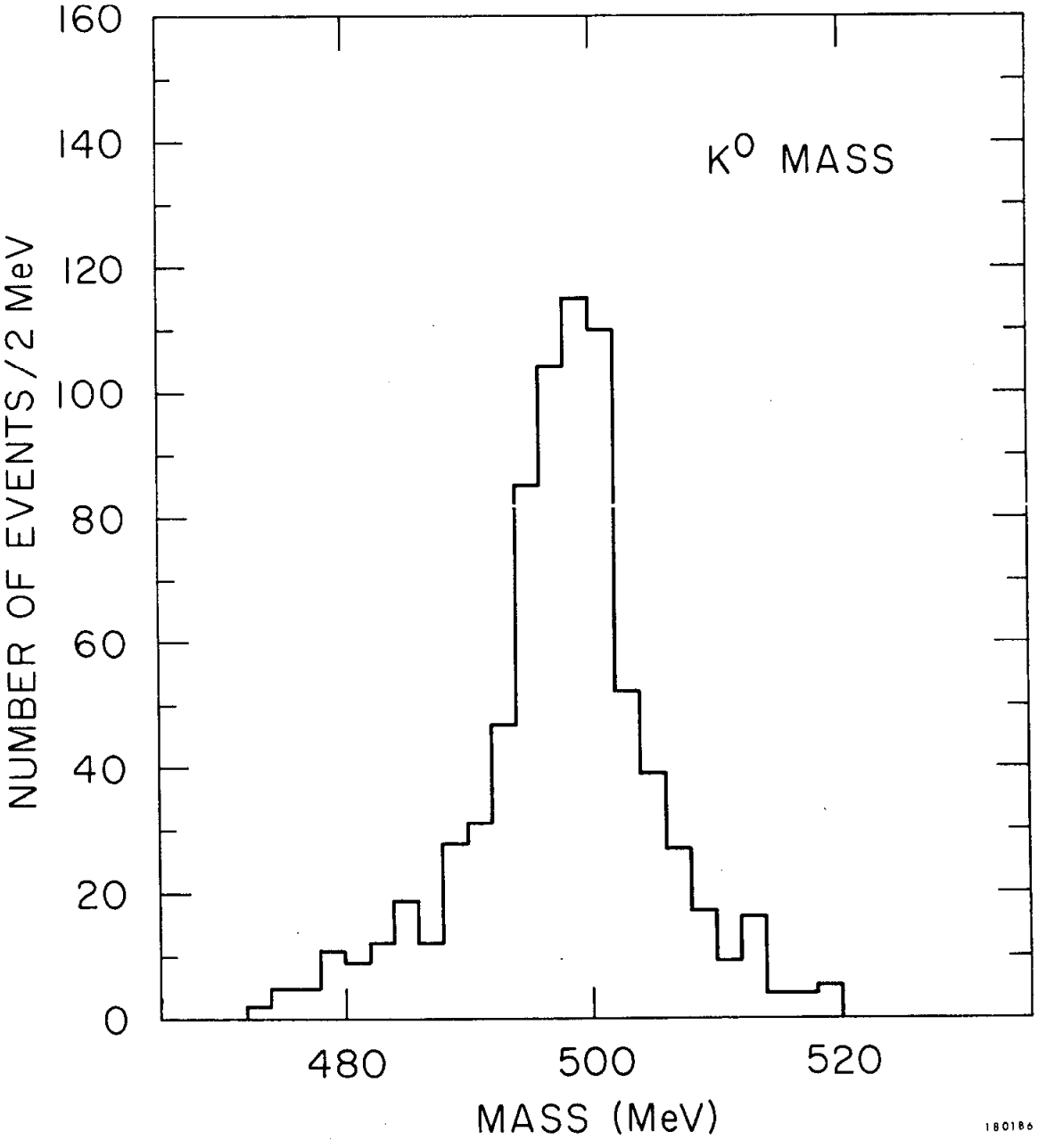

FIG. 5--Invariant mass of $(\pi^+\pi^-)$ from K^0 decays.

TABLE II

Magnet Currents and Central Field Values

Chamber	I(amps)	Field (kG)	Momentum Range (MeV/c)
72-inch	2,400	10.254	956 - 995
	2,600	11.025	1004 - 1024
	3,102	13.85	924
	3,690	14.54	1024 - 1042
	4,600	17.77	1125 - 1174
30-inch	12,000	20.98	556 - 853
	20,000	32.566	853 - 1602

1801A31

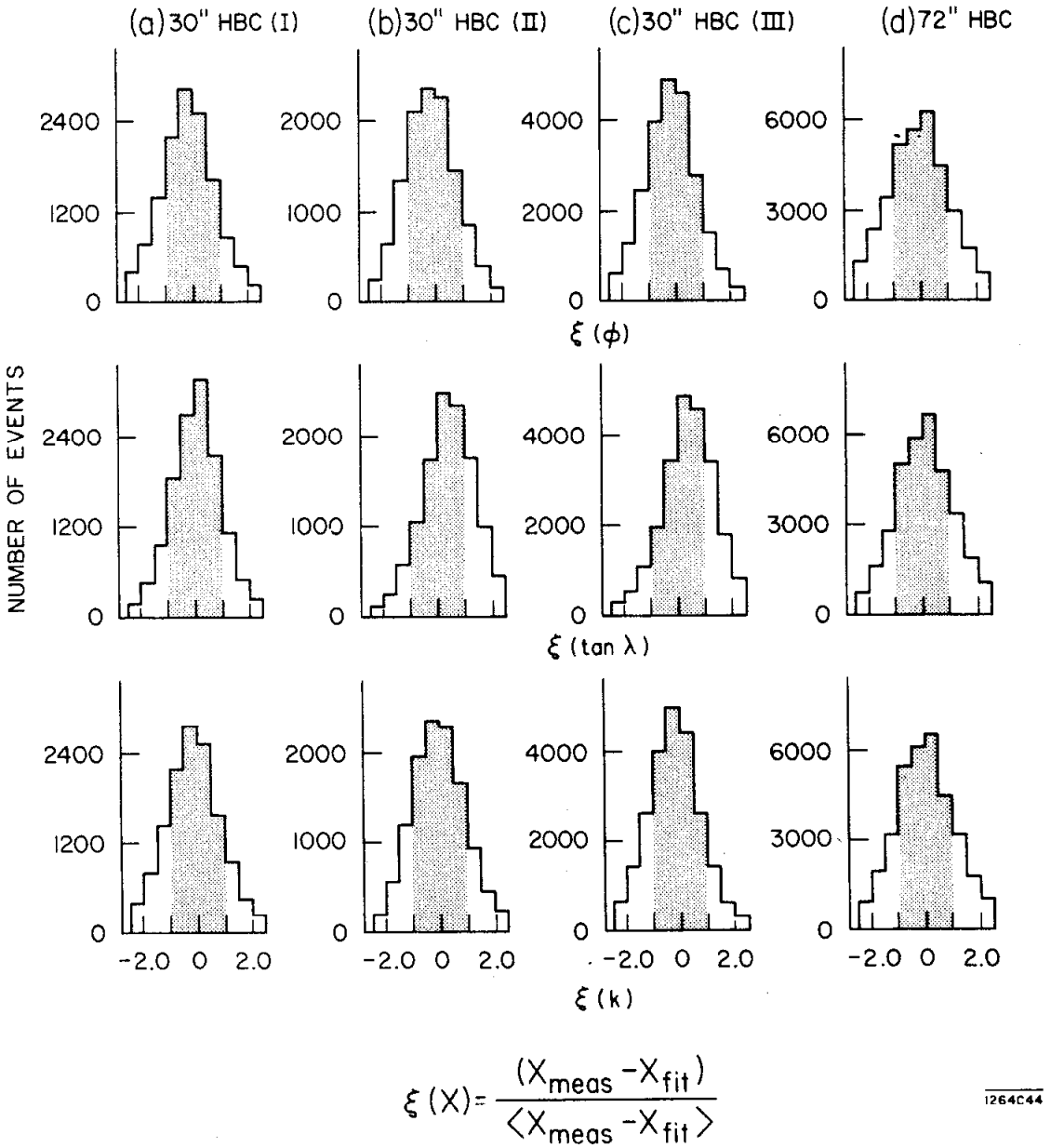

FIG. 6--Beam track pull quantities in elastic events for each exposure. (a)-(c) 30-inch HBC. (d) 72-inch HBC.

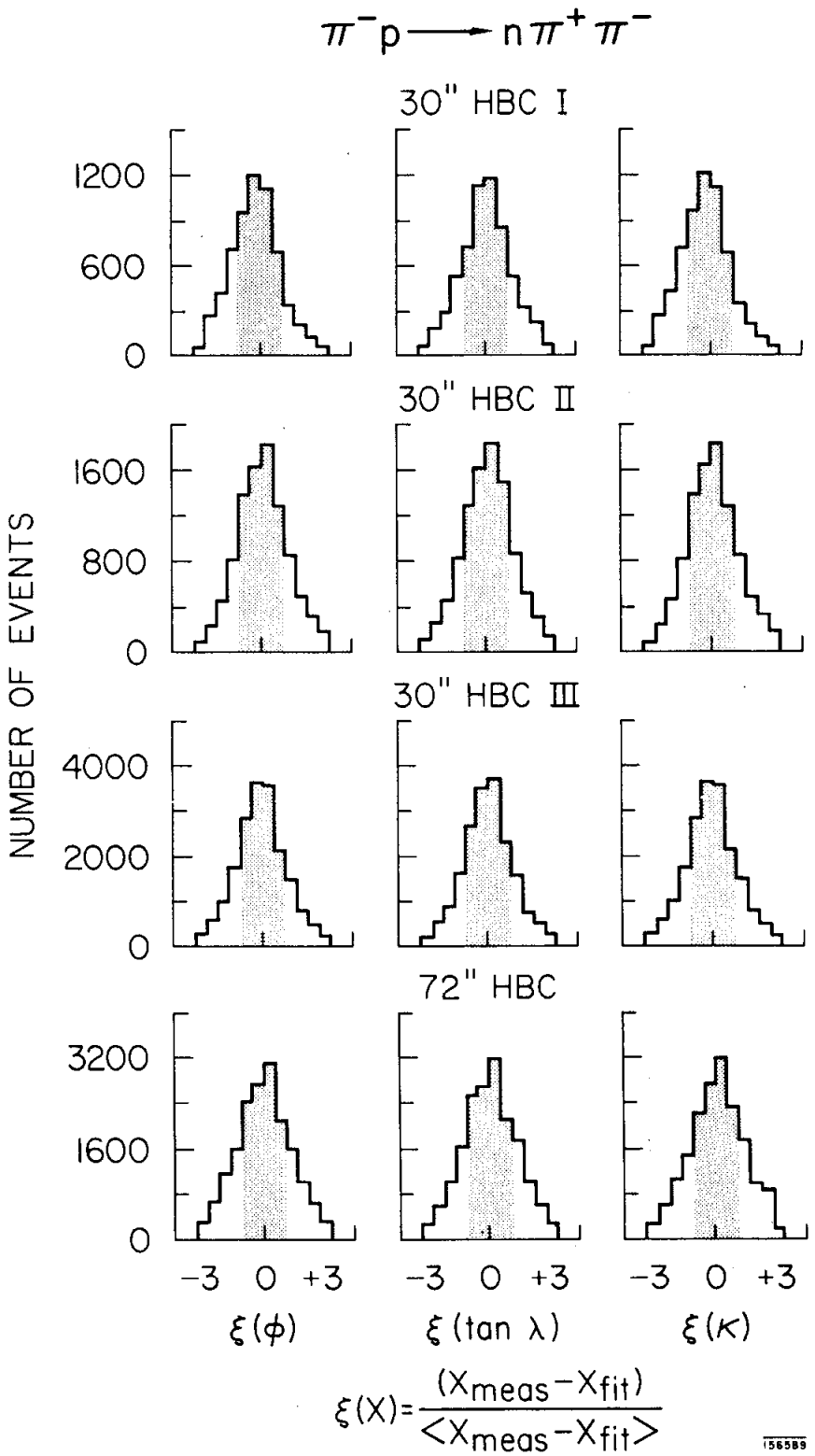

FIG. 7--Beam track pull quantities in the reaction $\pi^- p \rightarrow n\pi^+\pi^-$ for each exposure.

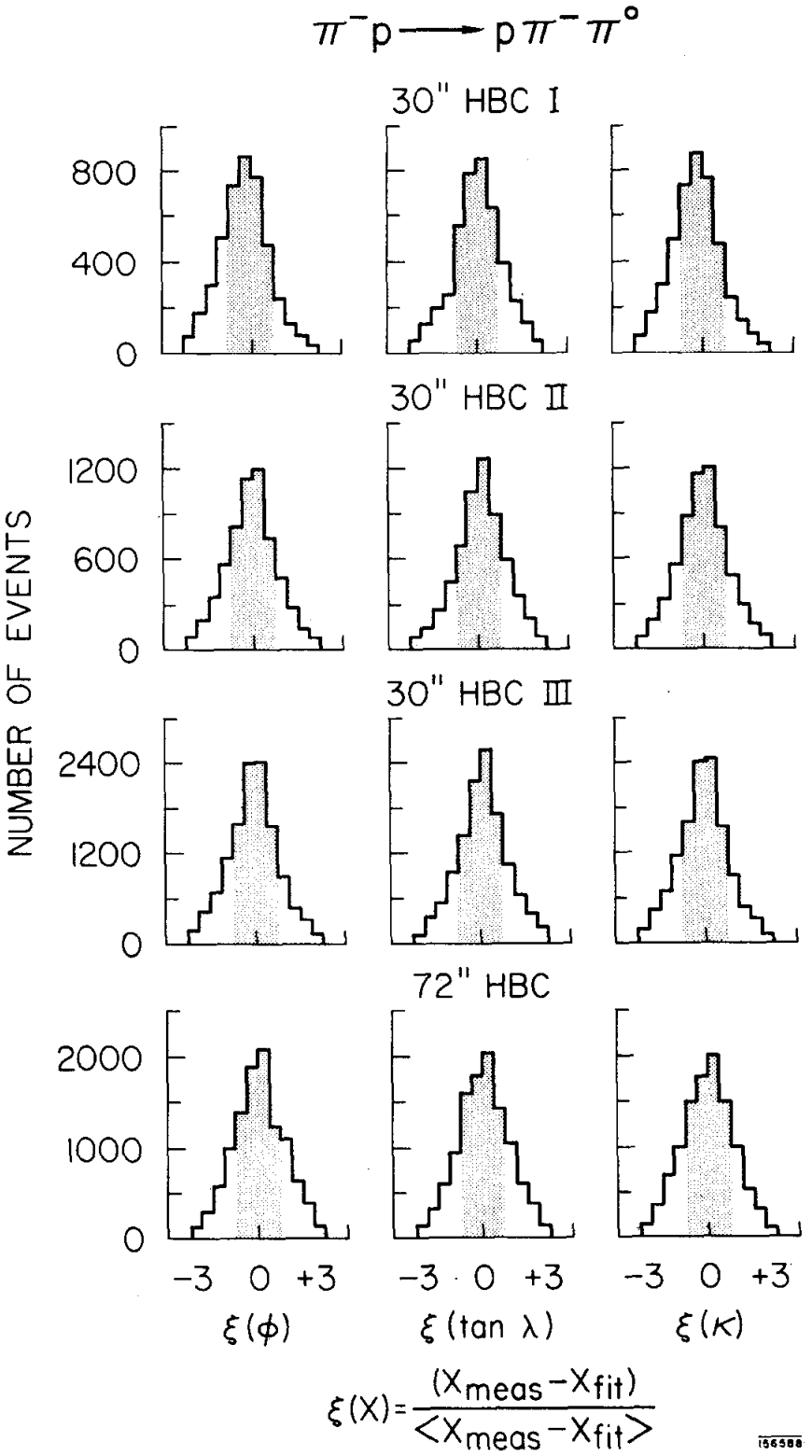

FIG. 8--Beam track pull quantities in the reaction $\pi^- p \rightarrow p\pi^- \pi^0$ for each exposure.

D. Measurement

The bubble chamber film was scanned at SLAC and measured by the Spiral Reader at LRL. The scanners recorded all two-prong events and all zero-prong events with one or two associated vees. Events in which the beam track disappeared for more than a projected length of 3mm before the vertex were classified as 0-prong, 1-vee events. Events were rejected if obscured in any way or if the beam track was less than 3 cm long. No bias is introduced by these rejects. Events in which both outgoing tracks were less than 1 cm were also rejected, introducing a loss of reactions with short protons. Such events correspond to C.M.S. scattering angles which are not included in our results and analysis (see Chapter III). However, a further bias is expected due to loss of short, dipping protons, and correction for this bias will be discussed in Section F. The scanning efficiency was evaluated by rescanning approximately 20 percent of the Argonne film and 10 percent of the Berkeley film. The master lists from the first and second scans were then compared by the computer program CONFLICT, which lists all discrepancies. These discrepancies were examined again on the scan table to determine whether they were valid events. Following this procedure, the combined scan efficiency was found to be 97 percent.

The film was measured on an LRL Spiral Reader,[17] a semiautomatic film digitizing machine. It has three major components. The first is the movable XY encoding stage of the conventional measuring machines such as the Frankenstein. The operator uses this stage to locate and record the position of the fiducials. The second component is the periscope through which light from the scan table is focused onto a photocell. The operator centers the slit of the periscope on the vertex of an event. Then the mirror

of the periscope moves in a combination of rotational and translational motion, causing measurement to proceed in a spiral path centered on the vertex. The photocell registers all track segments crossed and digitizes them in polar coordinates. The Spiral Reader records not only the position but also the pulse height of the track segments and hence affords valuable information on track ionization.

The third component of the Spiral Reader is the PDP4 on-line computer. This computer reads the scan information, controls the film advance, stores and packs the digitizations and pulse heights and writes an output tape for further processing. Measurement of this machine proceeded at a rate of approximately 100 - 200 events/hour.

The measurements are then processed by a FORTRAN filter program POOH[18] which requires about 3 seconds per event on a CDC 6600. POOH sorts out the tracks associated with the vertex and then matches corresponding tracks found in the three views. The sorting is accomplished by first examining all data points lying within a small radius of the vertex. POOH tries to fit these points to the equation:

$$\theta = \theta_0 + \alpha r + \beta/r + \gamma r^3$$

This equation describes a circular track passing through the vertex and includes corrections for finite setting accuracy at the vertex. The derivation of this equation involves a small angle approximation ($\theta - \theta_0 \ll 1$). Thus, it is difficult to fit steeply dipping tracks and the loss of such tracks constitutes a bias that will be discussed in a subsequent section.

The efficiency for passing events through the measuring process and the filtering program was found to be 97 percent after the first measurement of the 72-inch bubble chamber film. We made a repeat measurement of about

17,000 events and found the combined efficiency then to be 99 percent. All of the 30-inch bubble chamber film was measured twice except for 43% that had unambiguous fits on the first measurement. The combined efficiency after the second measurement for all events in the 30-inch chamber was 93 percent. Those events that failed twice were examined on the scan table, and no evidence for topological bias was found apart from the bias against short protons mentioned previously.

E. Fitting Programs

The measured two-prong events are processed by the SIOUX-ARROW system of programs. SIOUX consists of a three-view geometry program that tries, in this experiment, each of the following hypotheses:

$$\pi^- p \rightarrow \pi^- p \tag{2.1}$$

$$\rightarrow n\pi^+\pi^- \tag{2.2}$$

$$\rightarrow p\pi^-\pi^0 \tag{2.3}$$

Because the four-constraint elastic hypothesis is more difficult to fit than the remaining one-constraint hypotheses, all events that satisfied this hypothesis with a value of chisquared for the kinematic fit, χ^2_k, less than 25 were accepted as elastic scattering events. Furthermore, we required that the ionization measured by the Spiral Reader be consistent with the fitted track momentum. A plot of missing mass determined by fitting these elastic events to the reaction

$$\pi^- p \rightarrow \pi^- pmm$$

is shown in Fig. 9 and illustrates that there is negligible contamination in this sample. (The histogram is sharply peaked at zero, with a slight pull to the negative side, as expected in plots of this type.[19])

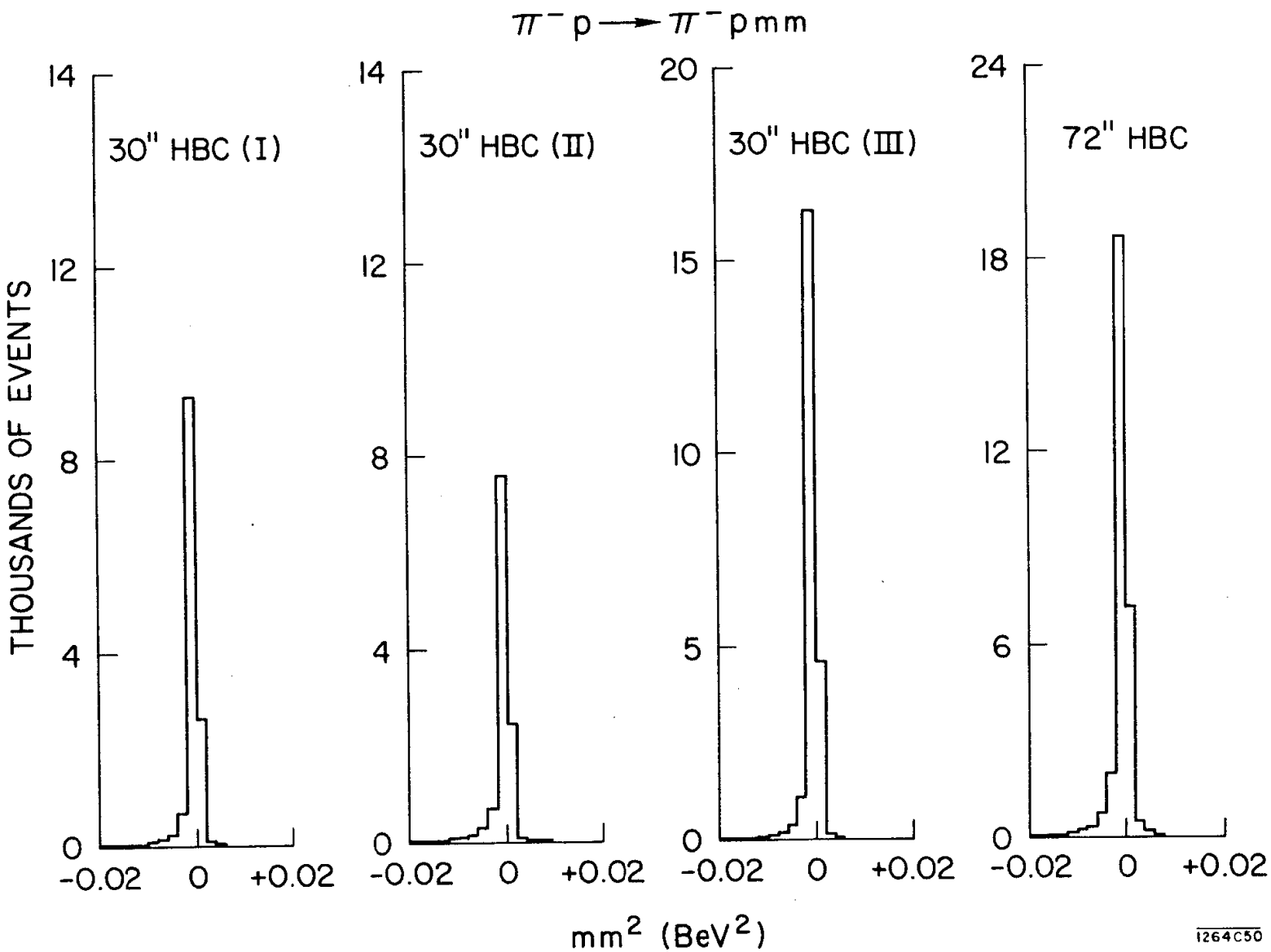

FIG. 9--Missing mass squared in the reaction $\pi^- p \rightarrow \pi^-$pmm for the 4C elastic events.

If an event satisfied hypothesis (2.2) or (2.3) only, with a value of χ_k^2 less than a prescribed maximum ($\chi_k^2 = 7$ for the Argonne film and $\chi_k^2 = 8$ for the Berkeley film), that hypothesis was unambiguously selected. However, if an event satisfied both of these hypotheses, we adopted certain criteria to select the "best" fit. Again we used the pulse height information recorded by the Spiral Reader. We computed a χ_{ion}^2 to describe the fit of the calculated bubble density to that determined experimentally from the pulse height. At the relatively low energies involved in the present experiment, the difference in bubble density between a proton and a positive pion should be decisive.

For the 72-inch bubble chamber film, we used the following criteria:

i. We chose the hypothesis that gave the lower value χ_{ion}^2, provided this difference was larger than 3.

ii. If the difference in χ_{ion}^2 for the two fits was less than 3, we chose the hypothesis that gave the lower value of kinematic chisquared, χ_k^2, provided this difference was larger than 1.5.

iii. If the difference in χ_k^2 was less than 1.5, we selected the hypothesis that gave the lower value of χ_{ion}^2.

For the 30-inch HBC film, we decided upon a simpler selection criterion. We formed a linear combination of χ_k^2 and χ_{ion}^2, which we call the combined chi-squared, χ_{comb}^2. It was sometimes necessary to multiply χ_{ion}^2 by a factor α before forming χ_{comb}^2 because the pulse height information varied in reliability. We set $\alpha = 2/\langle\chi_{ion}^2\rangle$ where $\langle\chi_{ion}^2\rangle$ is the average over 100 events in a region of film. We classified an event as either reaction (2.2) or (2.3), depending on which hypothesis gave the lower value of χ_{comb}^2. To compare the results of the two selection procedures, we made the selection both ways for a sample of events. The resulting classifications were essentially identical.

As in the elastic events, we can illustrate the low contamination of our samples of $n\pi^+\pi^-$ and $p\pi^-\pi^0$ final states by plotting the square of the missing mass in the reactions

$$\pi^- p \rightarrow \pi^- \pi^+ mm$$

$$\pi^- p \rightarrow \pi^- p \ mm$$

These mass plots are shown in Fig. 10 and peak at the square of the masses of the neutron and the neutral pion, respectively.

To study whether events have been correctly assigned to a reaction type ($n\pi^+\pi^-$ or $p\pi^-\pi^0$) in the sample of ambiguous events, we can plot the square of the missing mass, as above, for both the "right" and "wrong" choice of events. Figures 11 and 12 contain these plots and show that the distributions for the "wrong" choice appear far too broad, especially in comparison with the corresponding plot for the "right" choice. The shaded histograms correspond to the samples of these events with χ^2_{ion} less than 12 for the wrong hypothesis. The distributions are not improved by this cut; this provides further evidence that these events are not examples of the reaction corresponding to the "wrong" choice.

One indication of the quality of the fits is the distribution of χ^2 for all the events. In most bubble chamber experiments, the experimental distributions match the theoretical distribution

$$p(\chi^2 \geq \chi^2_0) = \int_{\chi^2}^{\infty} \frac{(\chi^2)^{n/2-1} e^{-\chi^2/2a} d\chi^2}{2^{n/2} \Gamma(n/2)} , \qquad n = \text{number of degrees of freedom}$$

once the scale factor a has been determined. The necessity for this scale factor usually arises from non-Gaussian errors. In Fig. 13, we plot the chisquared distribution for all elastic events, together with a curve that

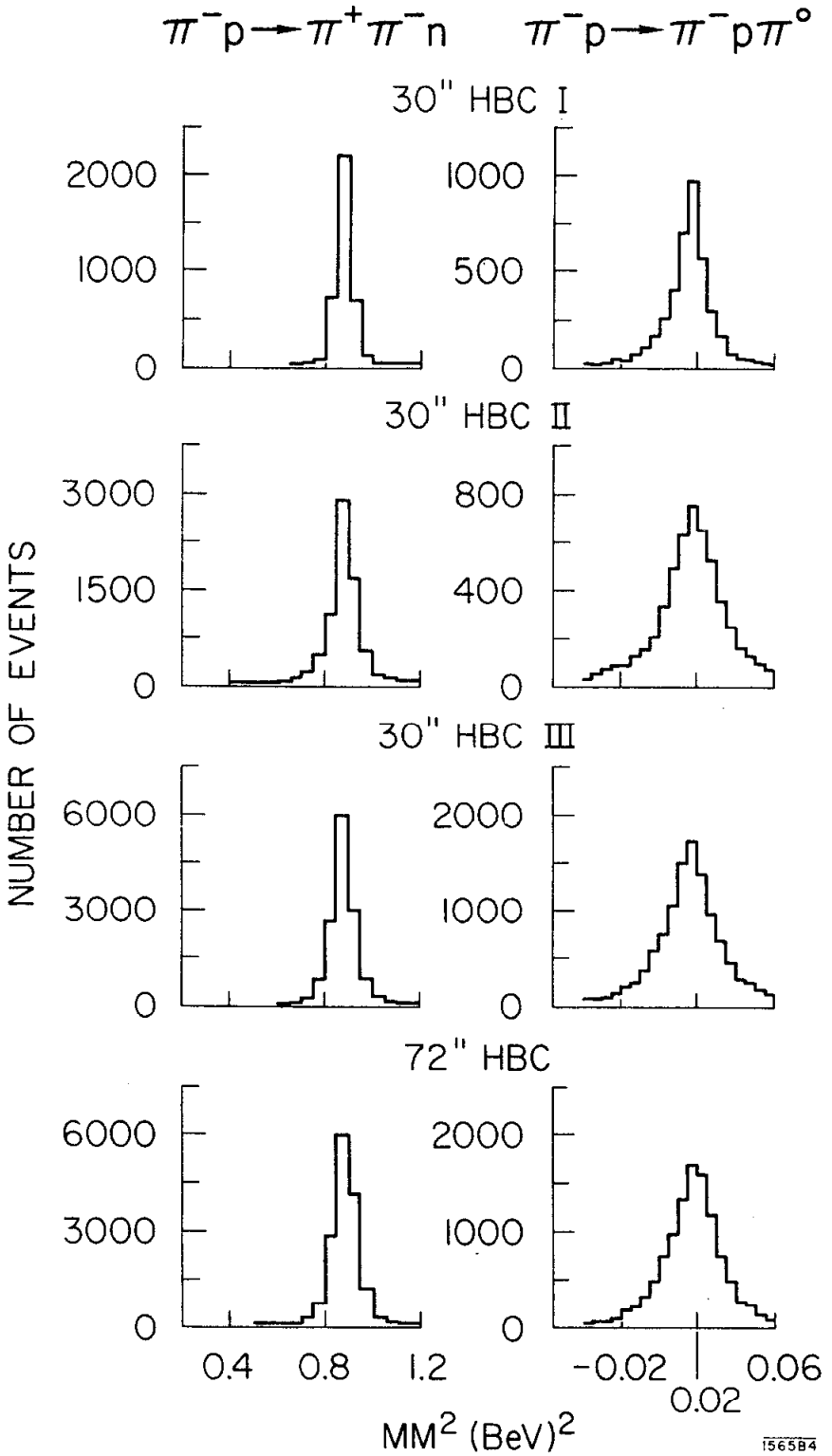

FIG. 10--(a) Missing mass squared in the reaction $\pi^- p \rightarrow \pi^+ \pi^-$mm for the 1C reactions $\pi^- p \rightarrow n \pi^+ \pi^-$.

(b) Missing mass squared in the reaction $\pi^- p \rightarrow \pi^- p$ mm for the 1C reactions $\pi^- p \rightarrow p \pi^- \pi^0$.

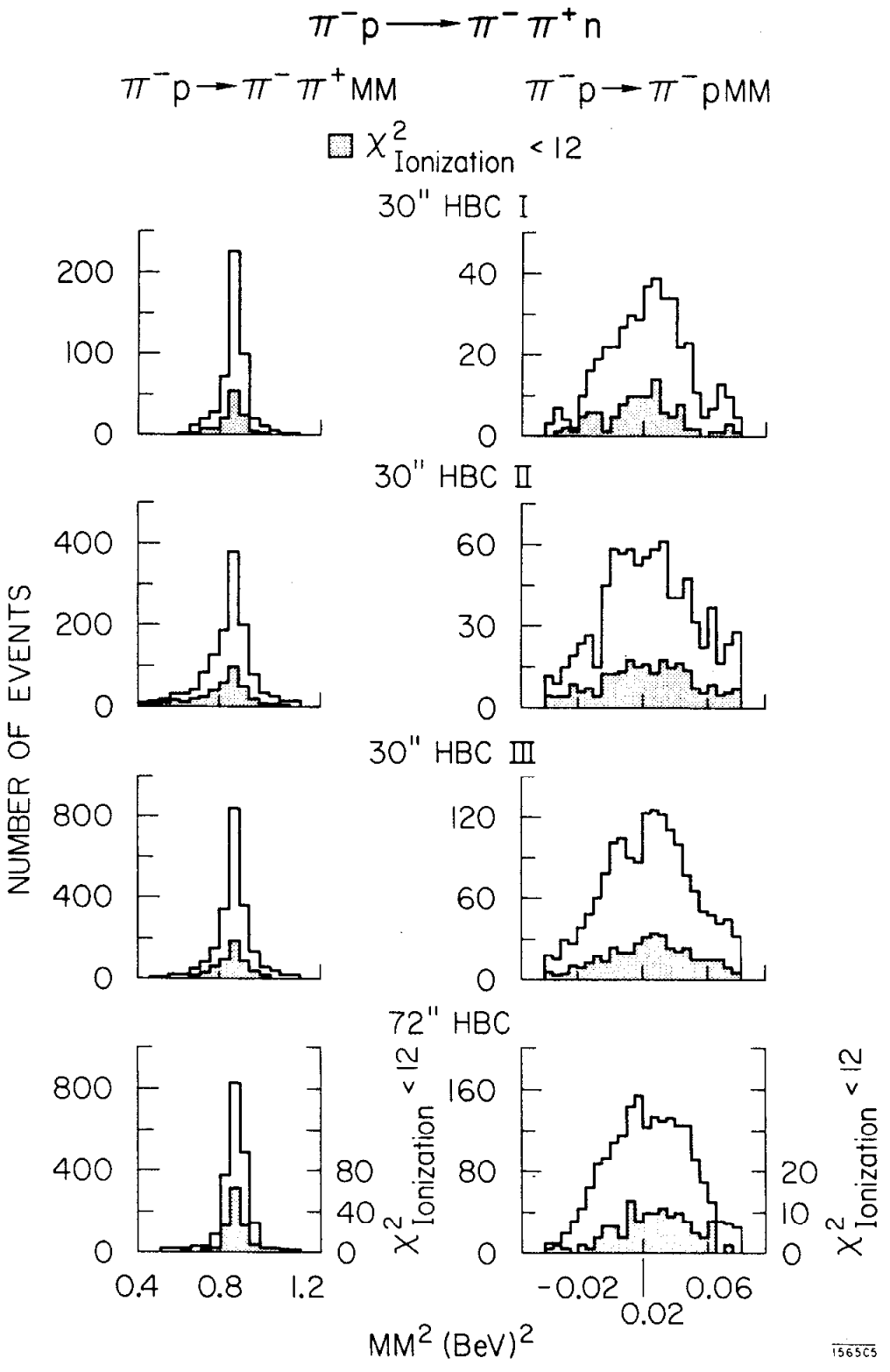

FIG. 11--(a) Missing mass squared in the reaction $\pi^- p \rightarrow \pi^+ \pi^-$ mm for ambiguous events selected as $\pi^- p \rightarrow n\pi^+\pi^-$.
(b) Missing mass squared in the reaction $\pi^- p \rightarrow \pi^- p$ mm for ambiguous events selected as $\pi^- p \rightarrow n\pi^+\pi^-$.

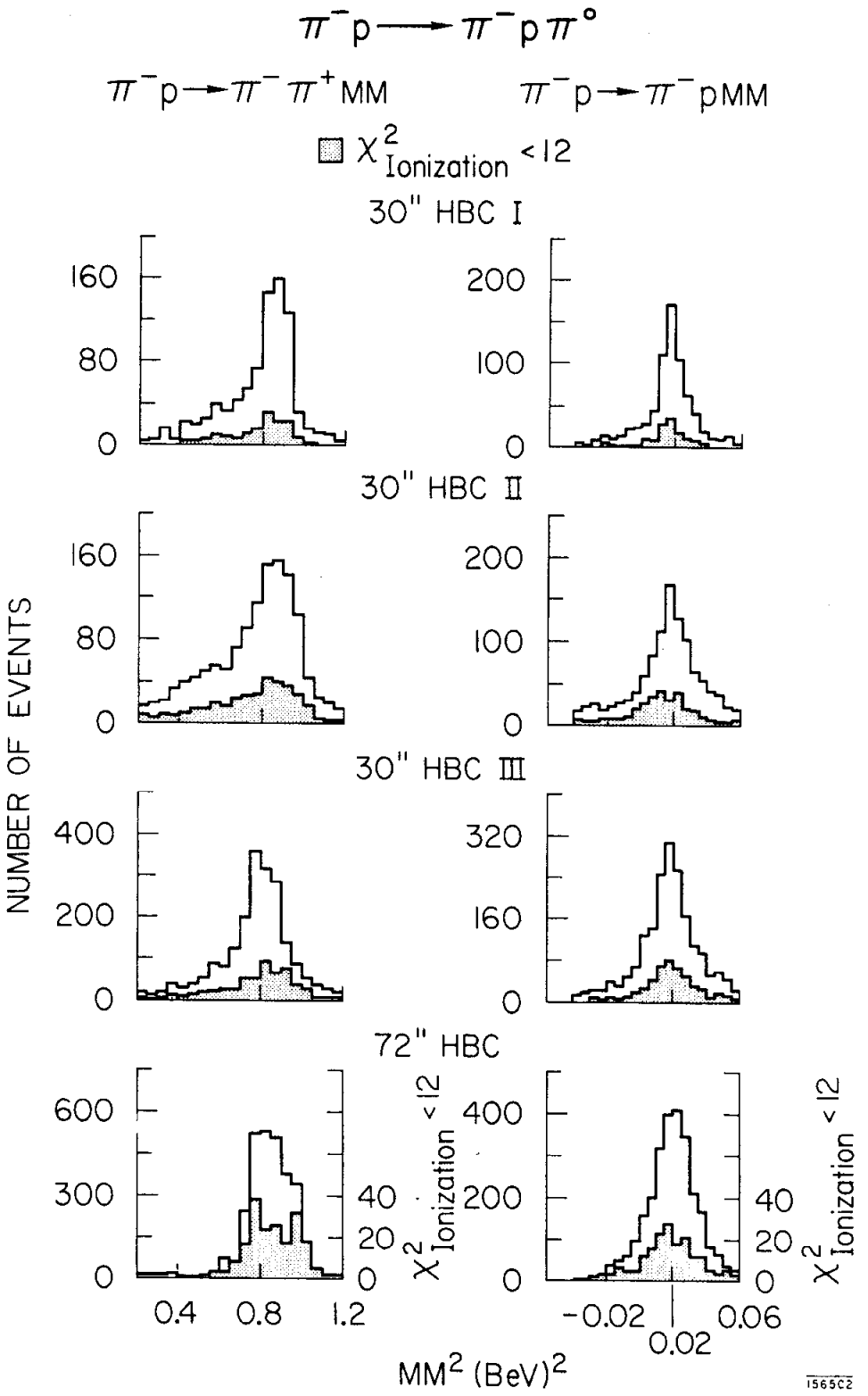

FIG. 12--(a) Missing mass squared in the reaction $\pi^- p \rightarrow \pi^+ \pi^-$mm for ambiguous events selected as $\pi^- p \rightarrow p \pi^- \pi^0$.
(b) Missing mass squared in the reaction $\pi^- p \rightarrow \pi^- p$ mm for ambiguous events selected as $\pi^- p \rightarrow p \pi^- \pi^0$.

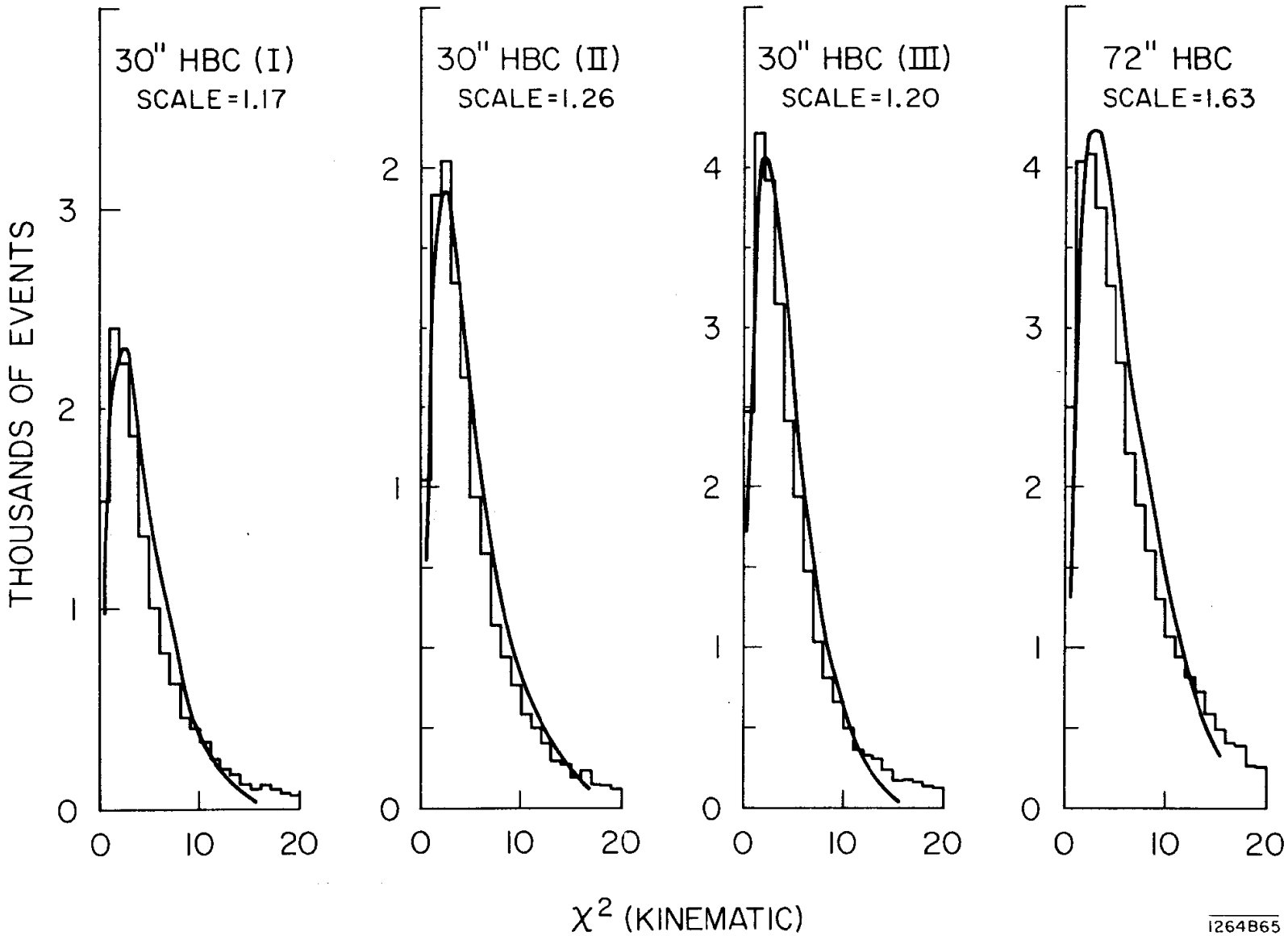

FIG. 13--χ^2 distributions for each exposure. (a)-(c) 30-inch HBC. (d) 72-inch HBC.

represents the theoretical distribution for a four-constraint fit. Rather than cutting off events with high χ^2 and then correcting for those lost, we kept all events with $\chi^2 \leq 25$. To check whether we thus bias the sample, we compared Legendre coefficients that describe the angular distributions for events with $\chi^2 \leq 25$ and $\chi^2 \leq 10$, and found the coefficients unchanged within their errors.

In Figs. 14a-c and 15a-c, we plot the distributions for χ^2_k, χ^2_{ion} and χ^2_{comb} for reactions (2.2) and (2.3), respectively. The $n\pi^+\pi^-$ and $p\pi^-\pi^o$ angular distributions are computed from events with χ^2_k below the maximum described above. As a further study of the resolution of ambiguous events, we display, in Figs. 16 and 17, the χ^2_{ion} and χ^2_{comb} distributions corresponding to the "wrong" choice of events. They do not display the correct characteristics of two- and three-constraint fits. From these observations we have concluded that the selection criteria we have adopted are reasonable and introduce negligible contamination in the total sample of events.

The fitted distribution of center-of-mass energies from the elastic events are used to determine the energy values for each region of film. A sample distribution of fitted center-of-mass energies is shown in Fig. 18. The beam has a low energy tail. Thus we apply an energy cutoff to the data when we determine the mean value of the c.m. energy in each region. These cutoffs are listed in Table VI.

Because of the high momentum resolution of the Berkeley film, the technique of beam averaging was used in processing this film. This technique pulls the value of measured momentum from an individual event closer to the "beam average" value, $p_{B.A.}$. First, all events are processed without beam averaging. Then $p_{B.A.}$ and its error, $\Delta p_{B.A.}$, are determined

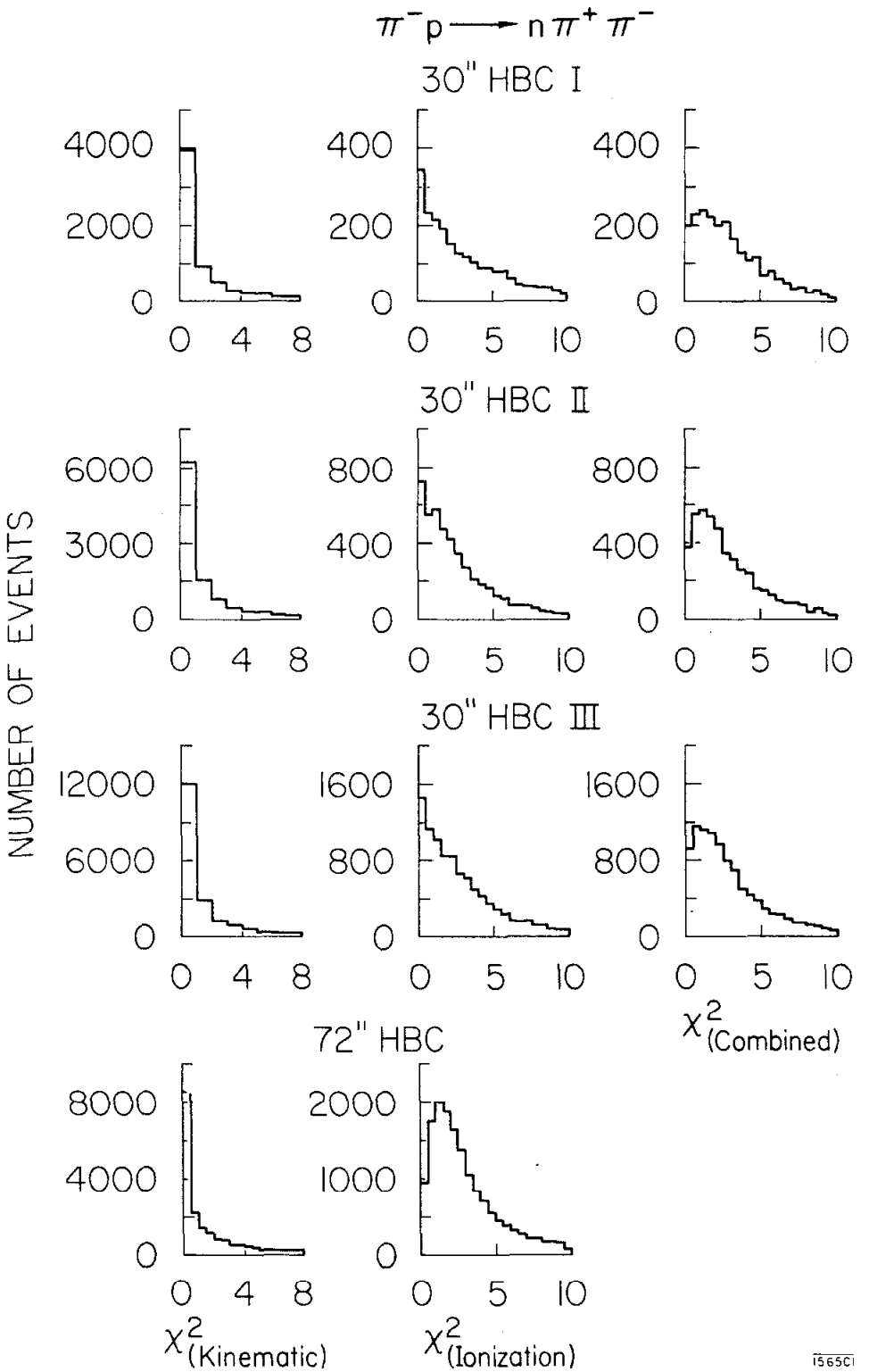

FIG. 14--Kinematic, ionization and combined chisquared distributions for the reaction $\pi^- p \rightarrow n\pi^+\pi^-$. Formation of χ^2_{ion} and χ^2_{comb} is discussed in Chapter II, Section E.

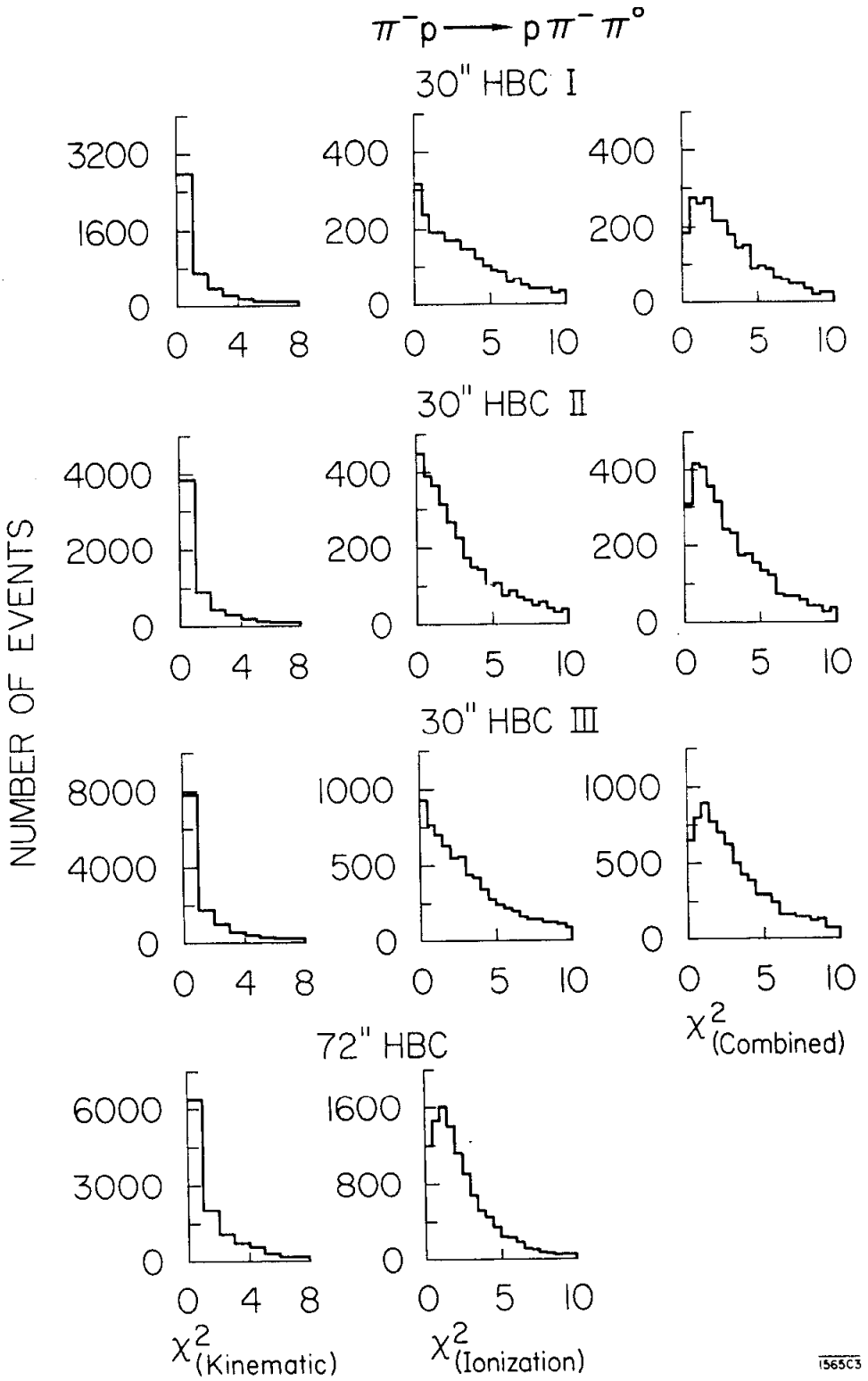

FIG. 15--Chisquared distributions for the reaction $\pi^- p \rightarrow p \pi^- \pi^0$.

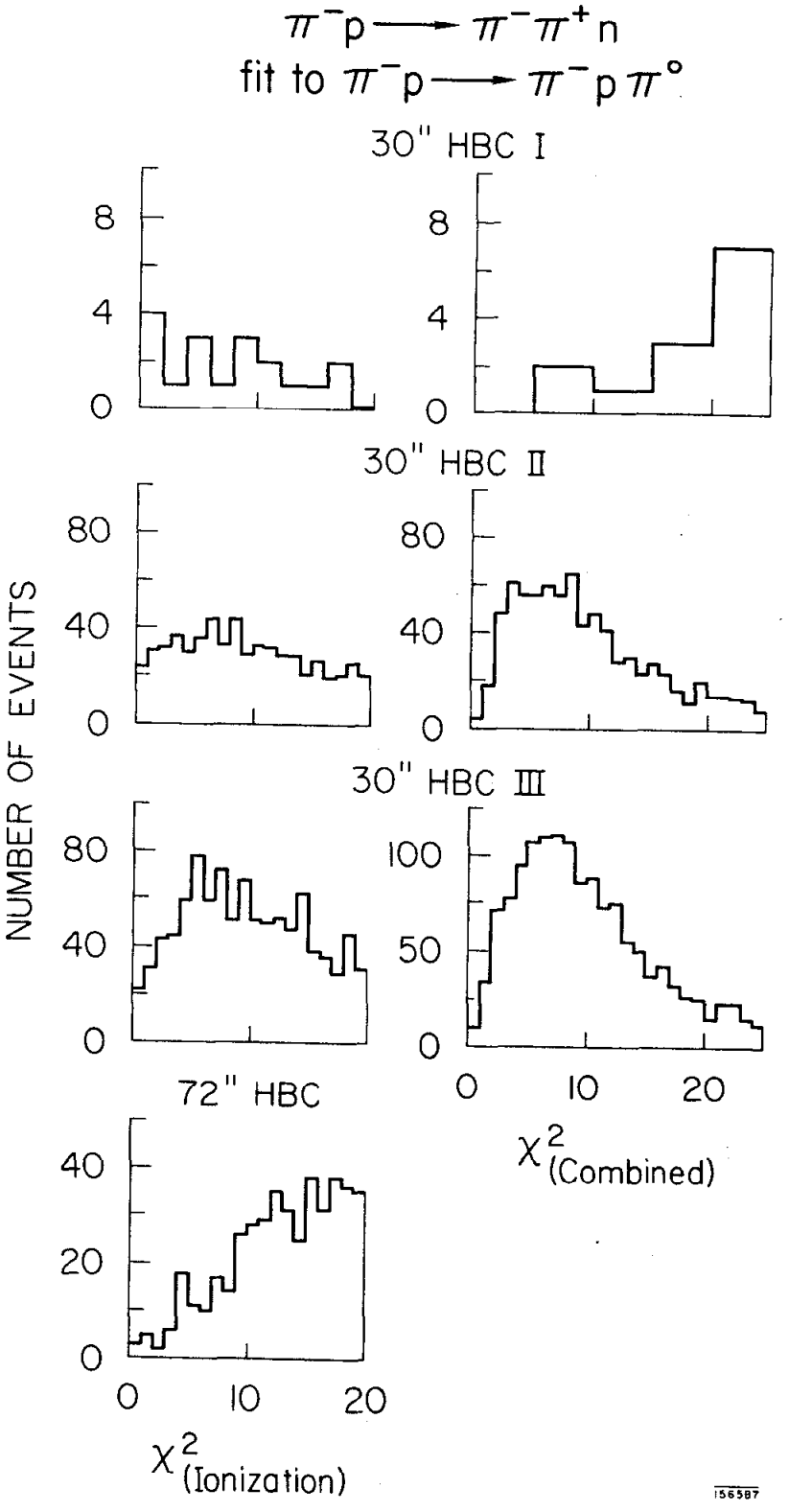

FIG. 16--Chisquared distributions χ^2_{ion} and χ^2_{comb} for ambiguous events assigned to the reaction $\pi^- p \rightarrow n\pi^+\pi^-$ but here fit to the "wrong" reaction $\pi^- p \rightarrow p\pi^-\pi^0$.

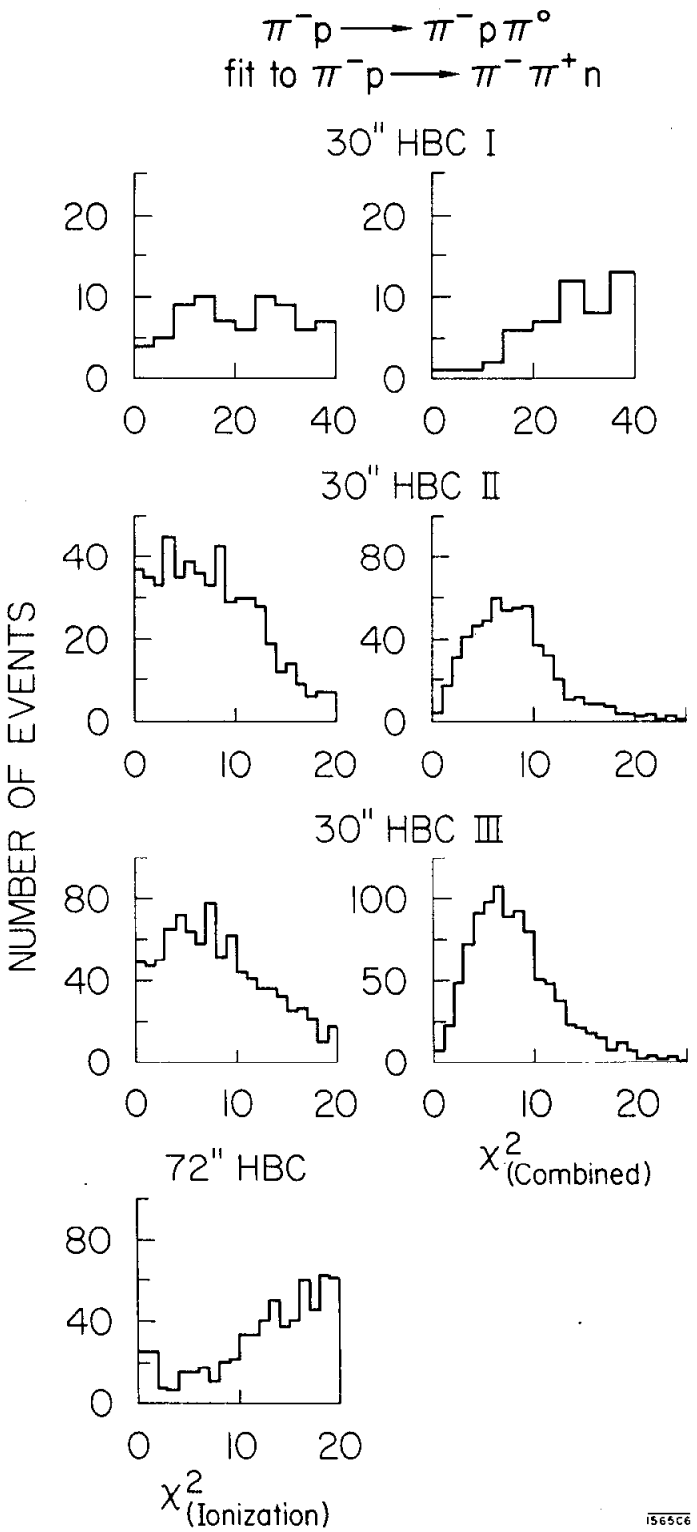

FIG. 17--Chisquared distributions χ^2_{ion} and χ^2_{comb} for ambiguous events assigned to the reaction $\pi^- p \rightarrow p \pi^- \pi^0$ but here fit to the "wrong" reaction $\pi^- p \rightarrow n \pi^+ \pi^-$.

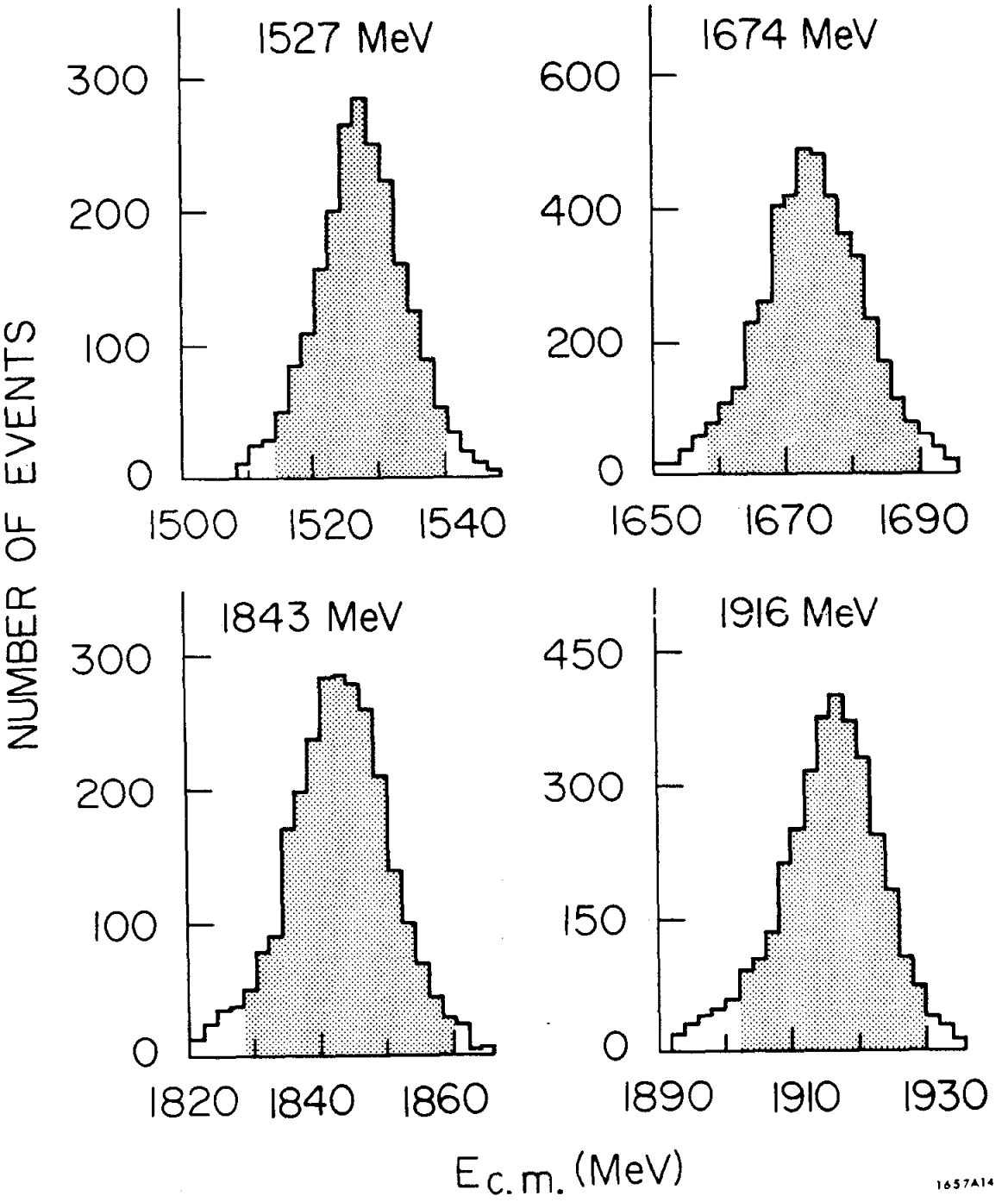

FIG. 18--Center-of-mass energies from 4C events for typical roll regions of the film. Shading indicates the data used in the analysis.

from the elastic events that have $\chi^2 \leq 10$. All events are then reprocessed, the momentum for each event now being a weighted average of "beam average" and measured momenta, according to the formula:

$$p = \frac{p_{meas}/(\Delta p_{meas})^2 + p_{B.A.}/(\Delta p_{B.A.})^2}{1/(\Delta p_{meas})^2 + 1/(\Delta p_{B.A.})^2}$$

After the events were measured, processed and separated according to reaction type, we obtained a total of approximately 80,000 events in the $\pi^- p$ final state, 51,000 in the $n\pi^+\pi^-$ final state and 34,000 in the $p\pi^-\pi^0$ final state. The statistics, broken down by energy regions, are listed in Table III and illustrated in Fig. 19.

F. Correction for Biases

As we mentioned earlier, there is a scan bias against short protons and a bias in the filtering program against steeply dipping tracks. To investigate these biases in the elastic events, we define α as the angle between the normal to the scattering plane and the camera axis. We expect to see a depletion of events near $\alpha = 90^\circ$, where tracks are sharply dipping. We further expect this effect to be worse at forward pion production angles where protons have a short range. Typical distributions of this azimuthal angle α are shown in Fig. 20 for backward, middle and forward production regions. The losses are evident in each region but are especially severe in the forward region. Corrections for this bias were made separately for production angular region and for energy region. These corrections are listed in Table IV.

To study the bias in inelastic events we examined the angle that the normal to the plane of the charged outgoing tracks makes with the camera axis. A small loss of events is observed when this angle is near 90°. The

TABLE III

Events Processed at Each Energy

Exposure	$E_{c.m.}$ (MeV)	$p^{\pi^-}_{lab}$ (MeV/c)	4-C Events $\chi^2 \leq 14$	1-C $n\pi\pi$ Events $\chi^2 \leq 8$	1-C $p\pi\pi$ Events $\chi^2 \leq 8$
30" HBC(I)	1406	556	648	255	80
	1440	609	500	215	82
	1472	660	1110	418	245
	1496	699	1854	675	499
	1527	750	2337	832	701
	1556	797	826	340	272
	1589	853	997	579	387
	1709	1067	1141	585	400
	1730	1105	1954	1046	836
	1762	1165	2230	1231	899
30" HBC(II)	1811	1259	1544	1096	651
	1843	1322	2777	2172	1337
	1872	1381	2920	2443	1568
	1904	1444	3160	2616	1694
	1935	1509	1606	1288	886
30" HBC(III)	1720	1084	687	392	262
	1761	1161	1200	786	488
	1787	1212	1210	798	476
	1806	1250	292	188	122
	1821	1278	1740	1098	687
	1853	1340	2213	1649	979
	1885	1404	2392	1970	1180
	1916	1469	3792	3203	2105
	1933	1503	1972	1735	1177
	1963	1567	4113	3512	2405
	1980	1602	3957	3416	2458
				$\chi^2 \leq 7$	$\chi^2 \leq 7$
72" HBC	1628	924	537	358	200
	1647	956	5482	3169	1968
	1660	979	2697	1430	879
	1669	995	5127	2562	1603
	1674	1004	4966	2673	1568
	1685	1024	4398	2281	1409
	1695	1042	2206	1299	871
	1740	1125	3594	2259	1786
	1766	1174	1733	1120	854
TOTALS			79,911	51,477	33,880

1801839

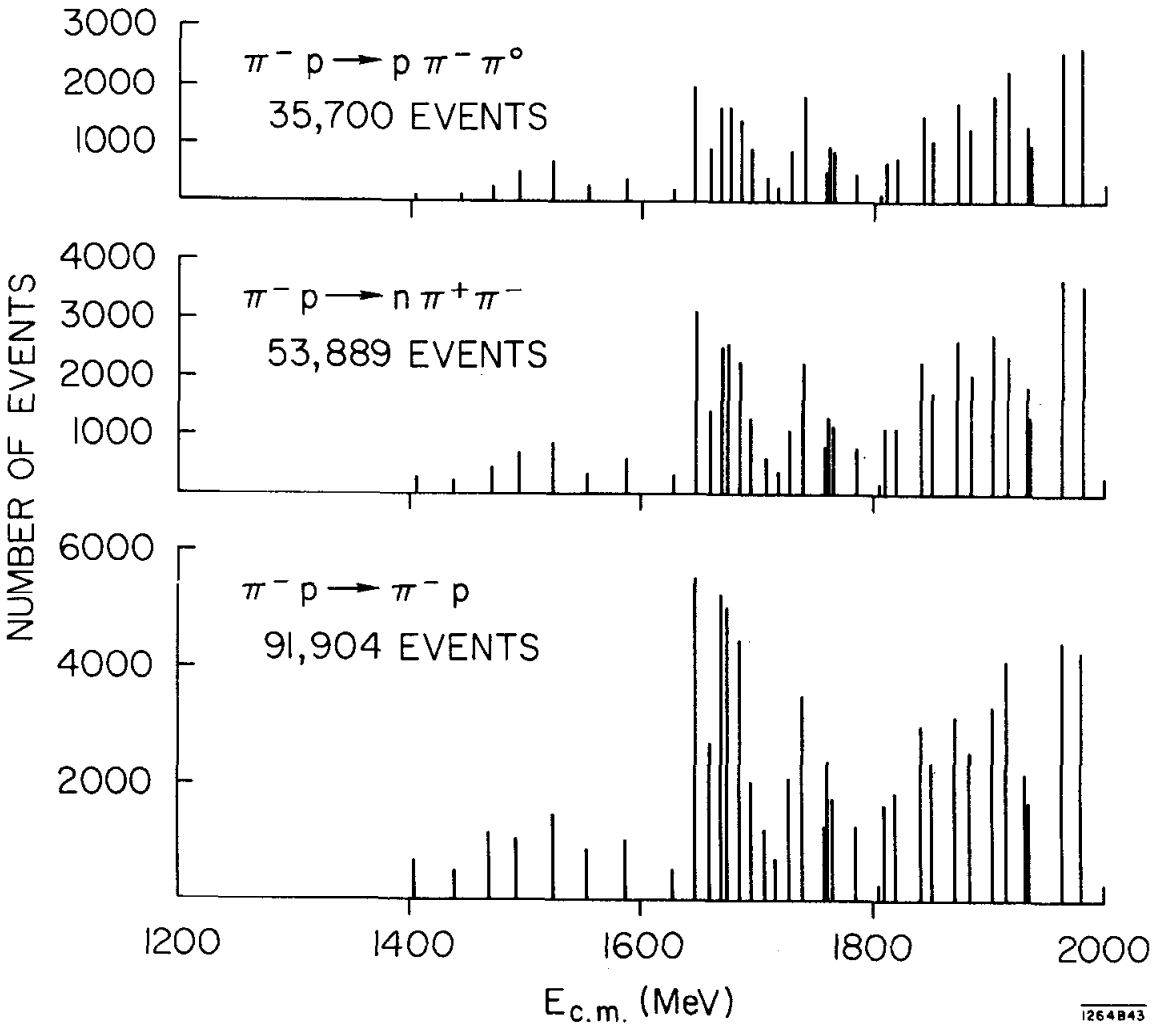

FIG. 19--Number of events of the three reaction types processed at each energy.

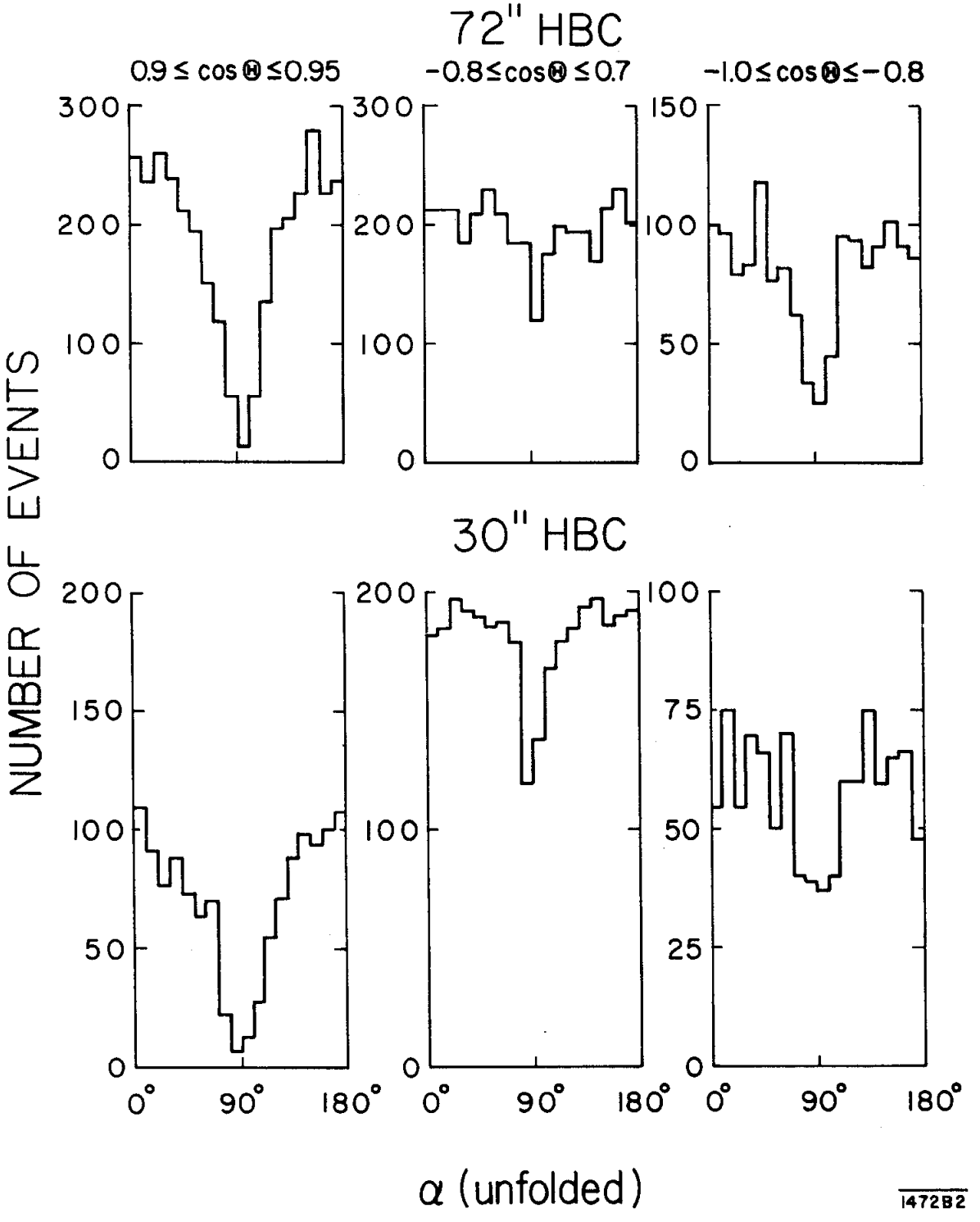

FIG. 20--Azimuthal angle for forward, middle and backward regions of pion production angle in elastic events. α is defined as the angle between the normal to the scattering plane and the camera axis.

TABLE IV

Azimuthal Correction Factors and Errors

$\cos\theta\ (\pi^-_{out}, \pi^-_{inc})$

$E_{c.m.}$ (MeV)	0.9 to 0.95	0.8 to 0.9	0.7 to 0.8	-0.8 to 0.7	-1.0 to -0.8
1406	1.50 ±0.20	1.25 ±0.10	1.10 ±0.08	1.08 ±0.04	1.02 ±0.08
1440	1.50 ±0.20	1.25 ±0.10	1.10 ±0.08	1.08 ±0.04	1.02 ±0.08
1472	1.50 ±0.20	1.25 ±0.10	1.10 ±0.08	1.08 ±0.04	1.02 ±0.08
1496	1.45 ±0.18	1.20 ±0.08	1.02 ±0.07	1.05 ±0.04	1.02 ±0.10
1527	1.45 ±0.14	1.13 ±0.07	1.10 ±0.07	1.01 ±0.03	1.10 ±0.10
1556	1.60 ±0.22	1.25 ±0.10	1.12 ±0.10	1.06 ±0.04	1.10 ±0.13
1589	1.60 ±0.22	1.25 ±0.10	1.12 ±0.10	1.06 ±0.04	1.10 ±0.13
1628	1.30 ±0.20	1.08 ±0.12	1.12 ±0.20	1.0 ±0.07	1.18 ±0.18
1647	1.28 ±0.06	1.08 ±0.04	1.05 ±0.05	1.05 ±0.03	1.14 ±0.06
1660	1.14 ±0.07	1.02 ±0.05	1.01 ±0.07	1.05 ±0.04	1.17 ±0.08
1669	1.22 ±0.05	1.07 ±0.04	1.04 ±0.05	1.04 ±0.03	1.16 ±0.07
1674	1.17 ±0.05	1.08 ±0.04	1.00 ±0.05	1.11 ±0.03	1.15 ±0.07
1685	1.29 ±0.07	1.07 ±0.05	1.07 ±0.06	1.05 ±0.04	1.12 ±0.06
1695	1.25 ±0.08	1.13 ±0.06	1.07 ±0.08	1.02 ±0.04	1.04 ±0.08
1709	1.30 ±0.10	1.08 ±0.05	1.05 ±0.06	1.03 ±0.04	1.10 ±0.09
1720	1.22 ±0.10	1.04 ±0.07	1.02 ±0.08	1.10 ±0.07	1.00 ±0.11
1730	1.30 ±0.10	1.08 ±0.05	1.05 ±0.06	1.03 ±0.04	1.10 ±0.09
1740	1.24 ±0.06	1.10 ±0.04	1.05 ±0.05	1.07 ±0.03	1.20 ±0.09

1801828

Table IV (cont'd.)

$E_{c.m.}$ (MeV)	0.9 to 0.95	0.8 to 0.9	0.7 to 0.8	-0.8 to 0.7	-1.0 to -0.8
1761	1.22 ±0.10	1.04 ±0.07	1.02 ±0.08	1.10 ±0.07	1.00 ±0.11
1762	1.19 ±0.07	1.13 ±0.07	1.03 ±0.06	1.07 ±0.04	1.17 ±0.10
1766	1.18 ±0.08	1.06 ±0.06	1.04 ±0.07	1.01 ±0.05	1.20 ±0.15
1787	1.11 ±0.07	1.08 ±0.05	1.05 ±0.06	1.05 ±0.04	1.01 ±0.10
1806	1.11 ±0.07	1.08 ±0.05	1.05 ±0.06	1.05 ±0.04	1.01 ±0.10
1811	1.18 ±0.11	1.05 ±0.07	1.09 ±0.09	1.00 ±0.05	1.00 ±0.11
1821	1.11 ±0.07	1.08 ±0.05	1.05 ±0.06	1.05 ±0.04	1.01 ±0.10
1843	1.17 ±0.06	1.07 ±0.05	1.10 ±0.08	1.06 ±0.05	1.07 ±0.11
1853	1.10 ±0.07	1.02 ±0.05	1.07 ±0.08	1.06 ±0.05	1.04 ±0.13
1872	1.10 ±0.06	1.05 ±0.04	1.10 ±0.07	1.03 ±0.04	1.05 ±0.10
1885	1.12 ±0.07	1.05 ±0.06	1.04 ±0.08	1.06 ±0.06	1.10 ±0.14
1904	1.05 ±0.05	1.06 ±0.04	1.09 ±0.07	1.04 ±0.04	1.11 ±0.14
1916	1.25 ±0.06	1.08 ±0.05	1.15 ±0.08	1.11 ±0.05	1.00 ±0.11
1933	1.16 ±0.08	1.13 ±0.06	1.16 ±0.10	1.10 ±0.06	1.12 ±0.20
1935	1.08 ±0.08	1.00 ±0.06	1.08 ±0.09	1.10 ±0.07	1.15 ±0.25
1963	1.12 ±0.05	1.07 ±0.05	1.01 ±0.01	1.05 ±0.04	1.15 ±0.15
1980	1.22 ±0.06	1.20 ±0.07	1.10 ±0.08	1.09 ±0.04	1.05 ±0.15

1801828

loss is independent of production angle and hence is primarily caused by the bias in POOH against steeply dipping tracks. The corrections, made by energy regions, are listed in Table V.

TABLE V

Azimuthal Correction Factors and Errors

C.M.S. Energy	$\pi^+\pi^-n$		$\pi^-\pi^0p$	
	Correction	Error	Correction	Error
1406	1.09	0.10	1.00	0.15
1440	1.08	0.10	1.00	0.15
1471	1.15	0.09	1.07	0.08
1496	1.15	0.06	1.06	0.06
1527	1.10	0.06	1.01	0.05
1556	1.08	0.09	1.08	0.09
1589	1.08	0.07	1.05	0.07
1629	1.09	0.07	1.05	0.09
1647	1.03	0.02	1.02	0.03
1660	1.05	0.03	1.01	0.04
1669	1.04	0.02	1.01	0.03
1674	1.10	0.03	1.03	0.03
1685	1.08	0.03	1.00	0.03
1695	1.07	0.04	1.06	0.05
1709	1.07	0.06	1.10	0.09
1720	1.05	0.07	1.08	0.10
1730	1.12	0.05	1.03	0.05
1740	1.05	0.03	1.05	0.03
1761	1.10	0.06	1.00	0.06
1762	1.07	0.05	1.00	0.04
1766	1.02	0.04	1.02	0.04
1787	1.03	0.05	1.02	0.07
1806	1.00	0.09	1.00	0.11
1811	1.05	0.04	1.02	0.05
1821	1.04	0.04	1.02	0.05
1843	1.05	0.03	1.01	0.03
1853	1.01	0.03	1.03	0.05
1873	1.08	0.04	1.00	0.03
1884	1.07	0.04	1.00	0.04
1904	1.01	0.03	1.02	0.03
1916	1.06	0.03	1.02	0.03
1932	1.08	0.04	1.04	0.04
1935	1.03	0.04	1.05	0.05
1963	1.07	0.03	1.02	0.03
1980	1.06	0.03	1.02	0.03

1801829

III. EXPERIMENTAL RESULTS - ELASTIC CHANNEL

A. Cross Sections

We normalized our data to the counter-experiment data of Duke et al.,[20] Helland et al.,[21] and Ogden et al.,[22] in a limited region of production angle, $-0.8 \leq \cos\theta \leq 0.7$. In this region, corrections for biases are not severe for either counters or bubble chambers. Also, this angular region contributes only 20 - 30% of the total cross section and it varies slowly with energy, as seen in the bottom curve of Fig. 21. Thus the sharp structure in the elastic cross section measured in our experiment should be largely independent of the experiments to which we normalized.

We do not have an accurate measurement of the total number of elastic events because we lose events corresponding to stopping protons in the very forward direction, $0.95 \leq \cos\theta \leq 1.0$. To calculate the total elastic cross section, we must first fit the angular distributions with an expansion in Legendre polynomials. The cross section is given in terms of the resulting Legendre coefficient A_0 according to the relation

$$\sigma_{el} = 4\pi A_0 \tag{3.1}$$

This cross section is shown in Fig. 21 along with the cross sections measured by the counter experiments.[20,21,22]

The same normalization procedure is followed for the inelastic events. We believe that the same cross section/corrected event should apply because the efficiencies for fitting the elastic and inelastic events are nearly the same. The cross sections for the $n\pi^+\pi^-$ and $p\pi^-\pi^0$ final states are plotted in Figs. 22 and 23 together with data from other authors.[23] In Fig. 24, we add these two inelastic cross sections to the elastic cross section and compare

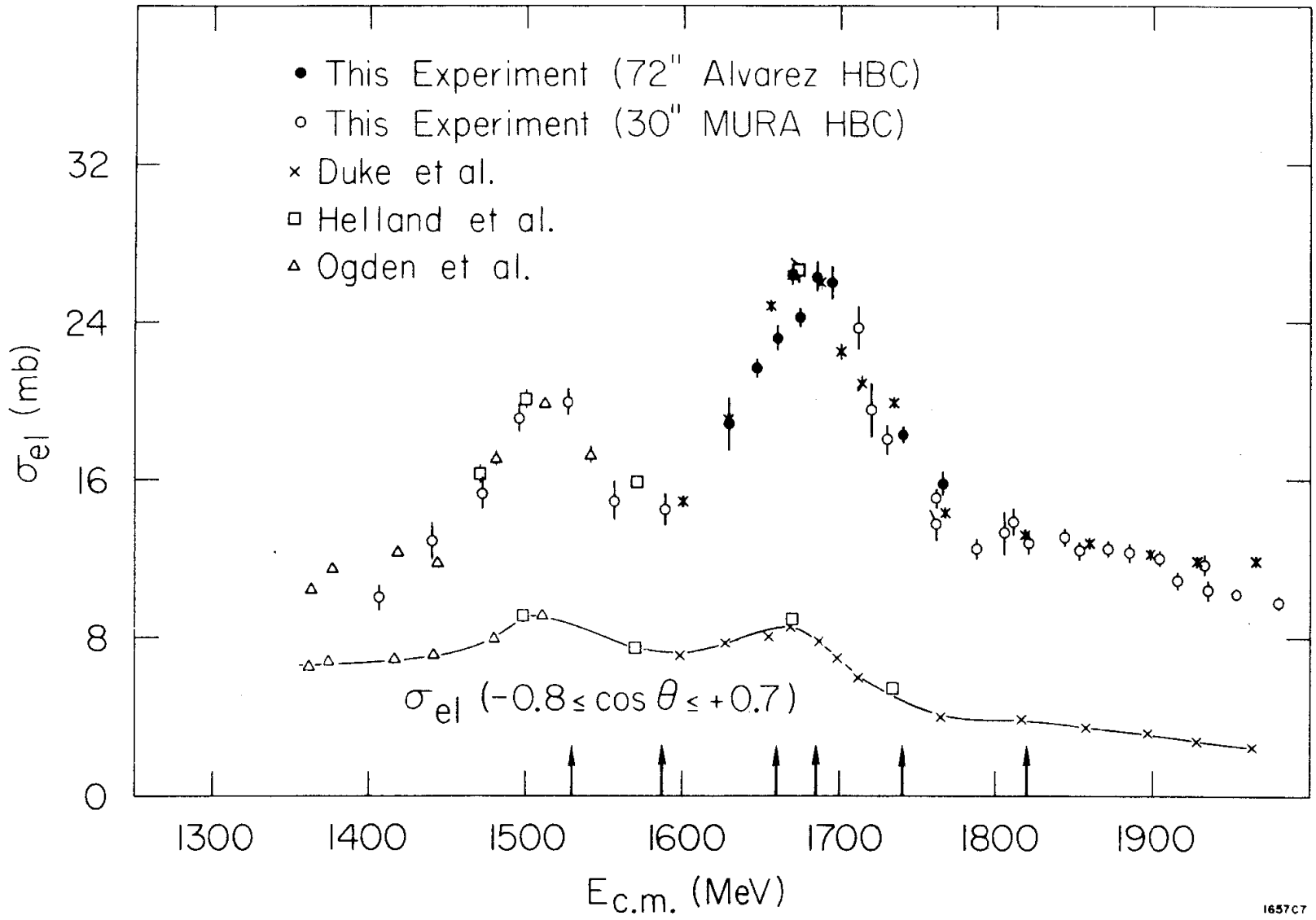

FIG. 21--π^-p elastic cross section measurements of Duke et al.,[20] Helland et al.,[21] Ogden et al.,[22] and this experiment. The lower curve is the cross section integrated over the region used for normalization, $-0.8 \leq \cos\theta \leq 0.7$. The arrows indicate energies chosen for comparison of differential cross sections with the results of phase shift analyses.

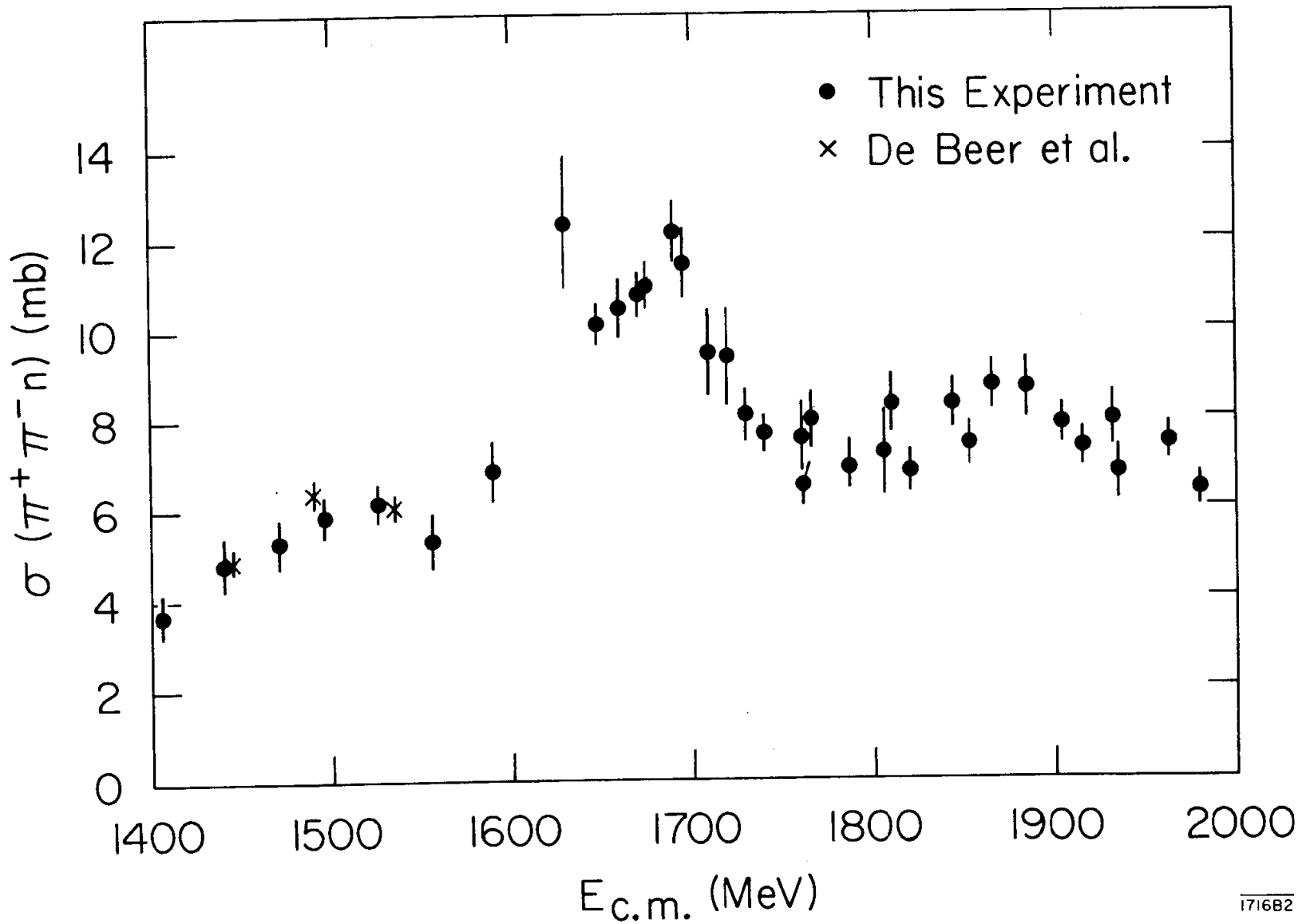

FIG. 22--Cross section for the reaction $\pi^- p \rightarrow n\pi^+\pi^-$ measured by De Beer et al.,[23] and this experiment.

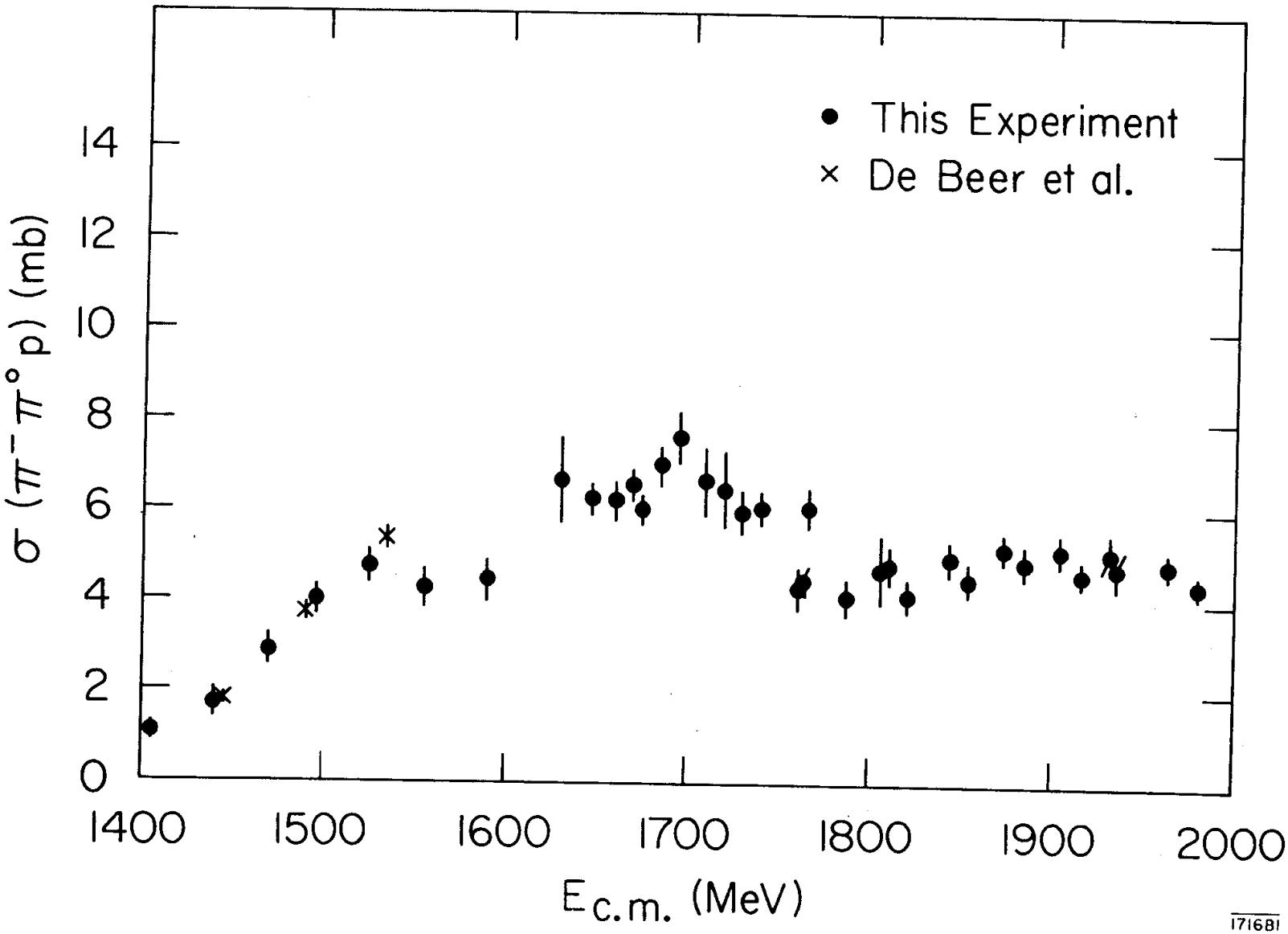

FIG. 23--Cross section for the reaction $\pi^- p \rightarrow p\pi^-\pi^0$ measured by De Beer *et al.*,[23] and this experiment.

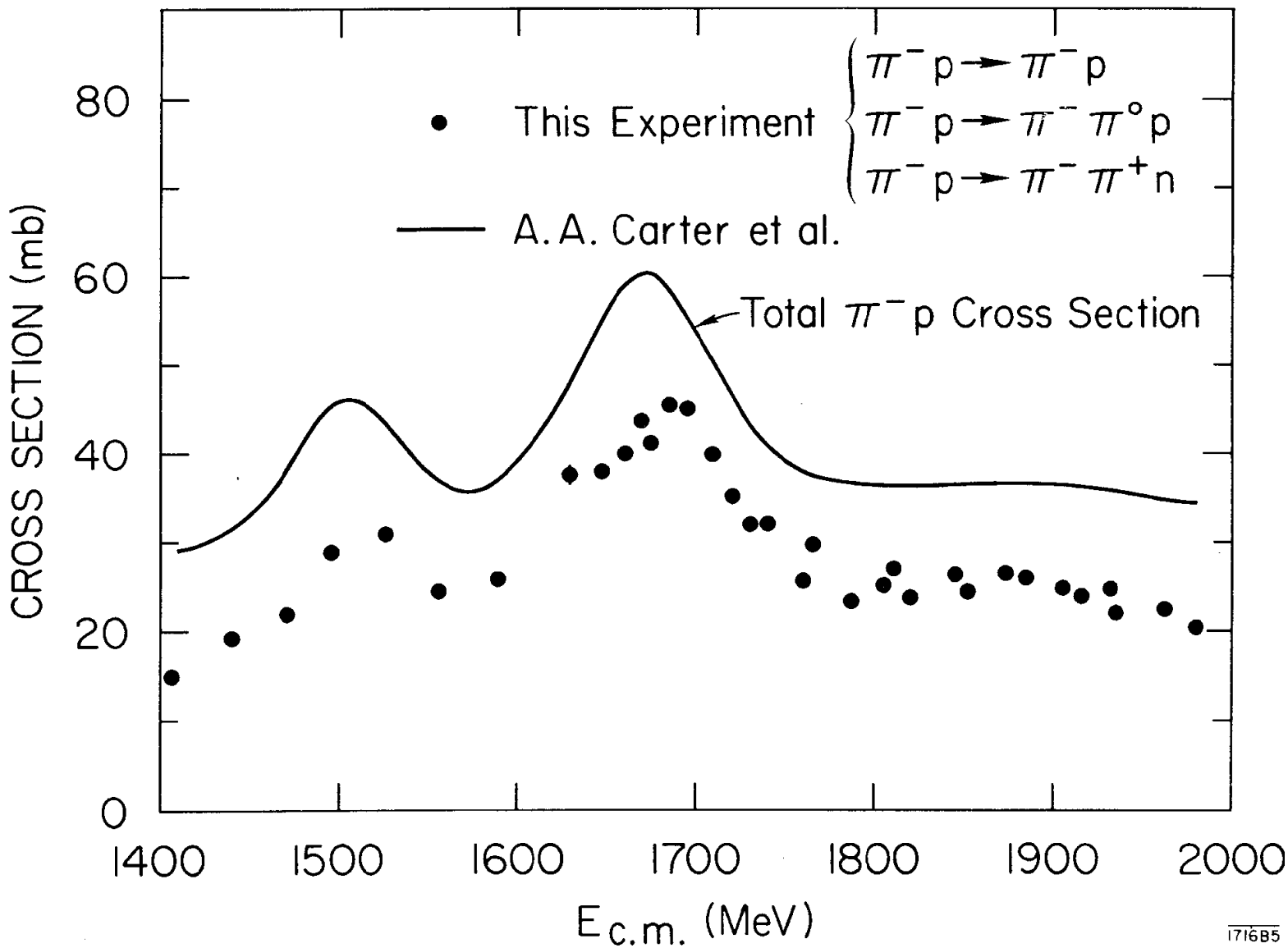

FIG. 24--Cross section for the reactions $\pi^- p \rightarrow \pi^- p$, $\pi^- p \rightarrow n\pi^+\pi^-$, $\pi^- p \rightarrow p\pi^-\pi^0$ compared with the total cross section measurements of A. A. Carter et al.[24]

them to the total cross section of A. A. Carter et al.[24] Finally, in Fig. 25, we present the ratio of cross sections, $\sigma(n\pi^+\pi^-)$ to $\sigma(p\pi^-\pi^0)$ as determined in our experiment and others. Table VI lists the cross sections for all three reactions.

B. Elastic Scattering Angular Distribution

The differential cross sections for elastic scattering events are presented in Fig. 26. (The data is also available in tabular form.[25]) The distributions extend up to $\cos\theta = 0.90$ below 1555 MeV and up to $\cos\theta = 0.95$ at higher energies; beyond these forward pion angles, the recoiling proton has nearly zero range. The production angle θ in these graphs is the angle between the outgoing and the incoming pion.

The smooth curves superposed on the data of Fig. 26 represent the best fit by a series expansion in Legendre polynomials, given by

$$d\sigma/d\Omega = \Sigma_n A_n P_n (\cos\theta) \tag{3.2}$$

In order to decide the order of fit required we looked for that fit where the confidence level rose to a significantly high value. Because of fluctuations in the quality of these fits, we kept that order which seemed to be required by most of the distributions in a given energy region. Below 1674 MeV an expansion to order $n=5$ was sufficient; above this order $n=6$ was required. Table VII lists the Legendre coefficients, the χ^2 and the confidence level for each of the 35 energies.

In Fig. 27, we plot the Legendre coefficients from our experiment and others.[20,22] We can make qualitative deductions about the behavior of the partial waves based on these coefficients, as we mentioned in the introduction. The coefficients A_n can be expressed in terms of the partial-wave amplitudes

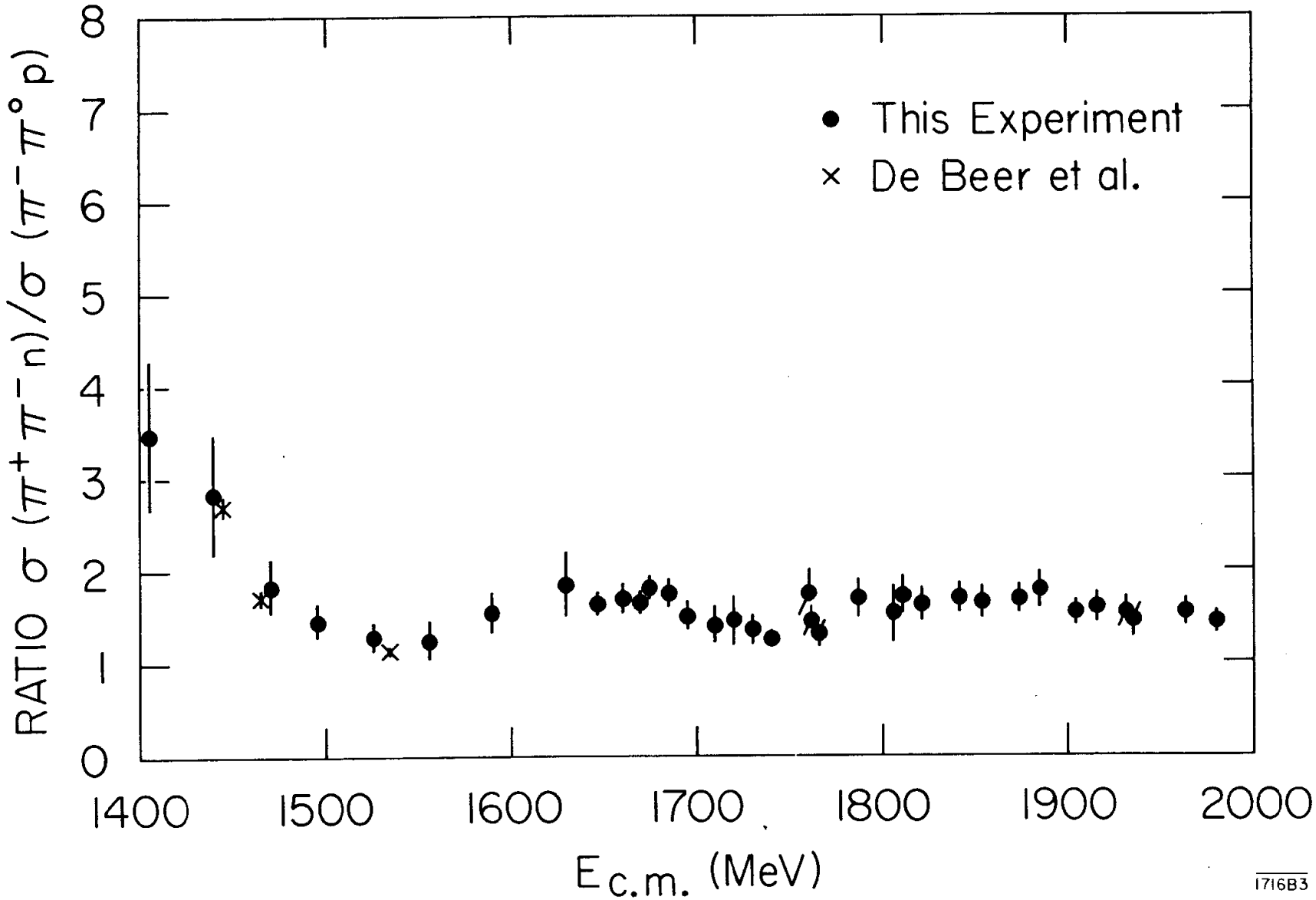

FIG. 25--Ratio $\sigma(n\pi^+\pi^-)/\sigma(p\pi^-\pi^0)$ as a function of energy.

TABLE VI

Cross Sections

C.M.S. Energy	$\pi^- p \to \pi^- p$		$\pi^- p \to \pi^- \pi^+ n$		$\pi^- p \to \pi^- \pi^0 p$	
	σ(mb)	$\delta\sigma$(mb)	σ(mb)	$\delta\sigma$(mb)	σ(mb)	$\delta\sigma$(mb)
1406	10.24	0.62	3.67	0.46	1.06	0.21
1440	12.86	0.94	4.79	0.62	1.69	0.33
1471	15.32	0.80	5.25	0.55	2.86	0.32
1496	19.07	0.74	5.84	0.47	3.98	0.35
1527	19.91	0.71	6.12	0.47	4.74	0.35
1556	14.91	0.96	5.30	0.60	4.24	0.49
1589	14.47	0.84	6.83	0.64	4.44	0.44
1629	18.80	1.32	12.38	1.47	6.66	0.93
1647	21.62	0.46	10.10	0.47	6.21	0.33
1660	23.16	0.66	10.47	0.64	6.19	0.43
1669	26.42	0.58	10.76	0.50	6.54	0.35
1674	24.22	0.54	10.92	0.54	6.00	0.32
1685	26.30	0.75	12.17	0.69	6.96	0.42
1695	26.01	0.86	11.45	0.77	7.60	0.58
1709	23.65	1.10	9.46	0.83	6.65	0.73
1720	19.48	1.35	9.33	1.06	6.41	0.87
1730	17.95	0.74	8.07	0.59	5.93	0.46
1740	18.29	0.47	7.64	0.40	6.04	0.32
1761	13.66	0.78	7.56	0.74	4.26	0.45
1762	15.01	0.50	6.49	0.47	4.43	0.31
1766	15.73	0.61	7.95	0.61	6.06	0.47
1787	12.45	0.59	6.92	0.55	4.09	0.40
1806	13.31	1.08	7.22	0.98	4.68	0.75
1811	13.80	0.61	8.30	0.64	4.79	0.41
1821	12.80	0.55	6.76	0.47	4.15	0.33
1843	13.09	0.45	8.33	0.54	4.93	0.34
1853	12.38	0.45	7.40	0.50	4.48	0.36
1873	12.53	0.39	8.73	0.55	5.19	0.32
1884	12.34	0.50	8.68	0.67	4.86	0.39
1904	11.95	0.36	7.84	0.47	5.13	0.31
1916	10.87	0.36	7.31	0.45	4.62	0.30
1932	11.69	0.49	7.97	0.61	5.21	0.41
1935	10.39	0.47	6.76	0.58	4.74	0.44
1963	10.21	0.29	7.43	0.42	4.85	0.28
1980	9.82	0.33	6.36	0.36	4.40	0.26

1801830

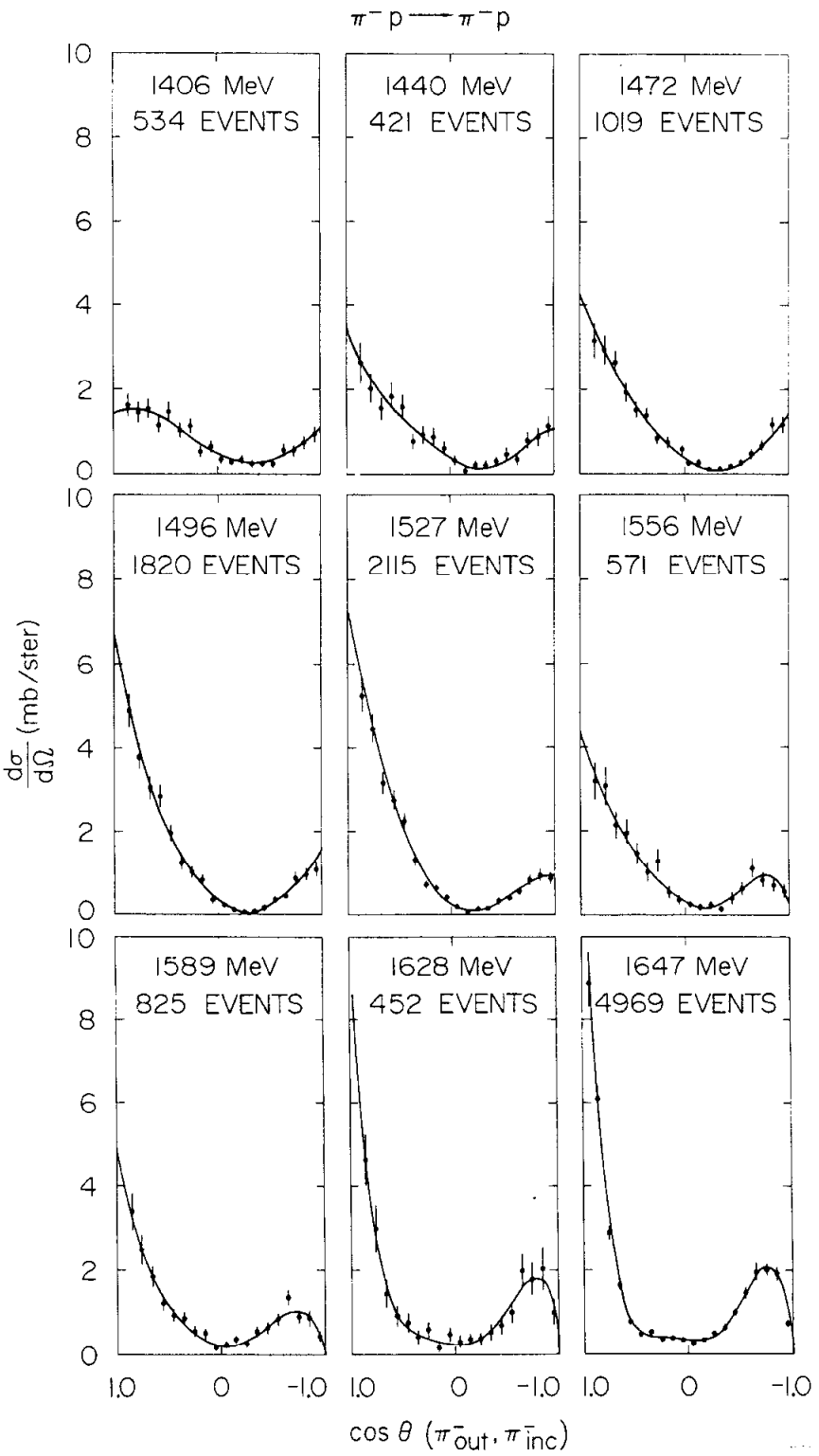

FIG. 26--π^-p differential cross sections measured in this experiment. Smooth curves represent the best fit by an expansion in Legendre polynomials.

FIG. 26 cont'd.

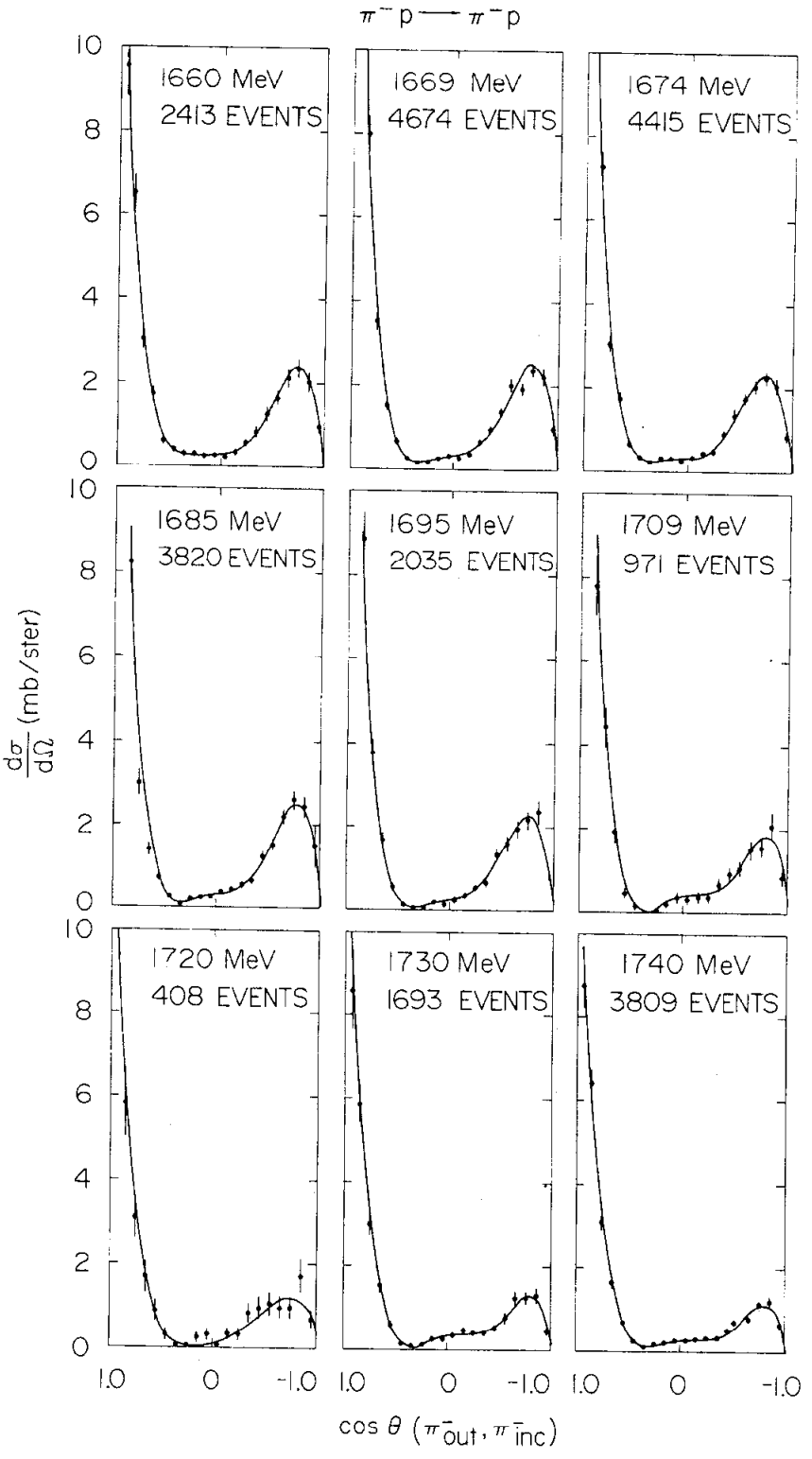
$\pi^- p \longrightarrow \pi^- p$
1660 MeV
2413 EVENTS
1669 MeV
4674 EVENTS
1674 MeV
4415 EVENTS
1685 MeV
3820 EVENTS
1695 MeV
2035 EVENTS
1709 MeV
971 EVENTS
1720 MeV
408 EVENTS
1730 MeV
1693 EVENTS
1740 MeV
3809 EVENTS
$\frac{d\sigma}{d\Omega}$ (mb/ster)
0
2
4
6
8
10
1.0
0
-1.0
cos θ (π^-_{out}, π^-_{inc})

FIG. 26 cont'd.

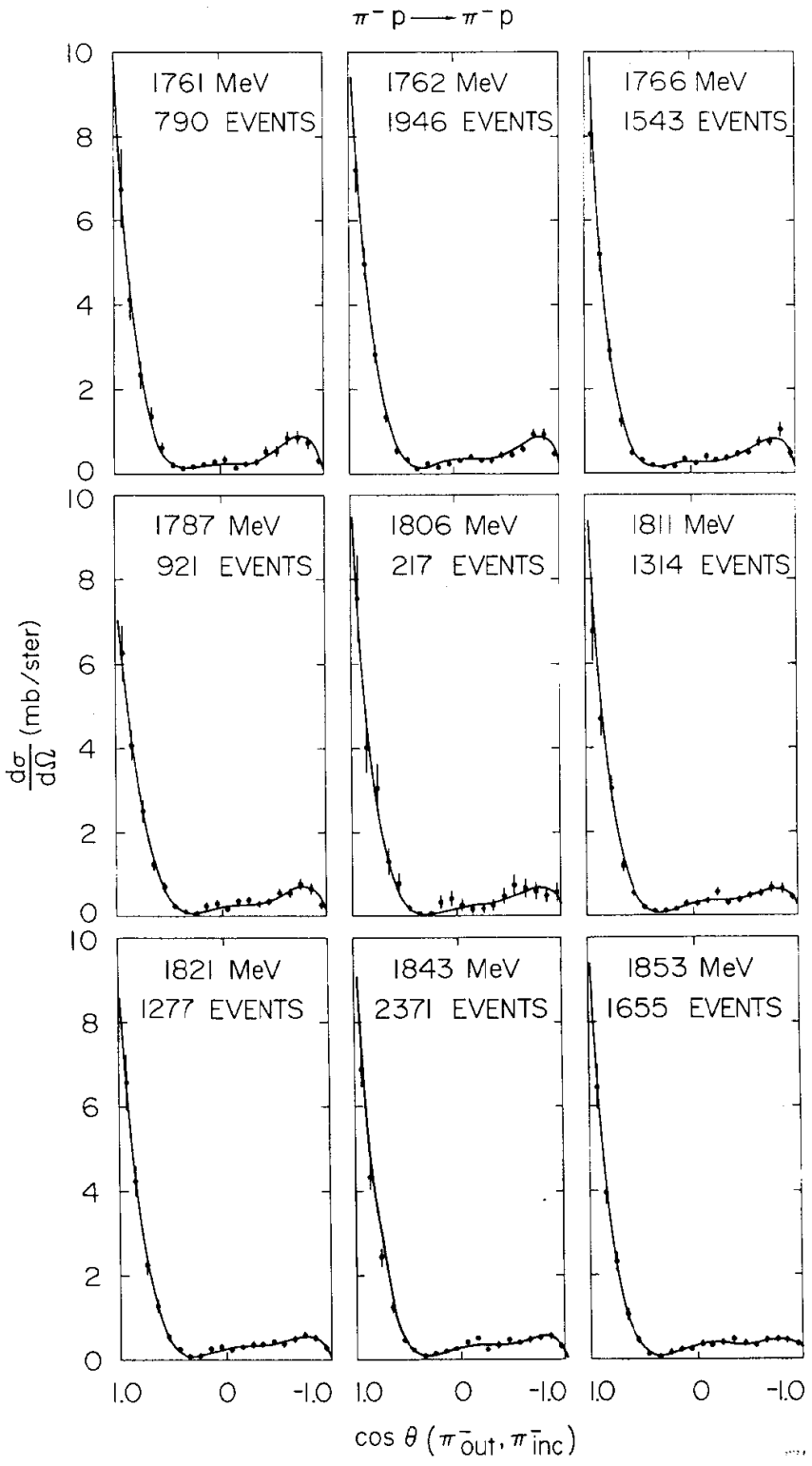
$\pi^- p \longrightarrow \pi^- p$
1761 MeV
790 EVENTS
1762 MeV
1946 EVENTS
1766 MeV
1543 EVENTS
1787 MeV
921 EVENTS
1806 MeV
217 EVENTS
1811 MeV
1314 EVENTS
1821 MeV
1277 EVENTS
1843 MeV
2371 EVENTS
1853 MeV
1655 EVENTS
$\frac{d\sigma}{d\Omega}$ (mb/ster)
0
2
4
6
8
10
1.0
0
-1.0
cos θ (π^-_{out}, π^-_{inc})

FIG. 26 cont'd.

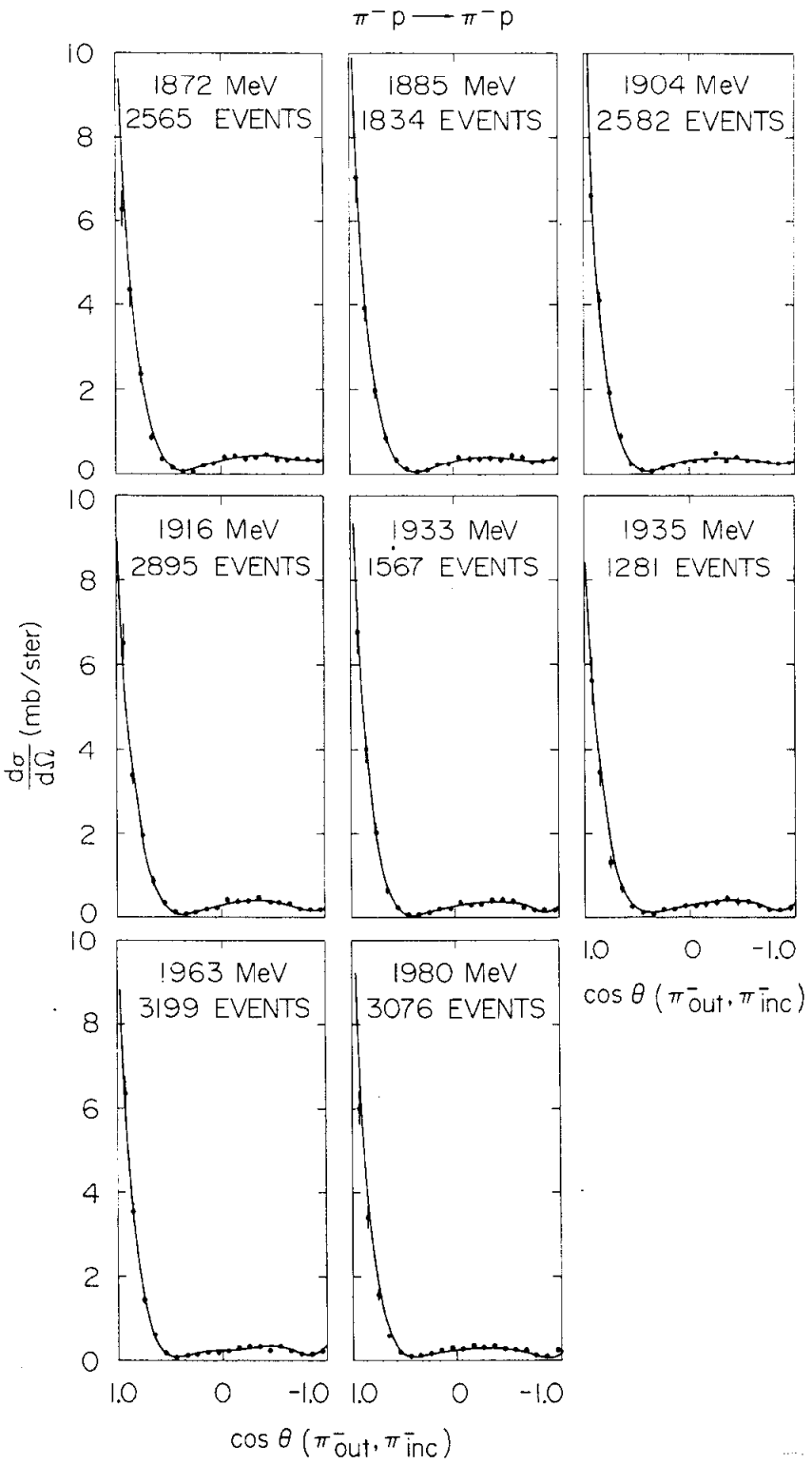
$\pi^- p \longrightarrow \pi^- p$
1872 MeV
2565 EVENTS
1885 MeV
1834 EVENTS
1904 MeV
2582 EVENTS
1916 MeV
2895 EVENTS
1933 MeV
1567 EVENTS
1935 MeV
1281 EVENTS
1963 MeV
3199 EVENTS
1980 MeV
3076 EVENTS
$\frac{d\sigma}{d\Omega}$ (mb/ster)
0
2
4
6
8
10
1.0
0
-1.0
$\cos\theta\ (\pi^-_{out}, \pi^-_{inc})$

TABLE VII

Legendre Coefficients

$$\frac{d\sigma}{d\Omega} = \sum_n A_n P_n (\cos\theta)$$

$E_{c.m.}$ (MeV)	1406	1440	1472	1496	1527	1556	1589	1628	1647	1660
Low Energy Cutoff	1394	1428	1456	1482	1514	1544	1576	1616	1632	1648
High Energy Cutoff	1418	1452	1486	1510	1540	1568	1602	1640	1662	1672
A_0	0.82 ±0.05	1.02 ±0.08	1.22 ±0.06	1.52 ±0.06	1.58 ±0.06	1.19 ±0.08	1.15 ±0.07	1.50 ±0.11	1.72 ±0.04	1.84 ±0.04
A_1	0.61 ±0.12	1.09 ±0.19	1.48 ±0.16	2.23 ±0.15	2.45 ±0.15	1.45 ±0.19	1.22 ±0.17	1.43 ±0.26	1.85 ±0.09	1.85 ±0.13
A_2	0.54 ±0.17	1.31 ±0.27	1.66 ±0.22	2.42 ±0.21	2.61 ±0.20	1.52 ±0.27	1.69 ±0.24	3.04 ±0.36	3.65 ±0.12	4.06 ±0.17
A_3	-0.46 ±0.21	-0.04 ±0.31	-0.08 ±0.25	0.41 ±0.24	0.69 ±0.22	0.36 ±0.30	1.04 ±0.25	2.21 ±0.38	3.17 ±0.12	3.57 ±0.17
A_4	-0.16 ±0.19	0.00 ±0.27	0.03 ±0.21	0.07 ±0.19	-0.10 ±0.18	-0.30 ±0.25	-0.14 ±0.21	0.78 ±0.30	1.16 ±0.10	1.26 ±0.14
A_5	0.00 ±0.17	0.20 ±0.23	0.08 ±0.17	0.20 ±0.15	0.07 ±0.14	0.39 ±0.21	0.39 ±0.18	1.11 ±0.30	1.72 ±0.10	1.82 ±0.14
A_6										
χ^2	13.37	16.18	6.85	9.21	14.00	10.31	12.7	9.75	11.89	4.86
$\langle\chi^2\rangle$	13	13	13	13	13	13	13	13	14	14
Confidence Level (%)	42.0	23.9	91.0	75.7	37.4	66.9	47.2	71.4	61.5	98.8

1801832

Table VII (cont'd.)

$E_{c.m.}$ (MeV)	1669	1674	1685	1695	1709	1720	1730	1740	1761	1762
Low Energy Cutoff	1656	1658	1670	1680	1696	1708	1716	1722	1750	1748
High Energy Cutoff	1682	1690	1700	1710	1720	1732	1744	1758	1772	1776
A_0	2.10 ±0.05	1.93 ±0.04	2.09 ±0.06	2.07 ±0.07	1.88 ±0.09	1.55 ±0.11	1.43 ±0.06	1.46 ±0.04	1.09 ±0.06	1.19 ±0.04
A_1	2.42 ±0.11	2.13 ±0.11	2.44 ±0.16	2.69 ±0.18	2.67 ±0.24	2.35 ±0.28	2.07 ±0.16	2.30 ±0.10	1.68 ±0.17	1.89 ±0.11
A_2	4.94 ±0.15	4.38 ±0.15	5.07 ±0.21	5.22 ±0.24	4.75 ±0.31	3.95 ±0.38	3.40 ±0.21	3.65 ±0.13	2.61 ±0.22	2.86 ±0.15
A_3	4.50 ±0.15	4.04 ±0.17	4.44 ±0.23	4.77 ±0.27	4.10 ±0.34	3.45 ±0.44	2.98 ±0.23	3.01 ±0.15	2.26 ±0.25	2.38 ±0.16
A_4	1.83 ±0.12	1.64 ±0.17	2.00 ±0.22	2.18 ±0.25	2.01 ±0.31	1.69 ±0.42	1.37 ±0.21	1.62 ±0.14	1.08 ±0.24	1.29 ±0.16
A_5	2.13 ±0.12	1.98 ±0.13	2.08 ±0.15	2.16 ±0.17	1.53 ±0.22	1.20 ±0.30	1.07 ±0.16	1.06 ±0.10	0.89 ±0.18	0.72 ±0.12
A_6		0.14 ±0.13	-0.04 ±0.15	0.17 ±0.17	-0.28 ±0.21	0.32 ±0.29	-0.37 ±0.14	-0.14 ±0.10	-0.14 ±0.16	-0.17 ±0.11
χ^2	20.09	14.75	14.91	9.23	9.86	14.78	6.52	10.45	8.83	15.1
$\langle\chi^2\rangle$	14	13	13	13	13	13	13	13	13	13
Confidence Level (%)	12.7	32.3	31.3	75.5	70.5	32.2	92.5	65.7	78.5	30.2

1801832

Table VII (cont'd.)

$E_{c.m.}$ (MeV)	1766	1787	1806	1811	1821	1843	1853	1872	1885	1904
Low Energy Cutoff	1754	1774	1794	1796	1808	1828	1838	1856	1872	1890
High Energy Cutoff	1778	1800	1818	1826	1834	1858	1866	1888	1898	1918
A_0	1.25 ±0.05	0.99 ±0.05	1.06 ±0.09	1.10 ±0.05	1.02 ±0.04	1.04 ±0.04	0.99 ±0.04	1.00 ±0.03	0.98 ±0.04	0.95 ±0.03
A_1	2.08 ±0.13	1.62 ±0.13	1.82 ±0.22	1.82 ±0.13	1.71 ±0.12	1.80 ±0.10	1.67 ±0.10	1.73 ±0.08	1.74 ±0.11	1.74 ±0.08
A_2	3.15 ±0.18	2.33 ±0.17	2.76 ±0.31	2.64 ±0.18	2.38 ±0.16	2.52 ±0.13	2.34 ±0.13	2.37 ±0.11	2.39 ±0.15	2.36 ±0.11
A_3	2.73 ±0.20	1.94 ±0.19	2.35 ±0.35	2.30 ±0.19	2.14 ±0.18	2.28 ±0.14	2.17 ±0.14	2.31 ±0.12	2.37 ±0.16	2.40 ±0.11
A_4	1.61 ±0.19	0.79 ±0.18	1.28 ±0.34	1.26 ±0.18	1.12 ±0.17	1.31 ±0.13	1.32 ±0.14	1.45 ±0.11	1.60 ±0.14	1.67 ±0.10
A_5	1.03 ±0.14	0.41 ±0.14	0.64 ±0.26	0.53 ±0.14	0.50 ±0.13	0.61 ±0.10	0.52 ±0.11	0.56 ±0.09	0.64 ±0.11	0.76 ±0.08
A_6	0.07 ±0.13	-0.29 ±0.12	-0.03 ±0.25	-0.11 ±0.12	-0.10 ±0.11	-0.06 ±0.09	-0.03 ±0.10	0.11 ±0.08	0.21 ±0.09	0.25 ±0.07
χ^2	13.73	12.85	12.20	9.71	7.38	15.87	9.40	9.69	8.34	10.67
$\langle\chi^2\rangle$	13	13	13	13	13	13	13	13	13	13
Confidence Level (%)	39.3	45.9	51.1	71.8	88.1	25.6	74.2	71.9	82.1	63.9

1801832

Table VII (cont'd.)

$E_{c.m.}$ (MeV)	1916	1933	1935	1963	1980
Low Energy Cutoff	1902	1917	1920	1948	1966
High Energy Cutoff	1930	1947	1950	1978	1994
A_0	0.87 ±0.03	0.93 ±0.04	0.83 ±0.04	0.81 ±0.02	0.78 ±0.03
A_1	1.59 ±0.08	1.79 ±0.10	1.53 ±0.10	1.56 ±0.06	1.56 ±0.07
A_2	2.05 ±0.11	2.40 ±0.14	2.02 ±0.14	2.09 ±0.09	2.01 ±0.10
A_3	2.13 ±0.11	2.55 ±0.15	2.13 ±0.15	2.20 ±0.09	2.15 ±0.10
A_4	1.37 ±0.10	1.79 ±0.13	1.47 ±0.13	1.65 ±0.09	1.59 ±0.09
A_5	0.52 ±0.08	0.87 ±0.10	0.68 ±0.11	0.84 ±0.07	0.80 ±0.07
A_6	0.20 ±0.06	0.41 ±0.09	0.34 ±0.09	0.45 ±0.05	0.37 ±0.05
χ^2	13.96	7.82	3.00	12.44	7.31
$\langle\chi^2\rangle$	13	13	13	13	13
Confidence Level (%)	37.6	85.5	99.8	49.2	88.5

1801B32

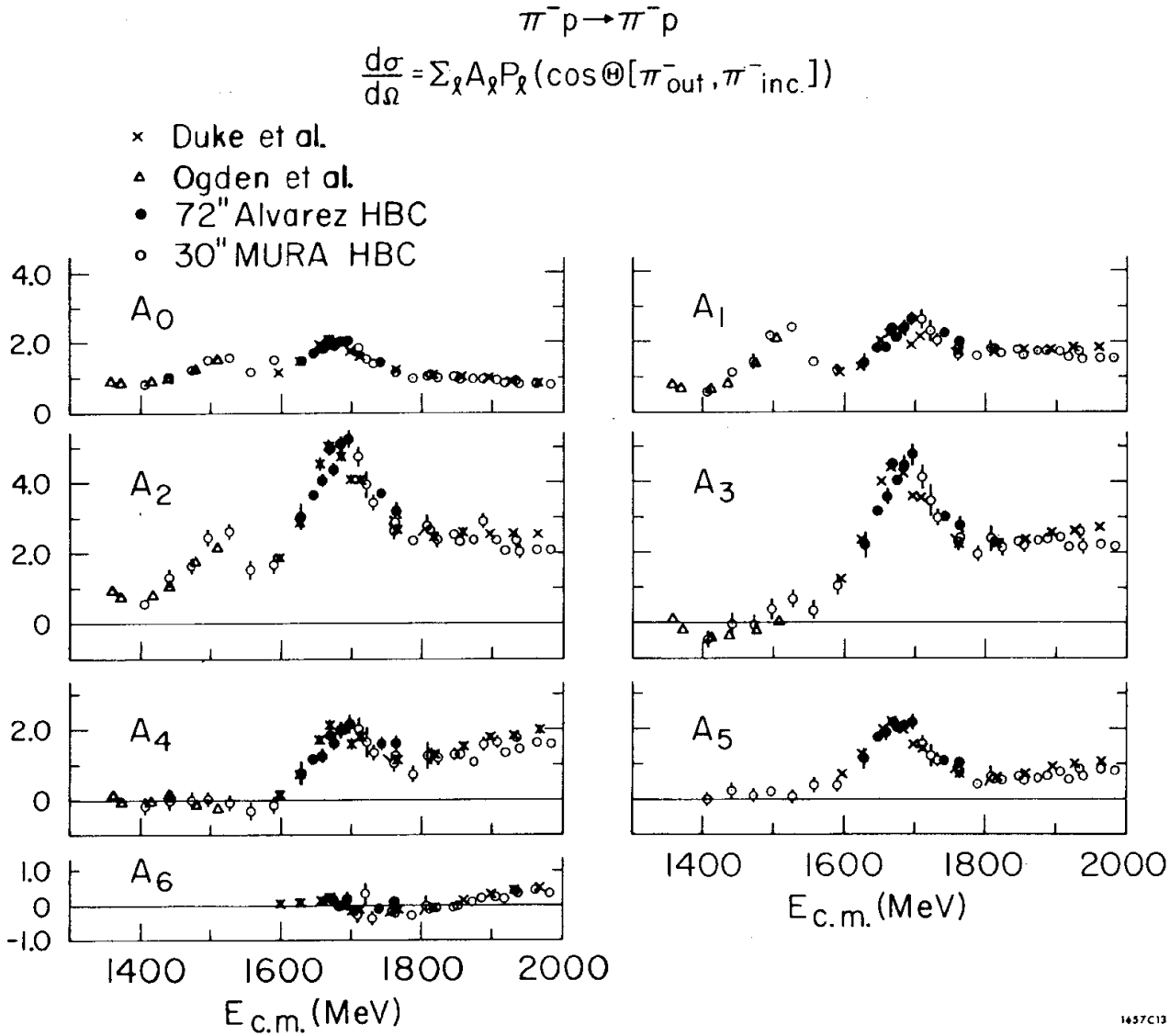

FIG. 27--Legendre coefficients from fit to π^-p differential cross sections.

$f_{\ell J}$ where ℓ is the angular momentum and J is the total spin.

$$A_n = \sum_{\ell J \geq \ell' J'} R^n_{\ell J, \ell' J'} \left\{ \mathrm{Re}\, f_{\ell J} \mathrm{Re}\, f_{\ell' J'} + \mathrm{Im}\, f_{\ell J} \mathrm{Im}\, f_{\ell' J'} \right\} \tag{3.3}$$

The numerical factors $R^n_{\ell J, \ell' J'}$ are listed in Table VIII. When a given $R^n_{\ell J, \ell' J'}$ is nonzero we expect A_n to show interference of partial waves $f_{\ell J}$ and $f_{\ell' J'}$ if this interference is significant. Note that we cannot distinguish the value of the isospin when we are looking only at the $\pi^- p$ final state; that determination requires data on the charge-exchange reaction or $\pi^+ p$ elastic scattering. Rigorously, the unambiguous determination of the parities further requires polarization data. Nevertheless, we can still learn something from the $\pi^- p$ data alone.

The coefficient A_0 is the elastic cross section, reflecting the coherent sum of individual partial waves. There is a sharp peak in coefficients A_1 and A_2 near 1520 MeV, while A_3 changes sign and higher coefficients are zero here. Table VIII indicates that the structure in A_2 is most likely caused by a D3 wave and that structure in A_1 probably reflects interference of D3 with a P1 wave. The change of sign in A_3 then represents interference of the D3 with the tail of the P33 resonance. (The sign changes because the real part of the D3 wave goes from positive to negative as the wave goes through resonance.) The fact that the interference in A_1 does not shift the peak from the D3 resonant energy is evidence that the P1 wave is purely imaginary.

The next region of activity lies near 1690 MeV, where all coefficients up through A_5 show structure. This implies that both D5 and F5 may be resonant. The odd coefficients A_1, A_3, and A_5 must reflect the interference of D5 and F5 waves. The absence of any change in sign or rapid variation of

TABLE VIII

$R^{n}_{\ell J, \ell' J'}$

ℓJ, ℓ'J'	0	1	2	3	4	5	6	7	8
S1, S1	1	0	0	0	0	0	0	0	0
P1, S1	0	2	0	0	0	0	0	0	0
P1, P1	1	0	0	0	0	0	0	0	0
P3, S1	0	4	0	0	0	0	0	0	0
P3, P1	0	0	4	0	0	0	0	0	0
P3, P3	2	0	2	0	0	0	0	0	0
D3, S1	0	0	4	0	0	0	0	0	0
D3, P1	0	4	0	0	0	0	0	0	0
D3, P3	0	4/5	0	36/5	0	0	0	0	0
D3, D3	2	0	2	0	0	0	0	0	0
D5, S1	0	0	6	0	0	0	0	0	0
D5, P1	0	0	0	6	0	0	0	0	0
D5, P3	0	30/5	0	24/5	0	0	0	0	0
D5, D3	0	0	12/7	0	72/7	0	0	0	0
D5, D5	3	0	24/7	0	18/7	0	0	0	0
F5, S1	0	0	0	6	0	0	0	0	0
F5, P1	0	0	6	0	0	0	0	0	0
F5, P3	0	0	12/7	0	72/7	0	0	0	0
F5, D3	0	36/5	0	24/5	0	0	0	0	0
F5, D5	0	18/35	0	16/5	0	100/7	0	0	0
F5, F5	3	0	24/7	0	18/7	0	0	0	0
F7, S1	0	0	0	8	0	0	0	0	0
F7, P1	0	0	0	0	8	0	0	0	0
F7, P3	0	0	72/7	0	40/7	0	0	0	0
F7, D3	0	0	0	8/3	0	40/3	0	0	0
F7, D5	0	72/7	0	8	0	40/7	0	0	0
F7, F5	0	0	8/7	0	360/77	0	200/11	0	0
F7, F7	4	0	100/21	0	324/77	0	100/33	0	0
G7, S1	0	0	0	0	8	0	0	0	0
G7, P1	0	0	0	8	0	0	0	0	0
G7, P3	0	0	0	8/3	0	40/3	0	0	0
G7, D3	0	0	72/7	0	40/7	0	0	0	0
G7, D5	0	0	8/7	0	360/77	0	200/11	0	0
G7, F5	0	72/7	0	8	0	40/7	0	0	0
G7, F7	0	8/21	0	24/11	0	600/91	0	9800/429	0
G7, G7	4	0	100/21	0	324/77	0	100/33	0	0
G9, S1	0	0	0	0	10	0	0	0	0
G9, P1	0	0	0	0	0	10	0	0	0
G9, P3	0	0	0	40/3	0	20/3	0	0	0
G9, D3	0	0	0	0	40/11	0	180/11	0	0
G9, D5	0	0	100/7	0	720/77	0	70/11	0	0
G9, F5	0	0	0	20/11	0	80/13	0	3150/143	0
G9, F7	0	40/3	0	120/11	0	120/13	0	2800/429	0
G9, G7	0	0	200/231	0	3240/1001	0	280/33	0	3920/143
G9, G9	5	0	200/33	0	810/143	0	160/33	0	490/143

1801835

the coefficients here indicates that these two waves must have a constant phase difference. Below 1690 MeV, A_1 manifests interference between F5 and D3. A_4 should be very sensitive to any interference between D5 and D3 because of the large value of $R^4_{D5,D3}$ here. Its value is near zero, most likely indicating that these two waves are 90° out of phase.

Above 1690 MeV, we can look for interference effects of the D5 and F5 waves with other possible resonances. All coefficients up through A_5 show a constant positive value in this region. There is a slow rise in both A_4 and A_6 after 1900 MeV. This behavior could arise from the onset of either an F7 or a G7 resonance. One might construe the slight negative value of A_6 below 1920 to indicate the interference of F7 with the F5 wave. A_5, which should show any G7-F5 interference, has no sharp structure in this region. Thus there is a tendency to prefer the F7 wave. The π^+p data, being pure isospin 3/2, offer more evidence in favor of the F7 interpretation. However, polarization data was historically required clearly to resolve this parity ambiguity.

The elastic differential cross sections thus confirm the presence of the D13(1520), D15(1670), F15(1688), and F37(1950) that are by now well established from the phase-shift analyses. They also suggest the P11(1470) "Roper" resonance.

IV. EXPERIMENTAL RESULTS - INELASTIC THREE-BODY

A. Mass Distributions

Because of the additional particle involved in the three-particle final state, three more parameters are required fully to specify the scattering. Information contained in these final states is more difficult to present and to interpret. The Dalitz plots give an indication of interactions between any two of the three particles. In Fig. 28 we plot $M^2(N\pi_1)$ against $M^2(N\pi_2)$ at four representative energies for both $n\pi^+\pi^-$ and $p\pi^-\pi^0$ final states. In Figs. 29 and 30 we present the corresponding projections as well as the $M^2(\pi_1\pi_2)$ distribution. These plots indicate strong production of $\Delta^-\pi^+$ throughout the energy region. At higher energies $\rho^0 n$ becomes increasingly important. Production of $\Delta^+\pi^-$ is also apparent but is not nearly as dominant. In the $p\pi^-\pi^0$ state, Δ^0 and Δ^+ are only weakly produced and decrease at higher energies. The previously observed[26] enhancement in the $\pi\pi$ mass at low energies is evident in the $n\pi^+\pi^-$ state but not in the $p\pi^-\pi^0$ state.

The Clebsch-Gordan coefficients favor the strong $\Delta^-\pi^+$ production that is observed. With interference effects neglected, the ratio $\Delta^-/\Delta^+ = 9/1$ for $n\pi^+\pi^-$ and $\Delta^0/\Delta^+ = 2/2$ for $p\pi^+\pi^-$ in a pure isospin 1/2 state. These ratios are 18/8 and 1/16, respectively, for a pure 3/2 state.

The dominance of the quasi-two-body intermediate states - $\Delta^-\pi^+$, $\Delta^+\pi^-$ and $\rho^0 n$ - implies that the $n\pi^+\pi^-$ final state might be described by an incoherent sum of these three processes plus phase space. We tried to fit the Dalitz plots with this description, taking the mass and width of the Δ and the ρ to be

$$M(\Delta) = 1236 \text{ MeV} \qquad \Gamma(\Delta) = 130 \text{ MeV} \tag{4.1}$$

$$M(\rho) = 765 \text{ MeV} \qquad \Gamma(\rho) = 130 \text{ MeV} \tag{4.2}$$

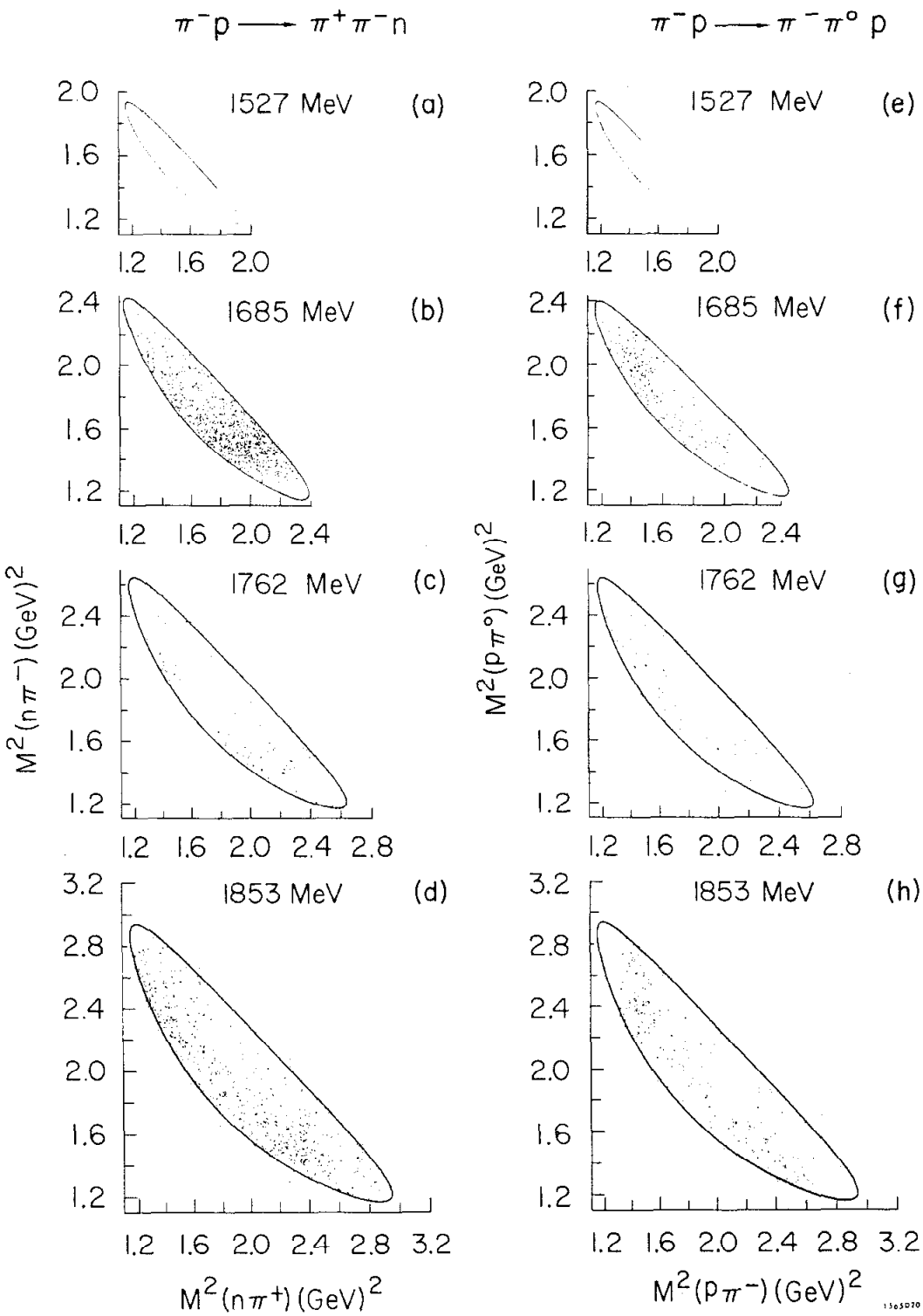

FIG. 28--Dalitz plots for the reactions $\pi^- p \rightarrow n\pi^+\pi^-$ and $\pi^- p \rightarrow p\pi^-\pi^0$ at four representative energies.

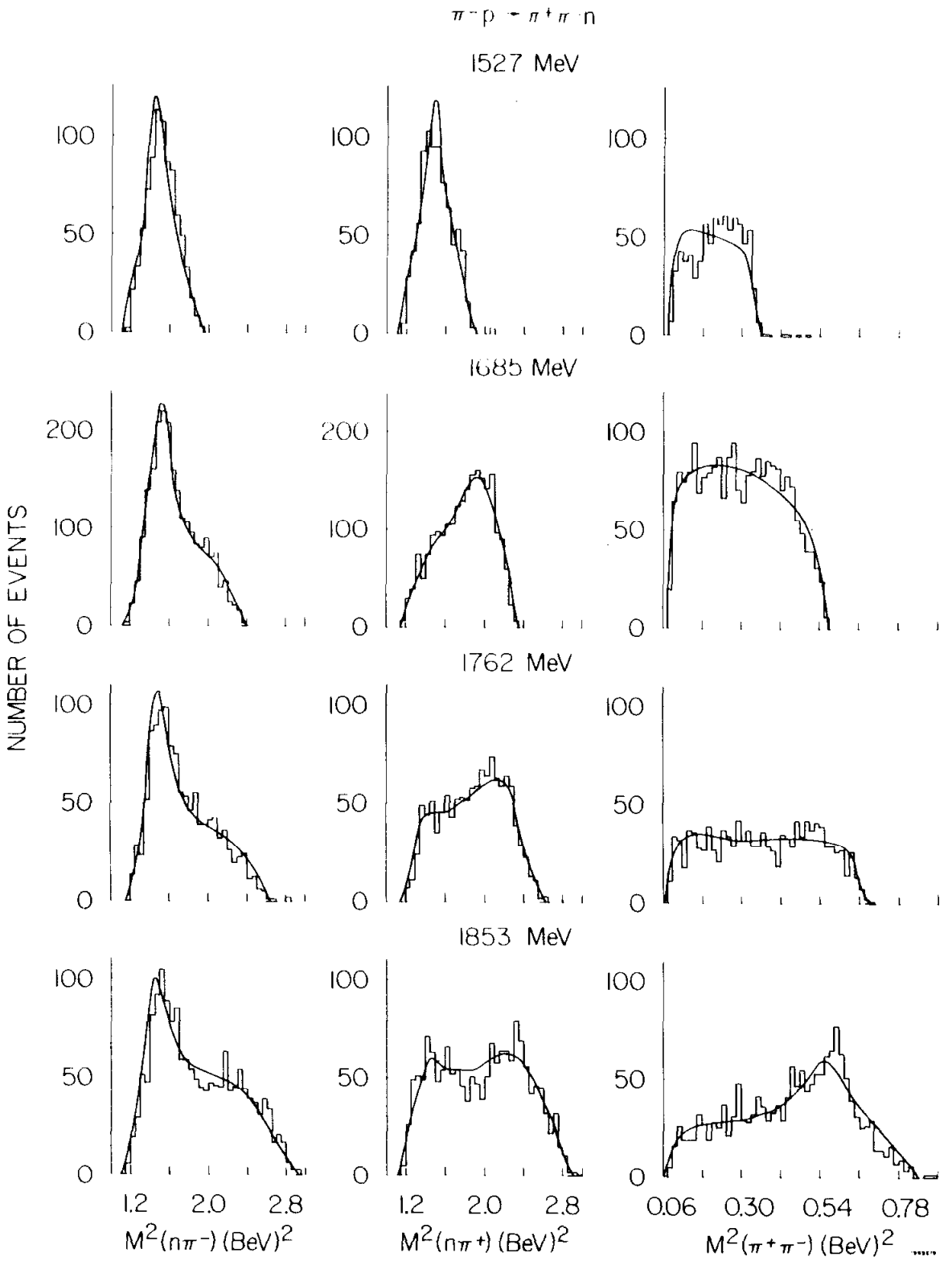

FIG. 29--Mass squared projections of the Dalitz plot in the final state $\pi^- p \to n\pi^+\pi^-$. The curves are from maximum likelihood fits to the Dalitz plot.

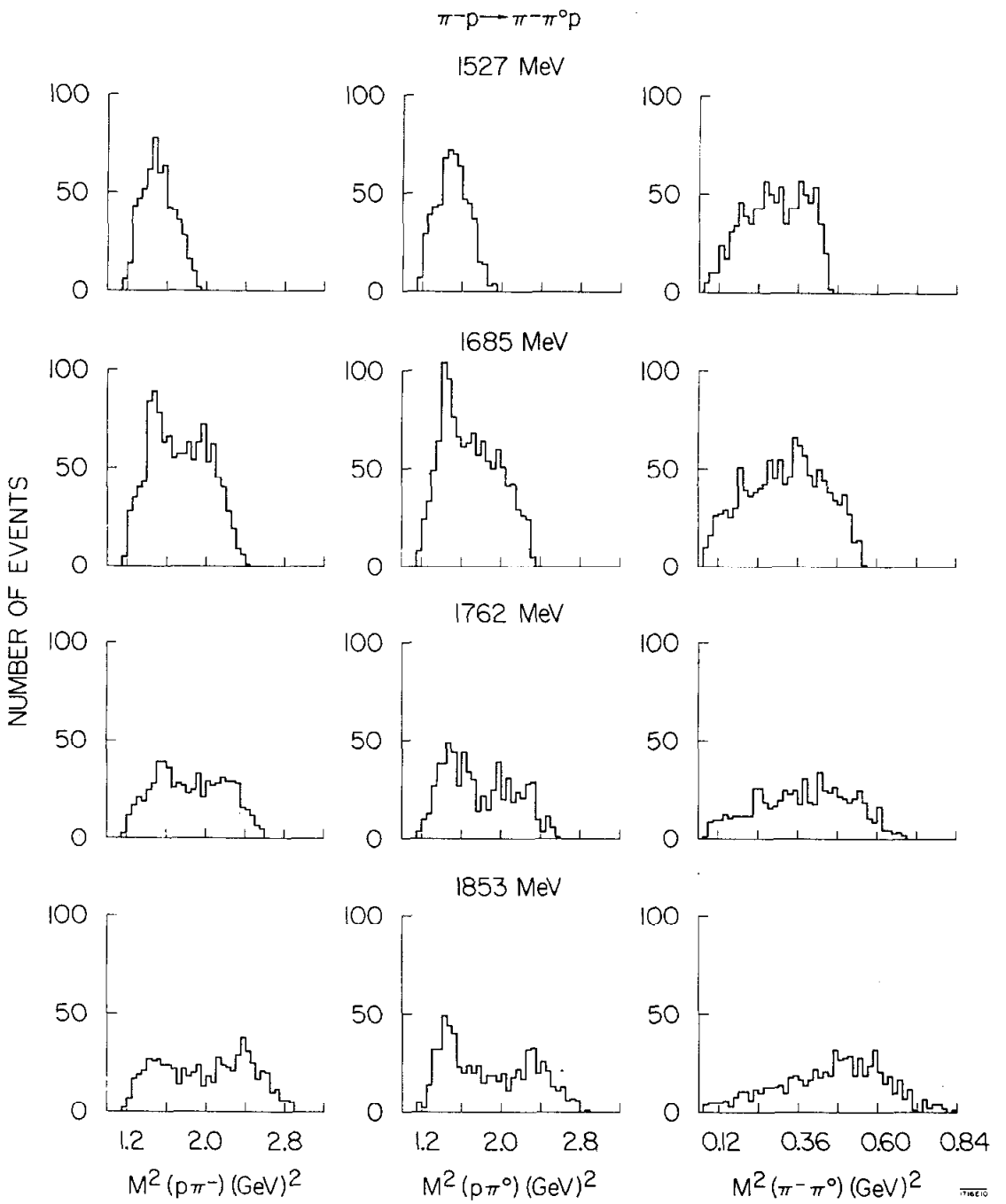

FIG. 30--Mass squared projections of the Dalitz plot in the final state $\pi^- p \rightarrow p\pi^-\pi^0$.

We used the maximum likelihood program, MURTLEBURT,[27] in which the resonance amplitudes are given the form of a relativistic Breit-Wigner[28]

$$T = \Gamma_0 \omega_0 \left(\frac{\omega}{\omega_0}\right)\left(\frac{q_0}{q}\right) \frac{\omega_0 \Gamma(\omega)}{(\omega^2-\omega_0^2)^2 + \omega_0^2 \Gamma^2(\omega)} \quad \cdots \tag{4.3}$$

with decay width

$$\Gamma(\omega) = \Gamma_0 \left(\frac{q}{q_0}\right)^{2L+1} \frac{B_L(qr)}{B_L(q_0 r)} \tag{4.4}$$

Here ω = the diparticle mass

q = the momentum of the decay particles in the diparticle rest frame

L = orbital angular momentum of the decay particles

$B_L(qr)$ = barrier penetration factor[29] with the radius of interaction taken to be 1 fermi

The subscript 0 refers to the values of these quantities at the resonance mass ω_0. Note that this amplitude is normalized to unity at resonance.

The results of the fitting program are summarized in Table IX and in Fig. 31, which present the fractions of the various intermediate states that contribute at each energy. Of note are the decrease in Δ^- above 1750 MeV and the rapid rise of the ρ^0 above 1700. Production of $\rho^0 n$ was ignored below 1600 MeV in the fits. The program failed to fit data below 1496 MeV because of the large overlap of the Δ^+ and Δ^- bands in the Dalitz plots. The mass distributions predicted by this program are represented by the smooth curve in Fig. 29.

Fractions of Resonance and Phase Space Production in the Reaction $\pi^- p \rightarrow \pi^+ \pi^- n$

C.M.S. Energy	Δ^-	Δ^+	ρ^0	Phase Space
1496	0.529 ± 0.087	0.052 ± 0.079	0.	0.419 ± 0.118
1527	0.500 ± 0.069	0.187 ± 0.066	0.	0.313 ± 0.095
1556	0.565 ± 0.086	0.337 ± 0.082	0.	0.098 ± 0.119
1589	0.639 ± 0.056	0.157 ± 0.050	0.	0.204 ± 0.075
1629	0.357 ± 0.072	0.017 ± 0.064	0.091 ± 0.049	0.535 ± 0.108
1647	0.551 ± 0.024	0.036 ± 0.020	0.011 ± 0.015	0.402 ± 0.035
1660	0.545 ± 0.035	0.051 ± 0.030	0.003 ± 0.021	0.401 ± 0.045
1669	0.535 ± 0.026	0.025 ± 0.021	0.010 ± 0.016	0.430 ± 0.037
1674	0.537 ± 0.026	0.016 ± 0.021	0.031 ± 0.015	0.416 ± 0.037
1685	0.576 ± 0.027	0.072 ± 0.023	0.003 ± 0.016	0.349 ± 0.039
1695	0.554 ± 0.036	0.006 ± 0.029	0.004 ± 0.020	0.564 ± 0.050
1709	0.440 ± 0.068	0.000 ± 0.052	0.011 ± 0.034	0.451 ± 0.092
1720	0.590 ± 0.064	0.114 ± 0.055	0.000 ± 0.037	0.296 ± 0.092
1730	0.452 ± 0.039	0.001 ± 0.031	0.082 ± 0.025	0.465 ± 0.056
1740	0.569 ± 0.026	0.075 ± 0.020	0.057 ± 0.017	0.299 ± 0.037
1761	0.590 ± 0.043	0.111 ± 0.036	0.097 ± 0.030	0.202 ± 0.064
1762	0.431 ± 0.036	0.096 ± 0.030	0.108 ± 0.025	0.365 ± 0.052
1766	0.348 ± 0.038	0.000 ± 0.028	0.225 ± 0.027	0.427 ± 0.054
1787	0.412 ± 0.044	0.087 ± 0.034	0.173 ± 0.033	0.328 ± 0.065
1806	0.363 ± 0.082	0.056 ± 0.068	0.278 ± 0.071	0.303 ± 0.128
1811	0.330 ± 0.034	0.081 ± 0.028	0.231 ± 0.029	0.358 ± 0.053
1821	0.279 ± 0.034	0.006 ± 0.026	0.293 ± 0.029	0.422 ± 0.053
1843	0.245 ± 0.023	0.045 ± 0.019	0.307 ± 0.029	0.403 ± 0.042
1853	0.250 ± 0.025	0.069 ± 0.022	0.337 ± 0.024	0.344 ± 0.041
1873	0.179 ± 0.020	0.042 ± 0.017	0.364 ± 0.020	0.413 ± 0.033
1884	0.249 ± 0.022	0.030 ± 0.017	0.411 ± 0.022	0.310 ± 0.035
1904	0.184 ± 0.018	0.079 ± 0.017	0.377 ± 0.020	0.360 ± 0.032
1916	0.174 ± 0.016	0.057 ± 0.014	0.424 ± 0.018	0.345 ± 0.028
1932	0.149 ± 0.021	0.061 ± 0.019	0.412 ± 0.024	0.378 ± 0.037
1935	0.154 ± 0.024	0.109 ± 0.023	0.404 ± 0.028	0.333 ± 0.043
1973	0.142 ± 0.014	0.075 ± 0.013	0.426 ± 0.017	0.357 ± 0.026
1980	0.125 ± 0.087	0.087 ± 0.013	0.426 ± 0.017	0.362 ± 0.090

1801842

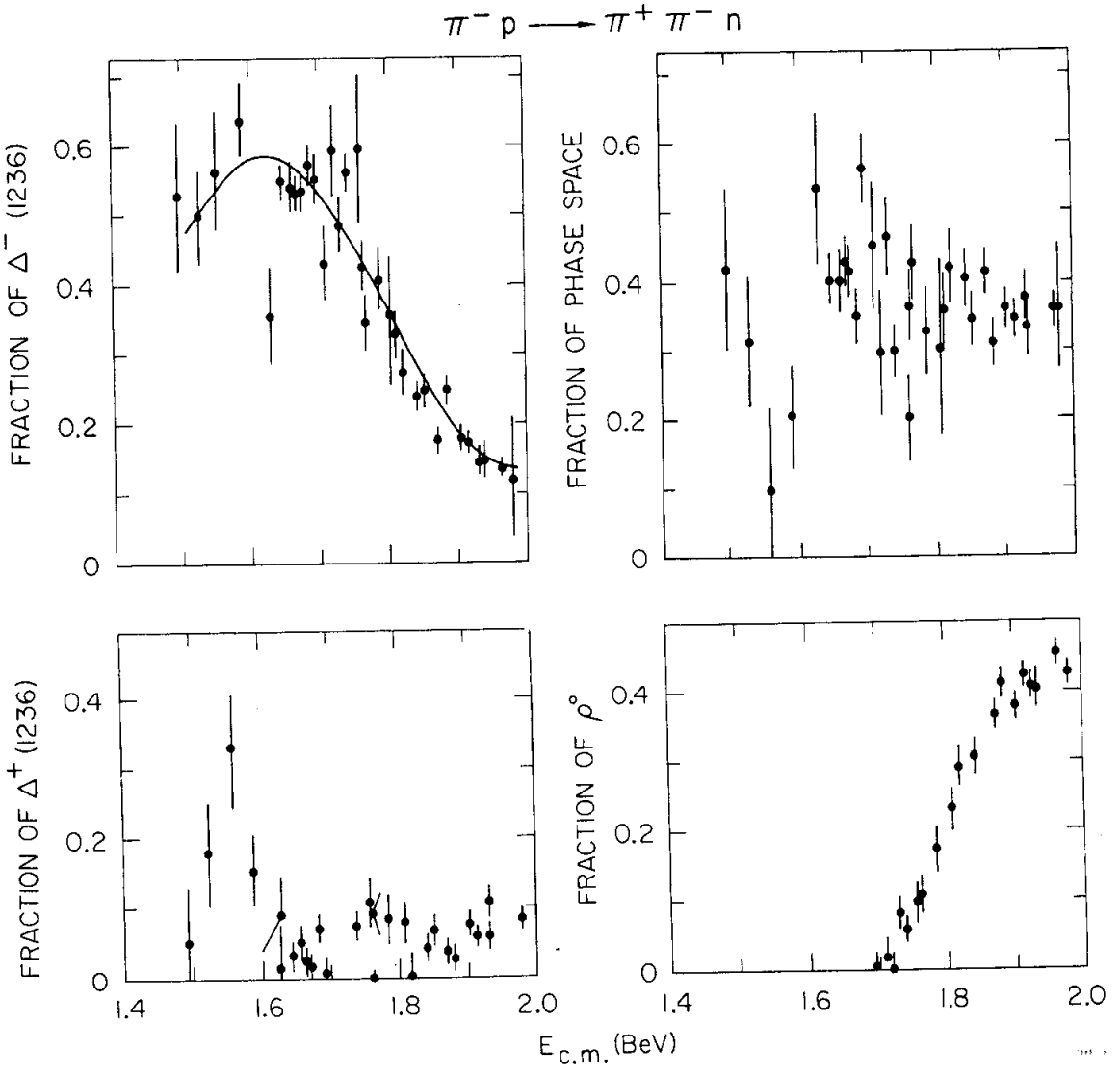

FIG. 31--The fractions of resonance and phase-space production in the reaction $\pi^- p \rightarrow n\pi^+\pi^-$.

B. Production Angular Distributions

There is little structure in the production angular distributions of the three final-state particles. Distributions at four representative energies are presented in Figs. 32 and 33. Most of this region is dominated by s-channel resonances whose decays are characterized by fairly symmetrical or isotropic distributions. However, the forward peaking of the final nucleon, especially at higher energies, is the earmark of peripheral interactions. A less prominant forward peak is also present in the distribution of the final π^+ in the $n\pi^+\pi^-$ reaction. If this peaking indicates a t-channel effect, it might be caused by the exchange of an exotic resonance with I=2. (See diagram of Fig. 34.) It would also contradict the observation that Δ^- production is falling rapidly at higher energies. An explanation is more likely to exist in terms of s-channel effects.

C. Moments Analysis

The mass distributions and production angular distributions display the behavior of only one or two of the five possible variables; information is lost by summing over the rest. Without building a model, a complete description of the data is practically impossible. However, we can examine the data in one final way that yields information on the states of total angular momentum that are present. We found the moments involved by fitting the data to the form

$$\frac{1}{\sigma}\left[d\sigma/d\Omega\right] = \left[\sum_{\substack{LM \\ L \geq 1}} \left(\frac{2L+1}{4\pi}\right)^{1/2} W_L^M \, Y_L^{M*}(\theta, \phi)\right] + \frac{1}{4\pi} \qquad (4.5)$$

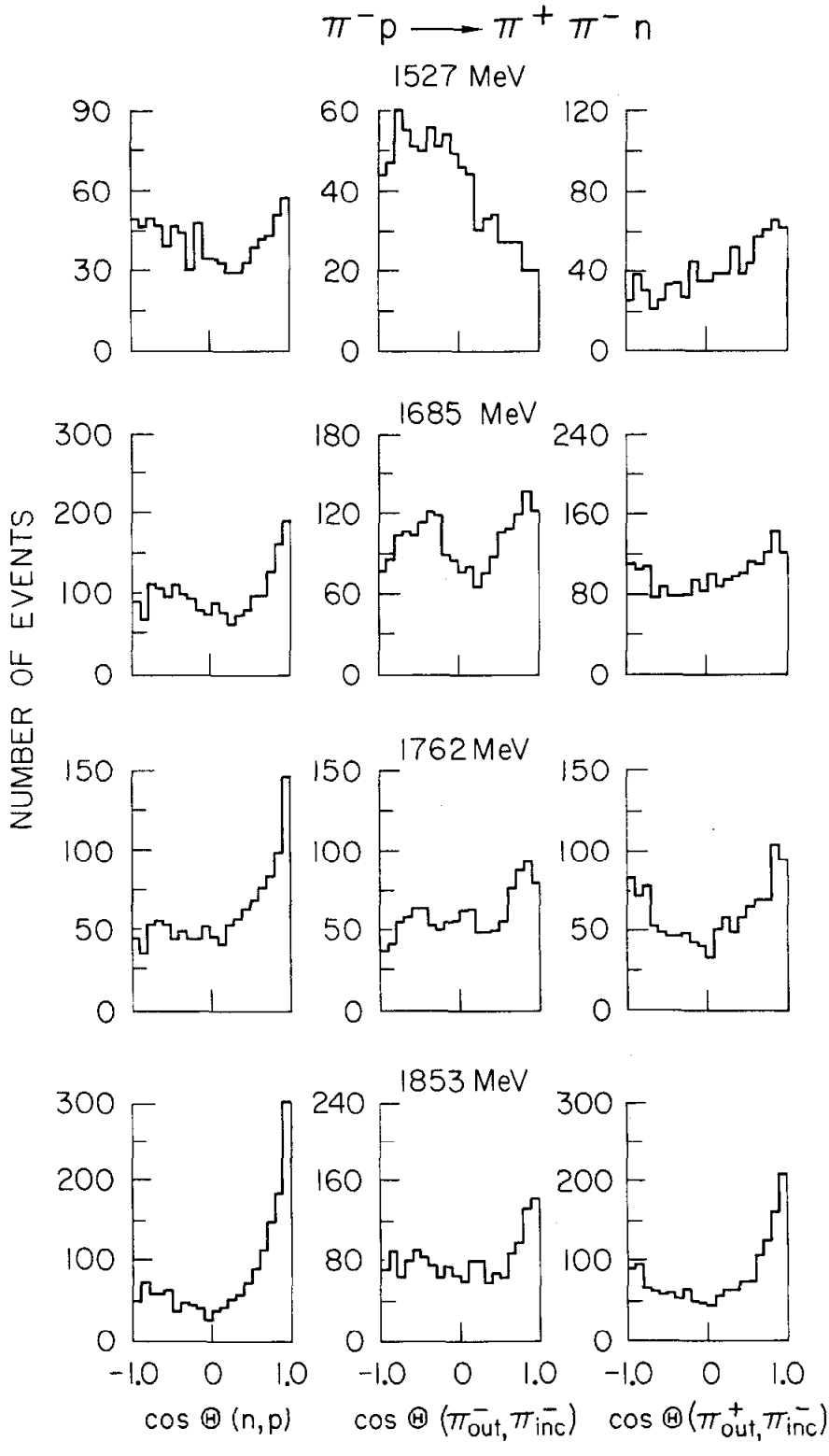

FIG. 32--Production angular distributions of each particle in the final state $\pi^- p \rightarrow n\pi^+\pi^-$ at four representative energies.

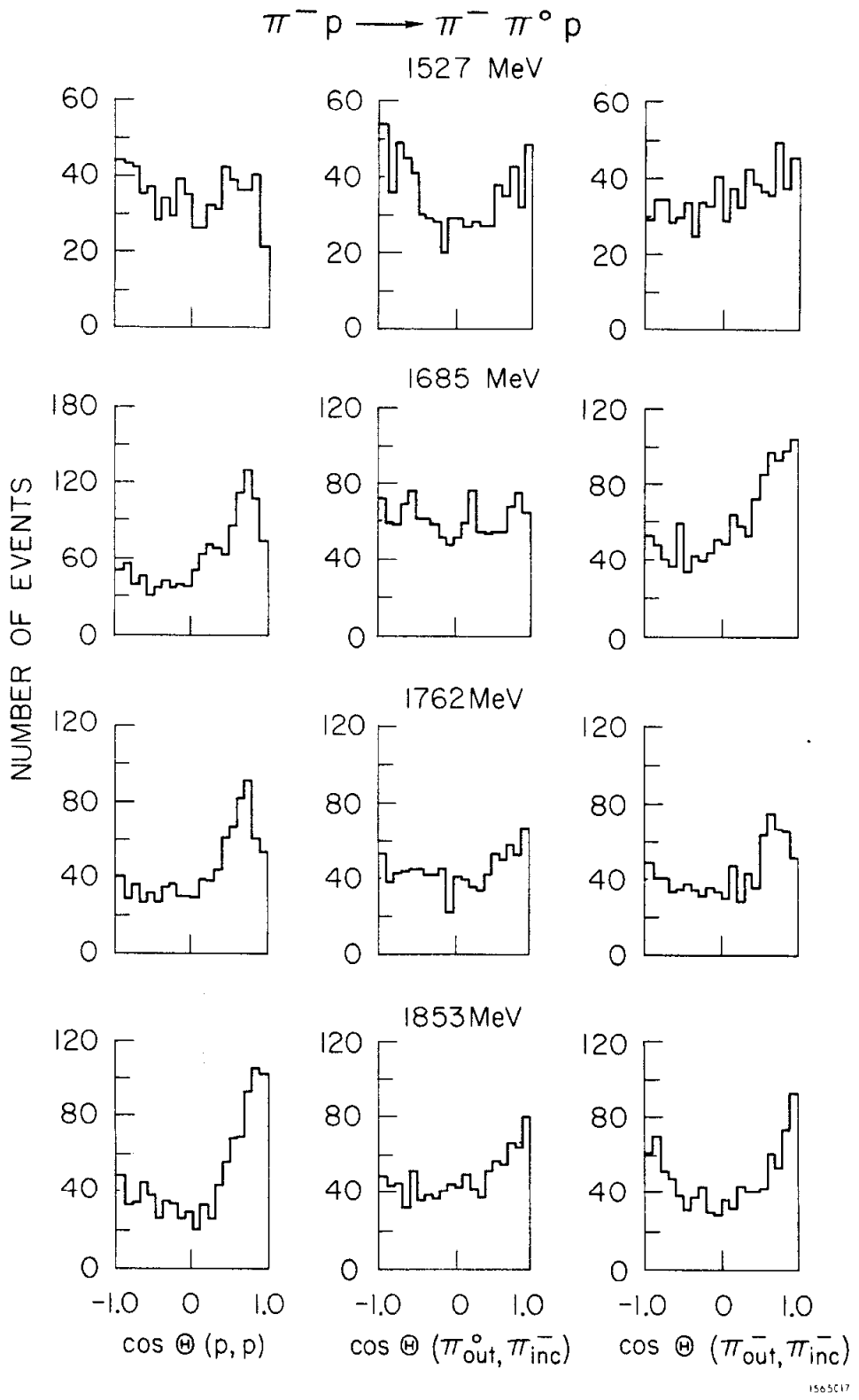

FIG. 33--Production angular distributions of each particle in the final state $\pi^- p \rightarrow p\pi^-\pi^0$.

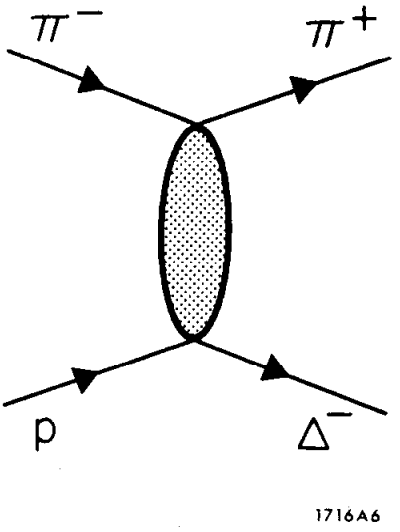

FIG. 34--Diagram for the production of forward π^+ mesons in the reaction $\pi^- p \rightarrow \Delta^- \pi^+$.

(Dividing by σ normalizes the coefficients to 1.) The beam coordinates θ and ϕ are defined in the system where

$$\hat{z} = \hat{p}_{\pi^-} \times \hat{p}_{\pi} \tag{4.6}$$

$$\hat{x} = \hat{p}_N \tag{4.7}$$

$$\hat{y} = \hat{z} \times \hat{x} \tag{4.8}$$

$\hat{p}_{\pi^-}$, $\hat{p}_{\pi}$ and $\hat{p}_N$ are unit vectors in the directions of the outgoing particles measured in the center-of-mass system.

The coefficients W_L^M contain the interference terms between states.[30,31,32,33]

$$W_L^M = \sum_{\lambda\mu} \sum_{\substack{JJ' \\ \Lambda\Lambda'}} \frac{1}{2(2L+1)} T_{J\Lambda}^{\lambda\mu} T_{J'\Lambda'}^{\lambda\mu *} F(J, \Lambda, J', L', L)\, \delta_{M,\Lambda-\Lambda'} \tag{4.9}$$

J = total angular momentum

Λ = z-component of J

λ = z-component of final nucleon spin

μ = helicity of initial state

The factors F are products of Clebsch-Gordan coefficients relating the product of states with $J\Lambda$ and $J'\Lambda'$ to give a state with LM. Because of parity requirements on the amplitudes $T_{J\Lambda}^{\lambda}$, the coefficients obey the rule

$$W_L^M = 0 \qquad \text{if } L+M \text{ is odd} \tag{4.10}$$

We can further deduce that states with the same parity contribute to coefficients with L even and those with opposite parity to L odd. The parity of a state is given by $(-1)^{\Lambda-\lambda}$. For states to have the same parity, Λ and Λ'

must differ by an even integer, so that $M = \Lambda - \Lambda'$ is even. According to rule (4.10), L must also be even. A similar argument applies to states of opposite parity.

A partial wave of total angular momentum J contributes to all W_L^M coefficients up to $L \leq 2J-1$. The terms with $J \leq 3/2$ contributing to W_0^0 through W_3^3 are listed in Table X. With these coefficients and the above rules in hand, let us examine the experimentally determined moments displayed in Figs. 35 and 36. The coefficients for $L > 5$ were all zero. Even W_5^M are nearly zero below 1800 MeV, where we would expect to see interference between the D15 and F15. Apparently the integration over the Dalitz plots led to cancellation of these interference effects. The moments for $L = 4$ should show the presence of the D15 and F15, and they are nonzero in the neighborhood of 1700 MeV. However, the small size of these coefficients may indicate either small coupling to the $n\pi^+\pi^-$ channel (unlikely) or again cancellations. The structure of W_2^0 in Table X illustrates how such cancellation may occur. In this case, the cancellation obscures the presence of the D13 wave, but the structure of W_1^1 from $n\pi^+\pi^-$ in the region of 1550 MeV probably signals interference of the D13 and P11 waves. The fact that a similar effect is not present in the $p\pi^-\pi^0$ coefficients might be explained by the existence of an I=0 $\pi\pi$ effect at low mass values.[23]

Clearly a model is required to extract the information lost in the integration over the Dalitz plot. One such model now being applied attempts to describe the three-body final state in terms of two-body interactions and their interference effects. A maximum likelihood fit is made to all variables of the data.

TABLE X

Contributions of Partial Wave Amplitudes to W_L^m

$$W_0^0 \quad |B_{11}|^2 + |B_{1-1}|^2 + |B_{3+3}|^2 + |B_{31}|^2 + |B_{3-1}|^2 + |B_{3-3}|^2$$

$$W_1^1 \quad \frac{1}{3}\left\{-\sqrt{2}\ B_{11}B^*_{1-1} - \frac{\sqrt{6}}{5}\ B_{33}B^*_{31} - 2\frac{\sqrt{2}}{5}\ B_{31}B^*_{3-1} - \frac{\sqrt{6}}{5}\ B_{3-1}B^*_{3-3}\right.$$

$$\left. + \sqrt{3}\ B_{33}B^*_{11} + B_{31}B^*_{1-1} - B_{11}B^*_{3-1} - \sqrt{3}\ B_{1-1}B^*_{3-3}\right\}$$

$$W_2^0 \quad \frac{1}{5}\left\{-|B_{33}|^2 + |B_{31}|^2 + |B_{3-1}|^2 - |B_{3-3}|^2 + \sqrt{2} \times\right.$$

$$\left.\left[B_{31}B^*_{11} + B_{11}B^*_{31} - B_{3-1}B^*_{1-1} - B_{1-1}B^*_{3-1}\right]\right\}$$

$$W_2^2 \quad \frac{1}{5}\left\{-\sqrt{2}\left[B_{33}B^*_{3-1} + B_{31}B^*_{3-3}\right] - 2\left[B_{33}B^*_{1-1} - B_{11}B^*_{3-3}\right]\right\}$$

$$W_3^1 \quad \frac{1}{7}\frac{6}{5}\left\{B_{33}B^*_{31} - \sqrt{3}\ B_{31}B^*_{3-1} + B_{3-1}B^*_{3-3}\right\}$$

$$W_3^3 \quad \frac{6\sqrt{5}}{7.5}\ B_{33}B^*_{3-3}$$

N.B. Each term of these expressions contains an implied sum over λ.

(See text.)

1801A36

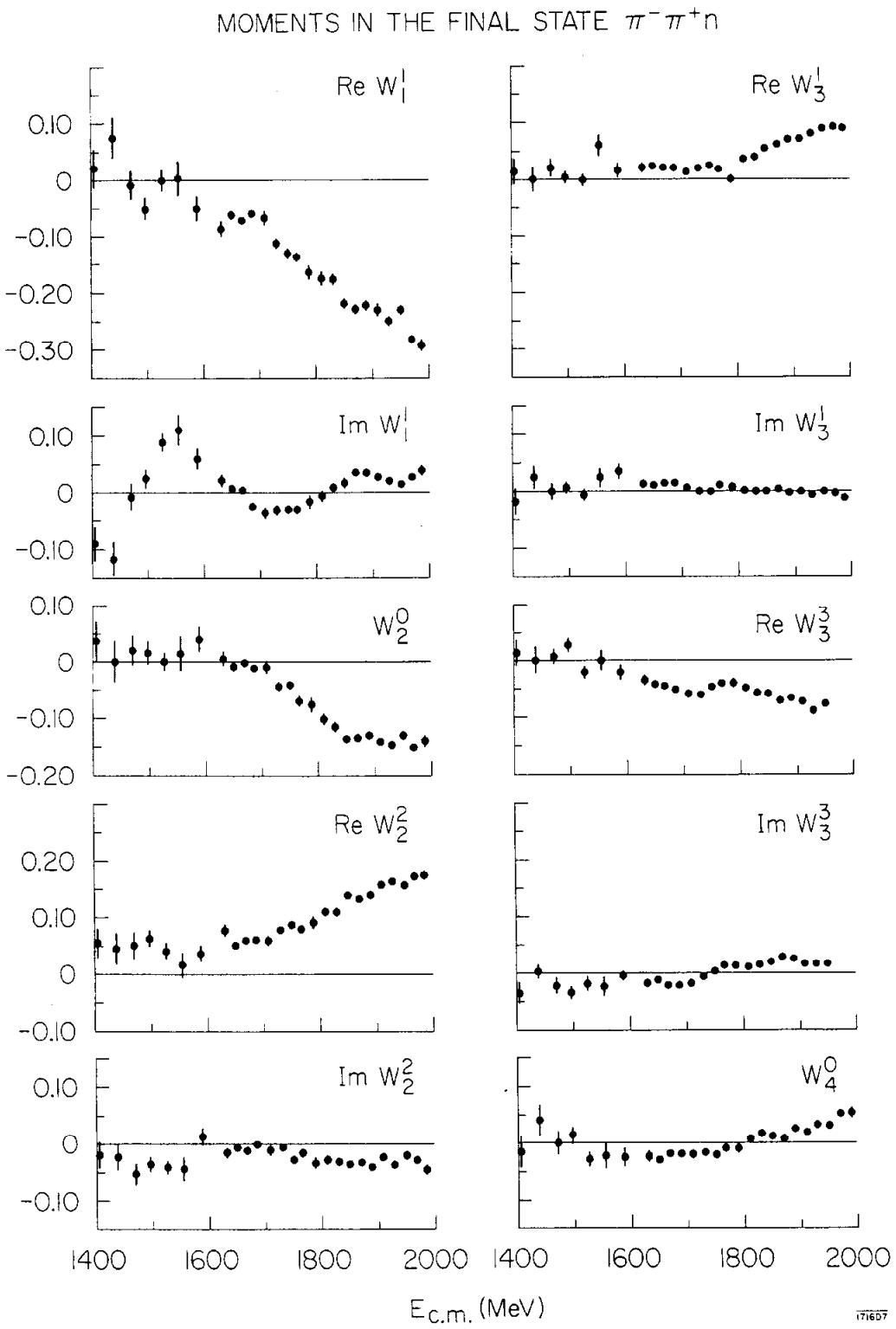

FIG. 35--The moments W_L^M as a function of energy in the final state $n\pi^+\pi^-$.

FIG. 35 cont'd.

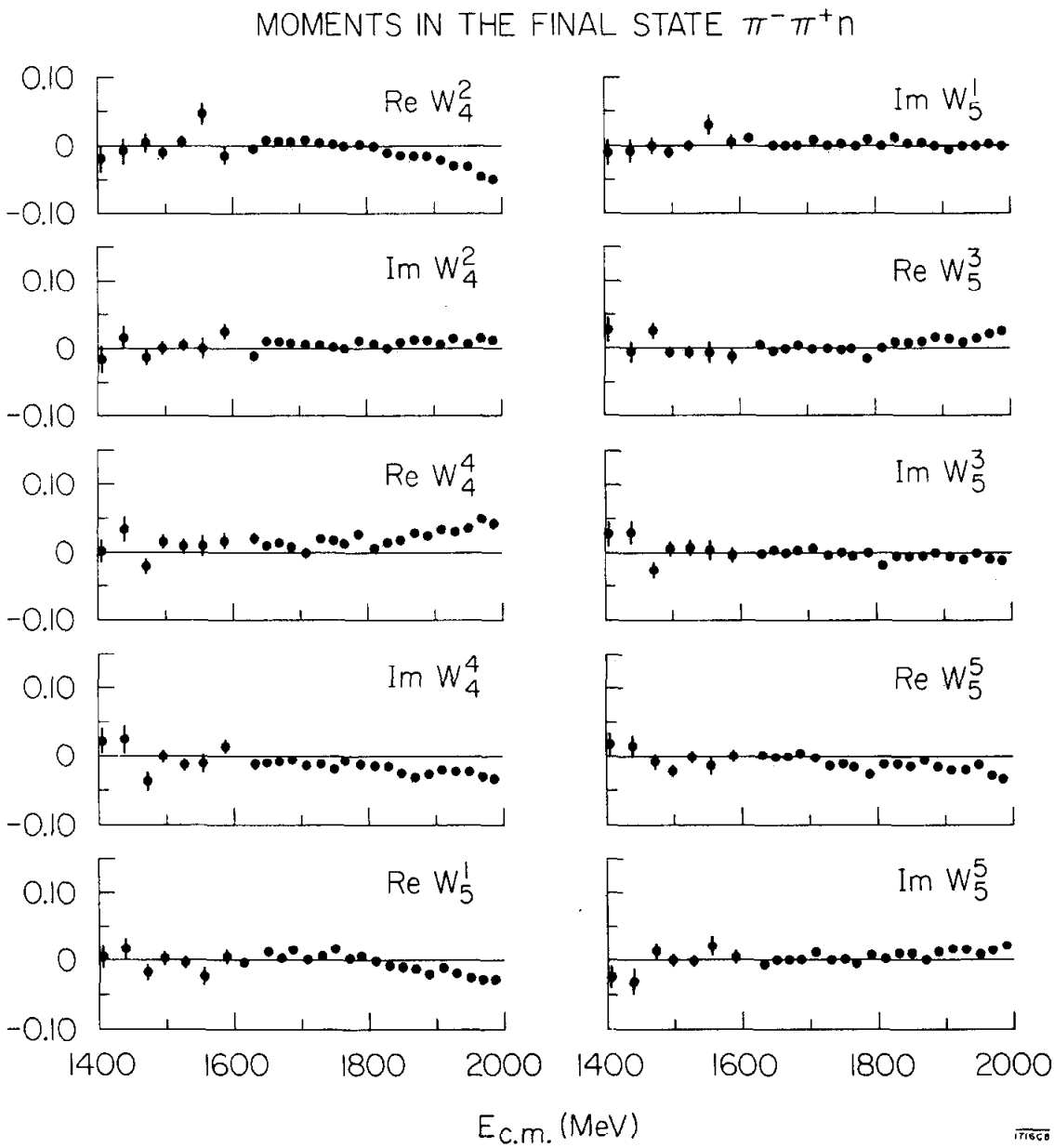
MOMENTS IN THE FINAL STATE $\pi^-\pi^+n$
Re W_4^2
Im W_5^1
Im W_4^2
Re W_5^3
Re W_4^4
Im W_5^3
Im W_4^4
Re W_5^5
Re W_5^1
Im W_5^5
0.10
0
-0.10
1400
1600
1800
2000
$E_{c.m.}$ (MeV)

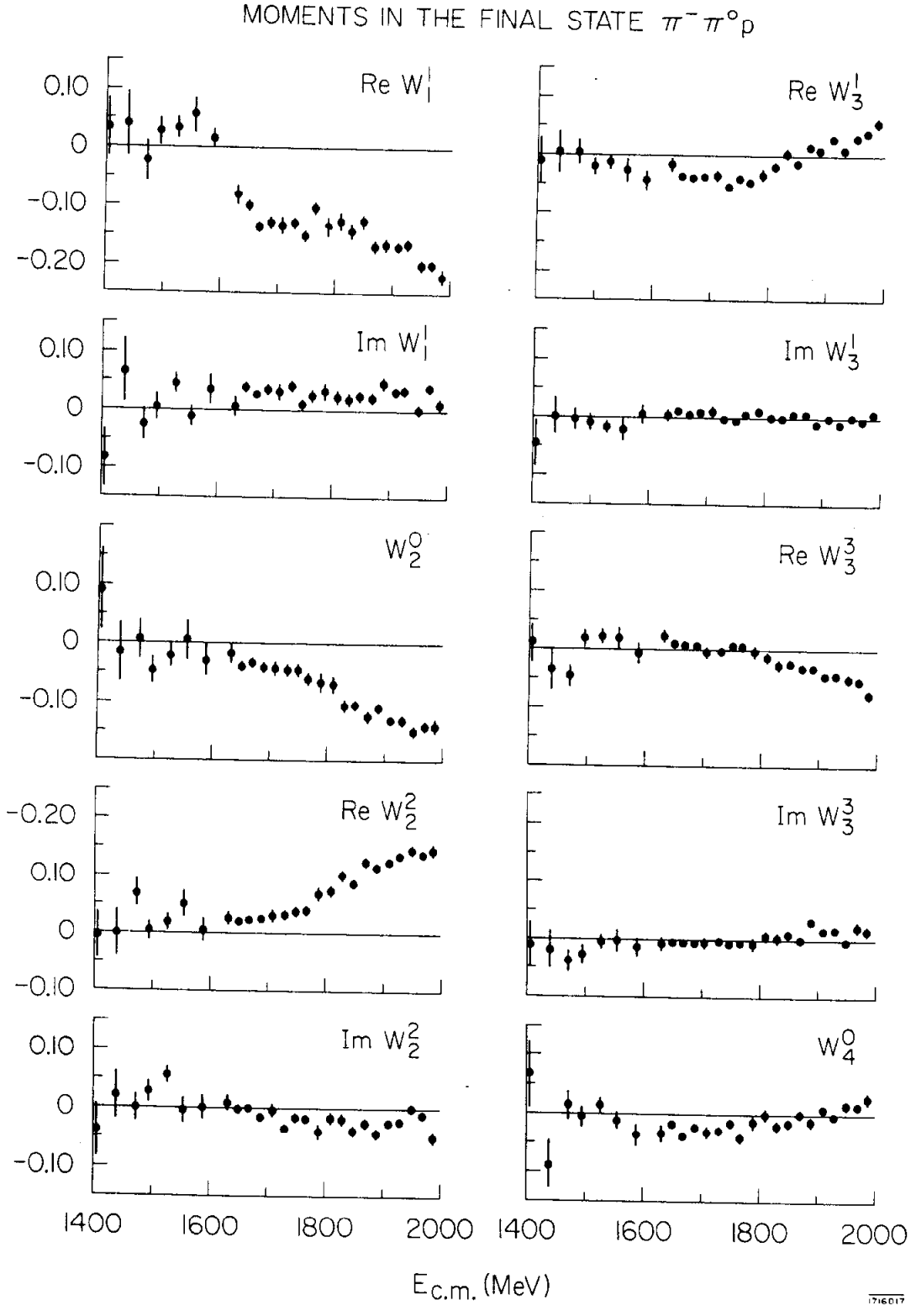

FIG. 36--The moments W_L^M as a function of energy in the final state $p\pi^-\pi^0$.

FIG. 36 cont'd.

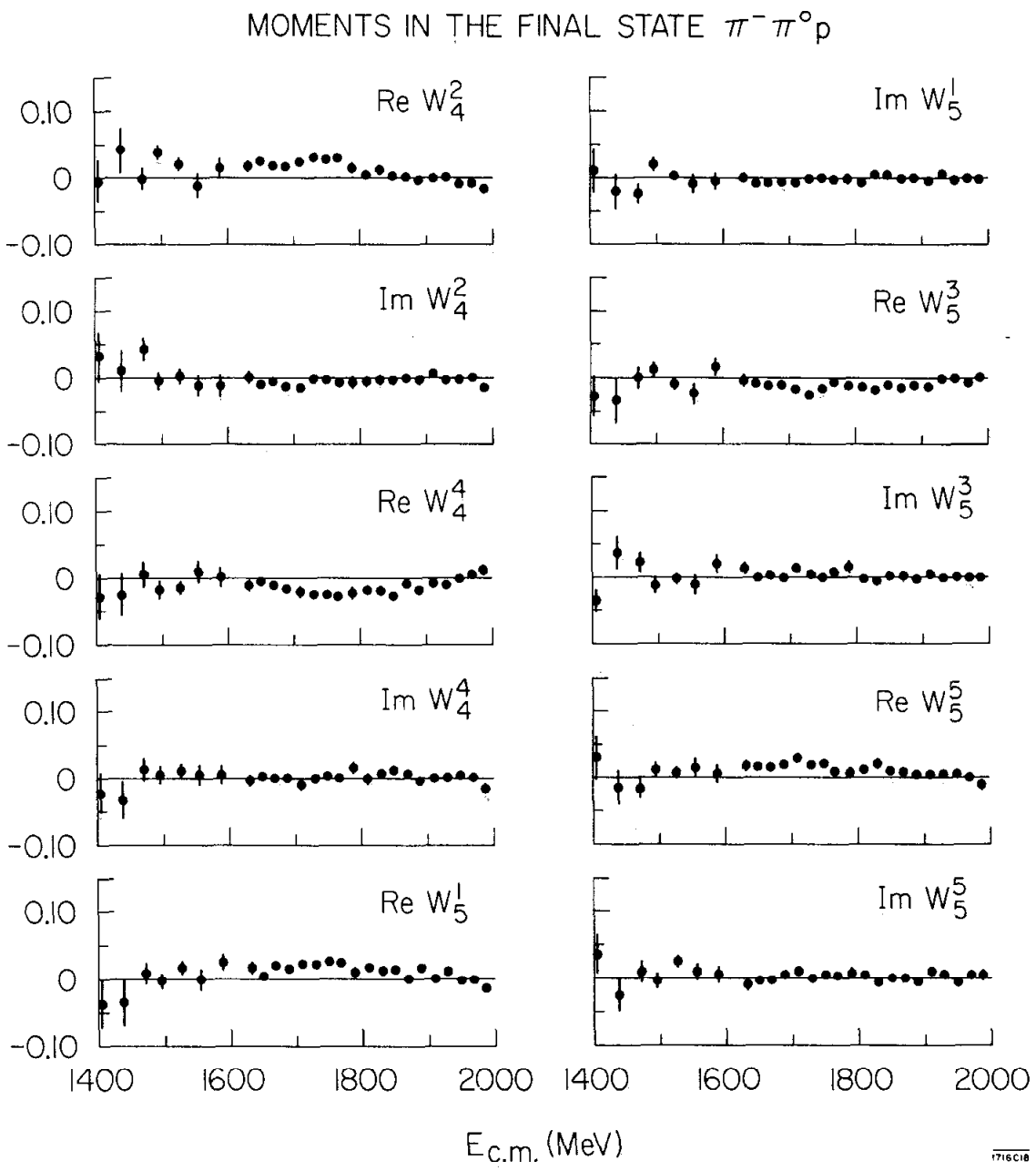
MOMENTS IN THE FINAL STATE $\pi^-\pi^0 p$
Re W_4^2
Im W_5^1
Im W_4^2
Re W_5^3
Re W_4^4
Im W_5^3
Im W_4^4
Re W_5^5
Re W_5^1
Im W_5^5
0.10
0
-0.10
1400
1600
1800
2000
$E_{c.m.}$ (MeV)
1716C18

V. ELASTIC PHASE SHIFT ANALYSIS

A. Formalism

Let us start by writing general expressions for the scattering of a spin 0 meson by a spin 1/2 baryon into a final state consisting of a spin 0 meson and a baryon. We may then consider the particular cases of elastic $\pi^- p$ scattering and, in the next chapters, inelastic $\Delta^- \pi^+$ production. The formalism for a three particle final state, leading to Eq. (4.5), will not be developed in this thesis.

1. Differential Cross Sections

The differential cross section can be expressed in terms of the helicity amplitudes $T^J_{\lambda\lambda'}$ [34, 35] for the scattering of a state with total angular momentum J and helicity λ into a state with helicity λ'.

$$d\sigma/d\Omega = 2\left(\frac{2\pi}{q}\right)^2 \sum_{\lambda\lambda'} |\langle\lambda'|T|\lambda\rangle|^2 \tag{5.1}$$

where

$$\langle\lambda'|T|\lambda\rangle = \frac{1}{4\pi}\sum_J (2J+1)\, d^J_{\lambda\lambda'}(\theta)\, T^J_{\lambda\lambda'} \tag{5.2}$$

and

q = center-of-mass momentum

$d^J_{\lambda\lambda'}$ = *rotation matrix elements*[36]

It is more customary to work with states having definite values of orbital angular momenta L and L' in the incoming and outgoing channels so we must expand $T^J_{\lambda\lambda'}$ in terms of the amplitudes $T^J_{LL'}$. (For elastic scattering, L'=L but for $\Delta\pi$, L'=L and $L' = \begin{matrix} L+2, & J=L+1/2 \\ L-2, & J=L-1/2 \end{matrix}$.) Using the relationship[34]

$$\langle JM;\, LS|JM;\, \lambda_1\lambda_2\rangle = \sqrt{\frac{2L+1}{2J+1}}\; C^{LSJ}_{0(\lambda_1-\lambda_2)(\lambda_1-\lambda_2)}\; C^{S_1S_2S}_{\lambda_1,-\lambda_2(\lambda_1-\lambda_2)} \tag{5.3}$$

where

$$C^{LSJ}_{0(\lambda_1-\lambda_2)(\lambda_1-\lambda_2)} = \text{Clebsch-Gordan coefficient}$$

$$\lambda_1, \lambda_2 = \text{helicities of the two particles}$$

$$S_1, S_2 = \text{spins of the two particles}$$

we find that

$$\langle\lambda'|T|\lambda\rangle = \frac{1}{4\pi}\sum_J\sum_{LL'}\sqrt{(2L+1)(2L'+1)}\; d^J_{\lambda\lambda'}(\theta)\, C^{LSJ}_{0\lambda\lambda}\, C^{L'S'J'}_{0\lambda'\lambda'}\, T^J_{LL'} \quad (5.4)$$

The elastic scattering amplitudes $\langle\frac{1}{2}|T|\frac{1}{2}\rangle$ and $\langle-\frac{1}{2}|T|\frac{1}{2}\rangle$ are related to the familiar spin-nonflip and spin-flip amplitudes, f and g

$$f(\theta) = \frac{1}{q}\sum_L\left[(L+1)\; T_{L+} + T_{L-}\right] P_L(\cos\theta) \quad (5.5)$$

$$g(\theta) = \frac{1}{q}\sum_L (T_{L+} - T_{L-}) \sin\theta\; P'_L(\cos\theta) \quad (5.6)$$

in terms of which the differential cross section becomes

$$d\sigma/d\Omega = |f|^2 + |g|^2 \quad (5.7)$$

Equation (5.1) reduces to Eq. (5.7) when the appropriate values for Clebsch-Gordan coefficients are substituted and the rotation matrices are written in terms of the first derivatives of Legendre polynomials, according to[34]

$$d^J_{\frac{1}{2}\frac{1}{2}}(\theta) = \frac{1}{L+1}\cos\frac{\theta}{2}\,(P'_{L+1} - P'_L) \qquad \text{for } J=L+\tfrac{1}{2} \quad (5.8)$$

$$d^J_{\frac{1}{2}-\frac{1}{2}}(\theta) = \frac{1}{L+1}\sin\frac{\theta}{2}\,(P'_{L+1} + P'_L) \qquad \text{for } J=L+\tfrac{1}{2} \quad (5.9)$$

2. Polarization

The polarization of the final baryon is usually measured with respect to the normal to the production plane, defined as

$$\hat{n} = \vec{q}_i \times \vec{q}_f / |\vec{q}_i \times \vec{q}_f| \tag{5.10}$$

where $\vec{q}_i$ and $\vec{q}_f$ are initial and final c.m. momenta. In the helicity frame, we are free to choose $\hat{n}$ as the y-axis. Then we may construct states with "spin up" and "spin down" as linear combination of the helicity states

$$\text{"spin up"} \qquad |\uparrow\rangle \equiv \frac{1}{2}\left(|\lambda\rangle + i\,|-\lambda\rangle\right) \tag{5.11}$$

$$\text{"spin down"} \qquad |\downarrow\rangle \equiv \frac{1}{2}\left(|\lambda\rangle - i\,|-\lambda\rangle\right) \tag{5.12}$$

The differential cross section for scattering into a state of spin up (down) is given by

$$\begin{aligned} d\sigma/d\Omega\left(\begin{smallmatrix}\uparrow\\ \downarrow\end{smallmatrix}\right) &= 2\left(\frac{2\pi}{q}\right)^2 \sum_\lambda |\langle \begin{smallmatrix}\uparrow\\ \downarrow\end{smallmatrix}|T|\lambda\rangle|^2 \\ &= \left(\frac{2\pi}{q}\right)^2 \sum_\lambda \Big[|\langle\lambda|T|\lambda\rangle|^2 + |\langle -\lambda|T|\lambda\rangle|^2 \\ &\quad \mp 2\,\mathrm{Im}\left(\langle\lambda|T|\lambda\rangle^* \langle -\lambda|T|\lambda\rangle\right)\Big] \end{aligned} \tag{5.13}$$

Polarization experiments measure the difference between the number of protons scattered with spins up and those with spin down. The expression for polarization thus becomes

$$\begin{aligned} P(\theta) &= \frac{d\sigma/d\Omega(\uparrow) - d\sigma/d\Omega(\downarrow)}{d\sigma/d\Omega} \\ &= 4\left(\frac{2\pi}{q}\right)^2 \sum_\lambda \frac{\mathrm{Im}(\langle -\lambda|T|\lambda\rangle^* \langle\lambda|T|\lambda\rangle)}{d\sigma/d\Omega} \end{aligned} \tag{5.14}$$

In terms of the usual spin-flip and spin-nonflip amplitudes, this becomes

$$P(\theta) = 2\mathrm{Im}(g^*f)/(d\sigma/d\Omega) \tag{5.15}$$

3. Total Cross Sections

Integration of Eq. (5.1) over the angle θ yields the total cross section.

$$\sigma = \frac{4\pi}{q^2} \sum_J (J+1/2) \sum_{LL'} |T^J_{LL'}|^2 \tag{5.16}$$

4. Isospin

The differential cross section (5.1) refers to states of pure isospin. We are interested in physical processes which are combinations of these. In particular, the $\pi^- p$ incoming channel could lead to elastic, charge exchange or $\Delta\pi$ production.

$$d\sigma/d\Omega|_{\pi^- p \to \pi^- p} = 2/3\, I_e^{1/2}(\theta) + 1/3\, I_e^{3/2}(\theta) \tag{5.17}$$

$$d\sigma/d\Omega|_{\pi^- p \to \pi^o n} = -\sqrt{2}/3\, I_e^{1/2}(\theta) + \sqrt{2}/3\, I_e^{3/2}(\theta) \tag{5.18}$$

$$d\sigma/d\Omega|_{\pi^- p \to \Delta^+ \pi^-} = \sqrt{1/3}\, I_r^{1/2}(\theta) - \sqrt{2/15}\, I_r^{3/2}(\theta) \tag{5.19}$$

$$d\sigma/d\Omega|_{\pi^- p \to \Delta^- \pi^+} = 1/3\, I_r^{1/2}(\theta) + \sqrt{8/45}\, I_r^{3/2}(\theta) \tag{5.20}$$

$I_e^{1/2}$, $I_e^{3/2}$ are the cross sections for elastic scattering into isospin states with $I = 1/2$, $3/2$ respectively. $I_r^{1/2}$, $I_r^{3/2}$ are the isospin cross sections for scattering into the reaction channel $\Delta\pi$. The same isospin coefficients apply to total cross sections.

B. Methods

The goal of phase-shift analyses is to describe the behavior of the matrix elements $T^J_{LL'}$. The method is to select a particular parameterization, then to adjust the parameters until the predicted values of physical measurables best fit the experimental quantities. The parameters may be simultaneously constrained by theoretical input. For example, all phase-shift analyses impose some form of unitarity on the amplitudes.

Naturally each group attacks the problem differently but there are two basic types of approach; energy dependent and energy independent. The energy independent fits represent the partial wave amplitudes by a phase shift δ and an absorption parameter η, according to

$$T^{\pm}_L = \frac{\eta^{\pm}_L e^{2i\delta^{\pm}_L} - 1}{2i}, \qquad J = L \pm 1/2 \tag{5.21}$$

A search is made for the set of $\eta^{\pm}_L$'s and $\delta^{\pm}_L$'s that best fits the data and satisfies the theoretical constraints. Usually there are numerous ambiguous solutions at each energy. Each group must develop a method to select the "best" fit and to match it to fits at different energies by applying some type of smoothing criterion.

Four out of the five phase-shift analyses[1,6,7,8,9] that span the region of our data are energy independent analyses. The group at Saclay,[1] which made the first analysis at these higher energies, eliminated ambiguous solutions by requiring that certain functions of the amplitudes $T^{\pm}_L$ as well as the amplitudes themselves have continuous behavior with energy.

The Berkeley phase-shift analysis[6] covers the same range as the Saclay analysis with essentially the same results. To select the best fits, Berkeley

defines a type of distance between the amplitudes as a function of energy. The "best" solutions at each energy are those that are connected by the shortest distance and have smallest changes in direction. A more recent analysis performed at Saclay,[9] also uses the criterion of minimal distance to select the best solution.

These two solutions still exhibit some fluctuations with energy, caused largely by inaccuracies or inconsistencies in the experimental data. The phase shift group at CERN[7] found a solution with much smoother energy variation by using constraints from partial wave dispersion relations. They fold the theoretical information back into the fit as data with large errors in an iterative procedure. As a result they obtain not only the largely experimental set of amplitudes (referred to hereafter as CERN-EXPT) but also a theoretical solution (referred to hereafter as CERN-TH) calculated from dispersion relations using the parameters of the final fit.

The plots of Fig. 37 show that the CERN-TH solution provides a reasonable (and smooth) fit to the phase shifts and absorption parameters of CERN-EXPT shown in 37(a1-r1) and 37(a2-r2). However, the partial wave cross sections shown in 37(a3-r3) and 37(a4-r4) predicted by these solutions are often in serious disagreement, as in the S11, D13, and F15 partial waves.

A fourth, limited, energy-independent analysis was made by a group at Rutherford Labs. They fit to their own $\pi^- p$ elastic scattering data in the c.m. energy region 1780 - 2000 MeV.[8] Because their data was confined to this one elastic channel they could not undertake an independent phase-shift analysis. Instead they sought to compare their data to the smoothed CERN-TH solution. The starting values were the CERN parameters. The parameters were constrained to lie near these starting values but the program had

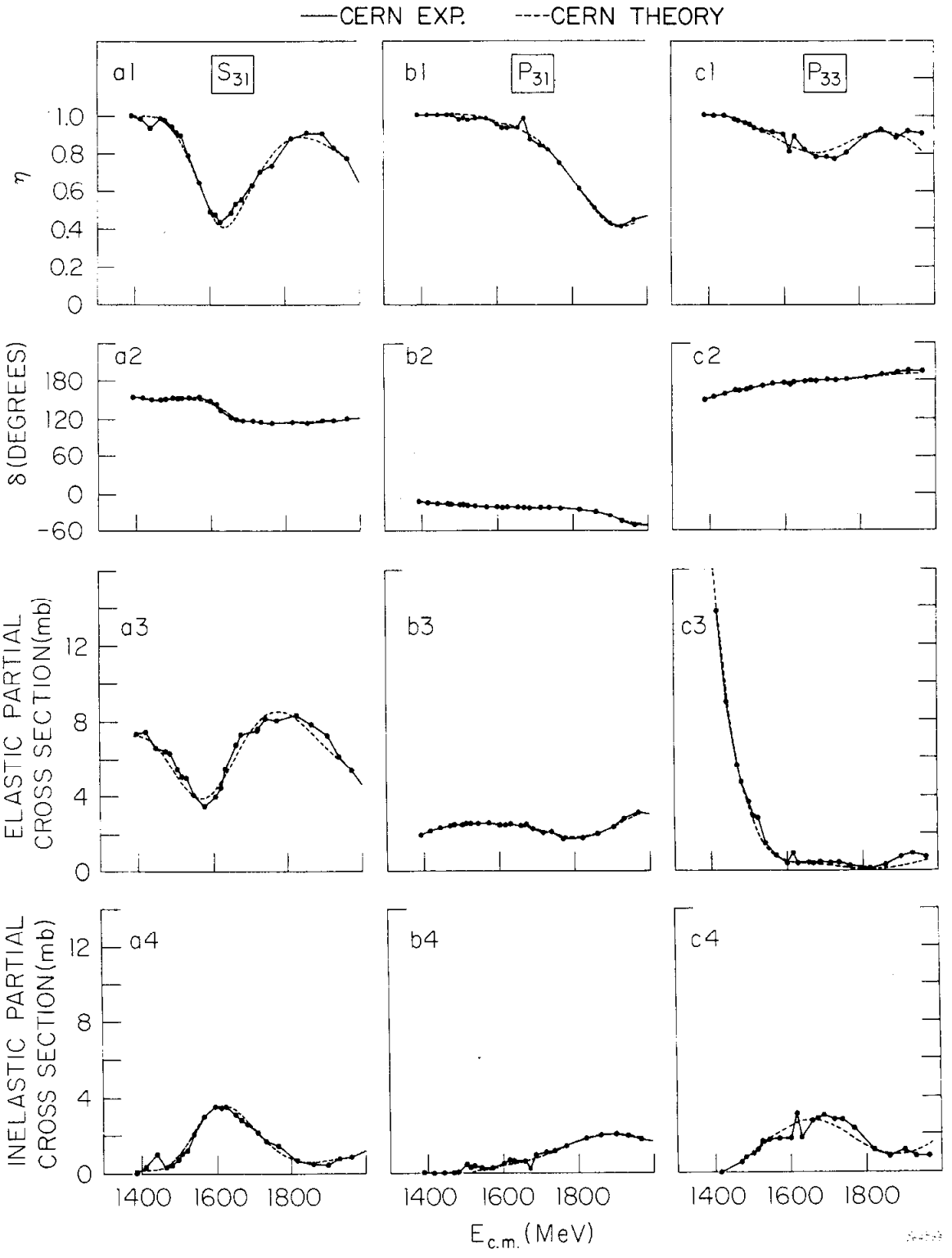

FIG. 37--Comparison of the results of the CERN-TH and CERN-EXPT phase-shift solutions. Solid lines denote CERN-EXPT and dotted lines denote CERN-TH. (a)-(r) Partial waves S_{31} through G_{19}.

FIG. 37 cont'd.

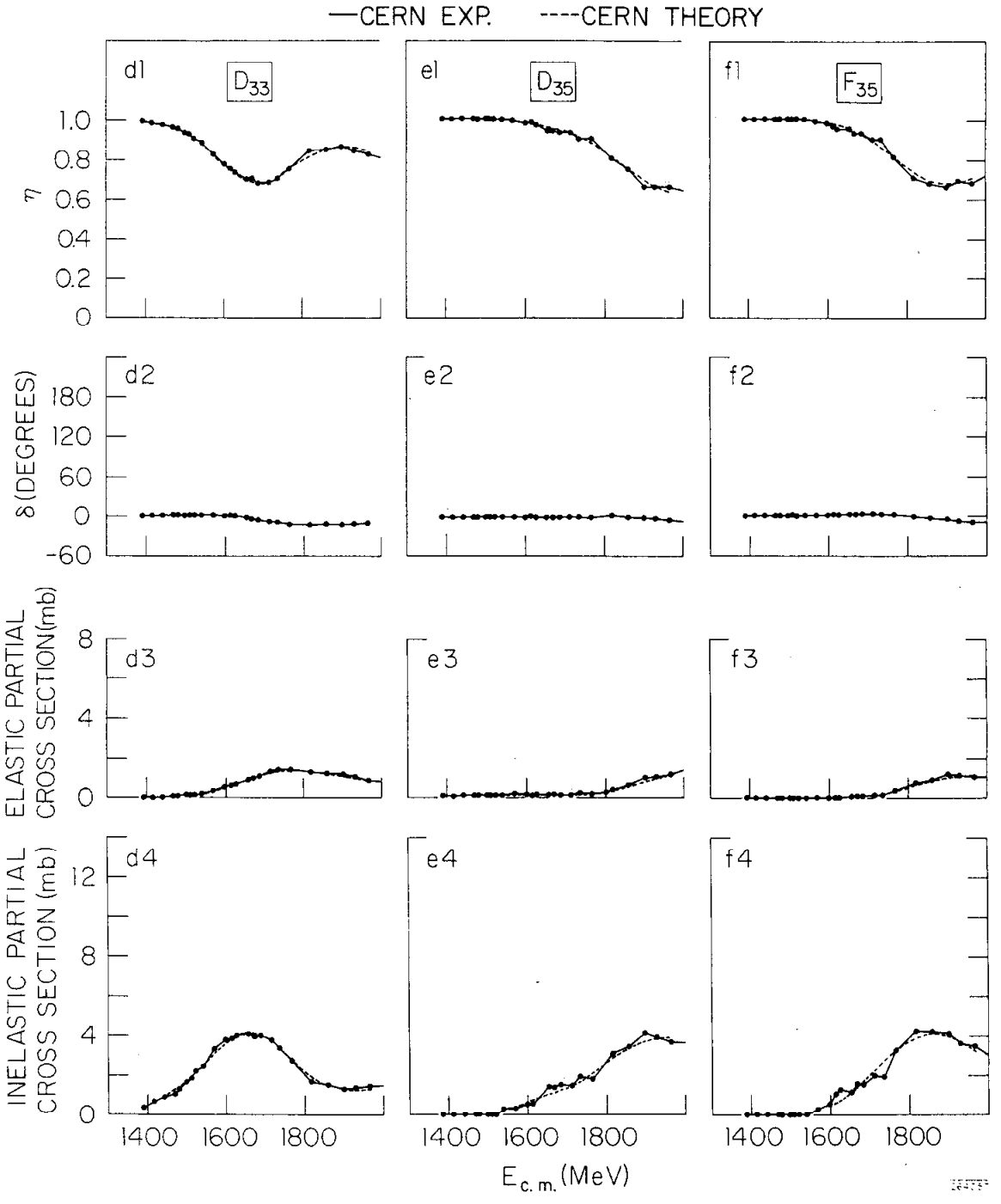
—CERN EXP. ----CERN THEORY
d1
D33
e1
D35
f1
F35
η
1.0
0.8
0.6
0.4
0.2
0
d2
e2
f2
δ (DEGREES)
180
120
60
0
-60
d3
e3
f3
ELASTIC PARTIAL CROSS SECTION(mb)
8
4
0
d4
e4
f4
INELASTIC PARTIAL CROSS SECTION (mb)
12
8
4
0
1400 1600 1800
1400 1600 1800
1400 1600 1800
E c. m. (MeV)

FIG. 37 cont'd.

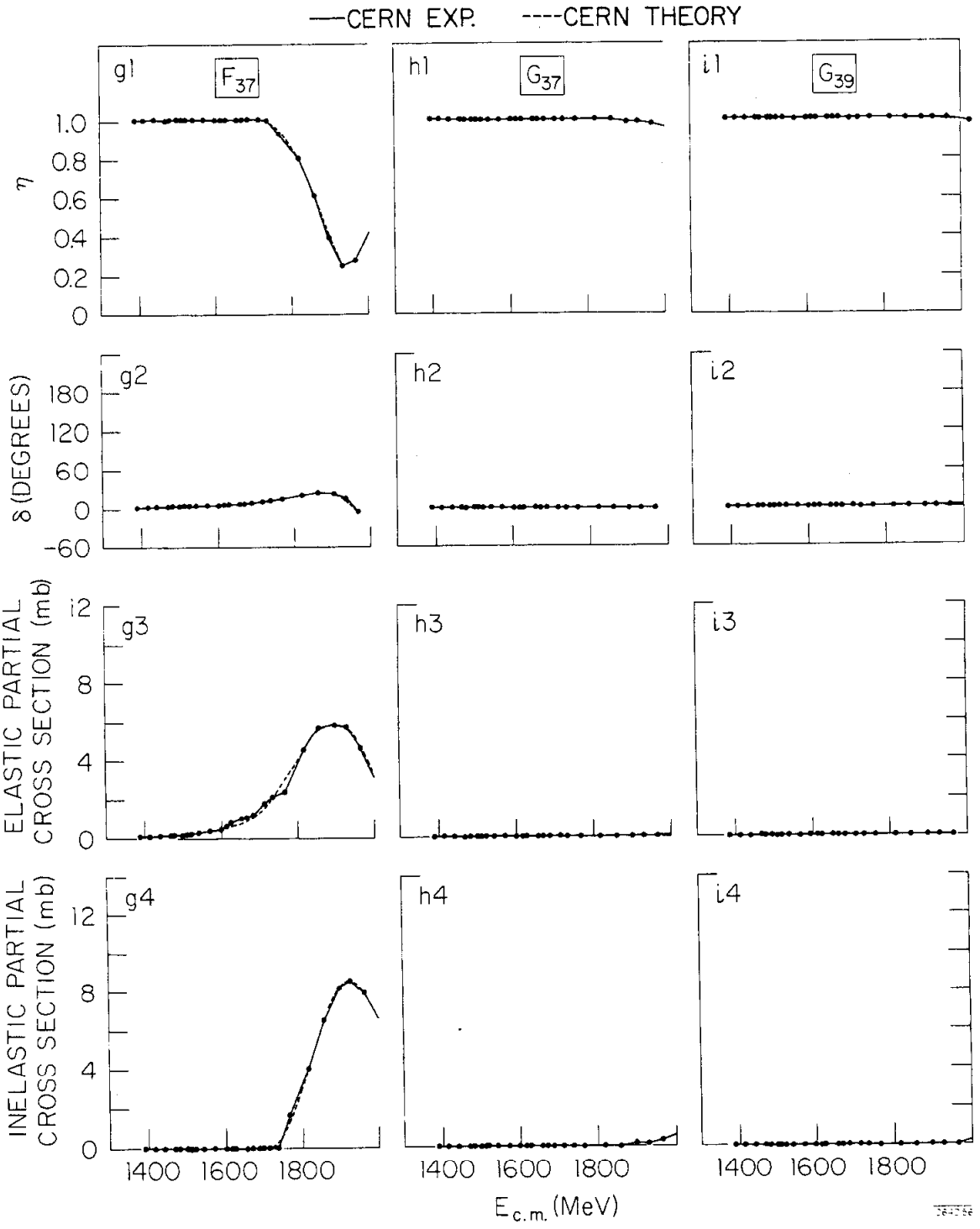
—CERN EXP. ----CERN THEORY
g1
F37
h1
G37
i1
G39
η
1.0
0.8
0.6
0.4
0.2
0
g2
h2
i2
δ (DEGREES)
180
120
60
0
-60
g3
h3
i3
ELASTIC PARTIAL CROSS SECTION (mb)
12
8
4
0
g4
h4
i4
INELASTIC PARTIAL CROSS SECTION (mb)
12
8
4
0
1400 1600 1800
1400 1600 1800
1400 1600 1800
E c.m. (MeV)

FIG. 37 cont'd.

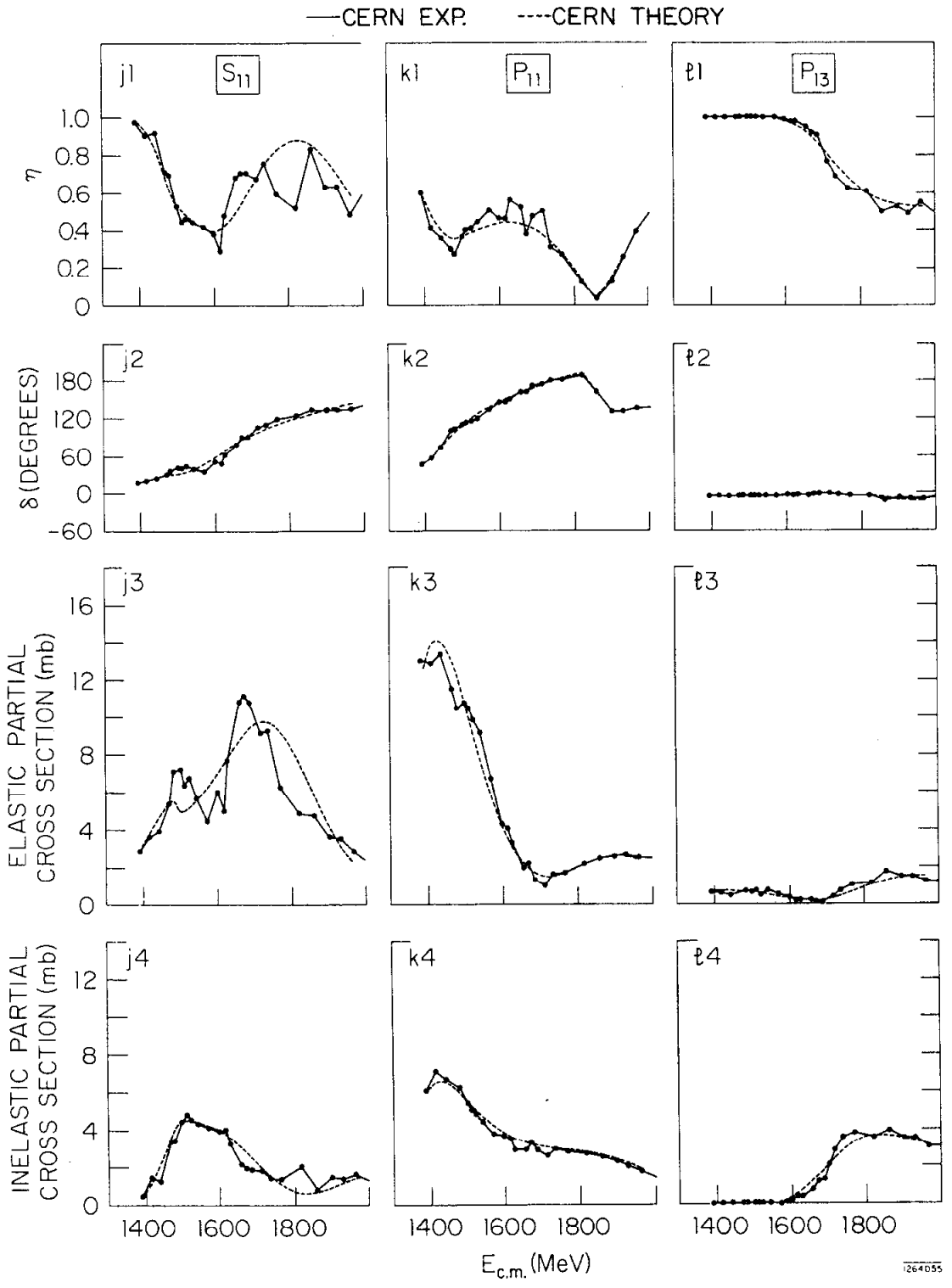
—CERN EXP.
----CERN THEORY
j1
S_{11}
k1
P_{11}
ℓ1
P_{13}
η
1.0
0.8
0.6
0.4
0.2
0
j2
k2
ℓ2
δ (DEGREES)
180
120
60
0
-60
j3
k3
ℓ3
ELASTIC PARTIAL CROSS SECTION (mb)
16
12
8
4
0
j4
k4
ℓ4
INELASTIC PARTIAL CROSS SECTION (mb)
12
8
4
0
1400
1600
1800
$E_{c.m.}$ (MeV)
1264055

FIG. 37 cont'd.

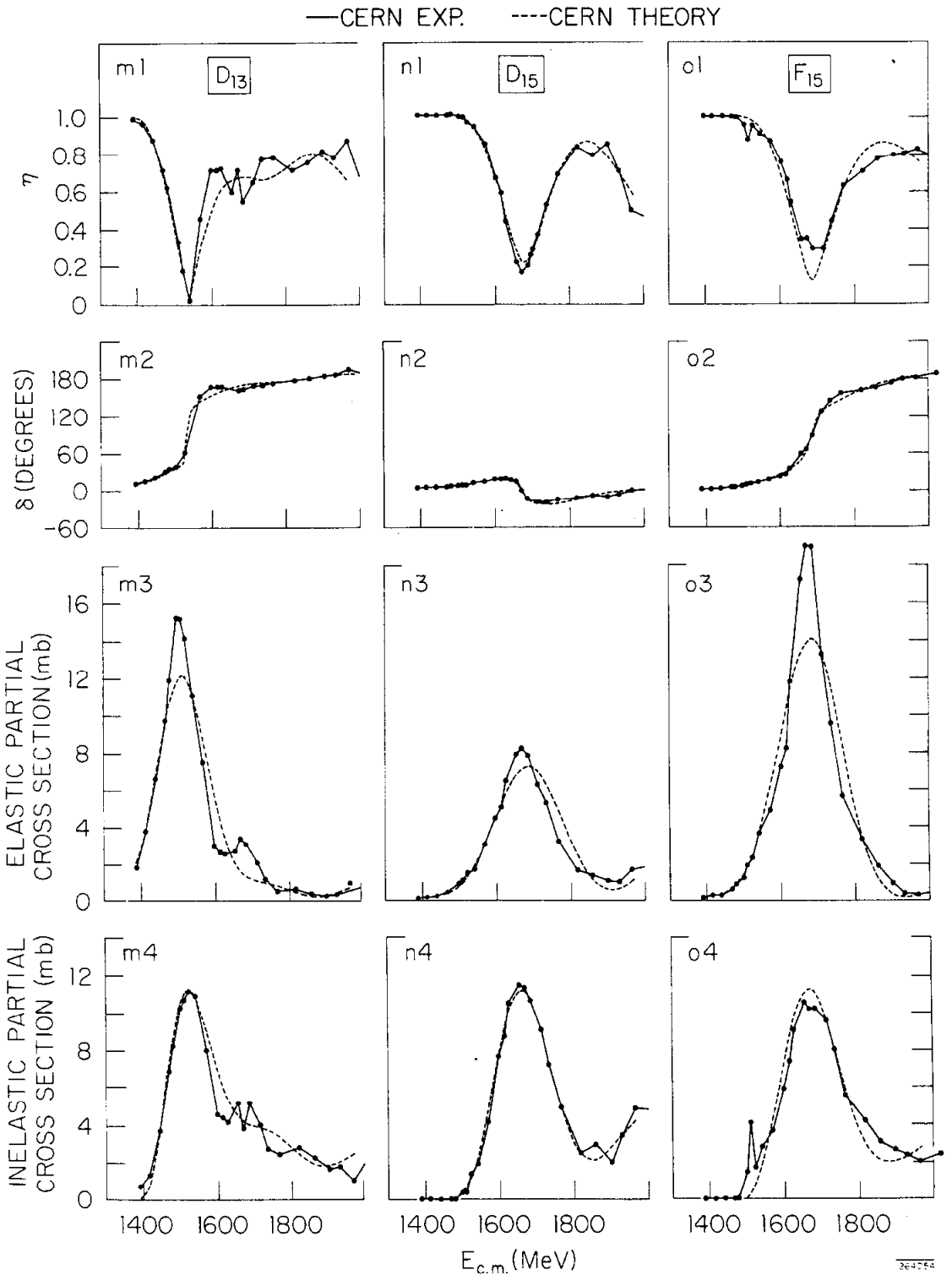
—CERN EXP. ----CERN THEORY
m1
D13
n1
D15
o1
F15
η
1.0
0.8
0.6
0.4
0.2
0
m2
n2
o2
δ (DEGREES)
180
120
60
0
-60
m3
n3
o3
ELASTIC PARTIAL CROSS SECTION (mb)
16
12
8
4
0
m4
n4
o4
INELASTIC PARTIAL CROSS SECTION (mb)
12
8
4
0
1400 1600 1800
1400 1600 1800
1400 1600 1800
E c.m. (MeV)

FIG. 37 cont'd.

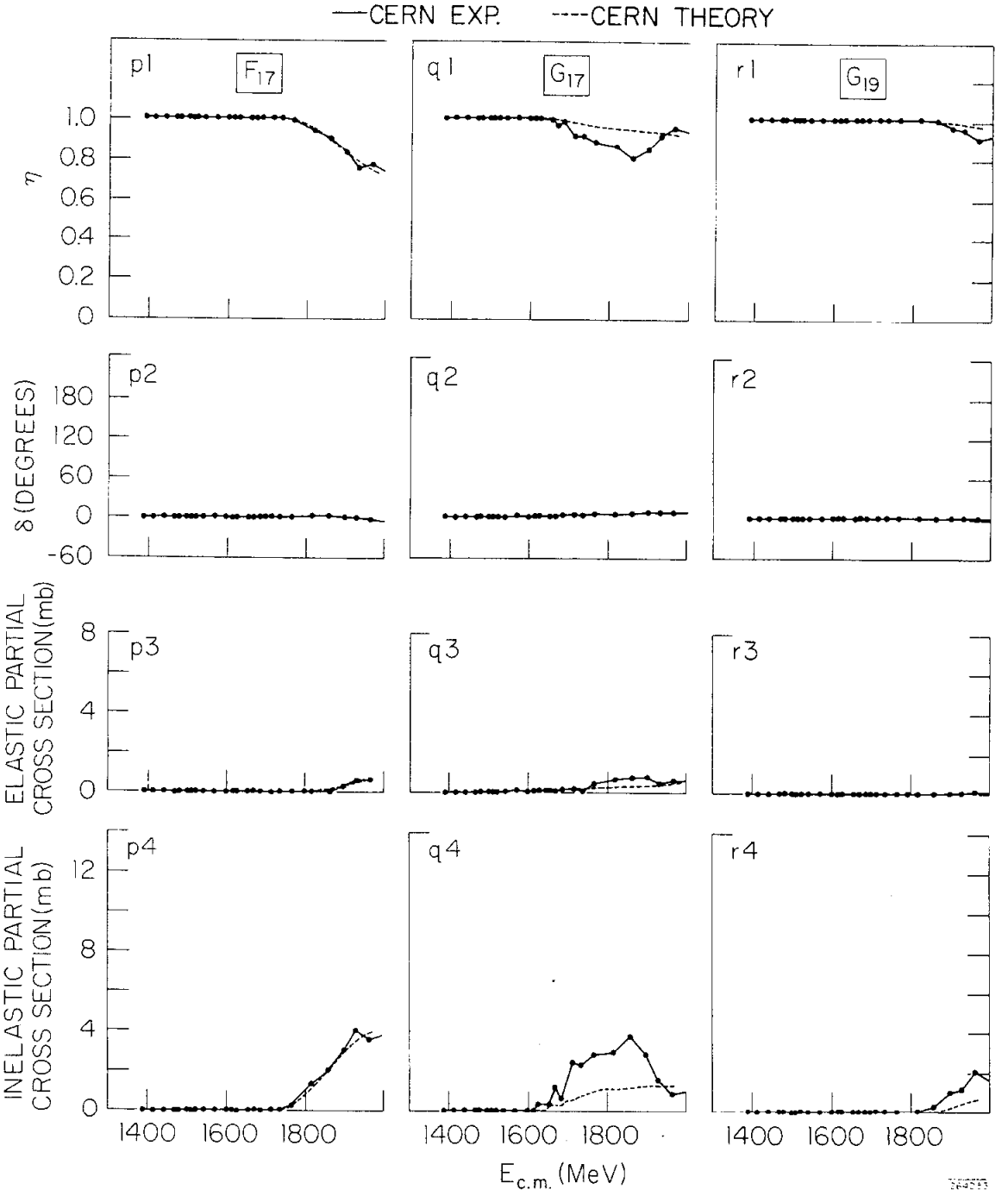
—CERN EXP. ----CERN THEORY
p1
F17
q1
G17
r1
G19
η
1.0
0.8
0.6
0.4
0.2
0
p2
q2
r2
δ (DEGREES)
180
120
60
0
-60
p3
q3
r3
ELASTIC PARTIAL CROSS SECTION (mb)
8
4
0
p4
q4
r4
INELASTIC PARTIAL CROSS SECTION (mb)
12
8
4
0
1400 1600 1800
1400 1600 1800
1400 1600 1800
E c.m. (MeV)

enough freedom to make significant alterations in the parameters where the data required it.

The final phase shift solution, performed at Glasgow,[10] is an energy dependent one. This type of analysis seeks to avoid the problems of unsmooth energy variation by building an energy dependence into the parameterization. An historical example of this method is the analysis by Roper and colleagues,[4] which resulted in the discovery of resonance-like behavior in the P11 wave near 1470 MeV. In this fit the P33 and D13 waves were parameterized as Breit-Wigner resonances while the phase shifts of all other waves were given a polynomial momentum dependence. Rutherford Laboratory[2] has also published some results in which the dispersion relations are used to provide an energy dependence. Although such methods provide smooth variation for the partial wave amplitudes they may bias the results by forcing nature to assume a prescribed behavior.

One of the Glasgow solutions (Glasgow A) attempts to minimize this forced behavior by using the "method of splines". They make a fit in a narrow energy region, expanding each phase shift or absorption parameter as a series about the central momentum. The end point of the fit in one region must be continuous with the starting point in the next region. The resulting parameters are then fit over the entire energy region by Breit-Wigner resonances and backgrounds. Finally a fit is made to the data itself with the resonance and background parameters free to vary. Glasgow B follows a similar procedure but uses the phase shifts and absorption parameters of CERN-TH as the starting point for the all-energy fit.

C. Comparisons and Results

The elastic and differential cross sections predicted by four of these five phase shift solutions are presented in Figs. 38 - 41. The agreement is good for all solutions except for the CERN-TH fit. As we might expect from the discrepancies in Fig. 37, this solution misses much of the sharp structure in the data. Thus this particular solution, while valuable as a smooth fit to phase shift parameters and useful as a starting point (as we have seen) for other fits, should not be taken as a valid representation of the data itself.[37]

It is convenient to discuss the various phase shift results in terms of the resonance parameters - masses, widths and elasticities. In an energy dependent analysis, such as the Glasgow solution, these parameters are directly determined. However, in an energy independent analysis these parameters must be extracted from the energy variation of the absorption and phase-shift parameters. Here lies another source of differences among the phase-shift groups.

One method of estimating the resonance parameters is to study the behavior of the partial wave amplitudes on an Argand diagram. The real part of the amplitude is plotted against the imaginary part, as illustrated on Fig. 42. A pure resonance will describe a counter-clockwise circular path on such a diagram. The radius of curvature is proportional to the elasticity; the energy at which the phase shift passes through 0° or 90°, or equivalently the energy at which the amplitude has its most rapid variation, is the mass of the resonance and the rapidity with which the phase shift changes determines the width of the resonance.

This method is called the "speed" method or "highest velocity criterion". In principle it gives a very specific formula for identifying resonance

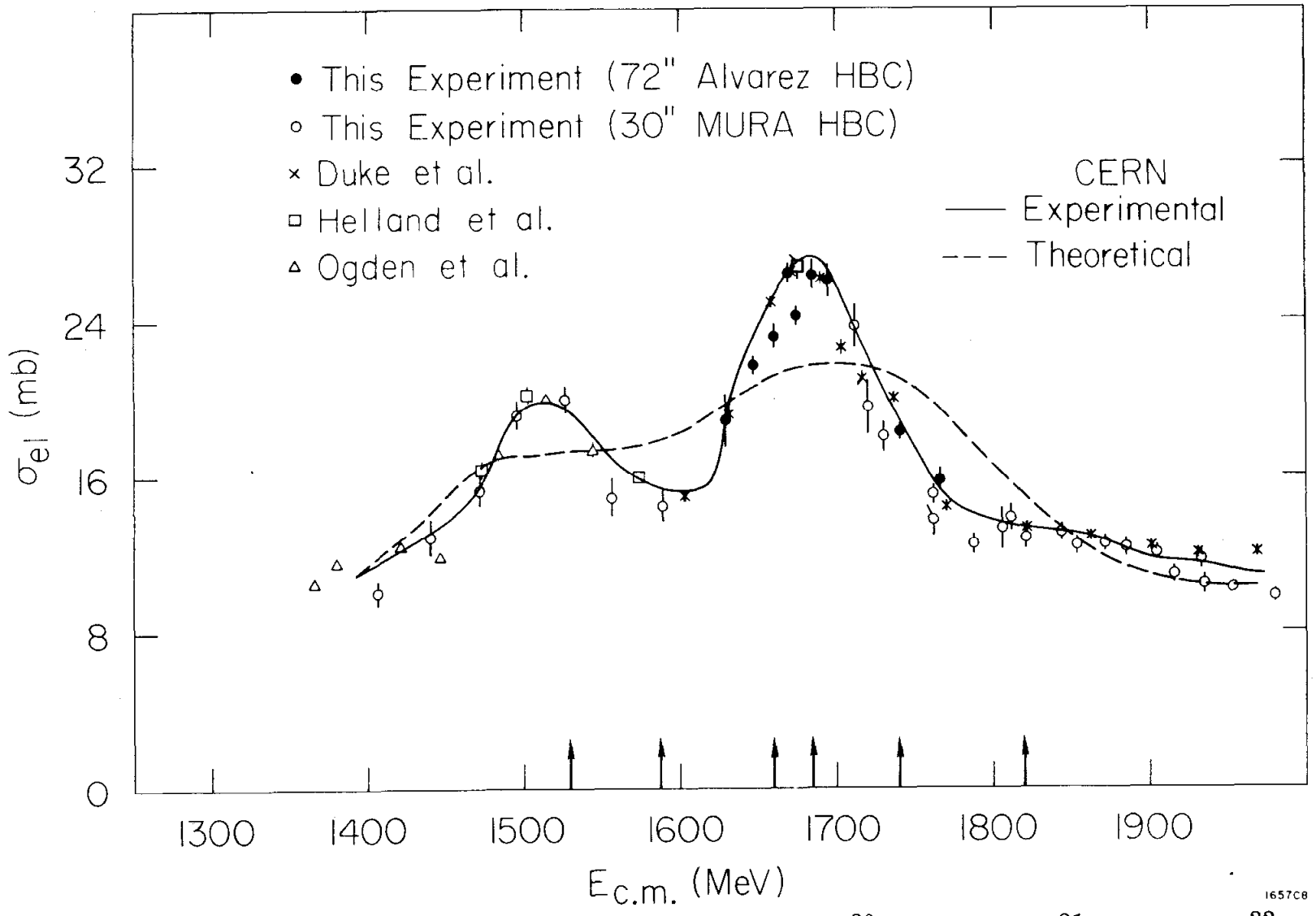

FIG. 38--π^-p elastic cross section measurements of Duke et al.,[20] Helland et al.,[21] Ogden et al.,[22] and this experiment. Solid and dashed lines represent the π^-p elastic cross section predicted by CERN-EXPT and CERN-TH phase shift, respectively. The arrows indicate the energies chosen for differential cross section comparison.

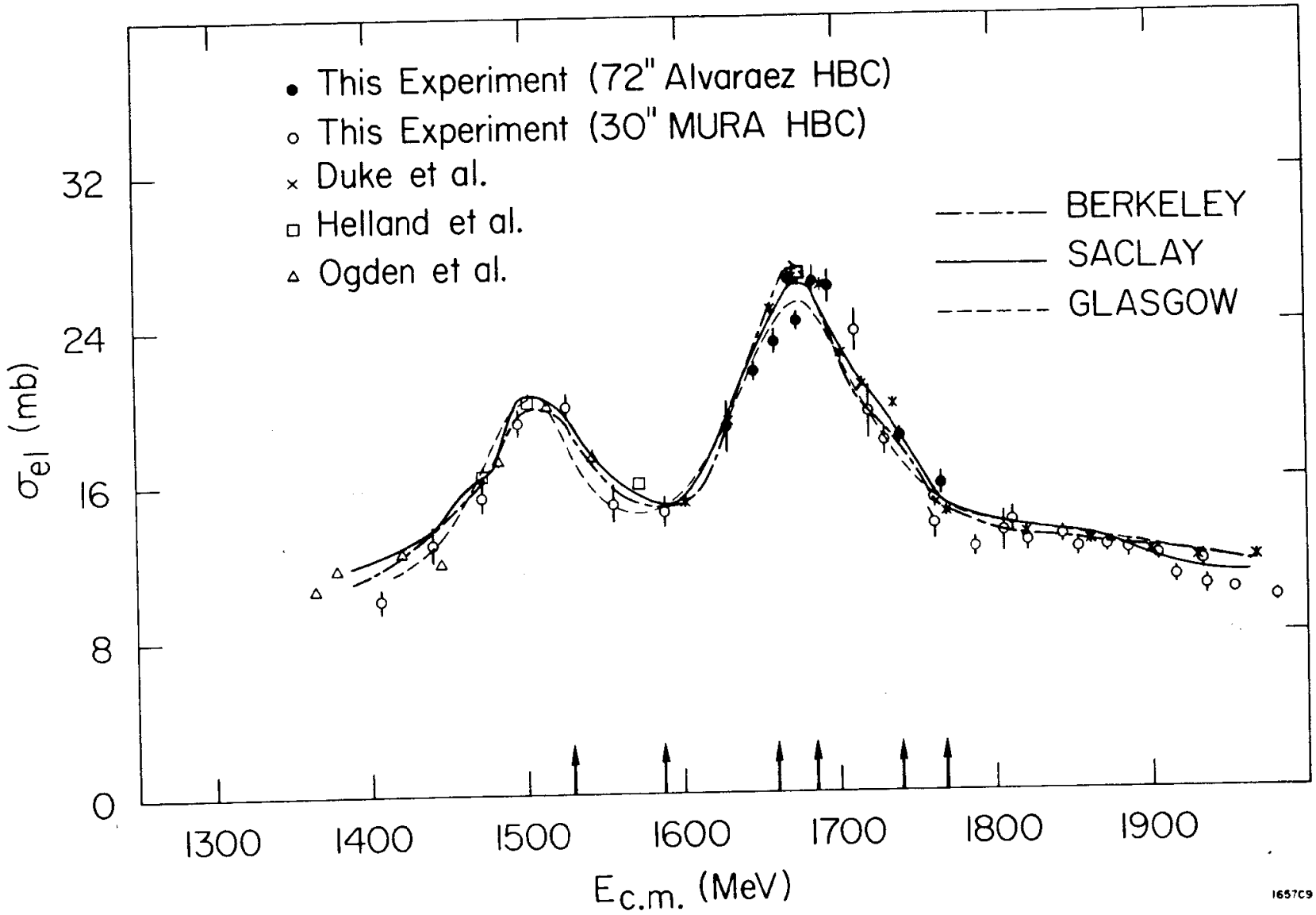

FIG. 39--π^-p elastic cross section predicted by Saclay,[1] Berkeley,[6] and Glasgow,[10] compared to the same data as Fig. 38.

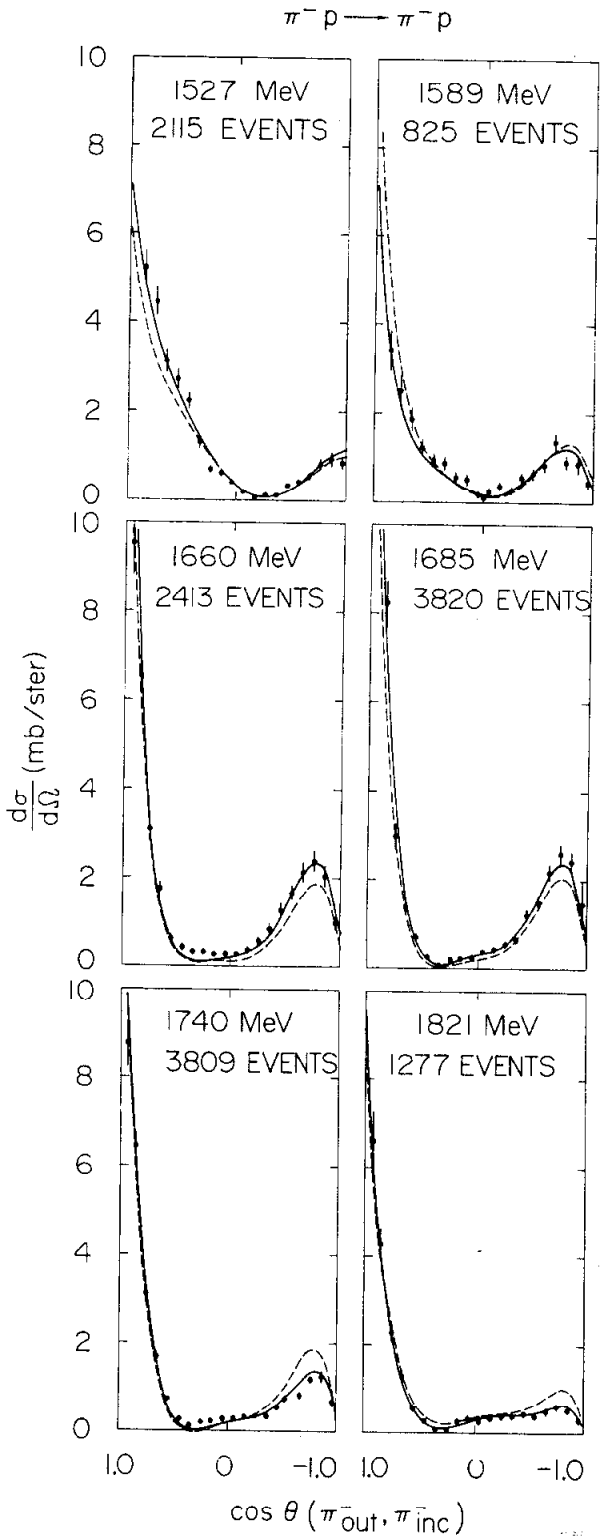

FIG. 40--π^-p differential cross section at six energies measured in this experiment. Solid and dashed lines are the predictions of CERN-EXPT and CERN-TH phase shifts, respectively.

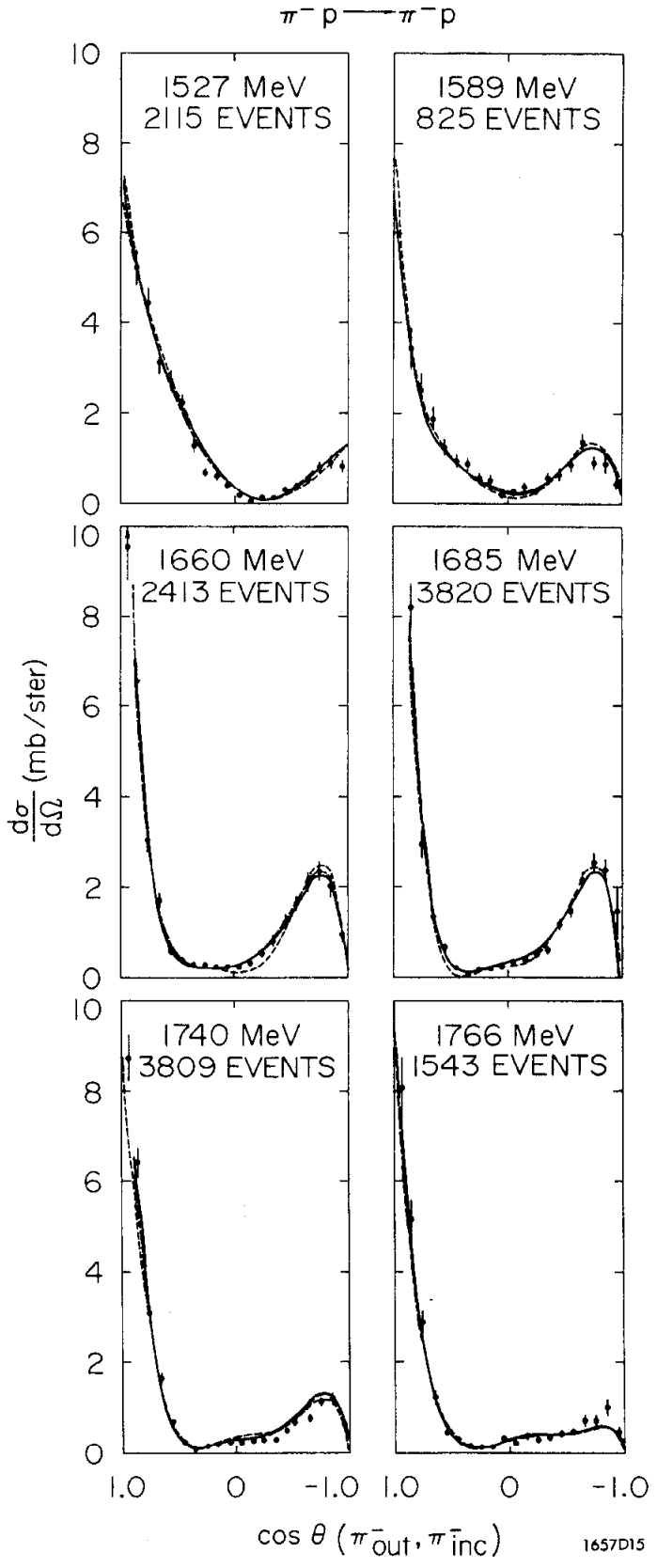

FIG. 41--$\pi^- p$ differential cross section predicted by Saclay,[1] Berkeley,[6] and Glasgow,[10] compared to the experimental data.

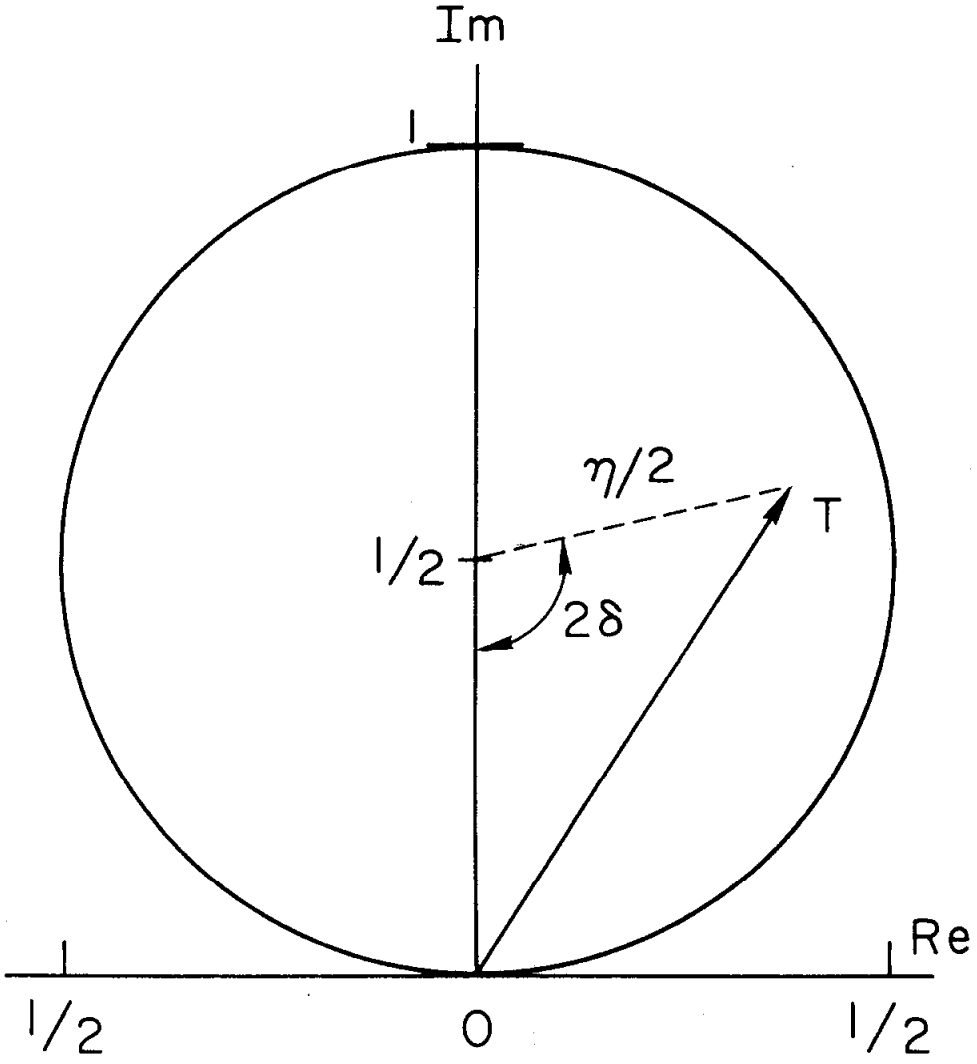

$$T = \frac{\eta e^{2i\delta} - 1}{2i}$$

1801A13

FIG. 42--Argand diagram.

parameters. In practice, the task is far more difficult because the resonance circle is displaced and distorted by background and other effects. The amplitudes themselves may also exhibit "experimental" fluctuations despite the efforts to obtain fairly smooth phase-shift parameters. The group at Rutherford Labs used this method to find the resonance parameters listed in Table I.

A second method is to plot the partial-wave cross sections as functions of energy. The energy where the cross section peaks is taken as the resonance mass. The Saclay group applied both this criterion and the velocity criterion to the same phase-shift solution. The two sets of resonance parameters that resulted are listed in Table I.

The CERN group uses a third method. They examine the plots of absorption and phase shift as functions of energy and search for behavior characteristic of resonances. For example, the onset of a fairly inelastic resonance is accompanied by a dip in the absorption and a simultaneous rapid change in the phase shift. The three sets of resonance parameters that have been reported at different times by CERN are also listed in Table I.

Let us now compare these various resonance parameters. All solutions listed in Table I show the P33 (1236), P11 (1470), D13 (1520), D15 (1670), F15 (1688) and F37 (1950) that were seen in the studies of the Legendre coefficients and in the lower energy phase shifts. In addition to these resonances, first Saclay then Berkeley found evidence for resonances in the S11 partial wave at 1535 and 1700 MeV and also in the S31 near 1650 MeV. The CERN analysis, which extended to higher energies, claimed evidence for nine new resonances — P33 (1688), D33 (1670), F35 (1890), P31 (1910), D35 (1960), P11 (1780), P13 (1860), F17 (1990) and D13 (2040). (The resonance masses

quoted are not necessarily the original values but the average of all values listed.) In subsequent communications,[12e,f] CERN also added to the list the S11(1700) that was seen by Saclay and Berkeley, a P33(2160) and a mass value for D13(1700).

Both Glasgow solutions confirm the resonances announced by CERN except for the P33(1690), D13(1700), D35(1960), P33(2160) and D13(2040); the latter three are close to or beyond the highest energy of the Glasgow fits. In addition, Glasgow A and Glasgow B differ with one another and with CERN on whether there is a G17 or F17 or both near 2000 MeV.

The Rutherford fit strengthens the resonance interpretation of the P13(1860). They find an anomalous behavior of the elasticity and absorption of the D13(2040) that weakens the resonance interpretation. Finally, the Rutherford group finds both a G17 and an F17 resonance near 2000 MeV and proposes a possible parity doublet like the D15/F15 doublet at 1680 MeV. In the I=3/2 partial waves, they see a D35(1950) and a P33 near 2000 MeV.

VI. PARTIAL WAVE ANALYSIS OF $\Delta^-\pi^+$

A. Method of Analysis

In the reaction $\pi^- p \rightarrow n\pi^+\pi^-$ the mass plots (Figs. 28 - 30) appear to be dominated by $\Delta^-\pi^+$ production from 1647 to 1766 MeV, as seen from the MURTLEBURT results in Fig. 31. In this region it is feasible to isolate events belonging to the intermediate state

$$\pi^- p \rightarrow \Delta^-\pi^+ \tag{6.1}$$

and to make a partial wave analysis of this quasi-two-body reaction. The method used was an energy dependent phase shift analysis.

The events belonging to reaction (6.1) were those for which the value of $(n\pi^-)$ mass fell within the range

$$1140 \leq M(n\pi^-) \leq 1320 \text{ MeV} \tag{6.2}$$

The selection includes background events which were estimated, on the basis of the MURTLEBURT results, to comprise about 25% of the sample. These events do not proceed through the $\Delta^-\pi^+$ intermediate state and are not expected to change the resonance parameters determined in the fit, although they might influence the background terms. The selection also excludes some true $\Delta^-\pi^+$ events and the fitted branching ratios were later corrected for this effect, as discussed below.

The analysis followed the procedure developed by Brody and Kernan.[38] Each final state is characterized by its value of outgoing orbital angular momentum L and total angular momentum J in the notation L2J. Thus D15 and F15 contribute to D5 and P5, respectively (outgoing states of higher orbital angular momentum — G5 and F5 in this case — have been ignored; barrier penetration factors prevent them from playing a very large role).

The D5 and P5 waves were parameterized as resonances and the rest — S3, P1, D1 and F7 — were parameterized as backgrounds.

The resonances were given the shape of a nonrelativistic Breit-Wigner amplitude:

$$T = \frac{1}{2} \frac{\sqrt{\Gamma_{el}(E)\ \Gamma_{\Delta\pi}(E)}}{(M_0 - E) - i\,\Gamma_{tot}(E)/2} \tag{6.3}$$

The widths have an energy dependence of the form

$$\Gamma_i(E) = x_i\ \Gamma^o_{tot}\ \frac{B_L(q_i)}{B_L(q^o_i)}\ \frac{q_i}{q^o_i}\ \frac{M_0}{E} \tag{6.4}$$

Here,

x_i = the branching ratio $\Gamma^o_i/\Gamma^o_{tot}$ with i referring to the elastic (el) or delta-pi ($\Delta\pi$) reaction

q_i = center-of-mass momentum

E = center-of-mass energy

$B_L(q)$ = barrier penetration factor[29] with radius of interaction equal to 1 fermi

L = orbital angular momentum in the particular channel

The superscript o refers to the values of these quantities at the resonance mass $E = M_0$.

The total width is the sum of partial widths

$$\Gamma_{tot}(E) = \Gamma_{el}(E) + \Gamma_{\Delta\pi}(E) + \Gamma_r(E) \tag{6.5}$$

With the approximation that the other reaction channels, collectively denoted by r, have the same energy dependence as the $\Delta\pi$ channel, the total decay

width may be written as

$$\Gamma_{tot}(E) = \Gamma_{el}(E) + \Gamma_{\Delta\pi} \frac{(1-x_{el})}{x_{\Delta\pi}} \tag{6.6}$$

The representation of the resonance described thus far has four free parameters: Γ^o_{tot}, x_{el}, $x_{\Delta\pi}$ and the resonance mass M_0. However, we may reduce the number of parameters by assuming for x_{el} the value determined by elastic phase shift analysis. The form of parameterization then becomes

$$T = \frac{1}{2} \frac{\Gamma^o_{tot} \sqrt{x_{el} x_{\Delta\pi}}\ f(E)}{(M_0 - E) - \frac{i}{2}\Gamma^o_{tot}\left[x_{el} \frac{B_L(q)}{B_L(q_0)} \frac{q}{q_0} + (1-x_{el}) \frac{B_L(q_{\Delta\pi})}{B_L(q^o_{\Delta\pi})} \frac{q_{\Delta\pi}}{q^o_{\Delta\pi}}\right]\frac{M_0}{E}} \tag{6.7}$$

where

$$f(E) = \frac{M_0}{E} \sqrt{\frac{B_L(q)}{B_L(q_0)} \frac{q}{q_0} \frac{B_L(q_{\Delta\pi})}{B_L(q^o_{\Delta\pi})} \frac{q_{\Delta\pi}}{q^o_{\Delta\pi}}} \tag{6.8}$$

The free parameters are $\sqrt{x_{el} x_{\Delta\pi}}$, M_0 and Γ^o_{tot}.

The backgrounds are given the momentum dependence

$$T = (a + bq_{\Delta\pi}) + i(c + dq_{\Delta\pi}) \tag{6.9}$$

with the real numbers a, b, c, and d as the four independent parameters. All these parameters are adjusted to fit the experimental distributions by minimizing the chisquared function

$$F = \sum_{\text{energies}} \sum_{\substack{\text{angular}\\ \text{distributions}}} \left[\frac{\left(\frac{dN}{d\Omega}\right)_{obs} - \left(\frac{dN}{d\Omega}\right)_{pred}}{\delta\left(\frac{dN}{d\Omega}\right)_{obs}}\right]^2 + \sum_{\text{energies}} \left[\frac{\sigma^{\Delta\pi}_{obs} - \sigma^{\Delta\pi}_{pred}}{\delta\sigma^{\Delta\pi}_{obs}}\right]^2 \tag{6.10}$$

with the minimization program MINFUN.[39]

B. Results

After random starts from numerous parameter values, the program found two distinct solutions, A and B, corresponding to the parameter values listed in Table XI. A differs from B in two striking ways: The relative sign of coupling for D15 and F15 is negative and the size of F15 coupling is considerably smaller. The Argand plots in Fig. 43 show the differences dramatically. The P5 wave for solution A falls below the real axis and the backgrounds are located in very different regions of the plots. Figure 44 displays the partial-wave cross sections predicted by the two sets of parameters. Their sum is compared to the experimental cross section $\sigma_{n\pi^+\pi^-}$ within the cut region. In solution A the large D1 and S3 backgrounds appear to compensate for the low value of the P5 resonance. In Fig. 45 the predictions of the two solutions are compared to the differential cross sections at three energies, where they give essentially the same result.

The fits were extended to lower energies in an attempt to determine the sign of the D13 coupling relative to the D15 and F15. However, the D13 contributes to the same channel as the s-wave background so the fits were inconclusive.

The errors associated with these parameters are determined by varying each parameter in turn and reminimizing. The amount by which the parameter value can be varied before it changes the chisquared function by a certain amount is a measure of the error associated with this parameter.

The fit can be extended to include the distributions of the π^- and the n from the decay of the Δ^-. When these data were included in the fits, solutions A and B were basically the same. The decay distributions are more sensitive than the angular distributions to the $n\pi^+\pi^-$ background and

TABLE XI

FIT PARAMETERS

Solution	F ($\approx \chi^2$)	Number of Data Points	P5 (F_{15})			D5 (D_{15})		
			Mass	Width	$\sqrt{x_{el}\, x_{inel}}$	Mass	Width	$\sqrt{x_{el}\, x_{inel}}$
A	219.12	231	1.690 ± 0.005	0.077 ± 0.022	- 0.252 {+ 0.039 - 0.024}	1.671 ± 0.004	0.112 ± 0.017	+ 0.468 {+ 0.012 - 0.018}
B	228.04	231	1.686 ± 0.009	0.130 {+ 0.035 - 0.053}	+ 0.447 {+ 0.025 - 0.053}	1.680 ± 0.009	0.158 {+ 0.090 - 0.020}	+ 0.468 {+ 0.014 - 0.035}

	S3				P1			
	a	b	c	d	a	b	c	d
A	0.284	- 0.733	0.337	- 0.072	- 0.009	0.393	- 0.527	0.638
B	0.219	- 0.726	- 0.333	0.553	0.314	- 0.290	- 0.078	0.615

	D1				F7			
	a	b	c	d	a	b	c	d
A	0.191	0.172	0.512	- 0.734	- 0.138	-	0.086	-
B	- 0.581	0.718	0.373	- 0.726	- 0.071	-	0.072	-

1801A40

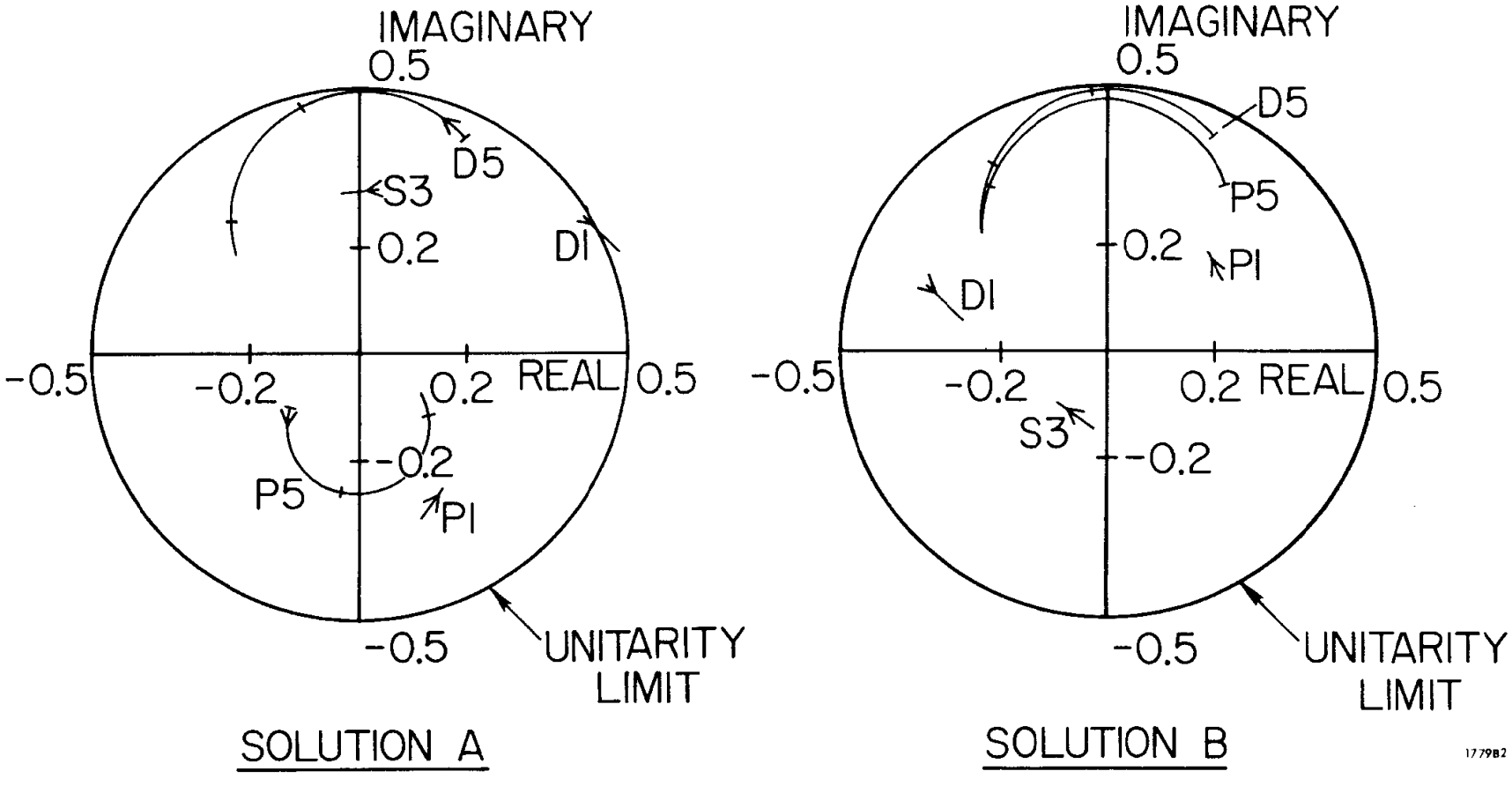

FIG. 43--Variation of the partial-wave amplitudes in two solutions A and B from a fit to the reaction $\pi^- p \rightarrow \Delta^- \pi^+$.

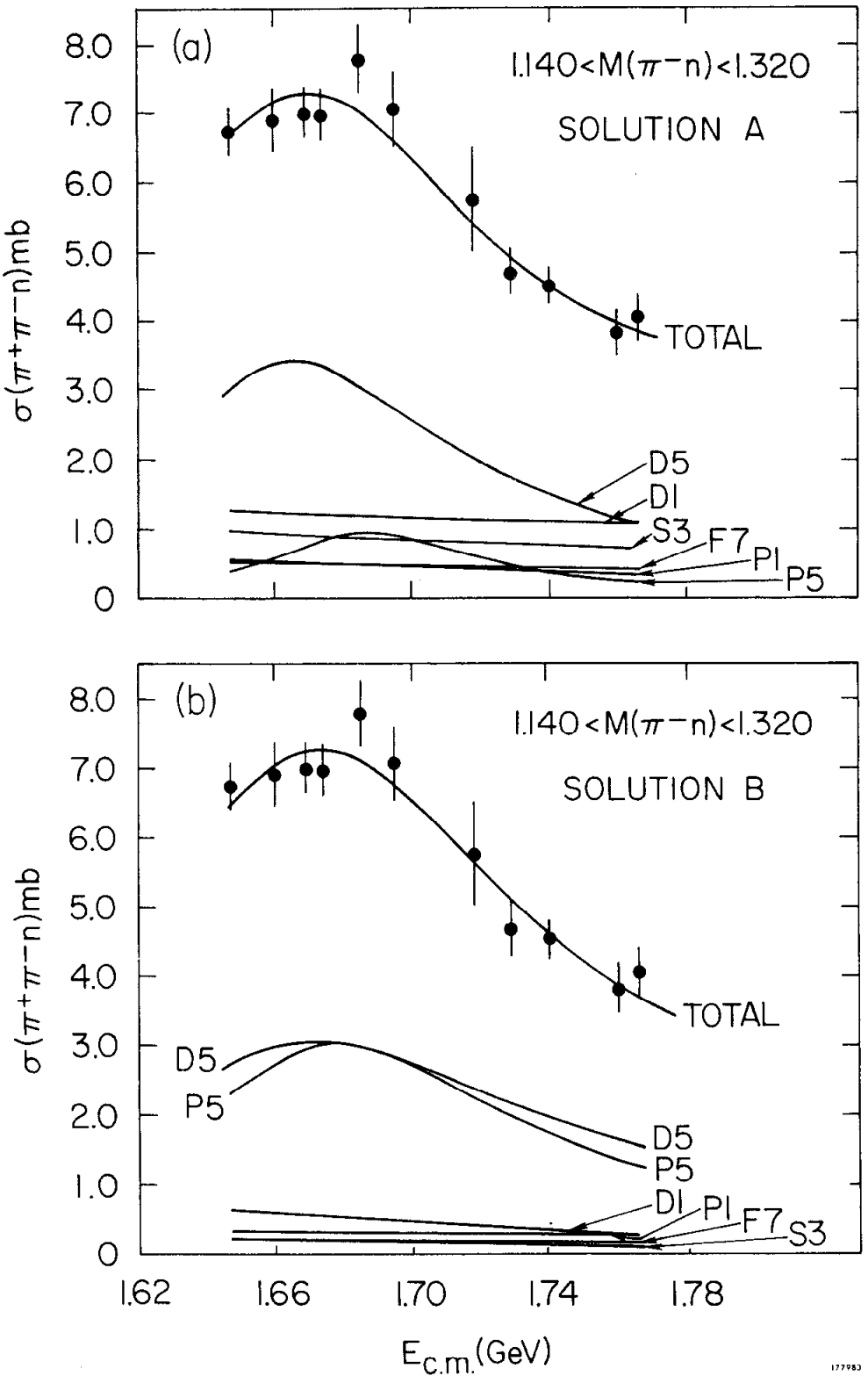

FIG. 44-The experimental $n\pi^+\pi^-$ cross section within the mass cut $1140 \leq M(\pi^- n) \leq 1320$ MeV, together with the contributions of the various partial waves in solutions A and B.

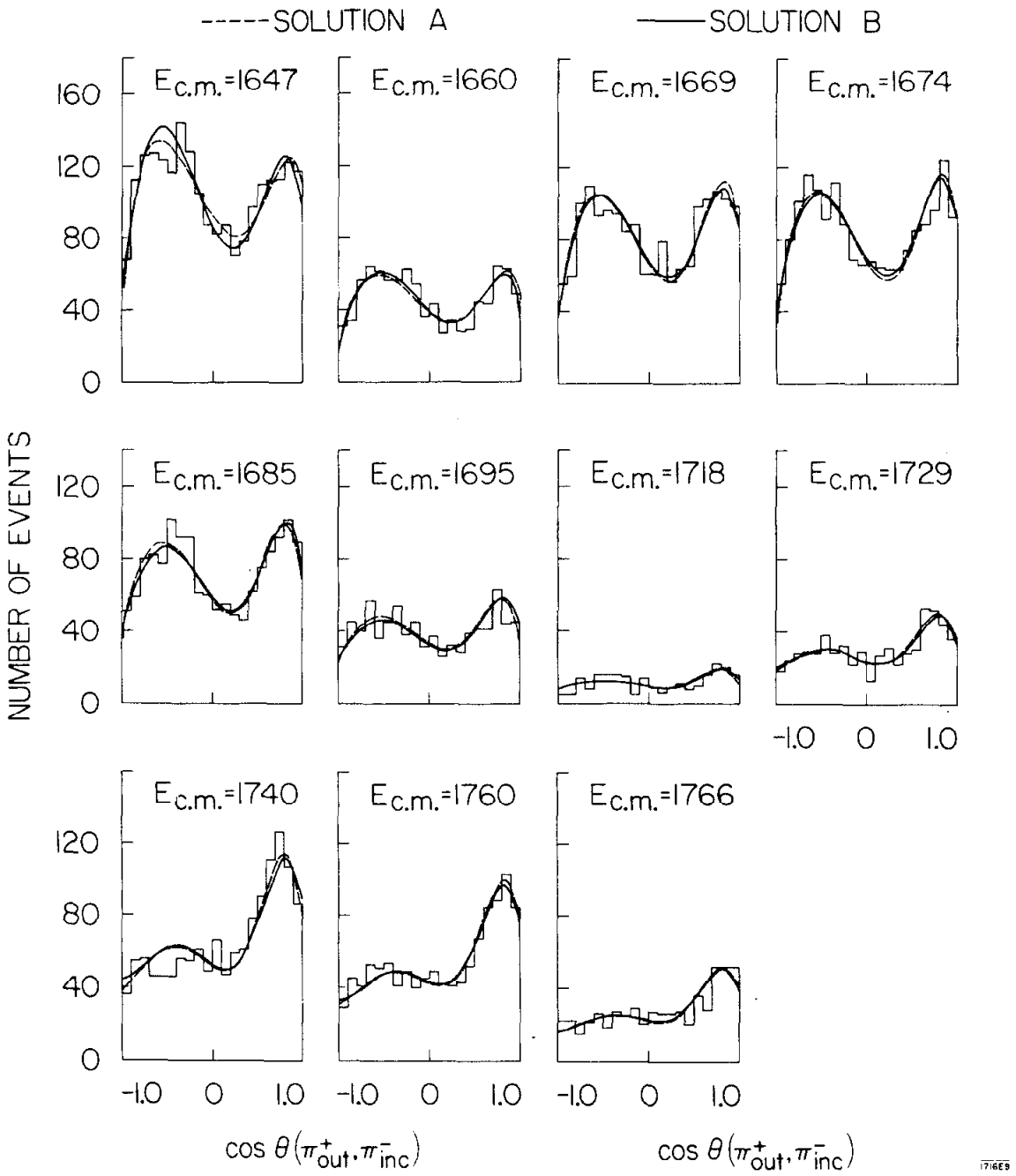

FIG. 45--Fits to the production angular distributions of the π^+ in the reaction $\pi^- p \rightarrow \Delta^- \pi^+$ in solutions A and B.

interference with the Δ^+. Thus we feel that the fits without the decay distributions are more reliable.

One of the fitted parameters is the product of branching ratios, $\sqrt{x_{el} x_{\Delta\pi}}$. The elastic branching ratios for D15 and F15 are relatively well established from the phase-shift analyses. For these ratios we take the average of all the phase-shift results[11b] ($x_{el} = 0.42 \pm .04$ for D15 and $x_{el} = 0.62 \pm .06$ for F15) and then solve for $x_{\Delta\pi}$ and the partial width. These values will be underestimates of the actual values because the mass region in which the analysis was made excluded some events that proceed through the intermediate state. To determine the number of events lost outside this region it is desirable to express the shape of the distribution in terms of the empirical $\Delta(1236)$ phase shift, δ_{33}. The form used was

$$|T_\Delta|^2 \propto \frac{\sin^2 \delta_{33}}{\Gamma(M)} \frac{M}{q} \left(\frac{q}{q_0}\right)^{2L} \tag{6.11}$$

where $\Gamma(M)$ is given by

$$\tan \delta_{33} = \frac{M_\Delta \Gamma(M)}{M_\Delta^2 - M^2} \tag{6.12}$$

In these equations, q and M are the momentum and mass in the decay frame of the delta. One may use this formula together with the appropriate value of orbital angular momentum to estimate the fraction of events lying outside the mass cuts. The correction factors determined in this way are 1.22 and 1.20 for the p-wave decay of the F15 and the d-wave decay of the D15, respectively. The branching ratios listed in Table XII, include these corrections.

TABLE XII

Octet	Particle	Mass and Width	Decay Mode	c^2	$\frac{\langle B_L(q_R)q_R\rangle M_p}{M_p}$	Solution A: Observed Branching Ratio	Solution A: g^2	Solution A: Predicted Width	Solution A: Predicted Branching Ratio	Solution B: Observed Branching Ratio	Solution B: g^2	Solution B: Predicted Width	Solution B: Predicted Branching Ratio
$5/2^-$	N(1680)	1.672 0.142	$\Delta(1238)\pi$	4/5	0.074	0.53 ± 0.07 $x_{el} = .42$	1.506 ± 0.167	Input	Input	0.63 + 0.07 - 0.11 $x_{el} = .42$	1.506 + 0.167 - 0.263	Input	Input
	$\Sigma(1765)$	1.765 0.100	$\Sigma(1385)\pi$	2/15	0.047	0.13 ± 0.02	-	0.009 ± 0.001	0.09 ± 0.01	0.13 ± 0.02	-	0.009 + 0.001 - 0.002	0.09 + 0.01 - 0.02
			$\Delta(1238)\bar{K}$	8/15	0.013			0.011 ± 0.001	0.11 ± 0.01			0.011 + 0.001 - 0.002	0.11 + 0.01 - 0.02
	$\Lambda(1830)$	1.835 0.075	$\Sigma(1385)\pi$	3/5	0.076	-	-	0.069 ± 0.008	0.92 ± 0.11	-	-	0.069 + 0.008 - 0.012	0.92 + 0.11 - 0.16
	$\Xi(1930)$	1.930 0.110	$\Xi(1530)\pi$	1/5	0.052	-	-	0.016 ± 0.002	0.16 ± 0.02	-	-	0.016 + 0.002 - 0.003	0.16 + 0.02 - 0.03
			$\Sigma(1385)\bar{K}$	1/5	0.008			0.002 ± 0.001	0.02 ± 0.01			0.002 ± 0.001	0.02 ± 0.01
$5/2^+$	N(1690)	1.688 0.125	$\Delta(1238)\pi$	4/5	0.160	0.13 + 0.03 - 0.04 $x_{el} = .60$	0.127 + 0.029 - 0.04	Input	Input	0.39 - 0.06 - 0.10 $x_{el} = .60$	0.386 + 0.058 - 0.097	Input	Input
	$\Sigma(1915)$	1.910 0.050	$\Sigma(1385)\pi$	2/15	0.178	-	-	0.003 ± 0.001	0.06 ± 0.02			0.009 + 0.001 - 0.003	0.18 + 0.02 - 0.06
			$\Delta(1238)\bar{K}$	8/15	0.140			0.009 + 0.002 - 0.003	0.18 + 0.04 - 0.06			0.028 + 0.004 - 0.007	0.56 + 0.08 - 0.14
	$\Lambda(1815)$	1.815 0.075	$\Sigma(1385)\pi$	3/5	0.142	0.17 ± 0.03	-	0.011 ± 0.003	0.15 ± 0.04	0.17 ± 0.03	-	0.032 + 0.005 - 0.008	0.43 + 0.07 - 0.11
	$\Xi(2030)$	2.030 0.050	$\Xi(1530)\pi$	1/5	0.159	-	-	0.004 ± 0.001	0.08 ± 0.02	-	-	0.012 + 0.002 - 0.003	0.24 + 0.04 - 0.06
			$\Sigma(1385)\bar{K}$	1/5	0.119			0.003 ± 0.001	0.06 ± 0.02			0.009 + 0.001 - 0.002	0.18 + 0.02 - 0.04

160/C34

C. SU3 Predictions

The D15 and F15 resonances are classified by SU3 as members of the $5/2^-$ and $5/2^+$ baryon octets. The coupling constants for the decays of these resonances into the $\Delta^-(1236)$ and the π^+ should be the same as those for other members of the octets into the 3/2 baryon decuplet and the 0^- meson octet. The branching ratio measured in this experiment can thus be used to calculate the coupling constant characterizing these octets.

The prescription for relating the coupling constant g to the partial widths for particular members of the multiplets is[40]

$$\Gamma = c^2 g^2 M_p \frac{\langle B_L(q_R)\, q_R \rangle}{M_R} \tag{6.13}$$

where

c = Clebsch-Gordan coefficient for $|8| \rightarrow |10| \times |8|$

M_p = proton mass

M_R = resonance mass

$\langle B_L(q_R) q_R \rangle$ = product of the barrier penetration factor, with radius of interaction equal to 1 fermi, and momentum of the decay particles. The product is averaged over the width of the resonance.

Table XII lists the values of g^2 determined from the two sets of solutions A and B. These coupling constants are used to predict the partial widths and branching ratios for the other members of the octets. Comparison with experimentally observed branching ratios is possible only in two cases, for $\Sigma(1765) \rightarrow \Sigma(1385)\pi$ [(41)] and $\Lambda(1815) \rightarrow \Sigma(1385)\pi$.[41] Solutions A and B lead to comparable predictions for the former but only solution A agrees with the

latter. One might hope that a partial-wave analysis of the reaction

$$K^- p \rightarrow \Sigma(1385)\pi \rightarrow \Lambda\pi\pi \tag{6.14}$$

would yield branching ratios for the $\Lambda(1830)$ and $\Sigma(1915)$ resonances as well as additional measurement of the $\Sigma(1765)$ and $\Lambda(1815)$ branching ratios. The relative coupling of $\Lambda(1830)$ and $\Lambda(1815)$ to the $\Sigma(1385)\pi$ channel must be the same as the D15-F15 coupling; measurement of this would distinguish between our two solutions.

VII. COUPLED CHANNEL ANALYSIS

A. Introduction

The elastic and delta-pi channels considered separately in Chapters V and VI are related to one another through the requirements of unitarity. This condition is usually expressed in terms of the scattering matrix S.

$$S^{+} S = I \tag{7.1}$$

If we write S in terms of the T-matrix as

$$S = I + 2iT \tag{7.2}$$

then the unitarity condition on the T-matrix becomes

$$\mathrm{Im}(T) = T^{+} T \tag{7.3}$$

In partial-wave analyses of one channel alone, unitarity is imposed on the amplitudes in the form of an upper limit. For example, the S-matrix element for elastic scattering is often represented by

$$S = \eta e^{-2i\delta} \tag{7.4}$$

In order not to violate unitarity, the absorption parameter is required to be less than one. If there is an appreciable scattering into a second channel, however, unitarity would require η to be significantly smaller than one and the upper limit imposed in the one-channel fit does not sufficiently restrain the amplitude.

In a coupled-channel analysis, two or more channels must simultaneously satisfy unitarity. In particular, let us consider the elastic and delta-pi channels of πN scattering. The formalism that will be developed can be extended to include the effects of other channels such as the $N\pi\pi$ background, or strange particle channels, but the πN and $\pi\Delta$ channels will account for a large

percentage of the total amplitude. Furthermore the data itself and the large number of parameters involved in the fits prevent one from distinguishing the effects of these other channels. We may lump them all together a one collective "background" channel.

The delta-pi channel must actually be considered as two channels; for each value of L in the incoming state there can be two values of L' (orbital angular momentum) in the final $\Delta\pi$ state. We thus seek a parameterization for a T matrix that describes πN scattering with four open outgoing channels and that satisfies (7.3). Actually, (7.3) applies to each 4×4 submatrix, $T^J_{LL'}$, corresponding to each set of the quantum numbers J (total angular momentum), L (orbital angular momentum in the incoming channel), and L' (orbital angular momentum in the outgoing channel).

To summarize, the four channels considered in the coupled-channel analysis are

$$\pi^- p \to \pi^- p \qquad L = L' \qquad (7.5a)$$

$$\to \Delta^- \pi^+ \qquad L = L' \qquad (7.5b)$$

$$\to \Delta^- \pi^+ \qquad L \neq L' \qquad (7.5c)$$

$$\to \text{background} \qquad L = L' \qquad (7.5d)$$

B. Formalism

1. K-Matrix Approach

R. H. Dalitz[42,43] has formulated an approach to the coupled-channel problem in $K^- p$ scattering. He chose to work with the reaction matrix, or K matrix, rather than the T matrix. The K matrix describes a process in which the scattered waves are standing waves rather than travelling waves. Naturally, the K matrix does not correspond to any physical process but is

simply related to the T matrix that does describe physical scattering:

$$T = (I-iK)^{-1} K \tag{7.6}$$

The great advantage of the K matrix is that if K is hermitian, the T matrix determined from it according to (7.6) will automatically satisfy unitarity. In addition, if K is real, both K and T will be time-reversal invariant. Thus instead of selecting n(n+1)/2 complex parameters to represent the T matrix then imposing the restraining equation, (7.3), one can simply choose n(n+1)/2 real parameters of the K matrix.

Dalitz worked extensively in the K matrix to describe the K^-p scattering near threshold. However, most of his techniques are inapplicable to π^-p scattering in the region of this experiment because the near-threshold approximations used are not valid so far above threshold. The rest of this section is therefore devoted to using the K matrix only to develop an appropriate parameterization for the T matrix.

Suppose we wish to calculate the T matrix for a process involving only two channels. First we select three real parameters — α, β, and γ — to define an arbitrary K matrix.

$$K = \begin{bmatrix} \alpha & \beta \\ \beta & \gamma \end{bmatrix} \tag{7.7}$$

Rather than calculating the T matrix directly from this K matrix we can simplify the computation by first diagonalizing K. If U is the unitary transformation that takes K into the diagonal K matrix K^D, that is, if

$$K^D = U^{-1} K U \tag{7.8}$$

then it is easily shown that the T matrix can be written in terms of K^D as

$$T = U\left[(I - iK^D)\, K^D\right] U^{-1} \tag{7.9}$$

Let the eigenvalues of K be tan δ_α and tan δ_β so that

$$K^D = \begin{bmatrix} \tan\delta_\alpha & 0 \\ 0 & \tan\delta_\beta \end{bmatrix} \tag{7.10}$$

The unitary matrix U may have the form

$$U = \begin{bmatrix} \cos\theta & -\sin\theta \\ \sin\theta & \cos\theta \end{bmatrix} \tag{7.11}$$

Then the T matrix resulting from (7.9) will have the following form:

$$T = \begin{bmatrix} \dfrac{\cos^2\theta}{\operatorname{ctn}\delta_\alpha - 1} + \dfrac{\sin^2\theta}{\operatorname{ctn}\delta_\beta - i} & \cos\theta\,\sin\theta\left(\dfrac{1}{\operatorname{ctn}\delta_\alpha - i} + \dfrac{1}{\operatorname{ctn}\delta_\beta - i}\right) \\ \cos\theta\,\sin\theta\left(\dfrac{1}{\operatorname{ctn}\delta_\alpha - i} + \dfrac{1}{\operatorname{ctn}\delta_\beta - i}\right) & \dfrac{\sin^2\theta}{\operatorname{ctn}\delta_\alpha - i} + \dfrac{\cos^2\theta}{\operatorname{ctn}\delta_\beta - i} \end{bmatrix} \tag{7.12}$$

The three parameters of the K matrix have been replaced by three new parameters, δ_α, δ_β, and θ. The two sets are related by the following equations:

$$\tan\delta_\alpha = \frac{\alpha\cos^2\theta - \gamma\sin^2\theta}{\cos^2\theta - \sin^2\theta} \tag{7.13a}$$

$$\tan\delta_\beta = \frac{\gamma\cos^2\theta - \alpha\sin^2\theta}{\cos^2\theta - \sin^2\theta} \tag{7.13b}$$

$$\tan 2\theta = 2\beta/(\alpha - \gamma) \tag{7.13c}$$

2. Resonance Parameterization

At this stage we must make some assumptions and lose generality in the interest of deriving a convenient and manageable parameterization for the T matrix. The result will not be the most complete expression for T but will be one that nevertheless satisfies unitarity and that has a suitable form for a computerized fit to the data.

Thus we assume that one of the eigenvalues of the K matrix is near zero. If tan δ_β is near zero then the second term in each of the matrix elements of (7.12) is also near zero and may be neglected. We are left with a T matrix of the form

$$T = \frac{1}{\operatorname{ctn} \delta_\alpha - i} \begin{bmatrix} \cos^2 \theta & \cos \theta \sin \theta \\ \cos \theta \sin \theta & \sin^2 \theta \end{bmatrix} \tag{7.14}$$

Near a resonance in the elastic (T_{11}) channel, the phase angle δ_α must pass rapidly through 90°. The eigenvalue, tan δ_α, may be expanded about the resonance energy, E_R, as follows:

$$\tan \delta_\alpha = \frac{\Gamma}{2(E_R - E)} + A + \ldots \tag{7.15}$$

Let us call the expression $2(E_R - E)/\Gamma$ by the term ϵ. Furthermore we can define $\cos^2 \theta$ to be the elasticity x, or Γ_{el}/Γ. Then the amplitude in the elastic channel has the appearance of a simple Breit-Wigner resonance and the T matrix assumes the familiar form:

$$T = \frac{1}{\epsilon - i} \begin{bmatrix} x & \sqrt{x(1-x)} \\ \sqrt{x(1-x)} & 1-x \end{bmatrix} \tag{7.16}$$

3. Resonance Plus Background

If there is background in the same channel as the resonance, the phase shift may be written as the sum of two angles, one of which (δ_α) passes rapidly through 90° while the other (δ_β) remains nearly constant as E approaches E_R.[43]

$$\text{Tan}\ \delta_\alpha = \tan(\delta_R + \delta_B) \tag{7.17}$$

When this expression is substituted into $1/(\text{ctn}\ \delta_\alpha - i)$, the result is

$$\frac{1}{\text{ctn}\ \delta_\alpha - i} = \frac{e^{2i\delta_B}}{\text{ctn}\ \delta_R - i} + \frac{1}{\text{ctn}\ \delta_B - i} \tag{7.18}$$

The effect of the background is thus to shift the position of the resonance by an angle of $2\ \delta_B$ and to add a constant background term.

4. Background Parameterization

Away from resonance the phase shift δ_α is small and the background amplitude for elastic scattering is simply

$$T_{11} = \frac{\cos^2\theta}{\text{ctn}\ \delta_\alpha - i}$$

or, equivalently,

$$T_{11} = \frac{\cos^2\theta}{-\tan\delta - i} \qquad \text{where } \delta = \frac{\pi}{2} + \delta_\alpha \tag{7.19}$$

In general the backgrounds have a slight energy dependence. This energy dependence can be put into the parameterization by giving the angles δ and θ a linear dependence on momentum

$$\theta = \theta_1 + q\theta_2 \tag{7.20a}$$

$$\delta = \delta_1 + q\,\delta_2 \tag{7.20b}$$

5. Extension to Four Dimensions

The 4×4 T matrix may be found using a procedure similar to that followed in the case of the 2×2 T matrix above. The most general 4×4 unitary transformation U has 6 independent variables. Together with the 4 parameters needed to describe the K matrix, this makes ten parameters to describe the four open channels; only three were required to describe the scattering with two open channels. One would expect, however, that only two parameters need be added to represent the effects of the two additional channels. Again we can assume that only one eigenvalue of the K matrix is nonzero. Then, it is found that only three of the variables that represent the unitary matrix U will enter the first row of the T matrix. Because we look only at physical scattering with $\pi^- p$ in the incoming channel, we are only concerned with this first row. Thus it is sufficient to select a unitary matrix represented by three independent variables.

Let us write this unitary matrix U as the product of successive rotations in a four-dimensional space. The rotation angles are the three parameters θ, α, and β. Using this matrix U in the Eq. (7.9) we find the following expression for the T matrix:

$$T = \frac{1}{\sin\delta_\alpha - i}\begin{bmatrix} \cos^2\theta & \cos\theta\sin\theta\cos\alpha & \cos\theta\sin\theta\sin\alpha\cos\beta & \cos\theta\sin\theta\sin\alpha\sin\beta \\ \sin\theta\cos\theta\cos\alpha & \sin^2\theta\cos^2\alpha & \sin^2\theta\sin\alpha\cos\alpha\cos\beta & \sin^2\theta\sin\alpha\cos\alpha\sin\beta \\ \sin\theta\cos\theta\cos\beta\sin\alpha & \sin^2\theta\sin\alpha\cos\alpha\cos\beta & \sin^2\theta\cos^2\beta\sin^2\alpha & \sin^2\theta\sin^2\alpha\sin\beta\cos\beta \\ \sin\theta\cos\theta\sin\beta\sin\alpha & \sin^2\theta\sin\alpha\cos\alpha\sin\beta & \sin^2\theta\sin^2\alpha\sin\beta\cos\beta & \sin^2\theta\sin^2\alpha\sin^2\beta \end{bmatrix} \tag{7.21}$$

We are concerned only with the first row of this matrix, which contains the scattering amplitudes for $\pi^- p$ in the incoming channel. Comparison with (7.16) reveals that the elastic term is still $\cos^2\theta = x$. The inelastic terms are still proportional to $\sqrt{x(1-x)}$ but they are now modulated by the terms $\cos\alpha$, $\sin\alpha\cos\beta$, and $\sin\alpha\sin\beta$. Obviously $\alpha=\beta=0$ corresponds to the situation where channels (3) and (4) are closed and returns us to the 2×2 T matrix.

C. Fitting Program

The formalism above is used to predict the amplitude for scattering in the three physical channels $\pi N \to \pi N$ and $\pi N \to \pi\Delta$. Depending on whether a particular partial wave is assumed to contain resonance, resonance plus background or background alone, the amplitude for scattering is proportional to

$$T \propto \frac{1}{\operatorname{ctn}\delta_\alpha - i} = \frac{1}{\epsilon - i} \qquad \text{resonance} \tag{7.22a}$$

$$= \frac{e^{2i\delta_B}}{\operatorname{ctn}\delta_R - i} + \frac{1}{\operatorname{ctn}\delta_B - i} \qquad \begin{matrix}\text{resonance}\\ \text{plus background}\end{matrix} \tag{7.22b}$$

$$= \frac{1}{-\tan\delta - i}\,, \qquad \delta = \delta_1 + q\,\delta_2 \qquad \text{background} \tag{7.22c}$$

with the constant of proportionality varying according to the channel in question:

$$x = \cos^2\theta \tag{7.23a}$$

$$\cos\theta\,\sin\theta\,\cos\alpha \tag{7.23b}$$

$$\cos\theta\,\sin\theta\,\sin\alpha\,\cos\beta \tag{7.23c}$$

$$\cos\theta\,\sin\theta\,\sin\alpha\,\sin\beta \tag{7.23d}$$

Thus for each partial wave there are five parameters — E_R, Γ, θ, α, and β — to describe a resonance with a sixth additional parameter — δ_B — to

include a background with the resonance. There are six parameters — θ_1, θ_2, δ_1, δ_2, α, and β — to describe a pure background.

For a particular set of parameters, the T-matrix amplitudes may be calculated and substituted into Eqs. (5.1), (5.14), and (5.16) to yield the differential cross section, polarization and total cross section for a particular channel and a particular value of isospin. The isospin amplitudes are then combined according to (5.17) through (5.20) to obtain predictions of the physical measured quantities. Note that (5.1), and (5.16) are general enough to apply to $\pi N \rightarrow \pi\Delta$ reactions as well as to $\pi N \rightarrow \pi N$; one merely changes the limits on the summation over final-state helicities to run from -3/2 to +3/2.

The value of the various quantities (x^i_{calc}) predicted with a given set of parameters are compared to the experimentally determined values (x^i_{meas}). The quality of the fit is described by the value of chisquared, defined as

$$\chi^2 = \frac{(x^i_{meas} - x^i_{calc})^2}{(\Delta x^i_{meas})^2} \tag{7.24}$$

The computer program MINFUN[39] then conducts a search in the parameter space for the minimal value of χ^2. The details of the subroutine FCN — flow chart, format of input cards, list of arrays and listing of the program itself — of MINFUN are given in Appendix I.

The input data to which the predictions are compared includes not only the elastic $\pi^- p \rightarrow \pi^- p$ and inelastic $\pi^- p \rightarrow \Delta^- \pi^+$ channels measured in the present experiment but also the charge-exchange data[44, 45] and polarization data[46] measured in other experiments. The charge-exchange data helps to distinguish the isospin of the various partial waves and the polarization data helps to determine the correct parity.

The proper normalization of the differential cross section $\sigma_{\pi^- p \to \Delta^- \pi^+}$ is not accurately known in the present experiment so an additional set of parameters was included in the fits to correct for the uncertainty in normalization. First the cross section was approximated by multiplying the $n\pi^+\pi^-$ cross section in the region of the delta mass cut by the $\Delta\pi$ fraction found in the MURTLEBURT fit (see Chapter IV). The $\Delta\pi$ fraction really applies to events both inside and outside the mass cut. But the mass cut includes events that may not be true delta-pi events. These two errors tend to cancel one another but the cancellation may not be exact. Thus we correct for possible normalization errors by including a set of parameters ϵ_i where

$$x^i_{calc} = \epsilon_i \, x^i_{calc} \tag{7.25}$$

and i denotes a measurement at a particular energy.

The fit was restricted to the energy region from 1640 to 1760 MeV in the center-of-mass because this is the only region where there is an appreciable cross section for the reaction $\pi^- p \to \Delta^- \pi^+$. Only partial waves up to F7 were included in the fits although the program is written to allow for waves up through G waves.

Table I indicates that the strong candidates for resonance in this energy region are S11(1700), D13 (1700), P11 (1780), D15 (1670), F15 (1688), S31 (1650), P33(1690), and D33(1670). Of these the D13, P33, and D33 are seen very weakly in the elastic phase-shift analyses. The coupled-channel analysis is more limited in scope than the phase-shift programs and can not be expected to detect these weaker resonances. The P11(1780) is a very broad resonance beyond the highest energy so the program can not distinguish between the tail

of this resonance and a background. Thus only S11, D15, F15, and S31 remain as candidates to be parameterized as resonances.

The starting values for resonance parameters were taken from the results of the various phase-shift solutions. Many sets of starting values were tried. In general, the fits with all four waves above treated as resonances gave better fits than those with only D15 and F15 resonances.

Initially it was hoped to include all channels in a simultaneous fit. However, it was soon found that because the errors on the $\Delta\pi$ channel were large compared to those on the elastic, charge-exchange and polarization data that this channel had little influence on the fit. A better procedure was to fit the elastic channels alone. The parameters, α and β, which determine the relative amounts of amplitude in the inelastic channels, were unaffected by this fit. Then the delta-pi channels alone were fit with the resonance and background parameters fixed at the best fit to the elastic channels and only α and β free to vary. Finally, all data was included in a last step, with most of the parameters free to vary.

D. Results

Only preliminary results are available so far. An examination of them reveals some interesting features but also suggests some improvements that should be tried before one might have full confidence in the results.

The χ^2 for the fit to the elastic data was 1476 for 459 data points and 42 parameters. The parameters — θ, M, Γ, and δ_B for resonances and θ_1, θ_2, δ_1, δ_2 for backgrounds — were fixed at values from this fit. Then the $\Delta\pi$ data was fitted with only the parameters α and β free to vary. The χ^2 was 975 for 180 data points and 16 parameters but came down to 643 when normalization parameters were included. The normalization parameters were on the

order of 10% or less. The branching ratios into $\Delta\pi$ for DD5 and FP5 partial waves agree well with those of solution A (except for the sign) of the $\Delta\pi$ partial wave analysis discussed in Chapter VI. The parameter β is essentially zero for all waves, an indication that the effects of a fourth channel are negligible — α is fixed at $\pi/2$ for S11 and S31 partial waves because there is only one outgoing channel open to them. Table XIII lists the parameters of the best fit obtained in the initial experimentation with the program. The parameters give rise to the amplitudes displayed in the Argand diagrams of Fig. 46. The resonant waves — S11, D15, F15, and S31 — are compared here to the results of elastic phase-shift analyses. The predicted cross sections are compared to the data for several representative energies in Figs. 47 - 50.

The partial waves D15 and F15 agree nicely with the results of phase-shift analysis. The partial waves that show the largest deviation from expected behavior are the S31 and S11 resonances. The phase-shift solutions find the S11 to be a pure resonance centered at 1710 MeV and the S31 to be highly inelastic and to move clockwise on the Argand diagram (pure resonances move counter-clockwise) as energy increases. However, in the preliminary coupled-channel solutions, the S11 rather than the S31 had the large background. The background in the S11 wave makes it look like a pure resonance at a lower energy.

Thus the weakness of this fit is its inability to correctly describe the behavior of the backgrounds in the lower partial waves. However, it is a reasonably good fit to the data, except at lower energies, where the backgrounds do not have the right shape.

These discrepancies might be eliminated by judicial choice of initial parameters. In most fits the background phase angles δ_B were started at

TABLE XIII

Parameters from Coupled Channel Analysis

A. Resonances

L 2I 2J	θ (radians)	M (MeV)	Γ (MeV)	δ_B (radians)	α	β	x_{el}	$\frac{L=L'}{\sqrt{x_{el}x_{\Delta\pi}}}$	$\frac{L\neq L'}{\sqrt{x_{el}x_{\Delta\pi}}}$
S31	.706	1640	180	- .09	1.57	0	.58	0	.495
S11	.176	1710	300	.663	1.57	0	.97	0	.168
D15	.867	1682	116	0	- .318	0	.42	.466	-.153
F15	.622	1676	115	0	1.054	0	.66	.232	.410

B. Backgrounds

	θ_1	θ_2	δ_1	δ_2	α	β	Re(T)	Im(T)
P31	1.06	-.60	.13	.88	0	0	-.36	.27
P33	1.38	-.29	.17	.16	.57	0	-.06	.18
D33	1.41	-.29	.08	.09	1.0	0	-.03	.17
D35	-	-	-	-	-	-	-	-
F35	1.17	-.30	-.05	1.36	.99	0	-.13	.05
P11	1.17	-.29	-.04	- .05	0	0	.03	.37
P13	1.61	.06	.17	.16	.01	0	0	0
D13	1.38	-.45	.08	.03	.93	0	-.03	.33

C. Normalizations

i =	1	2	3	4	5	6	7	8	9
ϵ_i	1.14	1.08	1.15	1.16	1.06	1.03	1.01	1.04	1.01

$\chi^2 = 647$ for 180 data points (fit to $\Delta\pi$ channel)

$\chi^2 = 1476$ for 459 data points (fit to elastic channels)

1801843

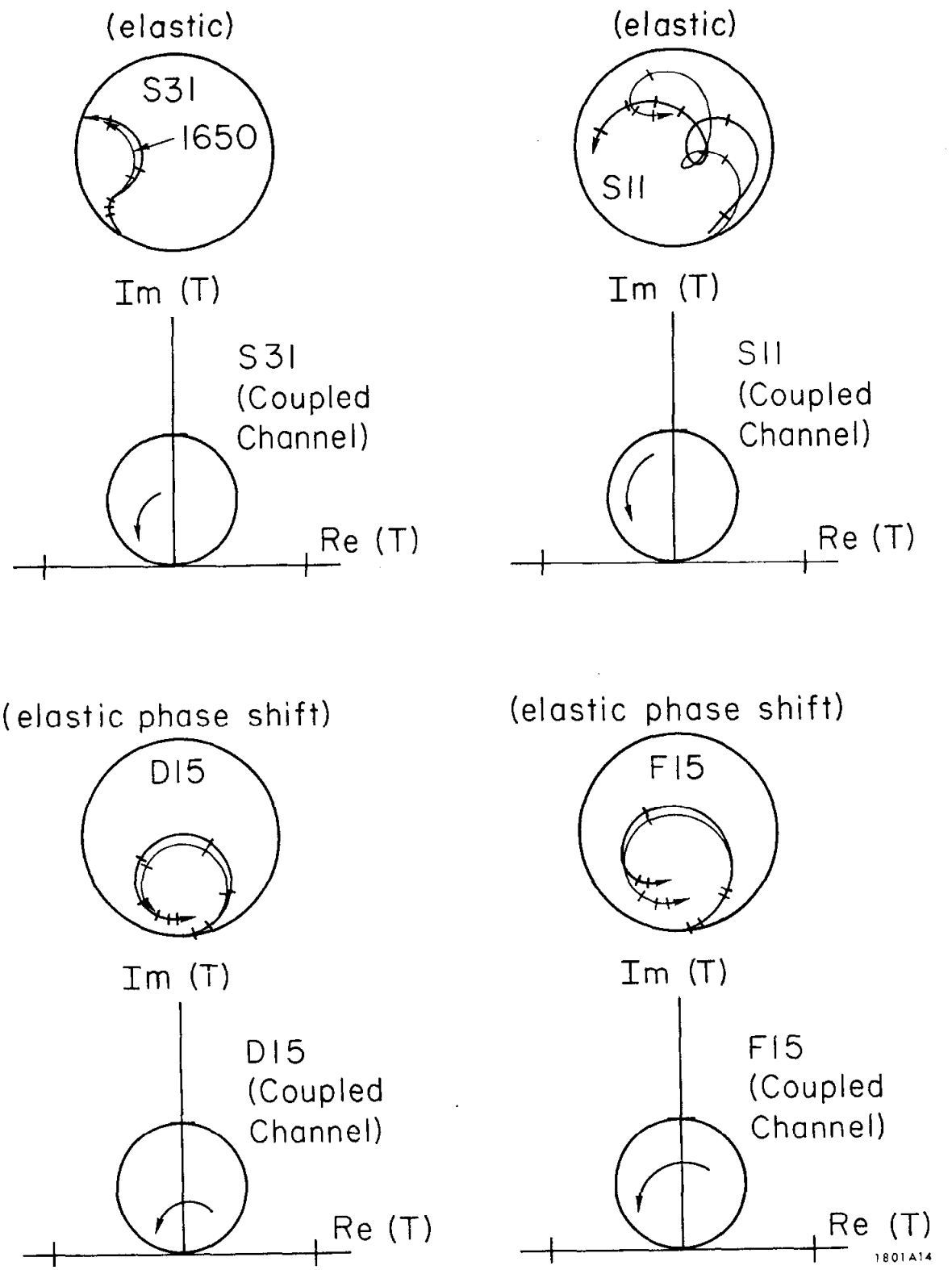

FIG. 46--Variation of the partial-wave amplitudes in a preliminary coupled-channel fit to the data of the present experiment. Resonant waves are compared to results of the Glasgow phase-shift analyses.

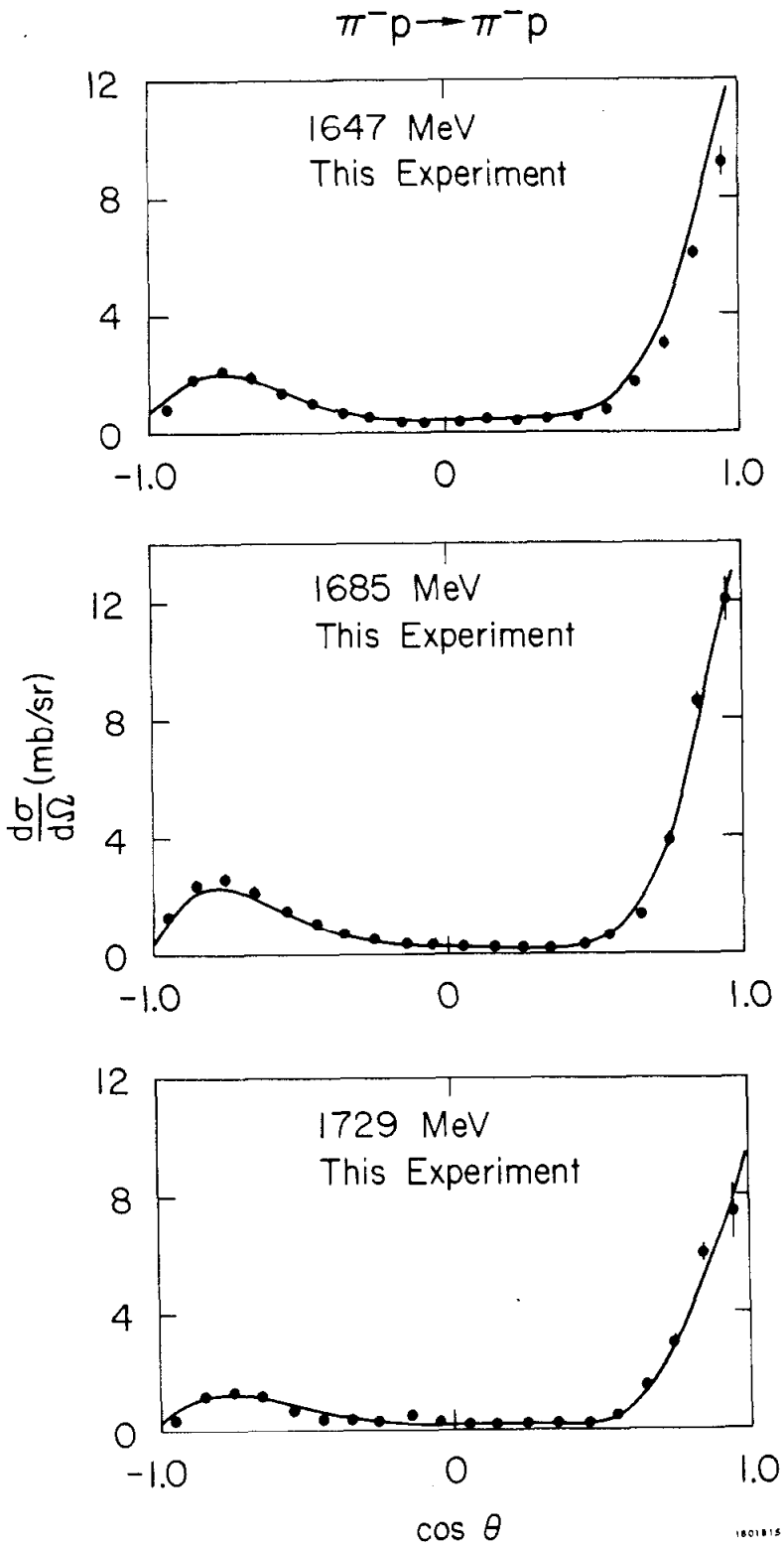

FIG. 47--The experimental elastic differential cross section compared to the predictions of a preliminary fit to the coupled-channel program.

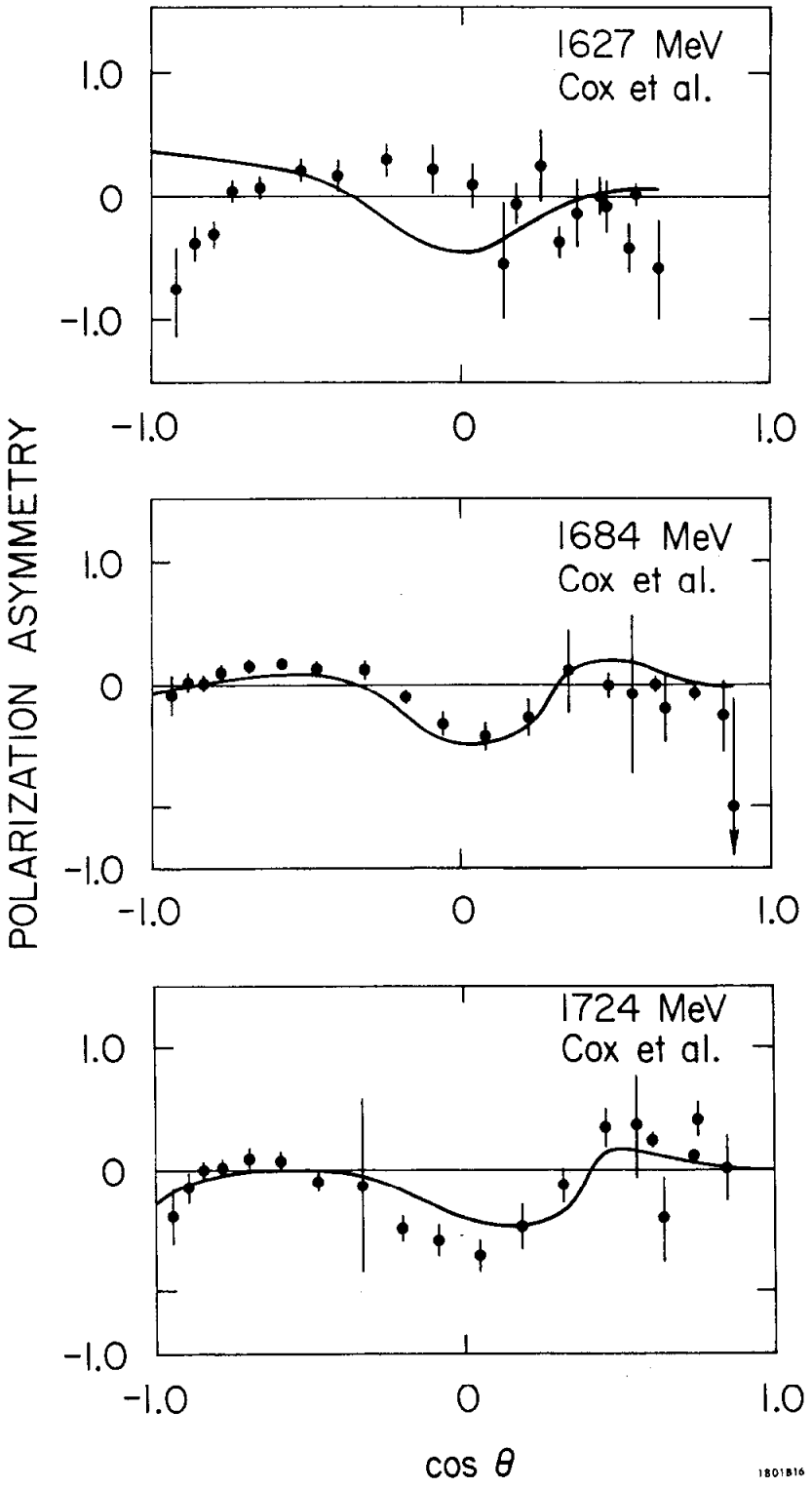

FIG. 48--The experimental polarization compared to the predictions of the coupled-channel program.

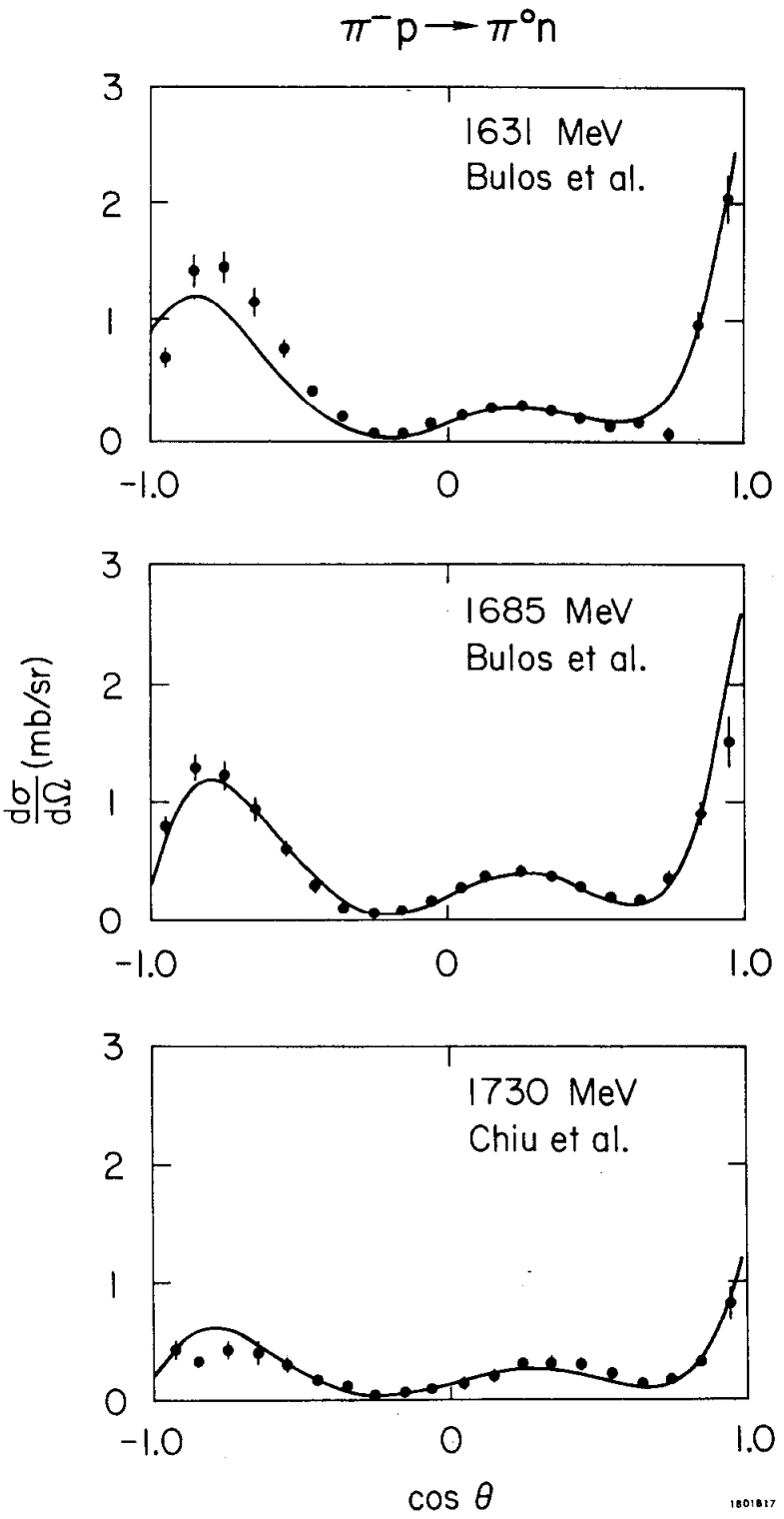

FIG. 49--The experimental charge-exchange differential cross section compared to the predictions of the coupled-channel program.

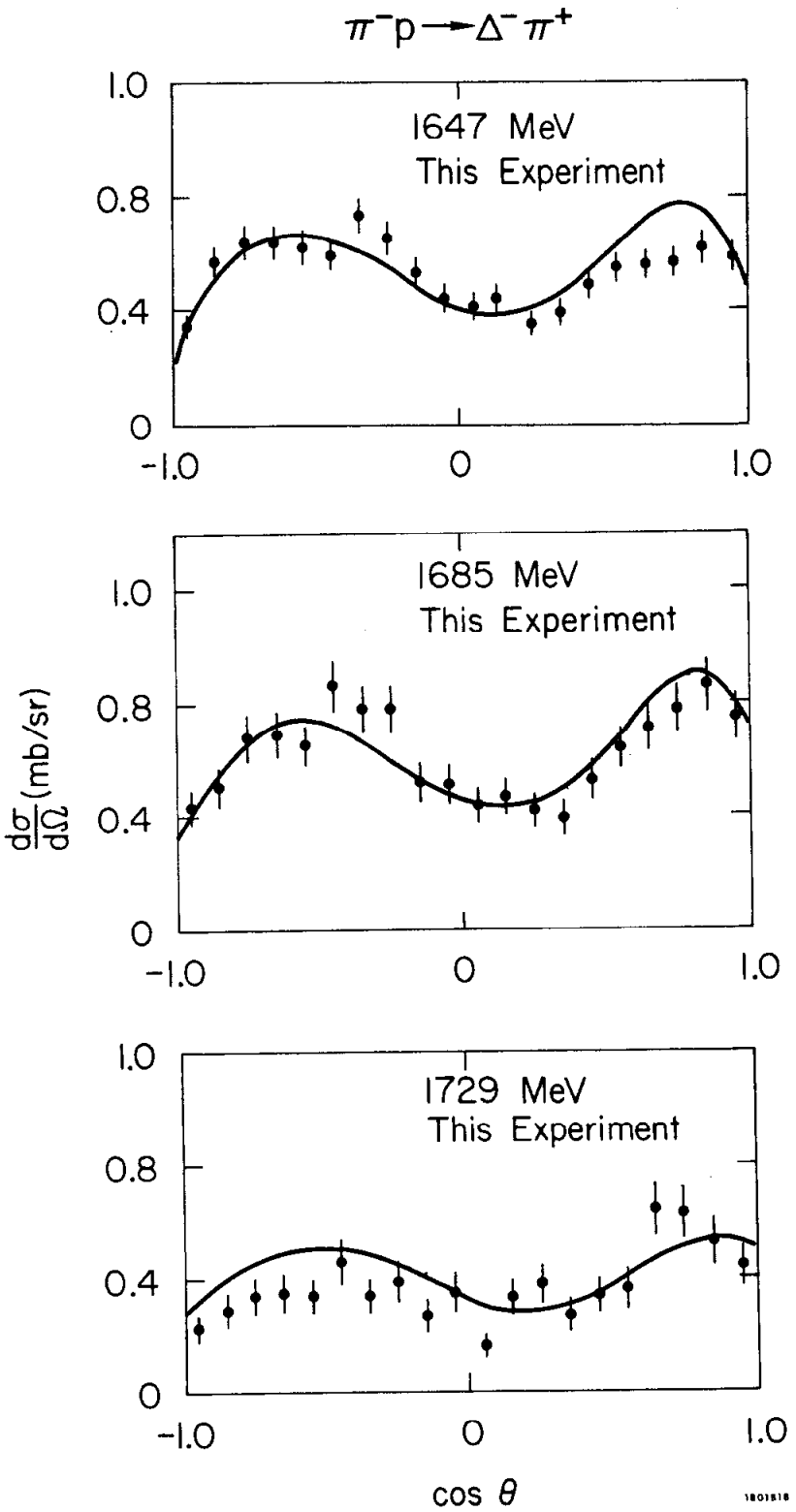

FIG. 50--The experimental $n\pi^+\pi^-$ differential cross section in the mass cut region $1140 \leq M(\pi^- n) \leq 1320$ MeV compared to the predictions of the coupled-channel program.

zero. However, more appropriate behavior for the S31 results only when the phase angle lies in a certain restricted angular region where the criterion of clockwise motion for the S31 is satisfied. This criterion can also be stated as a requirement that the imaginary part of the amplitude increase with energy when the real part is negative. For a resonance plus background the amplitude has the form

$$\mathrm{Re}(T) = \frac{\epsilon \cos 2\,\delta_B - \sin 2\,\delta_B}{1+\epsilon^2} + \frac{\mathrm{ctn}\,\delta_B}{\mathrm{ctn}^2\,\delta_B + 1} \tag{7.26a}$$

$$\mathrm{Im}(T) = \frac{\epsilon \sin 2\,\delta_B + \cos 2\,\delta_B}{1+\epsilon^2} + \frac{1}{\mathrm{ctn}^2\,\delta_B + 1} \tag{7.26b}$$

Over the energy region of the fit, ϵ goes from nearly 0 to approximately -1.3. Thus we must select an angle δ_B such that Im(T) at $\epsilon = 0$ is less than Im(T) at $\epsilon = -1$. This condition is satisfied if δ_B lies between 45° and 67°. If δ_B is in this range, the real part of the amplitude will automatically be negative. If this guide for an initial guess at δ_B for S31 is tried, it might lead to more reasonable behavior for both the S31 and the S11.

The backgrounds in this fit remain more constant than they really are. Apparently the energy dependence of the parameterization is too weak in the region of the starting values to produce much variation. To force a stronger energy dependence on the amplitudes the coefficients δ_2 and θ_2 of the momentum should be made as large as possible. Again a study of the form of the amplitudes may suggest the most appropriate region for these parameters. The background amplitudes are proportional to terms of the form:

$$\mathrm{Re}(T) \propto \frac{x}{1+x^2} \tag{7.27a}$$

and

$$\mathrm{Im}(T) \propto \frac{1}{1 + x^2} \tag{7.27b}$$

where

$$x = \tan(\delta_1 + q\,\delta_2) \quad .$$

These two functions are sketched in Fig. 51 where it is clear that the most rapid variation of the function occurs for $0 < x < 1$. We should select δ_1 and δ_2 so that $\tan(\delta_1 + q\,\delta_2)$ covers a large portion of this range as q goes from .87 to .96 (corresponding to the energy range 1640 to 1730 MeV). This condition is satisfied if δ_2 is around 3.0 and if δ_1 is approximately -2.3. This educated guess to the background parameters might help to adjust the parameters of the resonant waves.

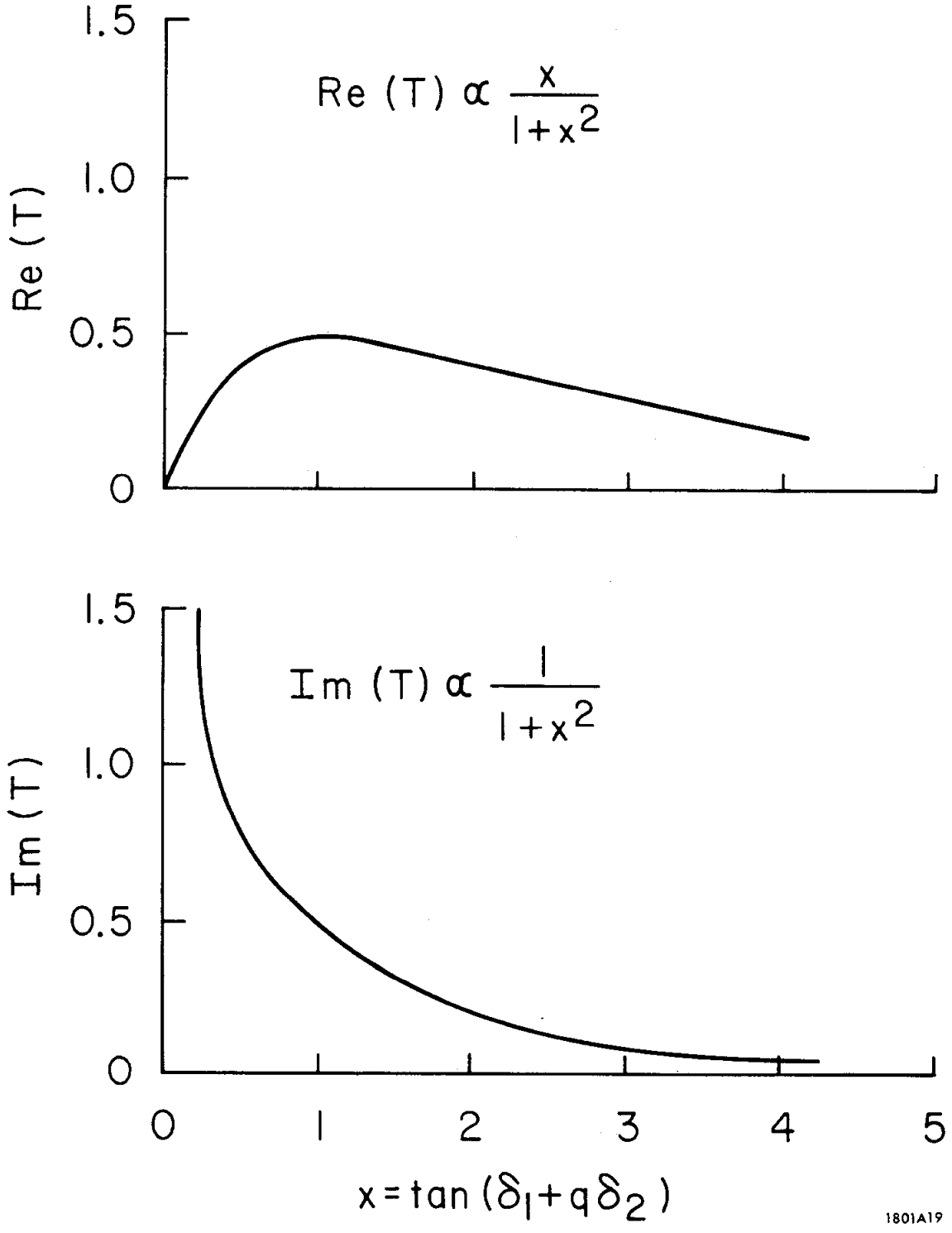

FIG. 51--Shape of real and imaginary parts of background parameterization of coupled-channel program.

VIII. STRANGE-PARTICLE CHANNELS

A. Introduction

In addition to the elastic πN and inelastic $N\pi\pi$ outgoing channels discussed so far, there are several strange-particle channels for πN scattering. In fact, the section of film exposed in the 72-inch HBC was originally exposed for the purpose of studying the following associated production resonances[47]:

$$\pi^- p \rightarrow \Lambda^o K^o \tag{8.1}$$

$$\rightarrow \Sigma^o_- K^o_+ \tag{8.2}$$

It seemed fruitful to complement these studies with measurements of the same reactions at the higher energies of the film taken in the 30-inch HBC at Argonne. Only the results of the $\Lambda^o K^o$ reaction will be presented in this thesis.

B. Data Processing

The scanners were instructed to look for all events of the following topologies:

a. zero prong, one vee

b. zero prong, two vee,

as illustrated in Fig. 52. To insure that none of the vees corresponded to an electron pair, the scanners rejected those vees where

1. the vertex had zero opening angle in all 3 views
2. the tracks were minimum ionizing and
3. the tracks were highly curved.

Furthermore, the scanners checked that the vee was truly associated with the zero-prong beam track.

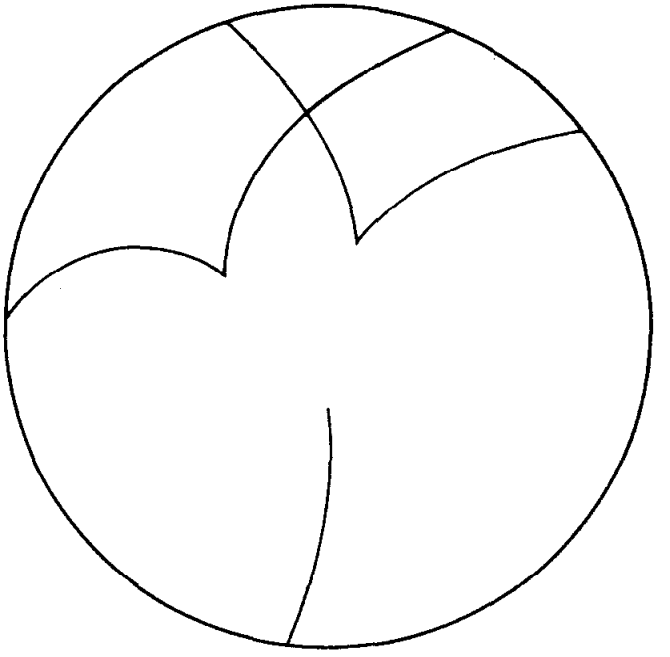

(a) Zero-prong, two-vee topology

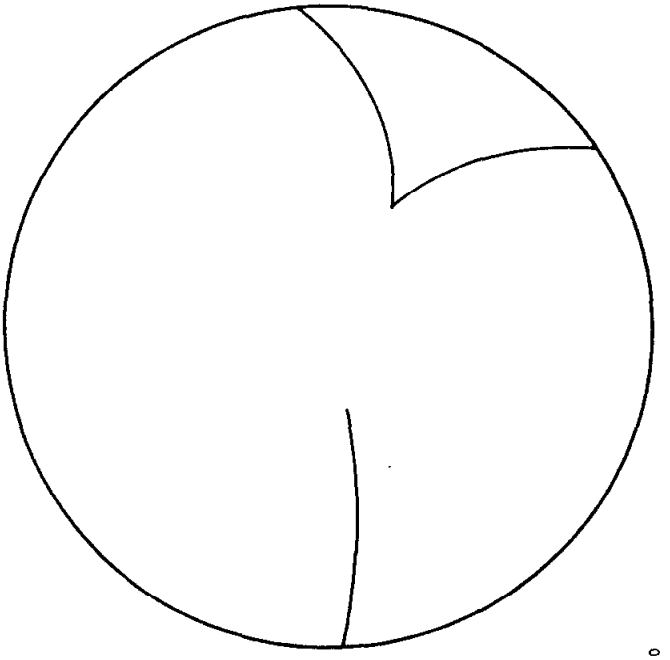

(b) Zero-prong, one-vee topology

1801A20

FIG. 52

Because some two-prong events can be confused with a zero-prong, one-vee event where the vee lies close to the end of the beam track, we applied a minimum cutoff on the length of the neutral tracks. The vertex had to lie at least 0.3 cm (on the scan table, corresponding to 0.8 cm in space) from the end of the beam track. Correction for this cutoff as well as for the maximum length cutoff caused by decays outside the chamber will be discussed later.

The original scan yielded 1343 events of topology (a) and 398 events of topology (b). The events were measured on the Vanguard measuring machines at SLAC, and then processed by the TVGP-SQUAW fitting programs. All of the events that failed in any portion of the fitting programs were remeasured. Those events that failed twice were examined on the scan table. Many were found to be wrong event types — electron pairs, two-prong events, unassociated vees, etc. Others were classified as unmeasurable because of faint tracks, gappy beam tracks, etc. The remaining events were measured for a third time. There was no evidence for any topological bias within this sample.

After remeasuring, the efficiency for passing events through the fitting programs was 95% for the one-vee events and 89% for the two-vee events.

C. Fitting Logic

The logic within the fitting program was a rather complex one; we were anxious not to lose events because statistics are already rather low for this reaction.

In the case of one-vee events, we first fit the vertex treating the neutral mass as an unknown but knowing its direction and assuming the charged tracks to be a π^+ and a π^-. If the mass determined by this fit fell within 25 MeV of the K^0 mass, we went on to fit the entire event to the

reactions

$$\pi^- p \rightarrow \Lambda^o K^o , \qquad K^o \rightarrow \pi^+ \pi^- \tag{8.3a}$$

$$\pi^- p \rightarrow mmK^o , \qquad K^o \rightarrow \pi^+ \pi^- \tag{8.3b}$$

We repeated the same procedure, assuming the charged tracks to be a proton and a π^-. If the mass determined by this fit lay within 15 MeV of the Λ^o mass, we tried to fit the event to the hypotheses

$$\pi^- p \rightarrow \Lambda^o K^o , \qquad \Lambda^o \rightarrow p\pi^- \tag{8.4a}$$

$$\pi^- p \rightarrow \Lambda^o mm, \qquad \Lambda^o \rightarrow p\pi^- \tag{8.4b}$$

If an event fit both (8.3a) and (8.4a), the program predicted the values of ionization for the outgoing tracks from the neutral decay corresponding to the two hypotheses. The ionizations were examined on the scan table, where the difference in ionization between the π^+ and p tracks afforded definite resolution of the ambiguities. There appeared to be no topological bias involved in this sample of ambiguous events.

In the case of two-vee events we still tried to fit each vertex alone in order to identify the neutral particle corresponding to the decays. If an event fit only one vertex satisfactorily it was then treated as a one-vee event. All other events were then fit to the following hypotheses:

$$\pi^- p \rightarrow \Lambda^o K^o , \qquad \left.\begin{array}{l} K^o \rightarrow \pi^+ \pi^- \\ \Lambda^o \rightarrow p\pi^- \end{array}\right\} \tag{8.5a}$$

$$\pi^- p \rightarrow \Sigma^o K^o , \qquad \left.\begin{array}{l} K^o \rightarrow \pi^+ \pi^- \\ \Sigma^o \rightarrow \Lambda^o \gamma, \quad \Lambda^o \rightarrow p\pi^- \end{array}\right\} \tag{8.5b}$$

$$\pi^- p \rightarrow \Lambda^o K^o mm , \qquad \left.\begin{array}{l} K^o \rightarrow \pi^+ \pi^- \\ \Lambda^o \rightarrow p\pi^- \end{array}\right\} \tag{8.5c}$$

$$\pi^- p \rightarrow \Lambda^o mm \ , \qquad \Lambda^o \rightarrow p\pi^- \tag{8.5d}$$

$$\pi^- p \rightarrow K^o mm \ , \qquad K^o \rightarrow \pi^+ \pi^- \tag{8.5e}$$

D. Resolution of Ambiguities

If a two-vee event fit both the $\Lambda^o K^o$ and $\Sigma^o K^o$ hypotheses we accepted it as a true $\Lambda^o K^o$ event. The $\Lambda^o K^o$ hypothesis is a four-constraint fit and it is unlikely that a true $\Sigma^o K^o$ event can be fit with this hypothesis. On the other hand a true $\Lambda^o K^o$ event can be readily fit to the one-constraint $\Sigma^o K^o$ hypothesis because the program is free to adjust the momentum and direction of the gamma ray. The gamma ray from such a forced fit will lie nearly parallel to the direction of the sigma whereas it would normally be distributed isotropically about the direction of the sigma. The angular distribution of the gamma ray thus provides a convenient test for the resolution of $\Lambda^o K^o - \Sigma^o K^o$ ambiguities.

We can define θ^γ as the angle that the gamma makes with the y-axis in the rest frame of the sigma.

$$\cos \theta^\gamma = \vec{p}_\gamma \cdot \hat{y} / |\vec{p}_\gamma| \tag{8.6}$$

where

$$\hat{y} = \vec{p}_\Sigma \times \vec{p}_\pi / |\vec{p}_\Sigma \times \vec{p}_\pi|$$

and $\vec{p}_\pi$ and $\vec{p}_\Sigma$ are the laboratory momenta of the pion beam and the neutral sigma, respectively. In Fig. 53a we plot the distribution of this angle for events that fit the $\Sigma^o K^o$ hypothesis unambiguously. It is isotropic as expected. In Figs. 53b and 53c we plot the distribution for ambiguous events that have lower and higher confidence level, respectively, for the fit to the $\Sigma^o K^o$ hypothesis. Both distributions are strongly peaked at $\cos \theta^\gamma = 0$, which corresponds to a gamma ray lying parallel to the sigma. It appears that these events, regardless of confidence level, are true $\Lambda^o K^o$ reactions. Our assignment of all these ambiguous fits to $\Lambda^o K^o$ is well justified.

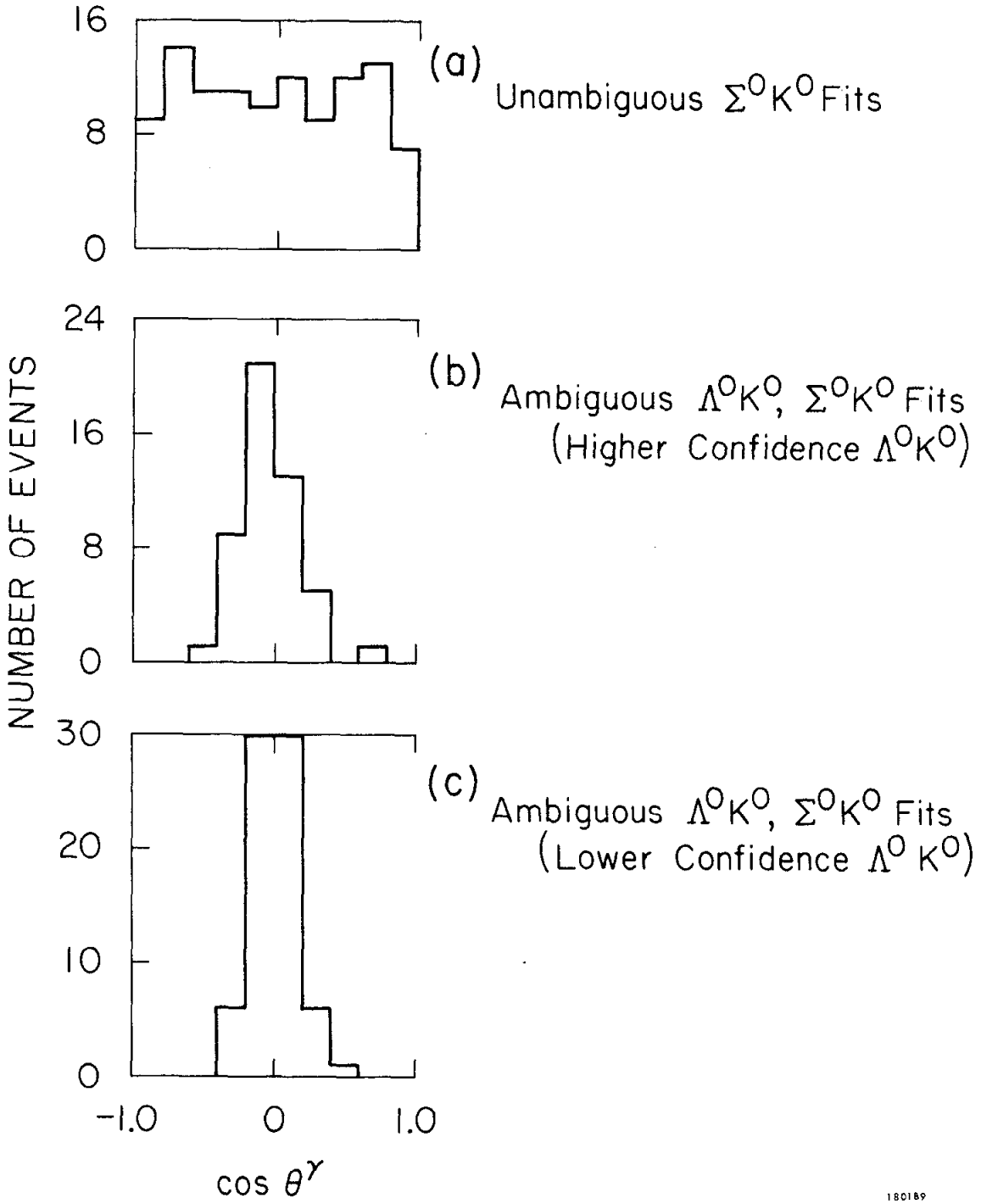

FIG. 53--Angle of gamma ray in rest frame of sigma in the reaction $\pi^- p \rightarrow \Sigma^0 K^0$.

Events that were ambiguous between the four-constraint Λ^0K^0 and one-constraint Λ^0K^0mm hypotheses were also assigned to be Λ^0K^0 reactions. To show that this selection introduces no contamination we plot in Fig. 54 the missing mass from fit (8.5c) for $\Lambda^0K^0 - \Lambda^0K^0$mm ambiguities. The peak lies near zero with the slight pull to the negative characteristic of plots of this sort, as we observed in Chapter II, Section E.

The separation of Λ^0K^0 and Σ^0K^0 events is more difficult in the samples of single-vee events. A guide for the selection is the plot of missing mass recoiling against the Λ^0 as determined from fit (8.5d) for two-vee events that have been unambiguously identified as Λ^0K^0 events. As seen in Fig. 55a the distribution is clearly peaked at the value of K^0 mass. A similar plot for unambiguous Σ^0K^0 events, shown in Fig. 55b, has a broad, flat distribution starting at approximately 525 MeV. It appears that the Λ^0K^0 reactions can be separated fairly cleanly by making a mass cut of

$$440 \leq \text{mm} \leq 530 \text{ MeV} \tag{8.7}$$

on the fit to reaction (8.4b) for events where only the Λ^0 is seen. The distribution for missing mass in this reaction is displayed in Fig. 55c for one-vee events. The cut appears to have been made low enough on the upper end to avoid contamination from Σ^0K^0 events.

A similar selection procedure was followed for events in which only the K^0 decay is seen. Here we clearly see the peak in two-vee Λ^0K^0 events (in Fig. 56b) corresponding to the Λ^0 and the peak in two-vee Σ^0K^0 (Fig. 56a) events corresponding to the Σ^0. The two peaks are clearly resolved and a cut on missing mass for one-vee events of

$$1060 \leq \text{mm} \leq 1155 \text{ MeV} \tag{8.8}$$

should give a clean sample of Λ^0K^0 events, as shown in Fig. 56c.

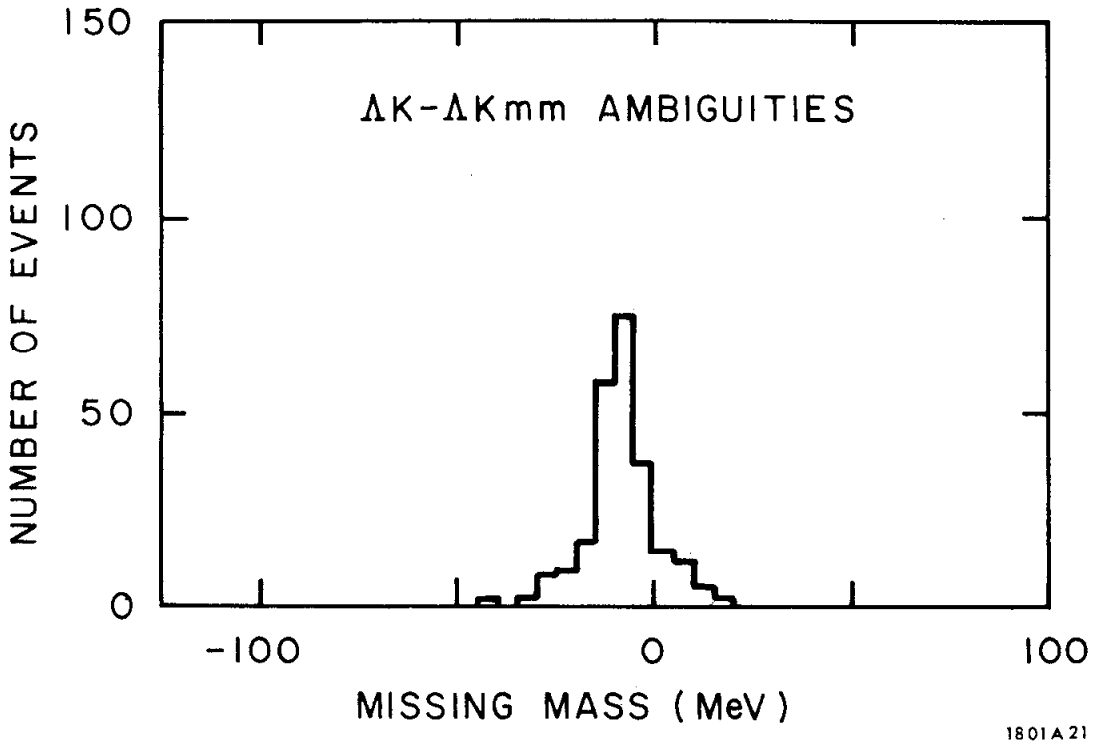

FIG. 54--Missing mass in the reaction $\pi^- p \rightarrow \Lambda^o K^o$mm for all two-vee events that fit the hypothesis $\pi^- p \rightarrow \Lambda^o K^o$.

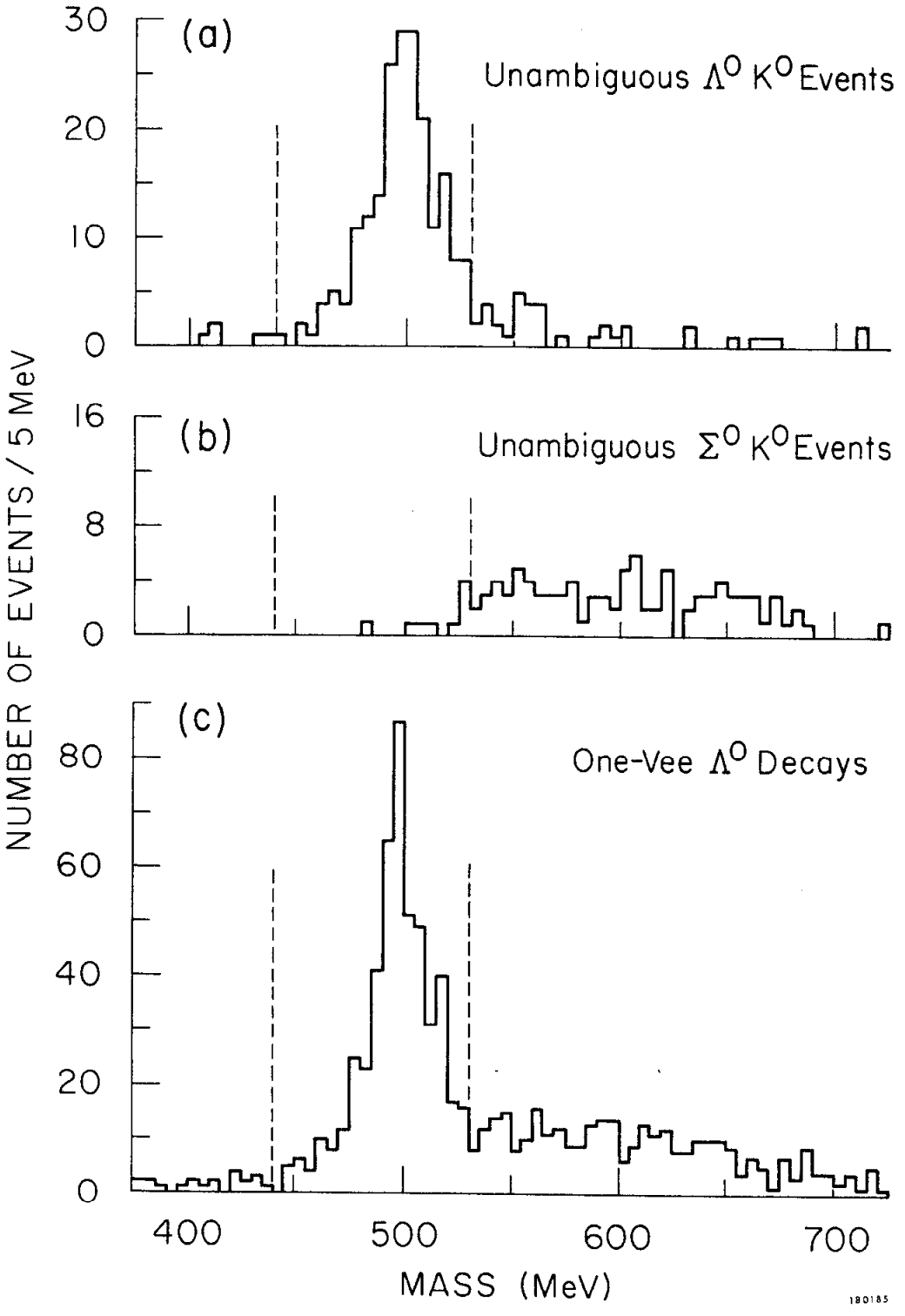

FIG. 55--Missing mass in the reaction $\pi^- p \rightarrow \Lambda^0 mm$. (a) For two-vee $\Lambda^0 K^0$ events. (b) For two-vee $\Sigma^0 K^0$ events. (c) For all one-vee events. The dotted lines indicate mass cuts used to select $\Lambda^0 K^0$ events.

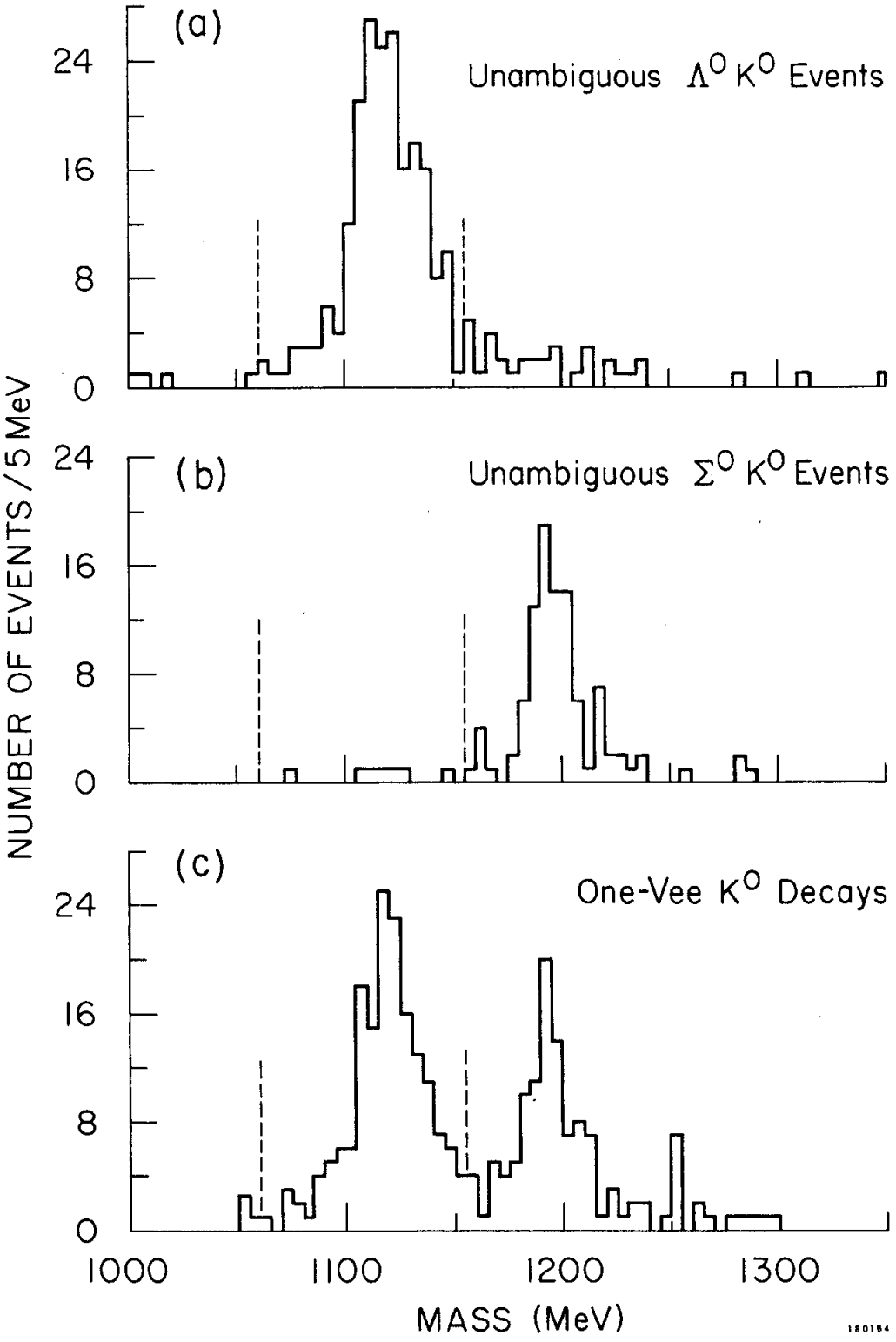

FIG. 56--Missing mass in the reaction $\pi^- p \rightarrow K^0 mm$. (a) For two-vee $\Lambda^0 K^0$ events. (b) For two-vee $\Sigma^0 K^0$ events. (c) For all one-vee events. The dotted lines indicate mass cuts used to select $\Lambda^0 K^0$ events.

The pull distributions for the three topologies (one-vee Λ^o decays, one-vee K^o decays and two-vee decays) are shown in Fig. 57 and the χ^2 distributions are shown in Fig. 58. The broad distributions in χ^2 indicate that the errors were underestimated, perhaps by 60%. In calculating $\Lambda^o K^o$ cross sections and angular distributions we used only those two-vee events with χ^2 less than 15 and only those one-vee events with χ^2 less than 8.

The resulting sample of $\Lambda^o K^o$ events with χ^2 cutoff applied contained 155 events where the K^o was seen, 471 events where the Λ^o was seen and 217 events where both the Λ^o and K^o were seen. After correcting for the differences in measuring efficiencies we find that the events lie in the ratio .179/.546/.274, compared to the theoretical ratio of .143/.570/.286 (or 1/4/2).

E. Corrections for Biases

1. Decay Time

The events had to be corrected for events lost because the neutrals decayed before reaching the minimum length of the scanning criterion or after they left the chamber. The probability that a particle decays in a time t is given by

$$1 - e^{-t/\tau}, \qquad \tau = \text{half-life of the particle} \tag{8.9}$$

In terms of the distance travelled ℓ and the particle velocity v, this expression becomes

$$1 - e^{-\ell/\beta\gamma c\tau} \qquad \begin{aligned} &\beta = v/c \\ &\gamma = (1-\beta^2)^{-1/2} \\ &c = \text{speed of light} \end{aligned} \tag{8.10}$$

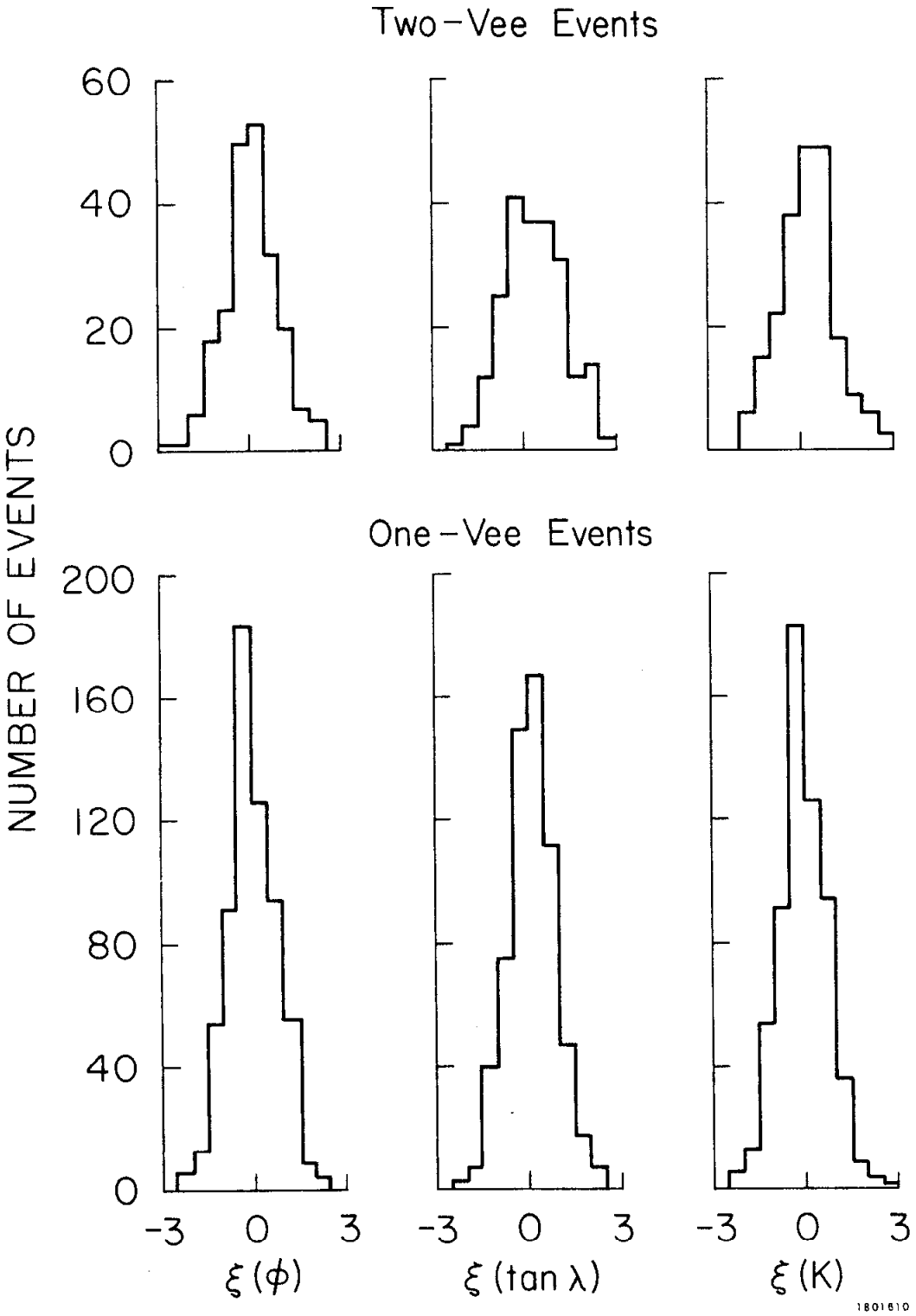

FIG. 57--Pull distributions for the fits to $\pi^- p \rightarrow \Lambda^0 K^0$ for topologies with two vees, one vee (lambda seen) and one vee (K seen).

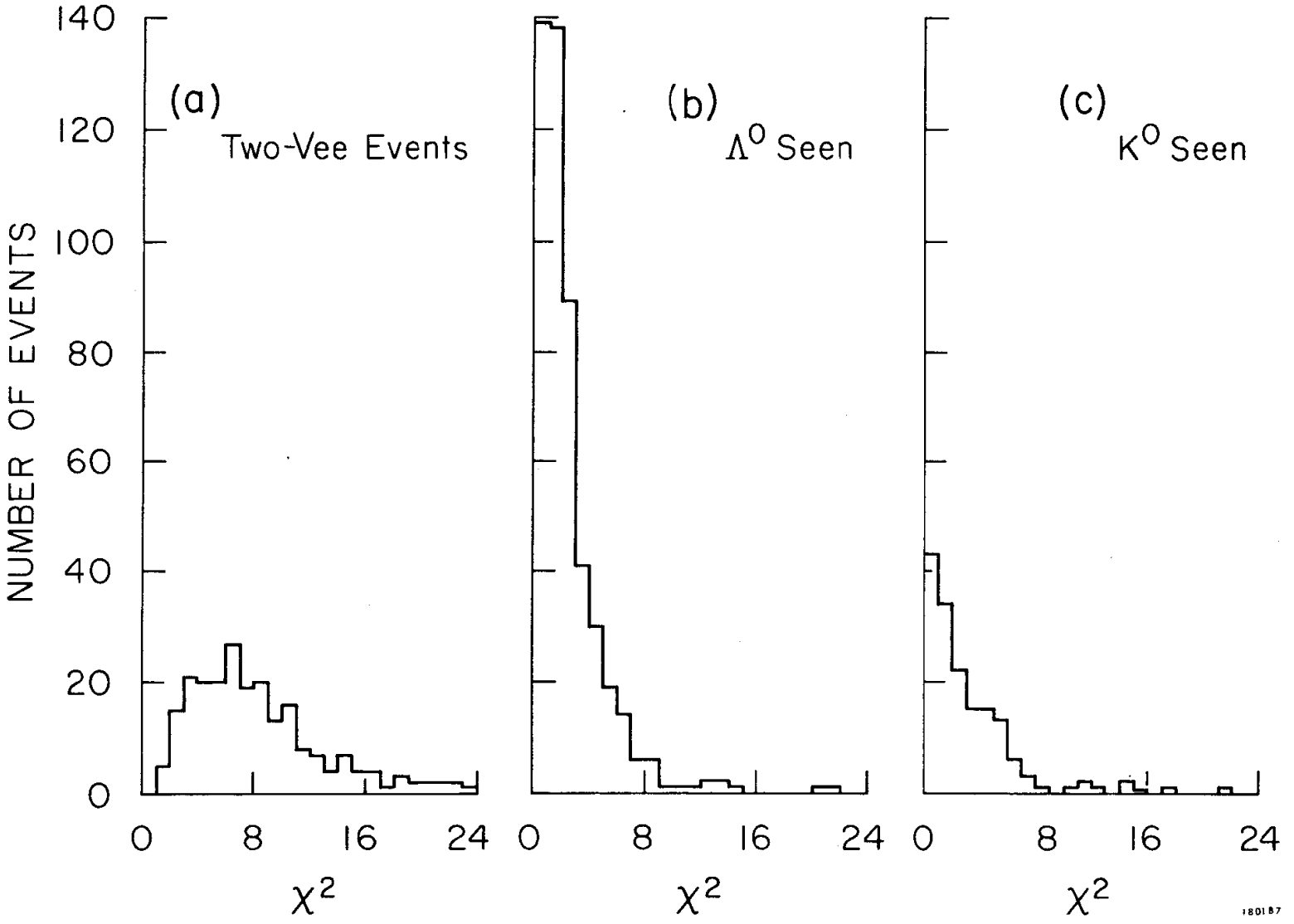

FIG. 58--Chisquared distribution for fits to the reaction $\pi^- p \rightarrow \Lambda^0 K^0$ for the three topologies.

and τ is 0.862×10^{-10} sec for the K^o and 2.51×10^{-10} sec for the Λ^o. Each event is weighted by the probability that the neutral particle does not decay before the minimum length $\ell_{min} = 0.8$ cm and the probability that it does decay before the maximum length $\ell_{max} = 30$ cm. The weighting factor was

$$W = \frac{1}{e^{-\ell_{min}/\beta\gamma c\tau} - e^{-\ell_{max}/\beta\gamma c\tau}} \tag{8.11}$$

Logarithmic plots of the number of events (weighted) vs. $\ell/\beta\gamma$ are shown in Figs. 59 and 60. The theoretical slopes are superimposed for comparison.

2. Scanning Bias

There are two possible sources of scanning bias in the one-vee and two-vee topologies. One is a loss of events where the outgoing tracks from a neutral decay lie in a plane that is nearly parallel to the camera axis; this bias is most severe when the tracks are steeply dipping. A second is a loss of so-called "hockey-stick" vees, in which the proton from a lambda decay has a very short range.

To search for evidence of bias of the first type, it is convenient to study the angular distribution of an angle that should be independent of reaction dynamics and hence isotropic. In two-prong elastic events, such an angle was the azimuthal angle. In the present case, however, it is more difficult to find an appropriate angle.

Parity arguments imply that the lambda cannot be polarized within the production plane. Let us work in the helicity frame of the lambda, where the z-axis lies along the Λ^o line of flight and the y-axis lies in the direction of the normal to the production plane. If we write the angular distribution for the decay proton in terms of an incoherent sum of Λ^o helicity states, the

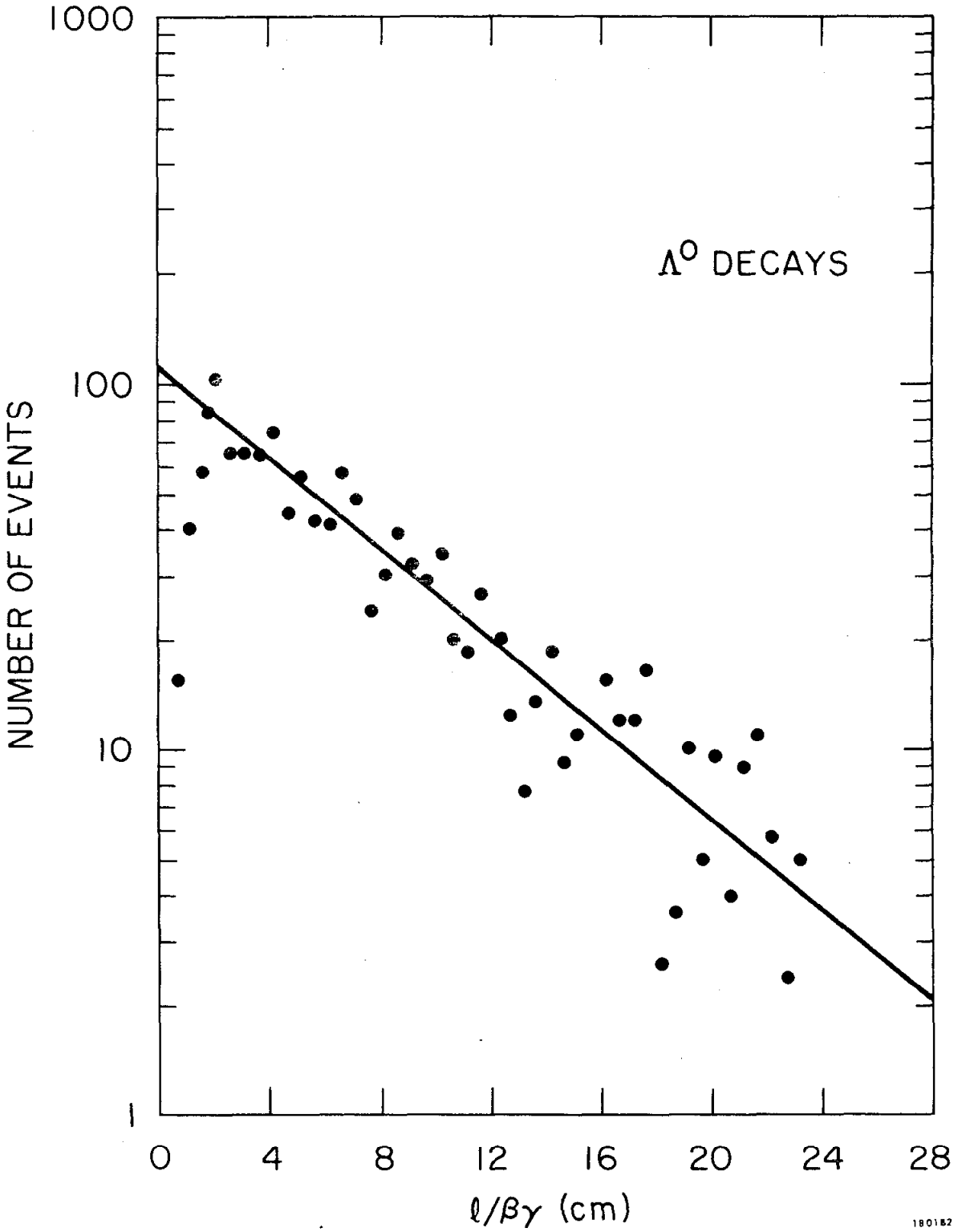

FIG. 59--Lifetime curve for Λ^0 decay. The abscissa is the lifetime of the particle observed divided by the speed of light, or length of track ℓ divided by $\beta\gamma$. Straight line represents slope based on accepted half life of 2.51×10^{-10} sec.

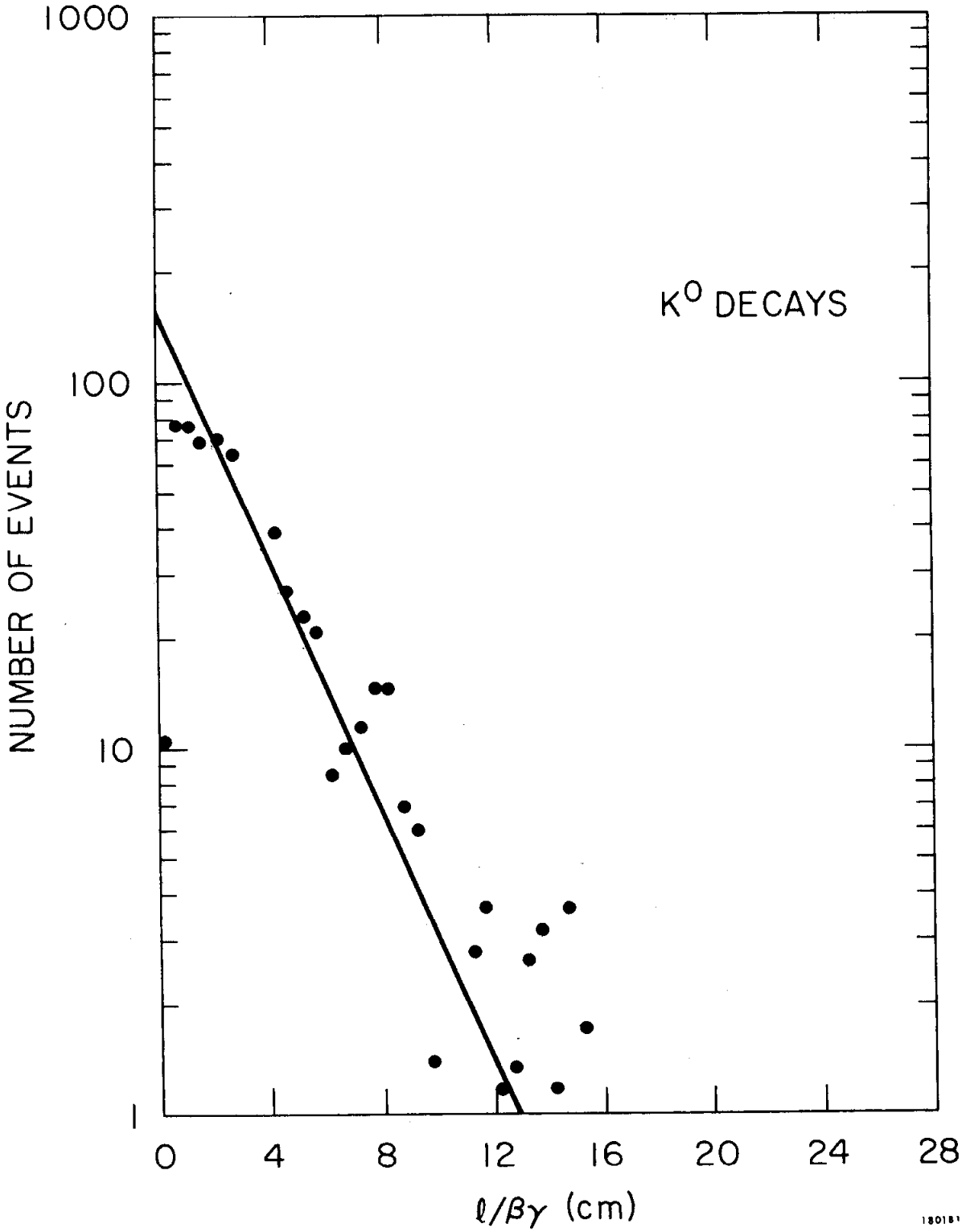

FIG. 60--Lifetime curve for K^0 decay. The abscissa is the lifetime of the particle observed or the length of the track ℓ divided by $\beta\gamma$. Straight line is based on accepted K^0 half life of 0.862×10^{-10} sec.

distribution will be isotropic. However, if the lambda is polarized, then we get a term proportional to sin θ sin ϕ, where θ and ϕ are the spherical coordinates of the decay proton in this frame. Nevertheless, when averaged over all angles ϕ, the distribution should be isotropic as a function of θ. We examined histograms of cos θ for different regions of lambda production angle and found the distributions to be isotropic, with no evidence of bias.

To search for a bias caused by hockey sticks we plotted a scatter diagram of the angle that the proton makes with the lambda (θ as defined above) against the lambda laboratory momentum. Because the proton scattered backwards should have the shortest range, we expect a depletion of events in this plot at cos = -1, especially at low values of lambda momentum. No strong bias was observed.

F. Results

1. Total Cross Section

The Λ^0K^0 cross sections were normalized to the elastic data in the same way that the inelastic two-prong data was normalized. The efficiency for passing events through the fitting routines is on the same order for the Λ^0K^0 reaction as for the elastic events so the procedure should still be valid. The total cross section based on weighted events is shown in Fig. 61 and listed in Table XIV. The new data appear shifted in energy with respect to the cross sections from the 72-inch chamber.[47] They do agree in general with other measurements and fill a gap in the existing data[48-59] as shown in Fig. 62.

The most striking feature of the cross section is the sharp rise from threshold at 1613 MeV to a peak near 1700 MeV. At first glance it is tempting to associate this peak with the D15 and F15 N* resonances seen in elastic scattering. However, the angular momentum barrier factor is too high for

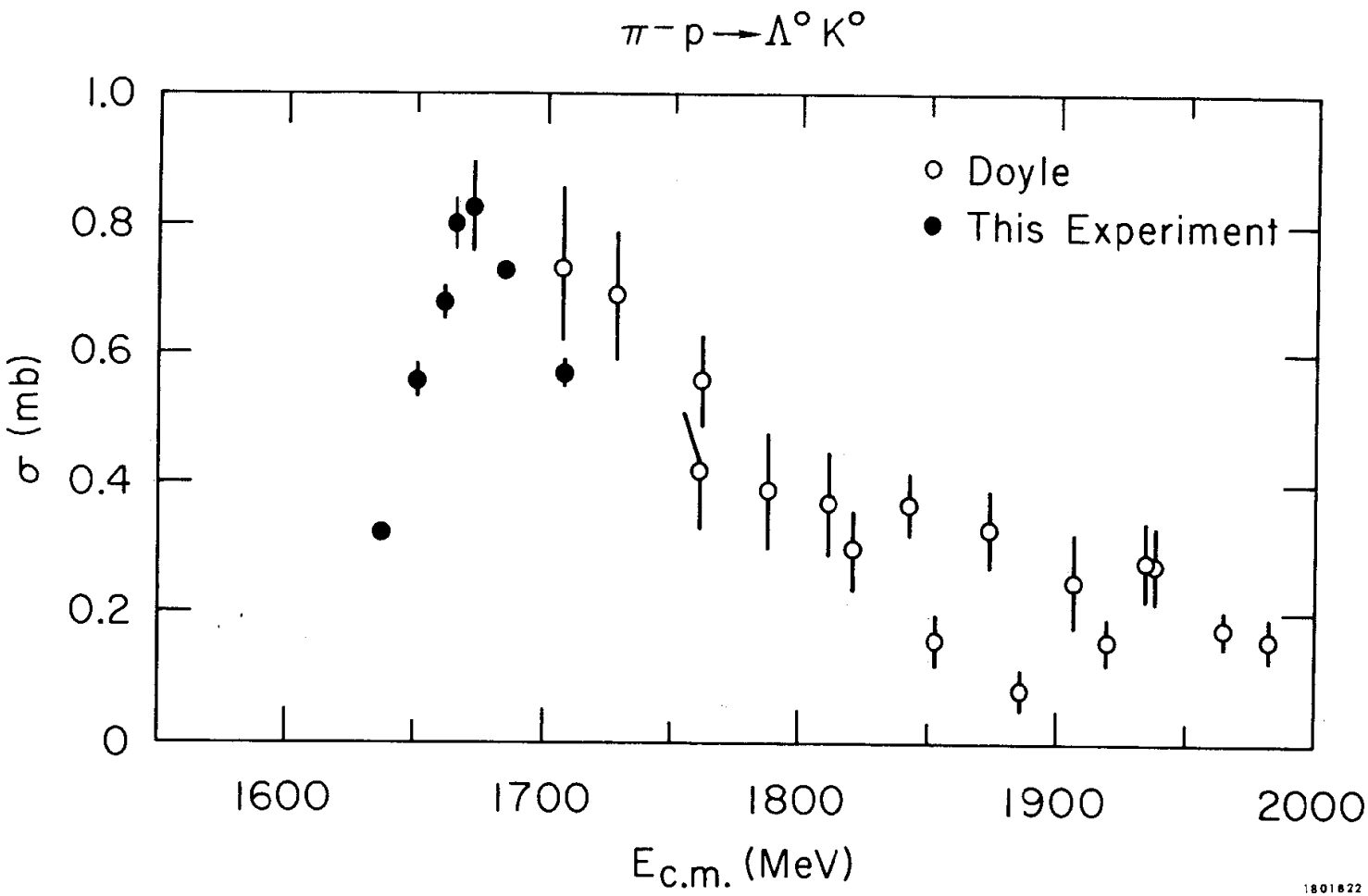

FIG. 61--Total $\Lambda^o K^o$ cross section measured in the present experiment compared to that measured by Doyle.[47a]

TABLE XIV

$\Lambda^{o}K^{o}$ Cross Sections

Energy (MeV)	Number of Weighted Events	Cross Section (mb)
1709	39.55	.765 ± .144
1720	6.75	Statistics too low
1730	78.06	.685 ± .098
1761	37.58	.418 ± .094
1762	88.81	.563 ± .071
1787	36.63	.394 ± .085
1806	12.99	Statistics too low
1811	39.87	.366 ± .083
1821	39.73	.300 ± .065
1843	79.56	.370 ± .053
1853	28.98	.164 ± .039
1872	78.53	.331 ± .056
1885	23.30	.075 ± .030
1904	66.21	.251 ± .067
1916	56.40	.156 ± .037
1932	51.53	.279 ± .058
1935	42.14	.276 ± .058
1963	69.05	.175 ± .027
1980	70.19	.158 ± .026

1801A33

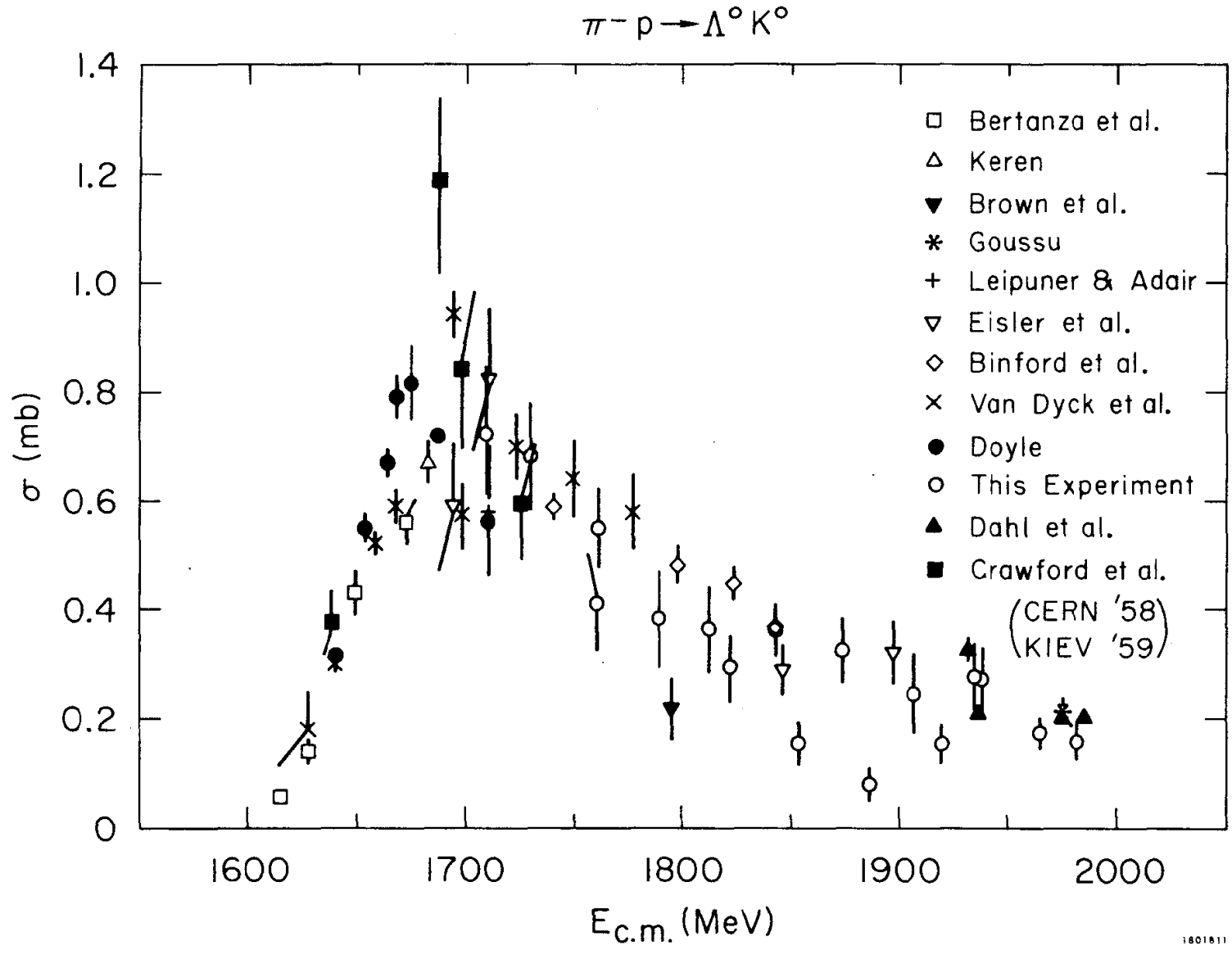

FIG. 62--Total $\Lambda^0 K^0$ cross section measured in the present experiment compared to that from all other experiments.[47-59]

these resonances to play a large role so close to threshold. More likely candidates are the resonances with lower angular momentum. Because the peak also coincides with the opening of the $\Sigma^0 K^0$ channel, one might further expect this channel to influence the $\Lambda^0 K^0$ reaction at this energy.

2. Differential Cross Section

Because the statistics at each one of the 19 energies are fairly low, neighboring energy regions were grouped into eight regions for the purpose of studying the angular distributions. These groupings are listed in Table XV. They have an average spread of about 30 MeV and contain around 100 events each. The angular distributions change very slowly in the energy region from 1700 to 2000 MeV so it is unlikely that this procedure will obscure any real structure. The central energy value in each region was found by cutting the regions at the bounds indicated in Table XV and calculating the central value of events within this cut region.

In Fig. 63 we display the differential cross sections for these eight energy regions. The distribution is strongly peaked in the region of backward scattered lambdas. The distributions were fit with a Legendre polynomial expansion of the form

$$d\sigma/d\Omega = \Sigma_n A_n P_n \left(\cos \theta^{\Lambda^0}_{cm}\right) \tag{8.12}$$

For most energies a fit to order $n = 4$ is sufficient. The ratios of Legendre coefficients A_n/A_0 are plotted in Fig. 64 and listed in Table XVI. For comparison the data of other experiments[47-52] was also fit to the Legendre polynomial expansion and the resulting coefficients are also plotted in Fig. 64.

Note that the kinematic formalism for $\pi^- p \rightarrow \Lambda^0 K^0$ is the same as that for $\pi^- p \rightarrow \pi^- p$; in both cases the final state consists of a 0^- meson and $1/2^+$ baryon.

TABLE XV

Combined Energy Regions - $\Lambda^{o}K^{o}$ Reactions

Region	Energy (MeV)	Energy Cuts (MeV)	Central Energy Value ± rms Deviation (MeV)	Number of Events (Weighted)
1	1709	1700 - 1740	1721 ± 12	124
	1720			
	1730			
2	1761	1740 - 1780	1763 ± 9	126
	1762			
3	1787	1780 - 1830	1806 ± 15	129
	1806			
	1811			
	1821			
4	1843	1830 - 1860	1845 ± 11	108
	1853			
5	1873	1860 - 1890	1874 ± 9	102
	1885			
6	1904	1890 - 1920	1908 ± 10	123
	1916			
7	1932	1920 - 1950	1936 ± 10	94
	1935			
8	1963	1950 - 1990	1971 ± 12	139
	1980			

1801A41

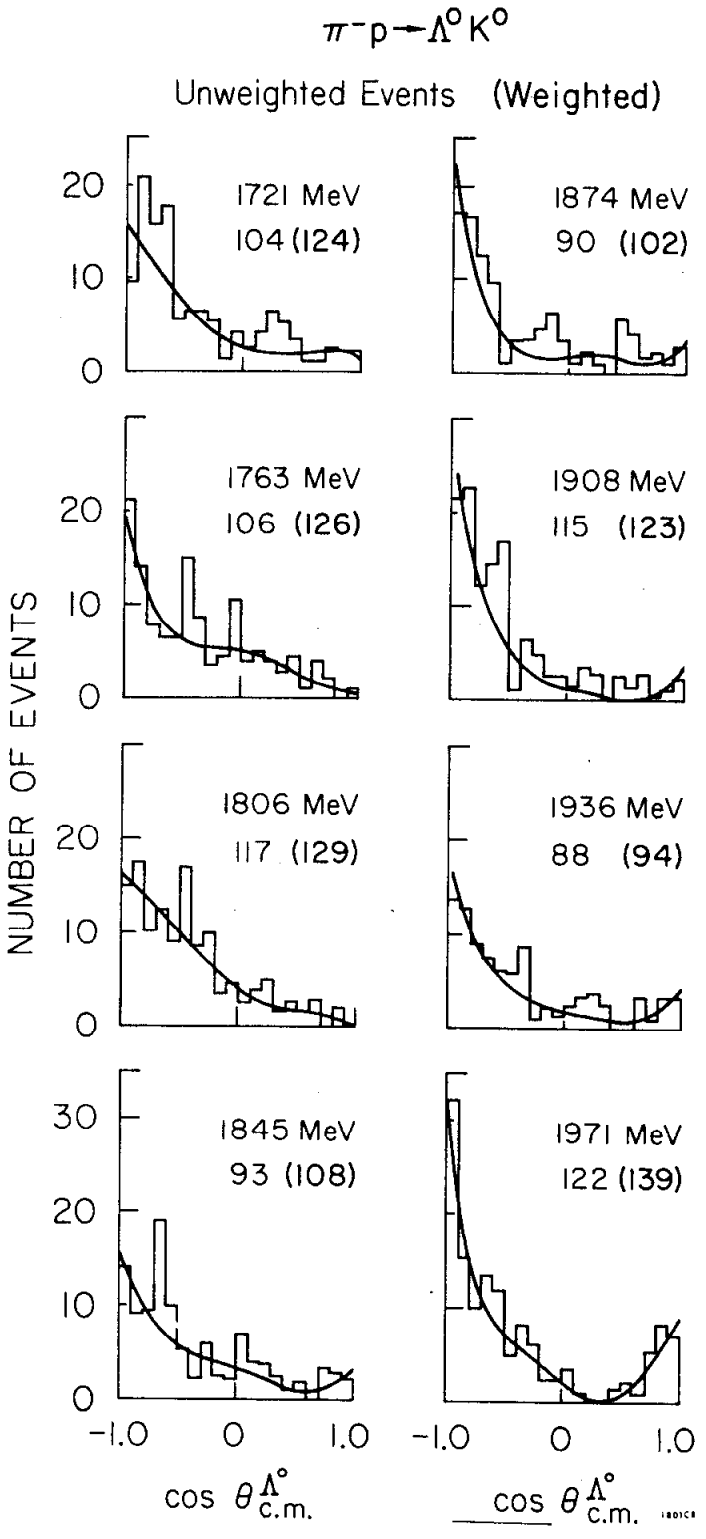

FIG. 63--Differential $\Lambda^0 K^0$ cross section. The smooth line represents the best fit by an expansion in Legendre polynomials.

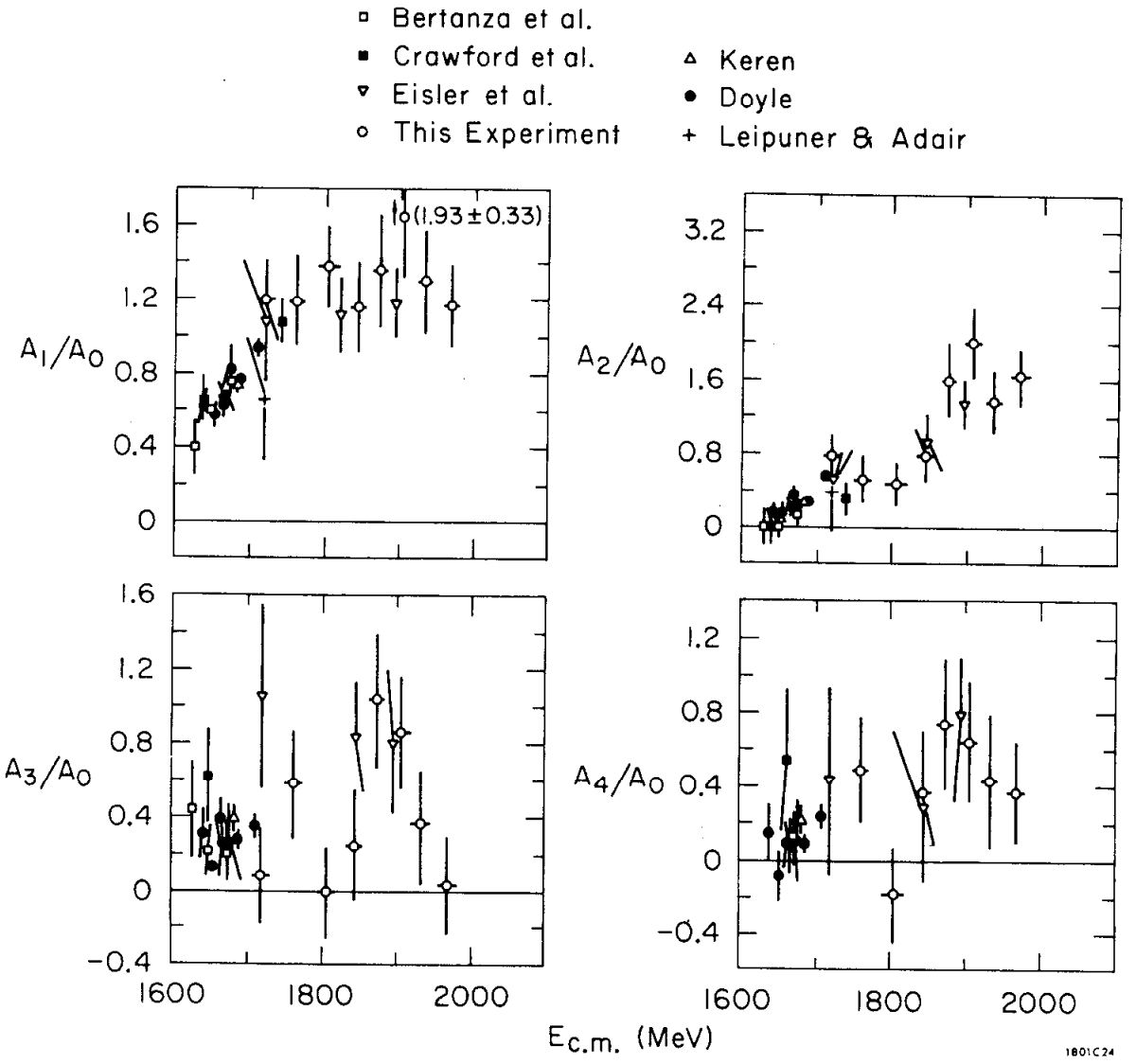

FIG. 64--Legendre polynomial coefficients A_n/A_0 measured in this experiment and others as a function of energy.

TABLE XVI

Legendre Polynomial Coefficients for Fits to Angular Distribution of the Reaction $\pi^- p \rightarrow \Lambda^0 K^0$

Energy (MeV)	A_1/A_0	A_2/A_0	A_3/A_0	A_4/A_0	Confidence Level (%)
1721	1.20 ± .22	.78 ± .22	.09 ± .25	- .65 ± .30	54
1763	1.19 ± .22	.53 ± .25	.58 ± .29	.49 ± .28	31
1806	1.38 ± .22	.47 ± .23	- .03 ± .27	- .18 ± .25	63
1845	1.16 ± .24	.78 ± .28	.25 ± .30	.37 ± .33	18
1874	1.36 ± .30	1.61 ± .39	1.04 ± .37	.74 ± .35	3
1908	1.93 ± .33	2.00 ± .38	.86 ± .29	.64 ± .31	0
1936	1.30 ± .28	1.36 ± .34	.37 ± .33	.43 ± .36	45
1971	1.17 ± .22	1.63 ± .30	.04 ± .26	.37 ± .27	48

1801A38

The only difference is that the $\Lambda^o K^o$ final state is pure isospin 1/2. Thus the Legendre coefficients may be written, as they were for elastic scattering, in terms of the amplitudes $f_{\ell J}$ and the coefficients $R^n_{\ell J, \ell' J'}$, listed in Table VIII.

$$A_n = \sum_{\ell J \leq \ell' J'} R^n_{\ell J, \ell' J'} \left\{ \mathrm{Re}\, f_{\ell J}\, \mathrm{Re}\, f_{\ell' J'} + \mathrm{Im}\, f_{\ell J}\, \mathrm{Im}\, f_{\ell' J'} \right\} \tag{3.3}$$

With the aid of Table VIII we may make a few rough deductions from the structure of the A_n's. The coefficient A_1/A_0 rises rapidly to a plateau starting at 1700. This activity most likely reflects interference of S1 with P1 or P3 wave. From elastic scattering we expect a P11 N* resonance near 1780 MeV but see no evidence for a P13 in this region so S1-P1 interference seems more probable. The coefficient A_2/A_0 has a small bump in the region of 1700, perhaps reflecting a small D3 amplitude here. The coefficient rises more rapidly near 1900, where we do see a P13 N* resonance in elastic scattering. The errors on the coefficients A_3/A_0 and A_4/A_0 are too large for us to make any reliable deductions.

In recent years, several authors[47a, 60, 61] have attempted partial wave analyses of $\Lambda^o K^o$ data. Deans et al.[60] made an energy-dependent fit, assuming the N* resonances based on CERN's set of elastic phase shifts.[7] They find that S11(1710) and P11 partial waves are dominant, where both P11(1460) and P11(1785) resonances contribute to the P11 wave. Small contributions come from P13(1855) and D13.

Doyle[47a] and Lovelace et al.[61] both undertook energy-independent analyses, connecting the solutions at each energy by a type of shortest distance criterion. Lovelace et al. confirm the results of Deans et al., that the S11 and P11 dominate, with small contributions from P13 and D13. However,

Lovelace et al. find that all the P11 comes from P11(1750). The difference is that the parameterization of Deans et al. does not allow for a background in P11 or S11 resonances although elastic phase shifts show that the backgrounds are certainly present in the elastic channels. Doyle finds that the S11 dominates in one solution and the P11 dominates in the other, with possible enhancement in P13 and D13. In all three fits, the D15 and F15 are small. The general trends seen in the Legendre coefficients agree well with these partial wave analyses. The present data may provide valuable input to these analyses because it falls in a region where there were previously large gaps in the data.[61]

3. Polarization

Another well known feature of the reaction $\pi^- p \rightarrow \Lambda^o K^o$ is the polarization of the lambda, which is strongest for backward scattered lambdas. The angular distribution of the proton from the decay of the lambda gives a measure of the lambda polarization P_{Λ^o}. The proton distribution is proportional to

$$P(\theta^P) = 1 - \alpha P_{\Lambda^o} \cos \theta^P \tag{8.13}$$

where θ^P is the angle between the proton momentum and the normal to the production plane $\hat{n}$ measured in the rest frame of the Λ^o. α is the asymmetry parameter of the Λ^o. $\alpha = -.62$.

$$\hat{n} = \vec{P}^{\pi}_{inc} \times \vec{P}_{\Lambda^o} / |\vec{P}^{\pi}_{inc} \times \vec{P}_{\Lambda^o}| \tag{8.14a}$$

$$\cos \theta^P = \vec{P} \cdot \hat{n} / |\vec{P}| \tag{8.14b}$$

$\vec{P}^{\pi}_{inc}$, $\vec{P}_{\Lambda^o}$ and $\vec{P}$ are the momenta of the pion beam, the Λ^o and the decay proton. The quantity αP_{Λ} can be estimated by measuring the number of

protons decaying in the forward (F) direction and the number decaying in the backwards (B) direction with respect to the normal to the production plane. In terms of F and B the Λ^0 polarization is

$$\alpha P_{\Lambda^0} = -2\left(\frac{F-B}{F+B}\right) \tag{8.15}$$

Experimentally the number of protons decaying backwards exceeds those decaying forward. The lambda polarization is a function of Λ^0 production angle and is largest for lambdas produced in the backwards direction. The polarization is usually antiparallel to the normal to the production plane. Thus protons like to go in the direction of Λ^0 polarization.

We determined αP_{Λ^0} by measuring (F-B)/(F+B) in three regions of lambda production angle and four-energy regions over the interval of the experiment. The results are summarized in Table XVII. Despite the large errors, the data show the general trend of large polarization for backward scattered lambdas.

4. Possible Test of Exchange Degeneracy

If a high-energy scattering process is dominated by the exchange of Regge trajectories that are exchange degenerate, then certain relations should hold between this s-channel and its crossed u-channel reaction. In the present case, $\pi^- p \rightarrow \Lambda^0 K^0$ may be related to the crossed-channel reaction $\bar{K}^0 p \rightarrow \Lambda^0 \pi^+$ if it is dominated by K*(890) and K*(1420) exchanges. The predicted relationships depend on the type of exchange degeneracy postulated.[62,63] Under "weak" exchange degeneracy, the differential cross sections $d\sigma/dt$ should be equal at high center-of-mass energies squared s and small values of momentum transfer $|t|$. In particular, the differential cross sections should have the

TABLE XVII

Lambda Polarization αP_{Λ^o} as a Function of Lambda Production Angle θ^{Λ^o}

Energy (MeV)	$-1.0 \leq \cos\theta^{\Lambda^o} \leq -.5$	$-.5 \leq \cos\theta^{\Lambda^o} \leq 0.0$	$0. \leq \cos\theta^{\Lambda^o} \leq 1.0$
1700 - 1780	.32 ± .21	.67 ± .27	.67 ± .29
1780 - 1860	.65 ± .19	.48 ± .30	.69 ± .37
1860 - 1920	.65 ± .18	- .13 ± .36	.06 ± .35
1920 - 1990	.59 ± .19	.40 ± .33	- .70 ± .30

1801A37

form

$$d\sigma/dt = a\,e^{bt} \tag{8.16}$$

For weak degeneracy to hold, at least two of the three quantities — intercept a, slope b and integrated cross section σ — must be equal for the two reactions.

Under the "strong" form of exchange degeneracy, the differential cross sections should still be equal but in addition there should be no polarization of the final baryon. The observed polarization of the Λ^0 at lower energies contradicts this prediction but comparison of the sign of polarization from $\pi^- p \rightarrow \Lambda^0 K^0$ to that from the reaction $\bar{K}^0 p \rightarrow \Lambda^0 \pi^+$ may indicate whether the polarization arises from interference of Regge trajectories of opposite signature or from interference of trajectories of the same signature but different slopes.[62]

Although the data of the present experiment is at relatively low energies and, according to the results of the phase-shift analyses, is still governed by s-channel resonances, the peak in the Λ^0 distribution at $\cos\theta\,(\Lambda_0^0, \pi^-) = 180^0$ indicates that t-channel exchanges are nevertheless already playing an important role. It was interesting to compare the slope of the momentum-transfer distribution $d\sigma/dt$ from the present experiment to that from the preliminary results of the measurement of $\bar{K}^0 p \rightarrow \Lambda^0 \pi^+$ in the region 1800-2100 MeV.[64] In Fig. 65 the momentum-transfer distribution is shown for all energies of the present experiment the slope did not change appreciable over this energy interval. The slope is $4.07^{+.15}_{-.08}$ (GeV)$^{-2}$, compared to the slope of $2.65^{+1.2}_{-0.5}$ for the crossed-channel reaction. This result agrees with results at higher energies, where the reaction $\pi^- p \rightarrow \Lambda^0 K^0$ has a slope of 7.3 ± 0.8 (GeV)$^{-2}$, significantly higher than the slope of 4.0 ± 0.6 (GeV)$^{-2}$ for the reaction $K^- N \rightarrow \Lambda\pi$.[63]

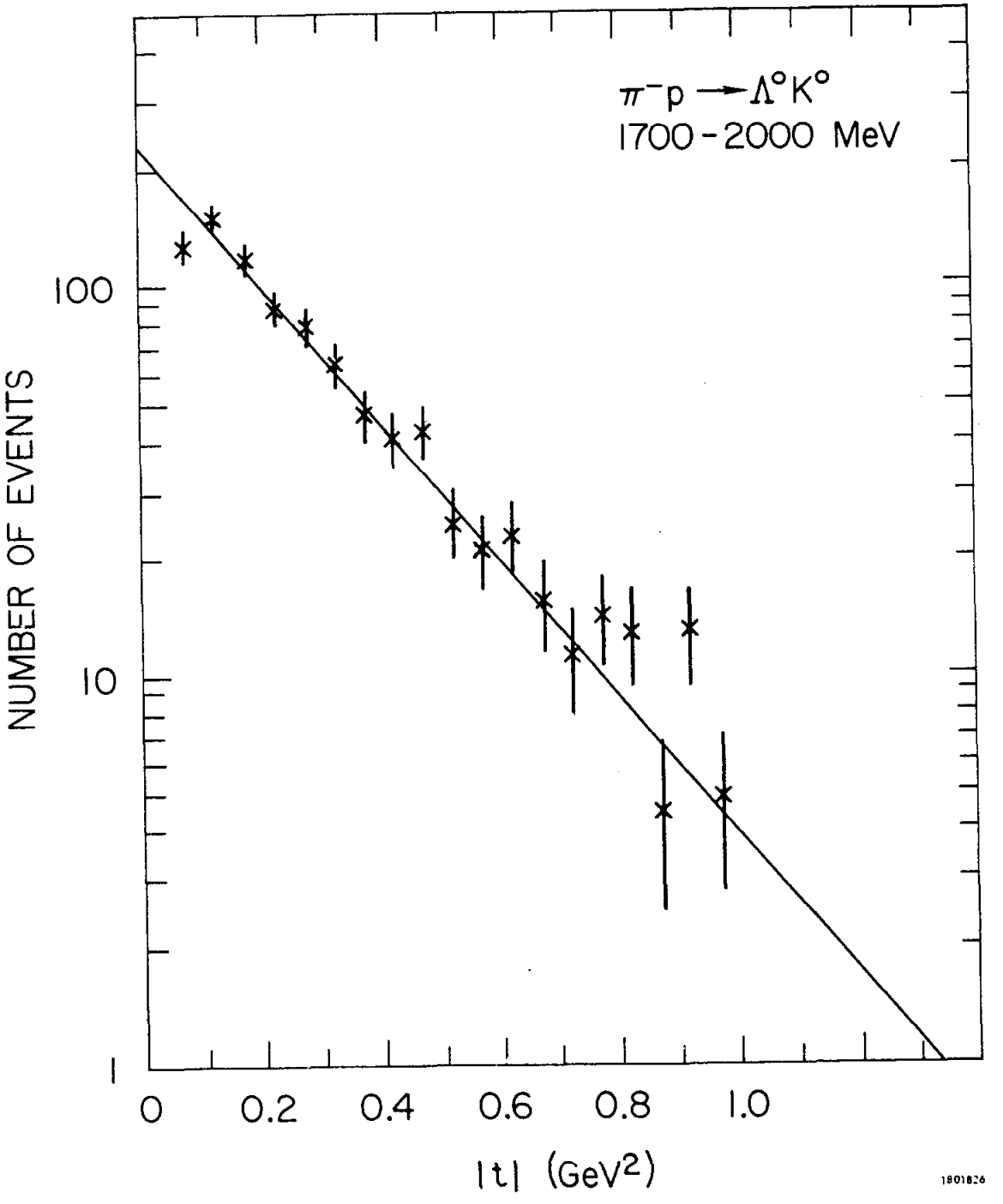

FIG. 65--Momentum-transfer distribution for all events in the reaction $\pi^- p \rightarrow \Lambda^0 K^0$.

REFERENCES

1. P. Bareyre, C. Bricman, A. V. Stirling and G. Vilet, Phys. Letters 18, 342 (1965); P. Bareyre, C. Bricman and G. Vilet, Phys. Rev. 165, 1730 (1968).
2. B. H. Bransden, P. J. O'Donnell and R. G. Moorhouse, Phys. Letters 11, 339 (1964); Phys. Rev. 139B, 1566 (1965); Proc. Roy. Soc. (London) A289, 538 (1966); Phys. Letters 19, 420 (1965).
3. P. Auvil, A. Donnachie, A. T. Lea and C. Lovelace, Phys. Letters 12, 76 (1964); 19, 148 (1965).
4. L. D. Roper, Phys. Rev. Letters 12, 340 (1964); L. D. Roper, R. M. Wright and B. T. Feld, Phys. Rev. 138B, 190 (1965); L. D. Roper and R. M. Wright, Phys. Rev. 138B, 921 (1965).
5. R. J. Cence, Phys. Letters 20, 306 (1966).
6. C. H. Johnson, Report No. UCRL-17683 (1967).
7. A. Donnachie, R. G. Kirsopp and C. Lovelace, Phys. Letters 26B, 161 (1968); C. Lovelace, Proceedings of the 1967 Heidelberg Conference (North-Holland Publishing Co., Amsterdam, 1967), p. 79, H. Filthuth, ed.; C. Lovelace, Invited paper at the Conference on πN Scattering, Irvine, 1967 (1967); CERN Preprint No. TH-839 (1967).
8. A. T. Lea, G. C. Oades, D. L. Ward, I. M. Cowan, W. M. Gibson, R. S. Gilmore, J. Malos, V. J. Smith and M.A.R. Kemp, Report No. RPP/H/57, Rutherford Laboratory (unpublished).
9. R. Ayed, P. Bareyre and G. Vilet, Phys. Letters 31B, 598 (1970).
10. A. T. Davies, Nucl. Phys. B21, 359 (1970).
11. For various reviews, see
    a. R. G. Moorhouse, Ann. Rev. Nucl. Sci. 19, 301 (1969).

b. D. Herndon, A. Barbaro-Galtieri and A. H. Rosenfeld, Report No. UCRL-20030 πN (1970), unpublished.

c. G. Giacomelli, P. Pini and S. Stagni, Report No. CERN/HERA 69-1.

d. G. L. Shaw, D. Y. Wang, N. Y. Wiley, Proceedings of the Pion-Nucleon Scattering Conference, Irvine, 1967 (1967).

12. The contents of this table are taken from Particle Data Group, Phys. Letters 33B, 1 (1970). The resonance parameters listed come from the following sources:

a. P. Bareyre, C. Bricman and G. Vilet, Phys. Rev. 165, 1730 (1968). These parameters are determined from the total cross section.

b. P. Bareyre, C. Bricman and G. Vilet, Phys. Rev. 165, 1730 (1968). These parameters are determined from the highest velocity criterion.

c. Clarborne H. Johnson, Jr., Report No. UCRL-17683, Lawrence Radiation Laboratory (1967).

d. A. Donnachie, R. G. Kirsopp and C. Lovelace, Phys. Letters 26B, 161 (1968).

e. C. Lovelace, Proceedings of the 1967 Heidelberg Conference (North-Holland Publishing Co., Amsterdam, 1967), p. 79, H. Filthuth, ed.

f. R. G. Kirsopp, Ph.D. Thesis (unpublished).

g. A. T. Davies, Nucl. Phys. B21, 359 (1970). These parameters correspond to solution A.

h. A. T. Davies, Nucl. Phys. B21, 359 (1970). These parameters correspond to solution B.

i. A. T. Lea, G. C. Oades, D. L. Ward, I. M. Cowan, W. M. Gibson, R. S. Gilmore, J. Malos, V. J. Smith and M.A.R. Kemp, Report No. RPP/H/57, Rutherford Laboratory (unpublished).

13. F. S. Crawford, Proceedings of the International Conference on High Energy Physics at CERN, 1962 (1962), p. 270; J. A. Anderson, Report No. UCRL-10838 (1963); J. Anderson, F. S. Crawford, Jr. and J. C. Doyle, Phys. Rev. 165, 1483 (1968); J. C. Doyle, Report No. UCRL-18139 (1969).

14. T. H. Fields, E. L. Goldwasser and U. E. Kruse, "Design for a 6 BeV/c separate K^- beam," A.N.L. Internal Report No. THF/ELG/UEK-1 (October 1961) (unpublished).

15. S. Wolf, N. Schmitz, L. Lloys, W. Laskar, F. Crawford, Jr., J. Button, J. Anderson and G. Alexander, Rev. Mod. Phys. 33, 439 (1961).

16. SLAC Physics Note, APE Data Processing Note No. 1.

17. J. Lynch, Report No. UCRL-17238 (1967).

18. J. Burkhard, "Programming for flying spot devices," Proceedings of a Conference on Flying Spot Devices at Columbia, October, 1965 (1965).

19. S. Wojcicki and F. Solmitz, "Missing mass calculations," Alvarez Group Memo No. 367 (unpublished).

20. P. J. Duke, D. P. Jones, M.A.R. Kemp, P. G. Murphy, J. D. Prentice, J. J. Thresher, Phys. Rev. 149, 1077 (1966).

21. J. A. Helland, T. J. Devlin, D. E. Hagge, M. J. Longo, B. J. Moyer, and C. D. Wood, Phys. Rev. 134B, 1062 (1964); J. A. Helland, C. D. Wood, T. J. Devlin, D. E. Hagge, M. J. Longo, B. J. Moyer and V. Perez-Mendez, Phys. Rev. 134B, 1079 (1964).

22. D. M. Ogden, D. E. Hagge, J. A. Helland, M. Banner, J. F. Detoeuf and J. Leiger, Phys. Rev. 137B, 115 (1965).

23. M. DeBeer, B. Deler, J. Dolbeau, M. Neveu, Nguyen Thuc Diem, G. Smadja, G. Valladas, Nucl. Phys. B12, 599 (1969); W. Chinowsky, J. H. Mulvey and D. H. Saxon, Phys. Rev. (to be published).

24. A. A. Carter, F. K. Riley, R. J. Tapper, D. V. Bugg, R. S. Gilmore, K. M. Knight, D. C. Salter, G. H. Stafford, E.J.N. Wilson, J. D. Davies, J. D. Dowell, P. M. Hattersley, R. J. Homer and A. W. O'Dell, Phys. Rev. 168, 1457 (1968).

25. A. D. Brody, R. J. Cashmore, A. Kernan, D.W.G.S. Leith, B. G. Levi, B. C. Shen, J. P. Berge, D. J. Herndon, R. Longacre, L. R. Price, A. H. Rosenfeld, P. Söding, Report No. SLAC-PUB-789, Suppl. 1.

26. J. Kirz, J. Schwarz, R. D. Tripp, Phys. Rev. 130, 2481 (1963).

27. MURTLEBURT, J. Friedman, Lawrence Radiation Laboratory, Berkeley, Alvarez Programming Group Note No. P-156 (unpublished).

28. J. D. Jackson, Nuovo Cimento 34, 1644 (1964).

29. J. M. Blatt, V. F. Weisskopf, Theoretical Nuclear Physics (John Wiley and Sons, Inc., New York, 1956).

30. D. Branson, P. V. Landshoff, J. C. Taylor, Phys. Rev. 132, 902 (1962).

31. R. C. Arnold, J. L. Uretsky, Phys. Rev. 153, 1443 (1968).

32. D. H. Morgan, Phys. Rev. 166, 1731 (1968).

33. R. J. Cashmore, D. Phil. Thesis, Oxford University, England (unpublished).

34. M. Jacob and G. C. Wick, Ann. Phys. 7, 404 (1959).

35. R. G. Roberts, Ann. Phys. 44, 325 (1967).

36. M. E. Rose, Elementary Theory of Angular Momentum (John Wiley and Sons, Inc., New York, 1957).

37. A. D. Brody, D.W.G.S. Leith, B. G. Levi, B. C. Shen, D. Herndon, R. Longacre, L. Price, A. H. Rosenfeld, P. Söding, Phys. Rev. Letters

22, 1401 (1969); A. Donnachie, C. Lovelace, Phys. Rev. D1, 956 (1970) (reply); A. D. Brody et al., Report No. SLAC-PUB-709 (1970)(reply).

38. A. D. Brody, A. Kernan, Phys. Rev. 182, 1785 (1969).

39. G. C. Sheppey, MINFUN, CERN 6600 Computer Program Library Write Up.

40. R. Levi-Setti, Rapporteur Talk on Strange Baryon Resonances, Proceedings of the Lund International Conference on Elementary Particles, Lund, 1969 (1969); R. D. Tripp, Rapporteur Talk on Strange Baryon Resonances, Proceedings of the 14th International Conference on High Energy Physics, Vienna, 1968 (1968); R. D. Tripp, D.W.G.S. Leith, A. Minten, R. Armenteros, M. Ferro-Luzzi, R. Levi-Setti, H. Filthuth, V. Hepp, E. Kluge, H. Schneider, R. Barloutaud, P. Granet, J. Meyer, J. P. Porte, Nucl. Phys. B3, 10 (1967).

41. The branching ratios listed in Table XII are taken from Particle Data Group: Phys. Letters 33B, 1 (1970). They are based on the following experiments.

    a. R. Armenteros, M. Ferro-Luzzi, D.W.G.S. Leith, R. Levi-Setti, A. Minten, R. D. Tripp, H. Filthuth, V. Hepp, E. Kluge, H. Schneider, R. Barloutaud, P. Granet, J. Meyer, J. P. Porte, Z. Phys. 202, 486 (1967).

    b. R. P. Uhlig, G. R. Charlton, P. E. Condon, R. G. Glasser, G. B. Yodh, N. Seeman, Phys. Rev. 155, 1448 (1967).

    c. W. H. Sims, J. R. Albright, E. B. Brucker, J. T. Dockery, J. E. Lannutti, J. S. O'Neall, B. G. Reynolds, J. F. Bartley, R. M. Dowd, A. F. Greene, J. Schneps, M. Meer, J. Mueller, M. Schneeberger, S. Wolf, Phys. Rev. Letters 19, 1413 (1968).

42. R. H. Dalitz, Strange Particles and Strong Interactions (Oxford University Press, London, 1962), pp. 51-69.

43. R. H. Dalitz, Ann. Rev. Nucl. Sci. 13, 339 (1963).

44. C. B. Chiu, R. D. Eandi, A. C. Helmholtz, R. W. Kenney, B. J. Moyer, J. A. Poirier, W. B. Richards, R. J. Cence, V. Z. Peterson, H. K. Sehgal, V. J. Stenger, Phys. Rev. 156, 1415 (1967).

45. F. Bulos, R. E. Lanou, A. E. Pifer, A. M. Shapiro, M. Widgoff, R. Panvini, A. E. Brenner, C. A. Bordner, M. E. Law, E. E. Ronat, K. Strauch, J. Szymanski, P. Bastien, B. B. Brabson, Y. Eisenberg, B. T. Feld, V. K. Fischer, I. A. Pless, L. Rosenson, R. K. Yamamoto, G. Calvelli, L. Guerriero, G. A. Salandin, A. Tomasin, L. Ventura, C. Voci, F. Waldner, Phys. Rev. Letters 13, 558 (1964).

46. C. R. Cox, P. J. Duke, K. S. Heard, R. E. Hill, W. R. Holley, D. P. Jones, F. C. Shoemaker, J. J. Thresher, J. B. Warren, J. C. Sleeman, Report No. RPP/H/46, Rutherford Laboratory.

47. Sections of this data have been reported in the following papers:

    a. J. C. Doyle, Report No. UCRL-18139 (1969).

    b. J. Anderson, Report No. UCRL-10838 (1963).

    c. J. Anderson, F. Crawford, B. Crawford, R. Golden, L. Lloyd, G. Meisner, L. Price, Proceedings of the 1962 International Conference on High Energy Physics at CERN (CERN, Geneva, 1962), p. 827.

    d. S. Wolf, N. Schmitz, L. Lloyd, W. Laskar, F. Crawford, J. Button, J. Anderson, G. Alexander, Rev. Mod. Phys. 33, 439 (1961).

48. J. Steinberger, Rapporteur Talk in the Proceedings of the 1958 Annual International Conference on High Energy Physics at CERN (CERN, Geneva, 1958), p. 147.

49. J. Steinberger, Rapporteur Talk in the Proceedings of the Ninth International Conference on High Energy Physics, Kiev, 1959 (Academy of Sciences, Moscow, USSR, 1959), p. 443.

50. F. Eisler, R. Plano, A. Prodell, N. Samios, M. Schwarz, J. Steinberger, P. Bassi, V. Borelli, G. Puppi, G. Tanaka, P. Woloschek, V. Zoboli, M. Conversi, P. Franzini, I. Mannelli, R. Santangelo, V. Silvestrini, Nuovo Cimento 10, 468 (1958).

51. J. Keren, Phys. Rev. 133B, 457 (1964).

52. L. Bertanza, P. L. Connolly, B. B. Culwick, F. R. Eisler, T. Morris, R. Palmer, A. Prodell, N. Samios, Phys. Rev. Letters 8, 333 (1962).

53. L. B. Leipuner and R. K. Adair, Phys. Rev. 109, 1358 (1958).

54. J. L. Brown, D. A. Glaser, M. L. Perl, Phys. Rev. 108, 1036 (1957).

55. O. Goussu, M. Sene, B. Ghidini, S. Mongelli, A. Romano, P. Woloschek, V. Alles-Borelli, Nuovo Cimento 42, 606 (1965).

56. L. L. Yoder, C. T. Coffin, D. I. Meyer, K. M. Terwilliger, Phys. Rev. 132, 1778 (1963).

57. O. I. Dahl, L. M. Hardy, R. I. Hess, J. Kirz, D. H. Miller, J. A. Schwartz, Phys. Rev. 163, 1430 (1967).

58. O. van Dyck, R. Blumenthal, S. Frankel, V. Highland, J. Nagy, T. Sloan, M. Takata, W. Wales, W. Werbeck, Phys. Rev. Letters 23, 50 (1969).

59. T. O. Binford, M. L. Good, V. G. Lind, D. Stern, R. Krauss, E. Dettman, Phys. Rev. 183, 1134 (1969).

60. S. R. Deans, W. G. Holladay, J. E. Rush, Proceedings of the 14th International Conference on High Energy Physics in Vienna (CERN, Geneva, 1968), paper 479; J. E. Rush, Phys. Rev. 173, 1776 (1968).

61. C. Lovelace, F. Wagner, J. Iliopoulos, Proceedings of the 14th International Conference on High Energy Physics in Vienna (CERN, Geneva, 1968), paper 256; F. Wagner and C. Lovelace, Report No. TH-1227-CERN (1970).

62. F. J. Gilman, Phys. Letters 29B, 673 (1969).

63. K. W. Lai and J. Louie, Nucl. Phys. B19, 205 (1970).

64. A. D. Brody, W. B. Johnson, D.W.G.S. Leith, J. S. Loos, G. J. Luste, K. Moriyasu, B. C. Shen, W. M. Smart, F. C. Winkelmann, R. J. Yamartino, B. Kehoe, private communication.

APPENDIX

MINFUN PROGRAM FOR COUPLED-CHANNEL ANALYSIS

A. Format of Input Cards

1. Control Cards for MINFUN[39]

2. Input Data

a. MAXEXP format I10

This card specifies the number of experiments to be read in. Each measurement of an angular distribution or polarization at one energy counts as one experiment.

b. (REFER (I), I = 1, 20) format 20A4

This is the reference to the next experiment.

c. ITYPE (N), ECM(N), TXS(N), DTXS(N) format I10, 3F10.3

The first number specifies the type of experiment, whether elastic, charge exchange, inelastic angular distribution, or polarization. (See Section V, No. 14.) The next three quantities are the center-of-mass energy, cross section and error on the cross section, respectively.

d. NPTS (N), SCALEX, XLOW format I5, 2F10.3

This card defines the values of cos θ (π^-_{out}, π^-_{inc}) at which angular distributions are measured. Since measurements are usually given in bins of equal size in cos θ, it is necessary only to specify the number of bins, the bin size and the lower edge of the first bin, respectively.

For polarization measurements, the values of cos θ are <u>not</u> equally spaced and must be read in explicitly, as described in (f).

e. ((Z(N,K), DZ(N,K)), K=1, NPTS (N)) format 16F5.2

This card contains the value of the measured quantity along with its error. N is the order of the experiment and K is the number of the bin in cos θ.

f. (X(N,K), K=1, NPTS(N)) format 10F5.3

Used for polarization experiments only. This card specifies the values of cos θ where measurements exist.

g. Repeat cards 2 through 6 for N=1, MAXEXP

3. Initial Values of Parameters

a. (TITLE (I), I = 1, 20) format 20A4

b. IWAVE (J), (PP (I), I = 1, 6) format I10, 6F10.3

The array IWAVE specifies the type of parameterization to be used for the Jth wave. (See Section V, No. 15.) The array PP contains the starting values for the parameters describing this partial wave.

	Resonance	Background	I
PP (I) =	θ	θ_1	1
	Γ	θ_2	2
	E_r	δ_1	3
	α	α	4
	β	β	5
	δ_B	δ_2	6

c. (IPP (I), I = 1, 6) format 6I5

This array tells which of the preceding parameters are to be varied by MINFUN and which are to be held fixed.

IPP (I) = 0	if	PP (I) is constant
= 1	if	PP (I) is variable.

d. Repeat cards 2 and 3 for each partial wave J = 1, 18 in the following order:

$J = 1, 2, \ldots, 9, 10, \ldots 18$ for $S_{11}, P_{11}, \ldots, G_{19}, S_{31}, \ldots, G_{39}$.

B. Definition of Arrays

1.	BOXDB (K) K = 1, 20	Value of the measured quantity in the Kth bin. Used for plotting every 1000 steps.
2.	C(J, L, IS) J = 1, 9, 2 L = 1, 5 IS = 1, 8	Clebsch-Gordon coefficient $C^{js\ell}_{0\lambda\lambda}$, where: $J = 2j$ $L = \ell+1$ $IS = 4\,(S-\frac{1}{2}) + LMBDA$ $LMBDA = \lambda + 5/2$
3.	CG (I, M) I = 1, 2 M = 1, 5	Isospin Clebsch-Gordon coefficient. Isospin is 1/2, 3/2 for I = 1, 2, respectively. M = ITYPE is the type of experiment as defined in (14) below.
4.	D(N, K, MK) N = 1, 25 K = 1, 20 MK = 1, 72	The rotation-matrix element $d^{j}_{\lambda\lambda'}(\theta)$ for the Kth bin of the Nth experiment, where: $MK = 8*(2j-1) + 4*(LMBIN-1) + LAMBDA$ $LMBIN = \lambda + 3/2$ $LAMBDA = \lambda' + 5/2$
5.	DTXS(N) N = 1, 25	Error on the cross section for the Nth experiment.
6.	DZ(N, K) N = 1, 25 K = 1, 20	Error on the measured quantity in the Kth bin of the Nth experiment.

7.	ECM(N) N = 1, 25	Center-of-mass energy of the Nth experiment.
8.	EPS (25) N = 1, 25	Normalization parameter for experiment N. Set equal to 1 if not read in.
9.	F	Value of χ^2 returned to MINFUN after call to FCN.
10.	FP (K, LMBIN, LAMBDA) K = 1, 20 LMBIN = 1, 2 LAMBDA = 1, 4	Value of $\langle\lambda'\|T\|\lambda\rangle$ for the Kth bin, where: LMBIN = $\lambda + 3/2$ LAMBDA = $\lambda' + 5/2$
11.	G (MPAR) MPAR = 1, 108	Derivatives of F with respect to the parameters P (MPAR). These are currently set to zero on the first call to FCN. MINFUN then estimates the derivatives numerically.
12.	IFLAG	Flag which is set as follows: IFLAG = 1 first entry to FCN 2, 4 normal entry to FCN 3 terminating entry to FCN
13.	IPARAM (MPAR) MPAR = 1, 108	Array specifying whether the MPARth parameter is to be varied or to remain fixed. See No. 18 below for order in which parameters are stored.

14. ITYPE (N)

N = 1, 25

Type of quantity measured by experiment N.

ITYPE (N) = 1 for $d\sigma/d\Omega$ $(\pi^- p \rightarrow \pi^- p)$

2 for $d\sigma/d\Omega$ $(\pi^- p \rightarrow \pi^0 n)$

3 for $d\sigma/d\Omega$ $(\pi^- p \rightarrow \pi^- \Delta^+)$

4 for $d\sigma/d\Omega$ $(\pi^- p \rightarrow \pi^+ \Delta^-)$

5 for polarization $(\pi^- p \rightarrow \pi^- p)$

15. IWAVE (JJI)

JJI = 1, 18

Type of parameterization used for JJIth wave where:

IWAVE = 1 for resonance, some parameters variable

2 for resonance, all parameters fixed

3 for background, some parameters variable

4 for background, all parameters fixed

and JJI = 1, ..., 9, 10, ... 18 for S_{11}, ..., G_{19}, S_{31}, ... G_{39}

16. NPTS (N)

N = 1, 25

Number of bins in the distribution for the Nth experiment.

17. P (MPAR)

MPAR = 1, 108

Parameters to be varied by MINFUN in search of a minimum.

18. PARAM (MPAR)

MPAR = 1, 108

All parameters (variable or fixed). These are stored in the following order:

$A(S_{11})$, $A(P_{11})$, ..., $A(G_{39})$, $B(S_{11})$, ..., $B(G_{39})$, $C(S_{11})$, ..., $C(G_{39})$, $D(S_{11})$, ..., $D(G_{39})$, $E(S_{11})$, ..., $E(G_{39})$ where:

Resonance	Background	MPAR
$A = \theta$	θ_1	1, 18
$B = \Gamma$	θ_2	19, 36
$C = E_r$	δ_1	37, 54
$D = \alpha$	α	55, 72
$E = \beta$	β	73, 90
$F = \delta_B$	δ_2	91, 108

19. PCM (N),

PCMOUT (N)

N = 1, 25

Incoming and outgoing center-of-mass momentum respectively, for Nth experiment. Expressed in MeV/c.

20. PPRINT (MPAR)

MPAR = 1, 108

Parameters converted to convenient form for printout every 500 entries to FCN.

	Resonance	Background	MPAR=
PPRINT(MPAR) =	$\cos^2\theta$	$\cos^2(\theta_1+q\theta_2)$	1, 18
	Γ	$\tan\theta_2$	19, 36
	E_r	$\tan\delta_1$	37, 54
	$\cos\alpha$	$\cos\alpha$	55, 72
	$\cos\beta$	$\cos\beta$	73, 90
	$\mathrm{ctn}\,\delta_B$	$\tan\delta_2$	91, 108

21.	QCM(N), QCMOUT(N) N = 1, 25	Incoming and outgoing center-of-mass momentum, expressed in $(mb)^{-1/2}$.
22.	TXS(N) N = 1, 25	Cross section for experiment N.
23.	V(N, LIN, LOUT) N = 1, 25 LIN = 1, 5 LOUT = 1, 5	Barrier penetration factor for Nth experiment. $$V = \left[\frac{(kR)^{2\ell+1}\,(k'R)^{2\ell'+1}}{D_\ell(kR)\;D_{\ell'}(k'R)}\right]^{1/2},$$ where: R is the radius of interaction, set equal to the pion Compton wavelength. k, k' are incoming and outgoing wave numbers, respectively. $D_\ell(kR)$ are functions given in Ref. 29. $LIN = \ell-1$ $LOUT = \ell'-1$.
24.	VR1(JJI, LIN) VR2(JJI, LIN, LOUT) JJI = 1, 18 LIN = 1, 5 LOUT = 1, 5	Barrier penetration factor at resonance, for a resonance in the JJIth partial wave. The formula is similar to that for 23 above, with k and k' replaced by k_R, k'_R, the wave numbers at resonance. VR1 is for elastic channels; VR2 for inelastic.
25.	X(N, K), Z(N, K) N = 1, 25 K = 1, 20	Values of cos θ and measured quantity f(cos θ) for the Kth bin of the Nth experiment.

26. ZCALC(N,K) Value of the calculated quantity for the Kth bin of the Nth experiment.

N = 1, 25

K = 1, 20

C. Description of Subroutines

1. Barrier (L,X,V)

This subroutine computes the barrier penetration factor V as described in (23) and (24) of Section V. L is the orbital angular momentum and X = kR.

$$V = \frac{(kR)^{2\ell+1}}{D_\ell(kR)}$$

2. COEF (J, L, MS, M, CC)

This subroutine computes the Clebsch-Gordon coefficients $CC = C^{js\ell}_{0\lambda\lambda}$ according to the formula given on p. 39 of Rose.[36] $J = 2j$, $L = \ell$, $M = 2\lambda$, and $MS = 2S$.

3. ROTATE (J, M, X, DD)

This subroutine computes the rotation matrix elements DD(1), DD(2) $= d^j_{-\frac{1}{2}\lambda'}(\theta)$, $d^j_{+\frac{1}{2}\lambda'}(\theta)$ according to the formula given on p. 52, Rose.[36] $J = 2j$, $M = 2\lambda$, $X = \cos\theta$.

4. PLOT 1 (PNT)

This subroutine plots histograms of the measured distributions with curves of the fitted distributions superposed.

5. HIGH

This subroutine is called by PLOT 1 to adjust the scale for plotting.